SAKARYA ÜNİVERSİTESİ

FEN BİLİMLERİ ENSTİTÜSÜ DERGİSİ

Sakarya University Journal of Science (SAUJS)

SAKARYA ÜNİVERSİTESİ

e-issn: 2147-835X

SAÜ Fen Bil Der/SAUJS

Cilt/Volume: 26

Sayı/Issue: 3

Haziran/June 2022

Sakarya Üniversitesi Fen Bilimleri Enstitüsü Dergisi
(Sakarya University Journal of Science)
Cilt/Volume: 26 No/ Issue:3 Haziran/June 2022

Editör Kurulu/Editorial Boards

Guest Editor

English Language Editor

Editorial Assistant

SAKARYA ÜNİVERSİTESİ FEN BİLİMLERİ ENSTİTÜSÜ DERGİSİ
(SAKARYA UNIVERSITY JOURNAL OF SCIENCE)
İÇİNDEKİLER/CONTENTS
Cilt/Volume: 26 – No/Issue3: (HAZİRAN/JUNE-2022)

RESEARCH ARTICLES

SAKARYA ÜNİVERSİTESİ
FEN BİLİMLERİ ENSTİTÜSÜ DERGİSİ

Sakarya University Journal of Science
SAUJS

ISSN 1301-4048 e-ISSN 2147-835X Period Bimonthly Founded 1997 Publisher Sakarya University
http://www.saujs.sakarya.edu.tr/

Title: Experimental Investigation on the Variation in Shear Strength of Clayey Soil Reinforced with Randomly Distributed Alkali-Resistant Glass Fiber

Authors: Ercüment KEKEÇ, Sedat SERT, Eylem ARSLAN, Ertan BOL, Aşkın ÖZOCAK

Recieved: 2022-01-29 00:00:00

Accepted: 2022-04-11 00:00:00

Article Type: Research Article

Volume: 26
Issue: 3
Month: June
Year: 2022
Pages: 438-447

How to cite
Ercüment KEKEÇ, Sedat SERT, Eylem ARSLAN, Ertan BOL, Aşkın ÖZOCAK; (2022), Experimental Investigation on the Variation in Shear Strength of Clayey Soil Reinforced with Randomly Distributed Alkali-Resistant Glass Fiber . Sakarya University Journal of Science, 26(3), 438-447, DOI: 10.16984/saufenbilder.1064811
Access link
http://www.saujs.sakarya.edu.tr/tr/pub/issue/70993/1064811

Sakarya University Journal of Science 26(3), 438-447, 2022

Experimental Investigation on the Variation in Shear Strength of Clayey Soil Reinforced with Randomly Distributed Alkali-Resistant Glass Fiber

Ercüment KEKEÇ[1], Sedat SERT*[2], Eylem ARSLAN[2],
Ertan BOL[2], Aşkın ÖZOCAK[2]

Abstract

Geotechnical investigations are one of the most crucial parts of the construction to save the time and effort spent on the projects. Particularly, in the case of the clays with high plasticity are encountered, the analysis of bearing capacity and settlement of structures such as buildings, roads, and dams governs the design. The possible solutions can be leaving the land, reaching a strong soil bypassing the weak one, removing the weak soil by replacing it with a higher strength of the material, and applying soil improvement methods. Glass fibers are one of the synthetic additives which may be used to address improving the weak soil properties. In this study, the effect of alkaline-resistant glass fiber additive on the undrained shear strength of the clayey soils was investigated. Fibers with distinct lengths were added to the natural soil at increasing rates, and the mixtures were prepared in the optimum water content. The prepared mixtures were compacted in a compaction mold with a diameter of 50 mm and a height of 100 mm with standard energy. Unconfined compression test (UC) were conducted on a total of 210 cylindrical samples, 10 of natural clay and 200 of fiber-reinforced. The maximum increase was at 0.5% of a fiber blend of 40 mm length. As a result of 210 UC tests, it was observed that the alkaline-resistant glass fiber additive increased the shear strength of the clay soil.

Keywords: Alkaline-resistant glass fiber, soil improvement, undrained shear strength, Unconfined compression test.

1. INTRODUCTION

The desired situation in soil stabilization is to increase the strength by reducing the void ratio in the existing soil with the necessary equipment and closing these voids with additives. Soil improvement and stabilization methods can be divided into three groups. These are temporarily effective, permanent effective without additive to the soil, and permanent effective with additives [1]. In the solution of stability problems such as soil liquefaction, settlement problem, bearing capacity problem, different shallow soil improving methods are used instead of deep stabilization methods due to economic requirement and application difficulty. Among these methods, the most widely used method is adding natural and artificial substances as

* Corresponding author: sert@sakarya.edu.tr
[1] ÇBS Yapı Denetim Ltd. Şti.
E-mail: kekecercu@icloud.com
ORCID: https://orcid.org/ 0000-0001-8301-013X
[2] Sakarya University, Engineering Faculty, Civil Engineering Department
E-mail: eylemarslan@sakarya.edu.tr, ebol@sakarya.edu.tr, aozocak@sakarya.edu.tr
ORCID: https://orcid.org/0000-0002-4114-6132, https://orcid.org/0000-0002-9053-1061, https://orcid.org/0000-0002-3903-0384, https://orcid.org/0000-0003-1102-1424

external additives. We can distinguish synthetic fibers as glass and polymer fibers used in the petrochemical industry among these additives. Fibers are substances that can be bent and obtained from natural resources with strength or produced industrially by human hands with desired properties [2]. The production of glass fiber and various products dates back to ancient times. Although Rene Ferchault de Reaumur produced glass fiber in 1734, its fabrication took place in the late 18^{th} century. The reason for this is that Reaumur had difficulty in weaving these fine glass fibers such as silk [3]. Glass material, which is the main product in the manufacture of glass fibers, is in the form of lime or soda silicate, or borax silicate. Glasses are complex mixtures of alkali and alkaline earth silicates containing borate and aluminate. Since the ratio of the additives added to the glass changes, the chemical structure of the glass fibers becomes uncertain. As a general rule, the ratios of sodium carbonate, calcium carbonate, aluminum-hydroxide, magnesium-silicon, and boric acid can be counted.

Although the elongation ability and friction resistance of glass, which is a fiber type, is not high, it is used as an additional product in plastic products as an insulating material for heat and electricity. It shows that it is important to use glass fibers in X-ray and radiation isolation, protective materials against fires such as awnings and curtains, oil tanker ships, filtration, impermeability of chemical substance pipes, coating of various boilers and cables, underground insulation, coating of building elements in dust and smoke filters, packaging papers, the automotive industry, in parts of boats, tanks and planes, in rocket and aerospace industries. With the Covid-19 pandemic, a separate bracket can be opened to use glass fiber in surgical masks.

It is known that glass powders and fibers have positive effects when used in concrete applications and cement-based composites [4]. It is known that the water-retaining fibers when the concrete is wet prevent shrinkage cracks as a result of curing as the concrete begins to set, and thus prolongs the life of the concrete by protecting it against chemicals. Due to the disadvantage of alkalinity, additional studies of glass fiber with high alkali resistance were carried out to prevent segregation in concrete. Although it is seen that glass powder studies are carried out in soil stabilization, it is seen that the number of works with alkali-resistant (ACR) glass fiber is not sufficient.

In this paper, the effect of glass fiber additive on the undrained shear strength of clay soil was investigated. In this experimental study, the physical properties of the clay soil obtained from Sapanca district of Sakarya province were determined. Fibers were cut into 10 mm, 20 mm, 30 mm, and 40 mm lengths. Fibers with different lengths were added to the natural soil at the rates of 0.25%, 0.5%, 1%, 1.5%, and 2% by dry weight, and the mixture was prepared in the optimum water content of the soil. The prepared mixtures were compacted in a compaction mold with standard energy. The compacted cylindrical samples with a diameter of 50 mm, a height of 100 mm were obtained. A total of 210 cylindrical samples, 10 of them formed from natural clay and 200 produced by mixing soil with glass fiber, were tested in Unconfined Compression (UCS) device to simulate rapid loading conditions.

2. LITERATURE REVIEW

When soil reinforcement with natural and artificial additives is examined in the literature, it is seen that there are sufficient studies [5]. Among the studies with different reinforcement materials, Diallo and Ünsever [6] determined that the strength of the soil can be increased while construction debris waste and lime were used as reinforcement materials in different percentages. Reinforcement was applied by adding 2% lime and construction debris at rates ranging from 5% to 35% with increasing rates of 5% to the soil. In the study, sieve analysis and Atterberg limit tests were carried out, and optimum water content was calculated as a result of compaction. Soil samples with 38 mm x 76 mm dimensions were prepared in the optimum water content and subjected to unconfined compression tests after curing for 3, 7, and 28 days. It was determined that the best

stabilization was obtained for the samples mixed with 2% lime and 20% construction debris.

On the other hand, Bilgen [9] examined the behavior of bentonite clay reinforced with 3, 5, 10, 20, and 25% of glass powder by dry weight of the soil through modified Proctor, unconfined compression and California bearing ratio (CBR) tests. While the strength of the natural bentonite clay cured for 28 days was 178 kPa, the 28-day strength of the 25% of glass powder added sample strength increased by 450% and became 795 kPa. It was observed that the CBR is increased by 400%. It has been reported that with the addition of glass powder, the water content decreased, the dry unit weight increased, and the CBR and unconfined compression values significantly increased.

In a study conducted by Maraşlı [4], 0, 1, 2, and 3% glass fiber reinforced concretes were prepared to form the estimation model of flexural and compressive strength using the maturity index method. The temperature sensors were placed in the compressive and flexural strength test samples, and by using the temperature measurements at 0.5, 1, 1.5, 2, 3, 5, 7, 14, 28, and 56 days, the maturity index values were found. Although it was observed that the concretes with 2% glass fiber added reached the maximum compressive strength, decreases were detected in the compressive strength of the concretes with 3% glass fiber addition. The maximum flexural strength was obtained in the case of the soil mixed with 3% glass fiber. The flexural strength of the 28-day fiber-concrete mixture increased by 55% compared to the fiberless concrete. As the concrete age progressed, the flexural strength values increased. Through the results obtained in the study, the necessary correlations were derived.

3. MATERIALS AND METHODS

3.1. Clayey Soil

Soil samples used in the study were obtained from the Sapanca district of Sakarya province (Figure 1). The physical properties of the soil given in Table 1 were determined as a result of the index and mechanical tests on the soil. The grain size distribution curve of the soil, in which the maximum grain size is 2 mm, is shown in Figure 2. The class of clayey soil was determined as CH (high plasticity clay) according to both TS 1500/2000 [10] and USCS [11] standards.

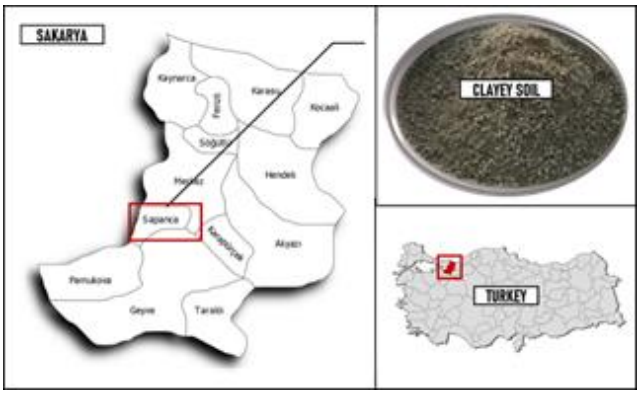

Figure 1 The sampling area and clayey soil used in the study

Table 1
Physical properties of the soil

Property	Value	Unit
-No 200	99.98	%
Liquid limit (LL)	72.00	%
Plastic limit (PL)	30.49	%
Plasticity index (PI)	41.51	%
Maximum dry unit weight ($\rho_{k,maks}$)	14.80	kN/m^3
Optimum water content (w_{opt})	25.00	%
Specific gravity (G_s)	2.65	-
Soil class: CH (according to TS 1500/2000 and the USCS) [10, 11]		

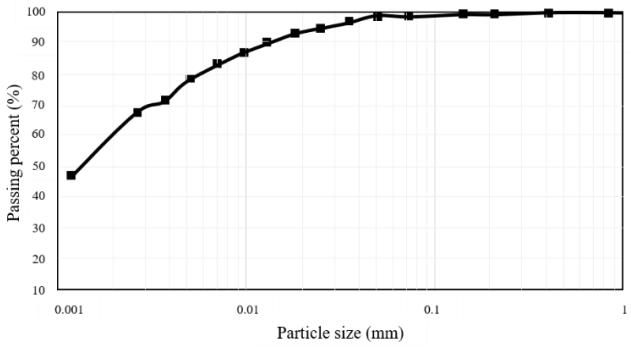

Figure 2 Particle size distribution of the soil

3.2. Glass Fiber

The high alkali-resistant glass fiber used in the study are produced by Nippon Electric Glass firm and was taken from Fibrobeton Structural Element company. Glass fiber samples and SEM images are presented in Figure 3. The properties of glass fiber are presented in Table 2. The glass fiber was cut into 10 mm - 20 mm - 30 mm, and 40 mm lengths. Filament diameters are 13.5 μm [12].

3.3. Sample Preparation and Test Process

In the experimental study, tests were carried out on natural clay and glass fiber reinforced clay samples. The fiber length, ratio, and weights used for a sample prepared in accordance with the geotechnical parameters are shown in Table 3.

To determine the shear strength of the high plasticity clay soil mixtures, they were prepared at the optimum water content obtained by the compaction test. The samples were kept in the refrigerator with nylon bags to avoid losing their water content. Compacted soil-fiber mixtures were hydraulically driven into thin-walled steel tubes with a diameter of 50 mm and a height of 100 mm. Due to the thickness and rigidity of the fiber, disturbances and ruptures occurred while the soil-fiber mixture was inserted into the steel tubes [13]. In other words, the fibers collected at the end of the thin-walled steel tube caused cracks in the sample. Decreases were observed in the unconfined compressive strength of the samples prepared without adding fiber. To get rid of this disadvantage, a specially made mold was used. The natural clay sample was mixed with the fiber ratios specified in Table 3, followed by the fiber amount. 25% of water was added to the mixture, and the mixture was compacted in special molds with an energy equivalent to twice the standard Proctor energy. In our special mold, to remove the cold joint disadvantage, which is in three stages, and allow it to behave as a whole in a monolithic structure, the compaction process was carried out by making equal numbers of drops from the lower and upper heads.

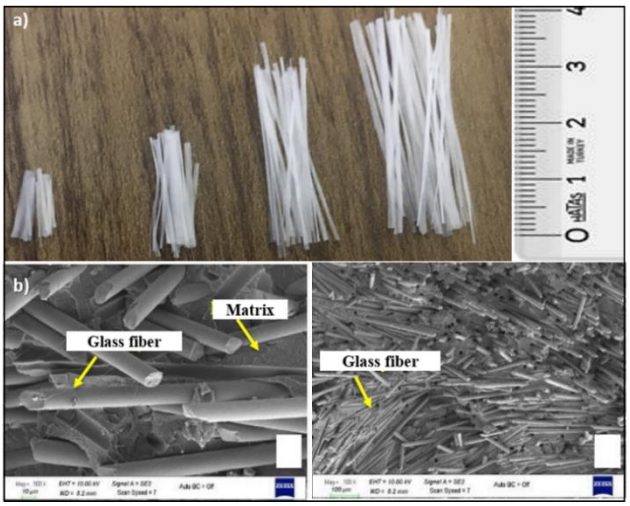

Figure 3 Glass fiber a) In different lengths used in this study b) SEM images [14]

Table 2
Physical and chemical properties of the glass fiber [4]

ACR Glass Fiber		
Physical Properties	Appearance	White – solid
	Smell	Odorless
	Melting point	820 °C
	Solubility in water	Unsoluble
	Specific density	2.8 kg/lt
	Stability	Stable in normal conditions
	Number of tex	2543
	Moisture content	%0.04
	Tensile strength	0.494 N/tex (min 0.245)
	Loss of glow	%1.22
	ZrO_2 content	%17.2
Chemical Properties	Component	Content (%)
	SiO_2	54-65
	ZrO2	16-2
	RO (MgO+Cao)	0-10
	MgO	-
	CaO	-
	TiO_2	1-7
	Al_2O_3	0-2
	R_2O ($LiO+Na_2O+K_2O$)	10-30
	Li_2O	-
	Na_2O	-
	K_2O	-

Table 3
Sample properties

No	Description of the sample	Diameter (mm)	Soil (g)	Fiber (g)	Fiber length (mm)	Fiber content (%)
1	Natural soil	50	300	0	0	0
2	%0.25 ACR fiber reinforced clay	50	300	0.75		0.25
3	%0.5 ACR Fiber reinforced clay	50	300	1.5		0.5
4	%1 ACR Fiber reinforced clay	50	300	3	10	1
5	%1.5 ACR Fiber reinforced clay	50	300	4.5		1.5
6	%2 ACR Fiber reinforced clay	50	300	6		2
7	%0.25 ACR Fiber reinforced clay	50	300	0.75		0.25
8	%0.5 ACR Fiber reinforced clay	50	300	1.5		0.5
9	%1 ACR Fiber reinforced clay	50	300	3	20	1
10	%1.5 ACR Fiber reinforced clay	50	300	4.5		1.5
11	%2 ACR Fiber reinforced clay	50	300	6		2
12	%0.25 ACR Fiber reinforced clay	50	300	0.75		0.25
13	%0.5 ACR Fiber reinforced clay	50	300	1.5		0.5
14	%1 ACR Fiber reinforced clay	50	300	3	30	1
15	%1.5 ACR Fiber reinforced clay	50	300	4.5		1.5
16	%2 ACR Fiber reinforced clay	50	300	6		2
17	%0.25 ACR fiber reinforced clay	50	300	0.75		0.25
18	%0.5 ACR Fiber reinforced clay	50	300	1.5		0.5
19	%1 ACR Fiber reinforced clay	50	300	3	40	1
20	%1.5 ACR Fiber reinforced clay	50	300	4.5		1.5
21	%2 ACR Fiber reinforced clay	50	300	6		2

Considering the ram weight and fall height data used in the Standard Proctor test, sixteen drops of the ram were calculated from the same formula for a mold volume of 196.35 cm^3. A total of thirty-two drops of ram were made by making sixteen drops from the upper and lower heads of the mold.

Unconfined compression tests were carried out after measuring the sample dimensions removed from the molds. To increase the reliability of the test results conducted on natural and glass fiber added mixtures, ten identical samples were prepared, and each of them was tested. The series was completed by mixing 10 mm - 20 mm - 30 mm and 40 mm long ACR glass fibers into the natural soil at 0.25, 0.5, 1, 1.5 and 2% by weight. The gap between the force bar and the upper plate was taken by placing the sample so that the top and bottom parts of the sample were in the center of the unconfined compression device. The maximum shear strength measurement was obtained by taking the readings until 14% strain or until the failure occurred. The failed sample was kept in an oven for 24 hours and recorded by weighing.

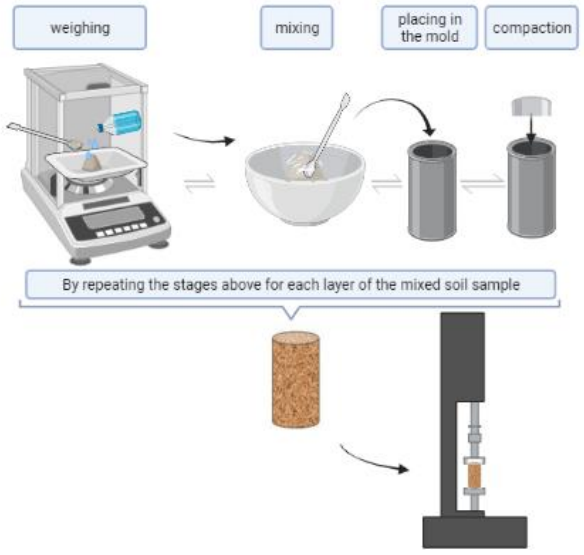

Figure 4 The test procedures followed

4. RESULTS AND DISCUSSIONS

The appearance of the natural and alkali-resistant glass fiber added samples after the unconfined compression test is given in Figure 5. While brittle failure and diagonal failure planes were observed in the natural samples as the fiber ratio and length increased, a significant decrease was observed in the failure surface and the increase in strength.

As shown in Figure 5, local disintegration was prevented in all reinforced samples, and fiber's adherence-increasing effect became more profound. Although there are local cracks, diagonal failure surfaces were not observed in the fiber-reinforced soils.

The results obtained from 210 unconfined compression tests (Figure 6) are shown in the graphs. The strength of 50 mm x100 mm samples increased in all lengths and ratios, and this increase was 135.47% on average. It was determined that the highest increase in strength was in 0.5% fiber reinforced samples with 40 mm length. With the fiber additive, it is easy for the soils to come out of the mold, and it is seen that the diagonal failure surface disappears.

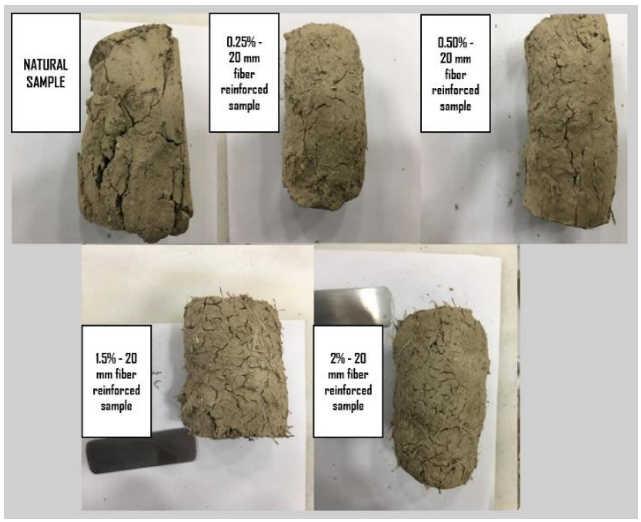

Figure 5 The failure of natural and fiber reinforced samples

Figure 6 The oven dried samples after the tests

In Table 4, the average maximum axial stresses and average strength increases of the 50 mm ×100 mm sample series obtained with different lengths of ACR glass fiber and the percentage prepared are shown. An increase in the maximum stress up to 351.95% and an average increase of 135.47% in the undrained shear strength were measured for the fiber-reinforced samples.

As seen in Figure 7, the strain value of the natural clay was found constant at 14%, while the stress value was around 20 kPa. Since it is soft clay, it was much more tiring to take shape compared to fiber-reinforced samples. It was observed from Figure 7 that the failures were evident in the natural clay and local separations took place in the clay. In addition, the significant increase in strength at the rate of 0.25% fiber was obtained with its maximum value at 12% strain, and there was an increase of approximately two times in the stress value. In 0.5% fiber reinforced soil, the axial stress increased by about 1.80% with displacement in the 12% band, approximately 2.5 times against 10-12% deformation in 1.5% fiber reinforced samples, it progresses steadily in the same displacement band in 2% fiber soil, and the stress increases approximately 2.14 times. Likewise, it was observed that the highest stress was observed in 1% fiber soil with an increase of roughly three times, and the strain value corresponding to the most significant stress was in the range of 12%.

Table 4
Strength increases with glass fiber reinforcement

Fiber length (mm)	Fiber Content (%)	$\sigma_{d\ max.avg.}$ (kPa)	Strength increase (%)	Fiber length (mm)	Fiber Content (%)	$\sigma_{d\ max.avg.}$ (kPa)	Strength increase (%)
-	-	16.88	-	30	0.25	31.20	84.83
10	0.25	25.23	49.47	30	0.50	41.30	144.67
10	0.50	36.33	115.23	30	1.00	60.03	255.63
10	1.00	30.64	81.52	30	1.50	51.07	202.55
10	1.50	26.94	59.60	30	2.00	46.33	174.47
10	2.00	25.64	51.90	40	0.25	43.76	159.24
20	0.25	34.46	104.15	40	0.50	76.29	351.95
20	0.50	31.20	84.83	40	1.00	39.14	131.87
20	1.00	51.24	203.55	40	1.50	26.85	59.06
20	1.50	41.28	144.55	40	2.00	39.88	136.26
20	2.00	36.15	114.16				

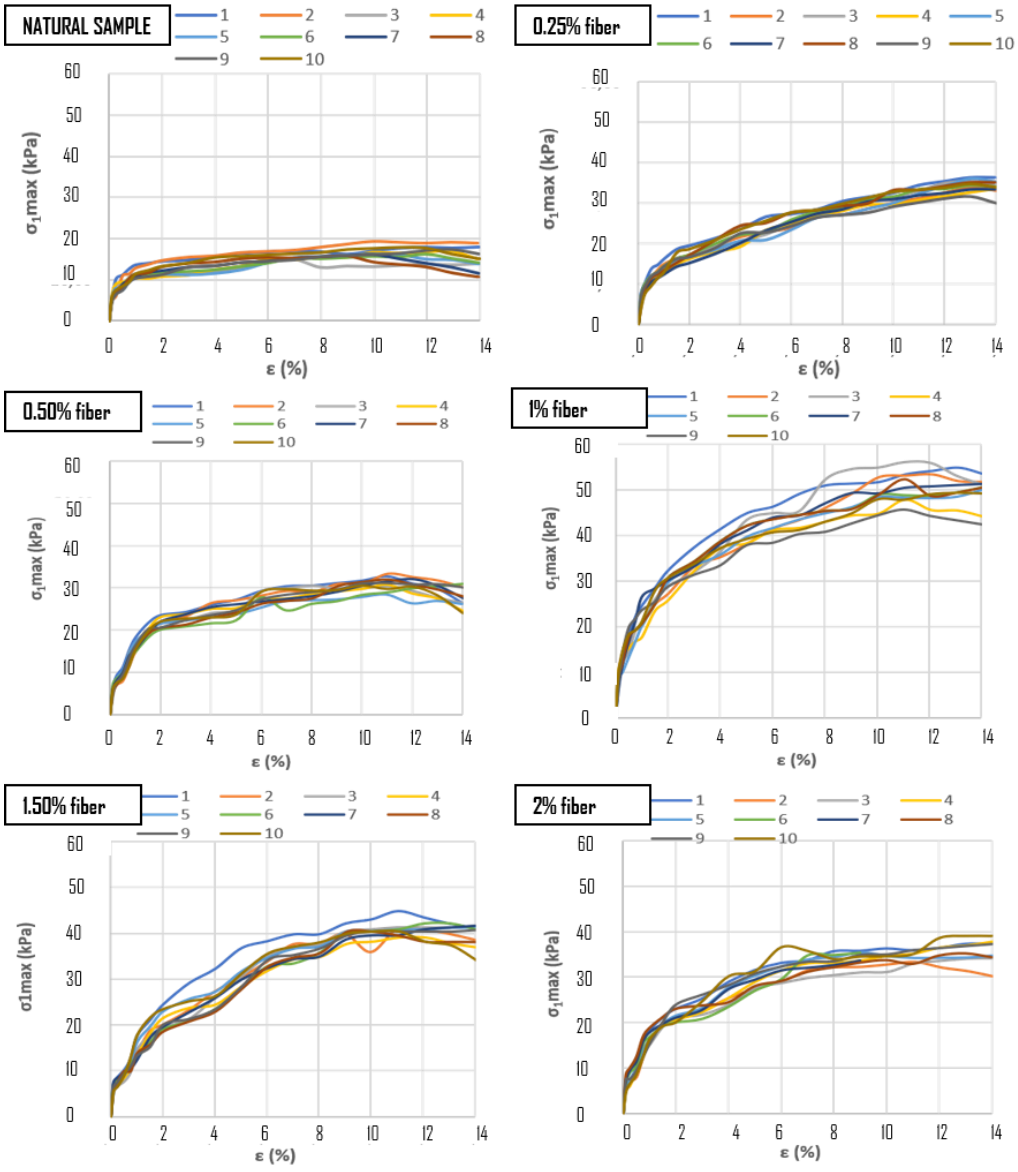

Figure 7 Test results of natural and 20 mm length fiber-reinforced soil samples

Figure 8 (a) shows the relationships between the maximum axial stresses and the strength increase ratios, depending on the glass fiber length and ratio. As reported, clay samples with 1% fiber added show the highest tensile and strength increases at 10 mm, 20 mm, and 30 mm fiber lengths, while the lowest values at 0.25% fiber lengths were obtained. In 40 mm fiber, unlike the others, at 0.5% fiber content, maximum stress, and at 1.5% fiber content, minimum stress was achieved. If we consider 50 mm diameter samples, in general, the ideal length of 30 mm can be selected in all proportions.

If the stresses shown in Figure 8 (b), depending on the fiber ratio, are examined, it is seen that the most significant stress increases were obtained at 1% fiber content in all lengths of fiber except 40 mm. After this ratio, it was seen that there is a decrease in strength as the amount of fiber increases. When the soils subjected to the test are examined, it is seen that the maximum strength was achieved with the increase in fiber length. It has been observed that samples with 20 mm fiber length behave like 30 mm samples.

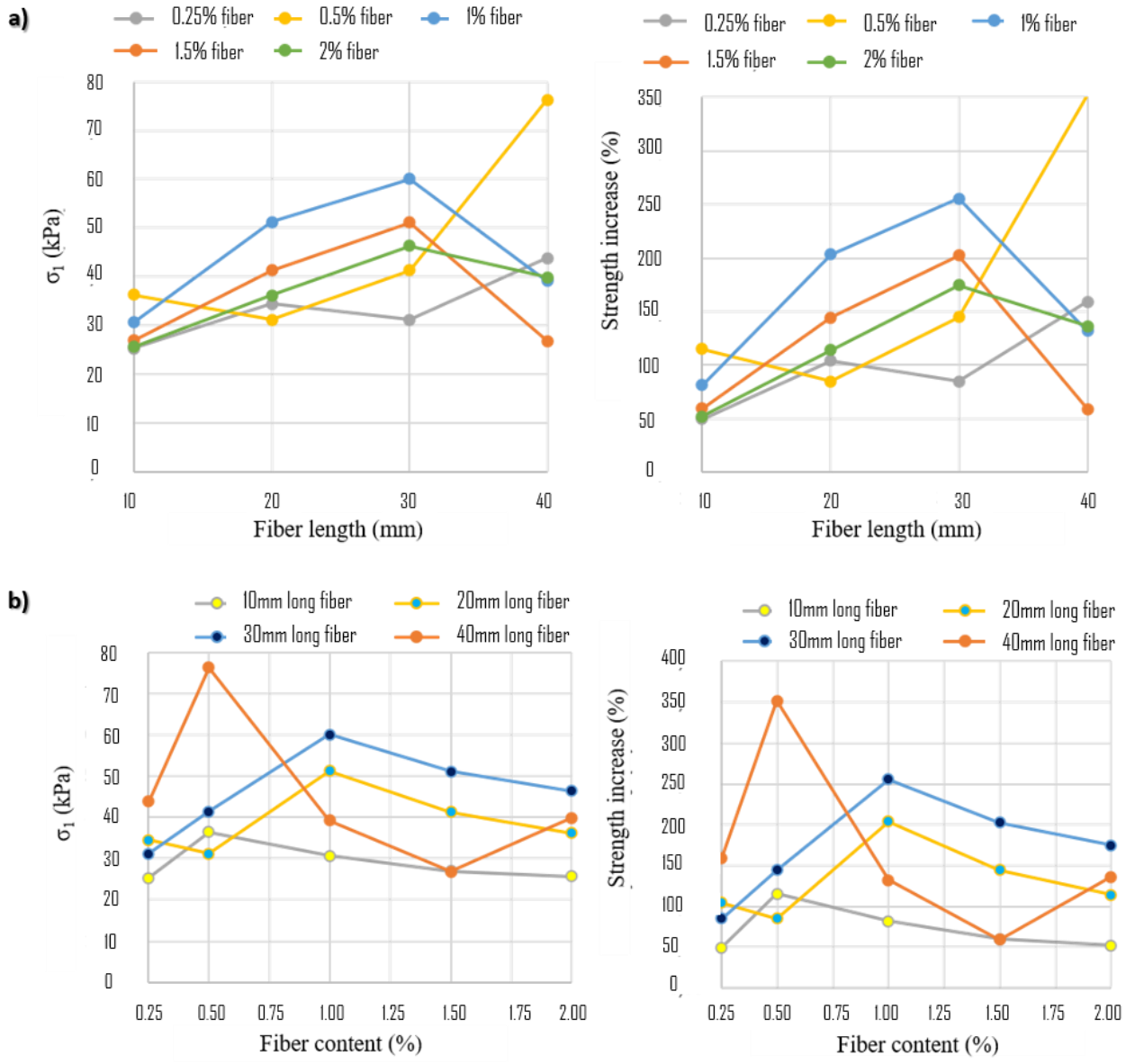

Figure 8 Test results of natural and 20 mm length fiber reinforced soil sample

5. CONCLUSIONS

In the experimental study, cylindrical samples with a diameter of 50 mm and height of 100 mm were prepared by adding 0.25, 0.5, 1, 1.5, 2 weight percent of 10, 20, 30, and 40 mm long glass fiber of high alkali resistant. The specimens were not prepared with the standard compaction mold but were prepared using a special compaction mold. A total of 210 samples, 10 of which are natural and 200 of which are glass fiber reinforced, were tested in an unconfined compression device to find the undrained shear strength of the samples. It has been observed that adding glass fiber to the soil in different lengths and proportions can increase the shear resistance of the clayey soils.

It was concluded that glass fiber increases the ductility and undrained shear strength of clay soil. According to the test data, the highest increase in unconfined compressive strength was observed in samples with 50 mm ×100 mm dimensions, 40 mm in length, and 0.5% fiber added soil samples. Due to the small diameter of the compaction mold, the monolithic structure of the sample was destroyed in case of compaction in 3 layers. That's why two-sided compaction was applied at once in the study. While the failure was evident in the natural clay soil, this surface started to disappear with the increase in the fiber ratio. In other words, it has been determined that the glass fiber holds the soil samples by providing adherence.

The Declaration of Conflict of Interest/ Common Interest

No conflict of interest or common interest has been declared by the authors.

The Declaration of Research and Publication Ethics

The authors of the paper declare that they comply with the scientific, ethical and quotation rules of SAUJS in all processes of the paper and that they do not make any falsification on the data collected. In addition, they declare that Sakarya University Journal of Science and its editorial board have no responsibility for any ethical violations that may be encountered, and this study has not been evaluated in any academic publication environment other than Sakarya University Journal of Science.

REFERENCES

[1] A. Önalp and S. Sert, Geotechnical Information III: Building Foundation, 3rd Ed. (in Turkish), İstanbul, Birsen Publishing, 2016.

[2] E. Karakan, S. Türker and A. Balanlı, "Building Materials (in Turkish)", Yıldız Technical University, İstanbul, pp. 45-72, 1992.

[3] N. Seventekin, Chemical Fibers (in Turkish), İzmir, Research and Application Center of Textile and Apparel Manufacturing, 2001.

[4] M. Maraşlı, "Development of predicting model of bending and compressive strength with maturity method in glass fiber reinforced concrete (in Turkish)", M.Sc. Thesis, Düzce University Institute of Science and Technology, Düzce, 2019.

[5] F. Işık, R.K. Akbulut, Ş.A. Zaimoğlu and S. Arasan, "The usability of waste natural fibers in soil improvement of clayey soil (in Turkish)", 6th Geotechnical Symposium, Paper No: S053, Adana, 2015.

[6] M.L. Diallo and Y.S. Ünsever, "An experimental study on the stabilization of a clay soil with construction wastes and lime (in Turkish)", Pamukkale University Journal of Engineering Sciences, vol. 26, no 6, pp. 1030-1034, Nov 2020.

[7] N. Ural, Ü. Kut and N. Gülsevinç, "Soil Improvement with Waste PVC (in Turkish)", El-Cezeri Journal Science and Engineering, vol. 7, no. 3, pp. 1471-1481, 2020.

[8] H. Bilici, D.V. Okur, M. Türköz and H. Savaş, "Comparative analysis of the effects of fly ash and blast furnace slag admixtures on the strength of clay soil", BEÜ Journal of Science, vol. 9, no. 2, pp. 910-919, Oct 2020.

[9] G. Bilgen, "Utilization glass powder for improving strength of bentonite clay (in Turkish)", 6th Geotechnical Symposium, Çukurova University, Adana, 2015.

[10] TS 1500, "Classification of Soil for Civil Engineering Purposes (in Turkish)", TSI, Ankara, pp. 25-57, 2000.

[11] ASTM D2487-06, "Standard Practice for Classification of Soils for Engineering Purposes (Unified Soil Classification System)", 2006.

[12] Nippon Electric Glass. (2022, 04 April). AR Cam Lif. [Online]. Available: https://www.neg.co.jp/en/product/a-chopped_strand_list/

[13] F. Küçük, "Investigation of the effect of high performance polypropylene fiber additive on the undrained shear strength of clay soil (in Turkish)", M.Sc. Thesis, Sakarya University Institute of Science and Technology, Sakarya, 2020.

[14] S. Çaylak, "The effect of alkyl ketene dimer on the performance properties of natural fiber and glass fiber reinforced biopolymer composites (in Turkish)", M.Sc. Thesis, Bursa Technical University Institute of Science and Technology, Bursa, 2021.

SAKARYA ÜNİVERSİTESİ
FEN BİLİMLERİ ENSTİTÜSÜ DERGİSİ

Sakarya University Journal of Science
SAUJS

ISSN 1301-4048 e-ISSN 2147-835X Period Bimonthly Founded 1997 Publisher Sakarya University
http://www.saujs.sakarya.edu.tr/

Title: Improvement of Strength Characteristics of a Highly Plastic Expansive Soil with Fly Ash

Authors: Gaye KODAZ, Hasan Emre DEMİRCİ, Hasan Fırat PULAT

Recieved: 2021-12-07 00:00:00

Accepted: 2022-04-12 00:00:00

Article Type: Research Article

Volume: 26
Issue: 3
Month: June
Year: 2022
Pages: 448-458

How to cite
Gaye KODAZ, Hasan Emre DEMİRCİ, Hasan Fırat PULAT; (2022), Improvement of Strength Characteristics of a Highly Plastic Expansive Soil with Fly Ash. Sakarya University Journal of Science, 26(3), 448-458, DOI: 10.16984/saufenbilder.1028003
Access link
http://www.saujs.sakarya.edu.tr/tr/pub/issue/70993/1028003

Sakarya University Journal of Science 26(3), 448-458, 2022

Improvement of Strength Characteristics of a Highly Plastic Expansive Soil by Fly Ash

Gaye KODAZ[1], Hasan Emre DEMİRCİ*[2], Hasan Fırat PULAT[2]

Abstract

Highly plastic expansive clays swell or shrink due to change in moisture content and they often have very low bearing capacity. Construction of engineering structures particularly pavements and lightweight buildings on problematic soils such as highly plastic expansive clays may create severe structural problems due to poor engineering properties of that kind of soil. This study focused on the influence of fly ash on strength properties of highly expansive clays which are problematic soils due to their undesirable engineering characteristics such as high plasticity index, liquid limit, swelling and shrinkage characteristics, and low bearing capacity. Atterberg's limit tests and hydrometer tests were conducted to obtain consistency limits and grain-size distribution of the highly plastic expansive clay. Standard proctor tests for clay samples with different fly ash contents such as 10%, 15%, and 20% were performed to determine maximum dry densities and optimum water contents of the mixtures of clay and fly ash. The clay and fly ash mixtures were prepared at optimum water content and maximum dry density for unconfined compression strength (UCS) and California Bearing Ratio (CBR) tests. Effects of fly ash content on the strength characteristics of a highly plastic expansive clay were investigated through unconfined compression and CBR tests. The experiment results showed that fly ash is a promising additive to enhance strength characteristics of highly plastic expansive clays. An approximately 66% increase in UCS and CBR values was observed with the addition of 20% fly ash into the clay mixture in weight.

Keywords: Highly plastic clays, soil strength, stabilization, fly ash

1. INTRODUCTION

Construction of lightweight buildings and pavements on highly plastic expansive clay soils is very risky due to poor strength and large volume change characteristics of these problematic soils [1, 2]. The highly plastic expansive clays can expand and shrink experiencing very large volume changes under wetting and drying conditions. Due to large volume changes in highly plastic expansive clays, engineering structures like lightweight buildings and pavements constructed on these types of soils may be damaged [1, 2]. There are several stabilization techniques reported in the literature to enhance the strength, expansion, and shrinking characteristics of the soils. One of the widely used

* Corresponding author: hasanemre.demirci@ikcu.edu.tr
[1] Izmir Institute of Technology
E-mail: gaye.kodaz@hotmail.com,
ORCID: https://orcid.org/ 0000-0001-6396-3419
[2] Izmir Katip Celebi University, Faculty of Engineering and Architecture, Civil Engineering Department
E-mail: hfirat.pulat@ikcu.edu.tr
ORCID: https://orcid.org/ 0000-0001-6455-9100, https://orcid.org/ 0000-0002-8298-7106

methods for the stabilization of expansive soils is chemical stabilization via using various admixtures such as lime, cement, bitumen and fly ash.

Amongst those additives, the use of fly ash as a stabilizing agent in soil stabilization applications is seen as an environmentally friendly solution as it will reduce the landfilling of these wastes. In Turkey, where more than half of the total electricity produced is obtained from burning coal in thermal power plants, an average of 15 million tons of fly ash is produced annually [3]. Forty-five thermal power plants are currently in operation and the production of fly ash is increasing in Turkey year by year as seen in Figure 1a. While Figure 1a shows the change in the amount of fly ash produced in Turkey between 1993 and 2012 and the amount predicted in 2020, the annual amount of fly ash produced in the world in 2005, especially for the top 12 countries in the production of fly ash, is shown in Figure 1b. In 2012, 19 million tons of fly ash was produced in Turkey and only 10% of the produced amount was used by the cement industry. The projected amount of fly ash production in Turkey in 2020 is 25 million tons [4] as seen in Figure 1a. A large amount of fly ash that is not recycled will need to be landfilled.

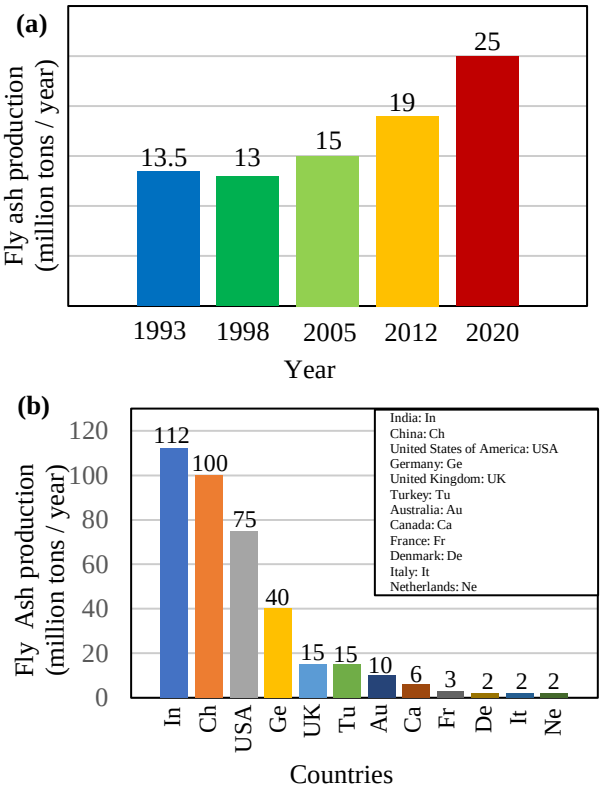

Figure 1 a) The amount of fly ash produced in Turkey between 1993 and 2012 and the amount predicted in 2020, (b) fly ash amount produced in the world in the year of 2005, especially for the top 12 countries in the fly ash production

In many projects in the world, fly ash was used to enhance the strength characteristics of highly plastic expansive soils [5]. Fly ash was also utilized as compacted fly ash columns to reduce swelling and increase the bearing capacity of expansive clay beds [6]. Fly ash was also successfully used in railways and highways to stabilize subgrades and bases, in embankments to improve slope stability and in backfills to reduce lateral earth pressure acting on retaining walls [7]. Using fly ash as a stabilizing agent can have two major benefits for societies: (1) mixing problematic soils with fly ash can enhance engineering properties of such soils and (2) recycling fly ash can help societies to sustain a pollution free environment.

2. A BRIEF LITERATURE REVIEW

Several experimental studies on the improvement in engineering properties of highly plastic expansive soils such as strength and deformation characteristics were reported in the literature. Details of some of these experimental studies and their key findings are summarised in this section. Çokca [8] conducted an experimental study to investigate the possible use of fly ash as an additive for the stabilization of expansive soil. Two different fly ash samples with high calcium and low calcium content which were taken from the Soma and Tuncbilek thermal power plants, respectively are used in their study. Expansive soil-lime and expansive soil-cement mixtures were also used to evaluate the performance of these additives to stabilize the expansive soil. Soma and Tuncbilek fly ash were added to expansive soil at 25% while lime and cement were added to the expansive soil at 0-8%. Chemical composition, consistency limits, grain size distributions and free swell characteristics of the mixtures were obtained in their study. The curing period were considered as 7 days and 28 days for the specimens with fly ash, after the oedometer free swell test. The study showed that fly ash can be successfully utilized for the stabilization of expansive soils.

Sezer et al. [9] reported their experimental investigation conducted on Izmir clay stabilized with a very high lime fly ash. The effects of various fly ash contents and curing period on the improvements in the engineering properties of the clay were studied. The study highlighted that the use of fly-ash increased the unconfined compressive strength of the clay and there was no substantial increase observed in unconfined compressive strength beyond 28 days. The study also showed that the cohesion of the clay containing high percents of fly-ash was considerably enhanced with an increase in curing period.

Zumrawi and Hamza [10] investigated the improvements in the mechanical properties of expansive soils with the addition of fly ash, lime and a combination of these two agents. The effects of the various percentage of fly ash, lime and their combination on strength and swelling characteristics of expansive soils were studied. A series of experiments including California Bearing Ratio (CBR), Unconfined Compression Strength (UCS), swelling pressure, and free swell tests were carried out on the expansive soil and the expansive soil stabilized with fly ash and lime. It was concluded from the study that the strength properties of the expansive soil stabilized with fly ash and lime were significantly improved as well as the reduction in swelling characteristics was observed.

Dahale et al. [11] provided the results of their experimental investigation conducted on clayey soil stabilized with hydrated lime and fly ash. Effects of fly ash and lime content, and curing time on California Bearing Ratio (CBR), Unconfined Compression Strength (UCS) and compaction parameters of the specimens were studied. The relationships between UCS and Brazilian Tensile Strength (BTS) of lime-fly ash stabilized soil at 56 days were obtained. The study highlighted that the addition of fly ash and hydrated lime into expansive clays can remarkably increase the strength of such clays, highlighting that these additives can effectively stabilize expansive clays.

Indiramma et al. [12] carried out an experimental study to investigate the effects of lime, fly ash and their combination on geotechnical characteristics of expansive soils. Various fly ash, lime and fly ash + lime contents were considered in their study. The study highlighted that the liquid limit, plastic limit, plasticity index, differential free swell index and optimum moisture content decreased with the addition of lime alone or with fly ash and lime in various percentages. The study also showed that the strength and maximum dry unit weight of the expansive soil stabilized with lime only and lime + fly ash mixture increased.

Experimental studies found in the literature also highlighted that fly ash was found effective in increasing strength properties and decreasing swelling potential of highly plastic expansive soils [8-12]. For instance, unconfined compressive strength of highly plastic expansive clay was increased by 110% for nonsoaked samples and 247% for soaked samples by adding

of 15% of fly ash [5]. Addition of fly ash decreased plasticity index properties and activity of highly plastic expansive soils [8, 12]. The optimum fly ash content was specified as 20% by considering swelling potential of the expansive soil in the research of Çokça [8].

As reviewed in the literature, there are several studies carried out to investigate the effects of additives such as lime and fly ash on engineering properties of expansive soils. In this research, fly-ash was used for the stabilization of highly plastic expansive clays. In particular, the effects of fly-ash on the mechanical properties of these problematic clays were investigated. Mechanical properties of fly ash and clay mixtures were determined by carrying out UCS and CBR tests. Three various fly ash contents were taken into consideration (10%, 15% and 20%) in the experiments and the effects of different fly ash contents on the strength properties of the clay were also investigated.

3. MATERIALS and TESTING

The thermal power plant fly ash received from Soma Power Plant, Manisa, Turkey was used in this study. The chemical composition of the fly ash was determined through X-ray fluorescence (XRF) analysis by Malikzada et al. [13] and it is presented in Table 1.

Table 1
Chemical composition of thermal power plant fly ash [13].

Main Compound	Percentage (%)
SiO_2	43.3
Al_2O_3	24.1
P_2O_5	0.2
CaO	14.9
Na_2O	0.3
SO_3	4.1
$Ti0_2$	0.9
K_2O	2.6
MgO	3.1

Considering ASTM C618-12a [14], the fly ash used in this study can be considered as Class C type fly ash. This type of fly ash does not require an activator for stabilization due to its self-cementitious characteristics. Class C fly ash often includes a large amount of lime along with pozzolanic materials [15, 16].

The kaolinite and bentonite used in this study are commercial products and the information about the chemical composition of these products were provided by the manufacturer. Main compounds in Kaolinite and Bentonite are presented in Table 2.

Table 2
Chemical composition of kaolinite and bentonite

Main Compound	Kaolinite (%)	Main Compound	Bentonite (%)
SiO_3	52	SiO_2	63
Al_2O_3	31	Al_2O_3	20
Fe_2O_3	0.8	Fe_2O_3	8
CaO	0.07	Na_2O	1
Na_2O	0.3	K_2O	0.9
SO_3	4	Ca0	2.4
TiO_2	0.08	Mg0	3.5
K_2O	1.1	$Ti0_2$	0.75
		MnO	0.03

The typical addition rate of fly ash based on the dry weight of soil ranges from 12% to 15% [7]. As observed in the literature, optimum fly ash content ranges between 15% and 20% [5, 9, 23] where optimum fly ash content is defined as the fly ash content at which the mixture has the maximum compressive strength. Also, considering fly ash contents used in the experimental studies in the literature, various fly ash contents ranging from 0% to 20% were used in the experimental study.

3.1. Consistency Limit Tests

Kaolinite and bentonite samples were mixed by using various bentonite contents such as 10%, 20% and 30% corresponding to 90%, 80% and 70% of kaolinite in weight in the mixture. By using the mixtures, consistency limit tests such as liquid limit (LL) and plastic limit (PL) tests were performed considering ASTM D4318 [17]. The consistency limit tests for kaolinite and bentonite samples were also performed. The table shows the consistency limit tests plan followed in this study. Figure 2 shows the variation of LL (%), PL (%),

and PI (%) of soil mixtures with varying bentonite content (%). As observed in the figure, the value of LL (%), PL (%) and PI (%) increase with an increase in bentonite content in the mixture. For instance, the value of LL of the clay mixture increases from 47 to 105 corresponding to an increase of 121% when the bentonite content in the mixture increases from 0% to 30%. The value of PL of the clay mixture increases from 40 to 73 corresponding to an increase of 80% when bentonite content in the mixture increases from 0% to 30%. A 360 % of the increase in the value of PI increasing from 7 to 32 was observed when the bentonite content in the mixture increases from 0% to 30%. The summary of Atterberg's Limit tests results is presented in Table 3. Kaolinite (K) and bentonite (B) samples were mixed in order to obtain a highly plastic clay sample. As seen in Figure 2, the mixture with 30% of bentonite has the highest liquid limit (LL) and plasticity index (PI). Hence, the mixture of "70K + 30B" is used for the following tests including hydrometer test, standard proctor tests, unconfined compression strength (UCS) tests and California Bearing Ratio (CBR) tests. The mixture which has a liquid limit of 105% and a plasticity index of 32% is considered as organic clay with high plasticity (OH) considering the Unified Soil Classification System.

Table 3
Consistency limit tests plan

Specimen	Abbreviation	Tests performed
Bentonite	B	LL and PL
Kaolinite	K	LL and PL
90% Kaolinite + 10% Bentonite	*90K + 10B	LL and PL
80% Kaolinite+ 20% Bentonite	*80K + 20B	LL and PL
70% Kaolinite+ 30% Bentonite	*70K + 30B	LL and PL

*The numbers in the abbreviation indicate the percent by weight of Kaolinite and Bentonite in the mixture.

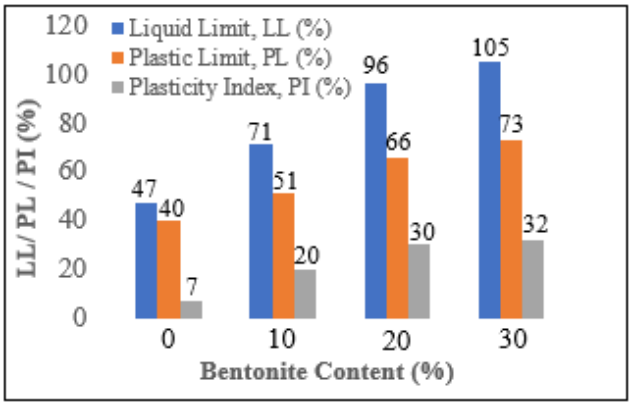

Figure 2 Liquid Limit (LL) (%), Plastic Limit (PL) (%) and (c) Plasticity Index (PI) (%) values for K, 90K+10B, 80K+20B, and 70K+30B

3.2. Hydrometer Test

The grain-size distribution of the mixture "70K + 30B" was obtained by performing a hydrometer test and it is shown in Figure 3. The soil whose grain size is between 0.075 mm and 0.002 mm is considered as silt while the soil whose particle size is smaller than 0.002 mm is considered as clay, as shown in Figure 3. The clay-size fraction by weight in the mixture is obtained as 23% from the figure. Skempton [18] defined a parameter called activity (A) which can be calculated by Equation 1:

$$A = \frac{PI}{(\%\ of\ clay - size\ fraction, by\ weight)} \quad (1)$$

Activity (A) is used as an indicator for assessing the swelling potential of clay soils. The value of the activity of the mixture of 70% Kaolinite and 30% Bentonite can be calculated as 1.4 since the plasticity index of the mixture is equal to 32 (see Figure 2) and % of the clay-size fraction by weight is equal to 23 (see Figure 3). The soil mixture used in the experimental study (70K + 30B) is considered as an active clay since its activity (A) is greater than 1.25 which is stated in the work of Skempton [18].

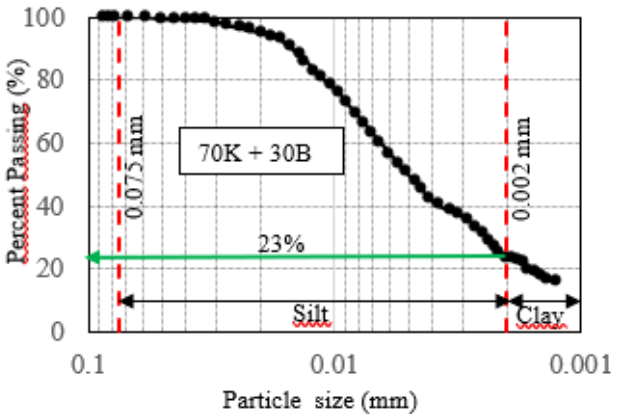

Figure 3 Sieve analysis results for the mixture of 70% Kaolinite (K) and 30% Bentonite (B)

3.3. Standard Proctor Test

Standard proctor tests were conducted considering ASTM D698-12 [19] to obtain maximum dry densities and optimum moisture contents of the mixture of the clay mixture and fly ash. Four tests were performed by using various fly ash content in the mixtures such as 0%, 10%, 15% and 20%. Figure 4 shows the variation of dry density with water content for these tests. Figure 5a-b shows column charts of maximum dry density versus fly ash content and optimum moisture content versus fly ash content. As observed in the figures, values of maximum dry densities and optimum water contents increase with an increase in the fly ash content in the mixture. The maximum dry density and moisture content values obtained from standard proctor tests are required for UCS and CBR tests.

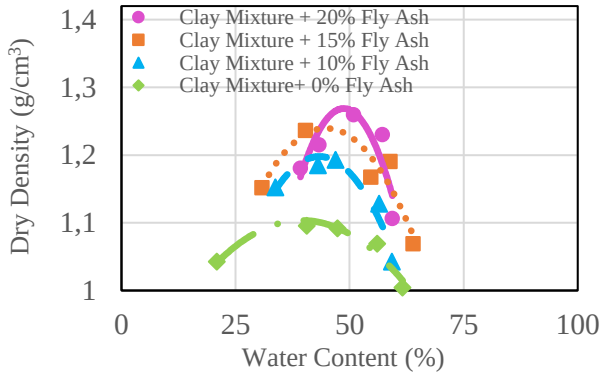

Figure 4 Dry density (g/cm^3) versus water content (%) for (1) C+0% FA, (2) C+10% FA, (3) C+15% FA, and (4) C+20% FA

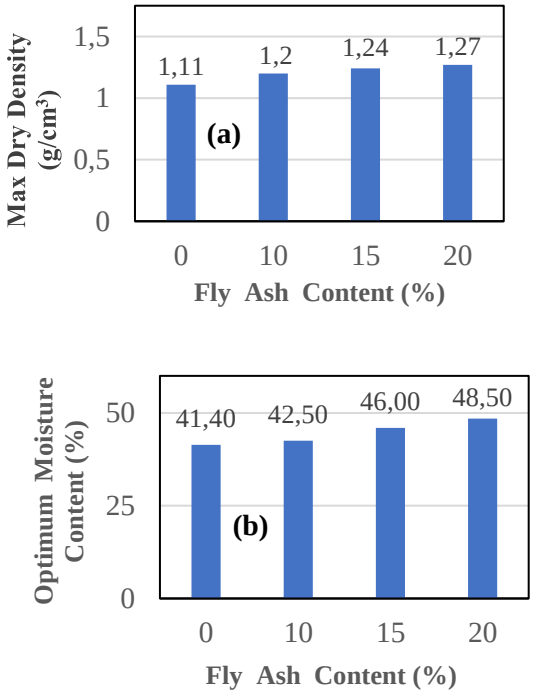

Figure 5 (a) The variation of maximum dry density (g/cm^3) with fly ash content (%), (b) the variation of optimum moisture content (%) with fly ash content (%)

3.4. Unconfined Compression (UCS) Test

Unconfined compression tests for four different mixtures were conducted as per ASTM D2166-16 [20]. The mixtures used in the tests are: (1) clay mixture + 0% fly ash content, (2) clay mixture + 10% fly ash content, (3) clay mixture + 15% fly-ash content, and (4) clay mixture + 20% fly-ash content. The photos of test specimens with various fly ash content after the tests are shown in Figures 6a-d. As observed in the figure, different failure patterns were observed for different soil specimens with various fly ash content. These failure patterns were shown in the figure by using red dashed lines. A curing period of one day is applied to the specimens before each test. Soil specimens for UCS tests were prepared at maximum dry density and optimum water content that was obtained from Standard Proctor tests. All necessary calculations in UCS tests were made considering the varying cross-sectional areas of soil samples under loading.

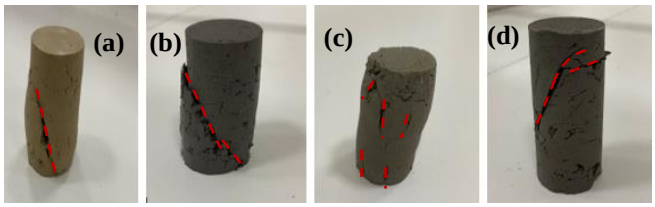

Figure 6 UCS test of clay mixture with various fly ash contents (a) clay mixture, (b) C+10% FA, (c) C+15% FA and (d) C+20% FA

Figure 7 shows stress-strain relationships obtained from UCS tests for four different soil specimens with various fly ash contents. The stiffness and strength of the clay-fly ash mixtures increase with an increase in fly ash content in the mixture. Table 4 summarises the values of UCS, the undrained shear strength of the mixtures of the clay mixture and fly ash and the increase in UCS values for various fly ash contents. The UCS of the clay mixture with 20% fly ash content is 35 kPa while the UCS of the clay mixture with 0% fly ash content is 21.2 kPa. This corresponds to an increase of 66% in UCS compared to the clay mixture with 0% fly-ash content.

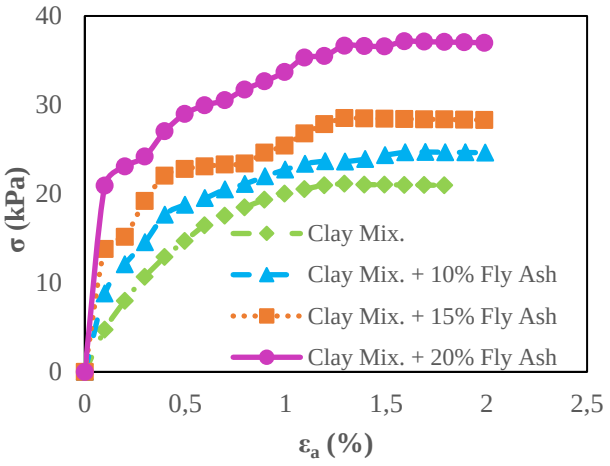

Figure 7 Stress (σ, kPa) versus axial strain (ε_a, %) graph obtained from UCS tests

Table 4
Summary of UCS Test Results

Clay mixture	Fly Ash (%)	UCS (kPa)	Shear strength, Su (kPa)	Increase in UCS (%)
70K+30B	0	21.1	10.6	
	10	24.7	12.4	17
	15	28.10	14.05	33
	20	35.00	17.5	66

3.5. California Bearing Ratio (CBR) Test

California Bearing Ratio (CBR) tests for four different mixtures were conducted as per ASTM D1883-16 [21]. For CBR tests, four various mixtures with the same content as the mixtures used in the UCS tests were used. The non-soaked and uncured samples were used in the CBR tests. Figure 8 shows photos of CBR tests conducted for clay mixture + 0% fly ash and clay mixture + 15% fly ash soil specimens. CBR test specimens were prepared at maximum dry density and optimum water content that was obtained from standard proctor tests. The relationships of stress (kPa) and penetration (mm) obtained from CBR tests for four specimens are shown in Figure 9. A column chart type of graph showing CBR values (%) for four specimens is given in Figure 10. As observed in Figures 9-10, an increase in fly-ash content in the specimens increases CBR (%) values. Typical CBR values of Organic Clays with high plasticity are less than 5% as stated in the 12th edition of AASHTO [22]. As seen in Figure 10, the CBR value of the clay mixture with 0% fly ash content is 3.9 % which is less than 5% while the CBR value of the clay mixture with 20% fly ash content is 6.4%.

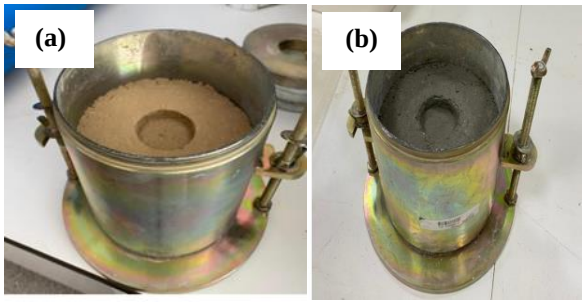

Figure 8 California Bearing Ratio (CBR) Test: (a) clay mixture + 0% fly ash; specimen after penetration, (b) clay mixture + 15% fly ash; specimen after penetration

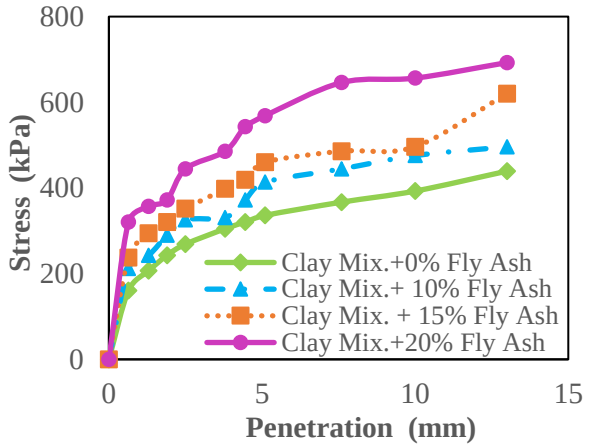

Figure 8 CBR Test results: Stress (kPa) versus Penetration (mm)

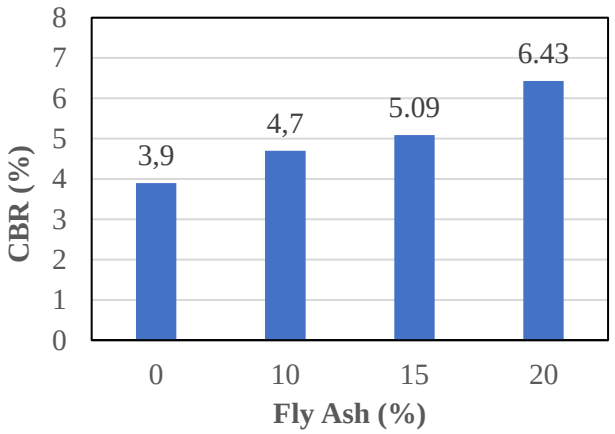

Figure 9 CBR values (%) vs. fly ash content (%)

Table 5 summarises CBR (%) values of four specimens with various fly ash contents and the increase in the CBR (%) values with varying fly-ash-content in the specimens. For instance, the increase in CBR value for the clay mixture + 20% fly ash content is 66 percent compared to the clay mixture + 0% fly ash content.

Table 5
Summary of CBR test results

Clay Mixture	Fly Ash (%)	CBR (%)	Increase in CBR %
70K+30B	0	3.9	
	10	4.7	21
	15	5.1	31
	20	6.4	65

4. DISCUSSIONS

The improvement in unconfined compressive strength (q_u) may be due to self-cementitious characteristics and pozzolanic activity of fly ash as reviewed from the studies in the literature [5, 9]. As observed in the work of Sezer et al. [9], fly ash addition did not substantially improve the unconfined compressive strength of the treated soil beyond 28 days. The treated soil with fly ash addition almost reaches its maximum compressive strength after 28 days like concrete reaching its maximum compressive strength after 28 days. This is similar to Portland cement bond aggregates to produce concrete. Soil particle movement within the stabilized soil by fly ash is restricted associated with the cementation of soil grains. Furthermore, the images of Scanning Electron Microscope (SEM) found in the literature revealed that a reduction in pore spaces was observed due to the formation of new cementitious compounds developed by pozzolanic reactions within soil stabilized by fly ash [23]. Horpibulsuk et al. [24] concluded from the SEM images that the strength development in the stabilized clay depends on the cementitious products which are emerged as a result of the combined effect of dispersion and hydration.

5. CONCLUSIONS

A series of California Bearing Ratio (CBR) Unconfined Compression Strength (UCS) tests were performed on a clay mixture consisting of 70% Kaolinite and 30% Bentonite (70K + 30B) with various fly ash contents. The clay mixture

(70K + 30B) used in the experiments is considered highly plastic since its plasticity index (PI) is specified as 32% from consistency limit tests. Hydrometer tests were conducted to obtain the grain size distribution of the clay mixture. To study the effects of various fly-ash contents on the strength characteristics of clays with high plasticity, three different fly-ash contents were considered in this study such as 10%, 15% and 20%. Standard proctor tests were performed for clay mixtures with various fly-ash contents to obtain maximum dry densities and optimum water contents. Unconfined compression and CBR tests were performed at maximum dry density and optimum water content of soil specimens.

The key findings obtained from the study are summarised below:

1. Maximum dry density and optimum water content of soil specimens increase with an increase in fly-ash content. The addition of 20% of fly-ash by weight increases the maximum dry unit weight of the clay mixture by 14% and optimum moisture content of the mixture by 17%.

2. An increase in fly-ash content in the mixture increases in UCS of the clay mixture. An increase of 66% in UCS is observed with the addition of 20% of fly-ash by weight into the clay mixture.

3. CBR values of the clay mixture increase with an increase in fly-ash content in the mixture. The addition of 20% of fly ash by weight increases the values of CBR of the clay mixture by 65%.

In the lights of UCS tests and CBR tests results, this study highlights that fly-ash can be considered as a reliable additive to improve strength characteristics of problematic soils such as highly plastic expansive soils. Various fly ash contents beyond 20% need to be considered in future experimental studies to determine optimum fly ash content where the clay mixture has the maximum unconfined compression strength and CBR values.

Funding

The authors have no received any financial support for the research, authorship or publication of this study.

The Declaration of Conflict of Interest/ Common Interest

No conflict of interest or common interest has been declared by the author.

Authors' Contribution

The contribution of the authors are 40%, 40% and 20% for the first, second and third author, respectively.

The Declaration of Ethics Committee Approval

This study does not require ethics committee permission or any special permission.

The Declaration of Research and Publication Ethics

The authors of the paper declare that they comply with the scientific, ethical and quotation rules of SAUJS in all processes of the paper and that they do not make any falsification on the data collected. In addition, they declare that Sakarya University Journal of Science and its editorial board have no responsibility for any ethical violations that may be encountered, and that this study has not been evaluated in any academic publication environment other than Sakarya University Journal of Science.

REFERENCES

[1] K. Farook, K.A. Virk, “Improvement of engineering characteristics of expansive clays by sand mixing” Proc. of the 17th ICSMGE, Alexandrina, Egypt., 2009.

[2] T.Y. Elkady, “Unsaturated characteristics of undisturbed expansive shale from Saudi Arabia” Arabian Journal of Geosciences vol. 7 no. 5, pp. 2031–2040, 2014.

[3] G. Guler, E. Guler, U. Ipekoglu, H. Mordogan, Ucucu Kullerin Ozellikleri ve Kullanim Alanlari, Turkiye 19. Uluslararasi Madencilik Kongresi ve Fuari, IMCET2005, Izmir, Turkiye., 2005.

[4] S. Uyanık, M. Topeli. "The opportunities and challenges of fly Ash in Turkey." *Report, September*., 2014.

[5] I.S. Unver, M.A. Lav, E. Cokca, Improvement of an Extremely Highly Plastic Expansive Clay with Hydrated Lime and Fly Ash. Geotechnical and Geological Engineering, vol. 39, pp. 4917–4932, 2021.

[6] B.R. Phanikumar, A.J. Mani, S. Sathiyasheelan, P.R. Reddy, "Fly Ash Columns (FAC) as an innovative foundation technique for expansive clay beds" Geomechanics and Geoengineering vol. 4, no. 3, pp. 183-188, 2009.

[7] American Coal Ash Association, ''Fly Ash Facts for Highway Engineers'' FHWA Report, No: FHWA-IF-03–019, Washington D.C., 2003.

[8] E. Cokca, "Use of Class C Fly Ashes for the Stabilization of an Expansive Soil" Journal of Geotechnical and Geoenvironmental Engineering, vol. 127, no. 7, pp. 568-573, 2001.

[9] A. Sezer, G. İnan, H.R. Yılmaz, K. Ramyar, "Utilization of a very high lime fly ash for improvement of Izmir clay" Building and Environment, vol. 41, no. 2, pp. 150-155, 2006.

[10] M.M.E. Zumrawi, O.S.M. Hamza, "Improving the characteristics of expansive subgrade soils using lime and fly ash" International Journal of Science and Research, vol. 3, no. 12, pp. 1124-1129, 2014.

[11] P. Dahale, P. Nagarnaik, A. Gajbhiye, "Effect of fly ash and lime on stabilization of expansive soil" Journal on Civil Engineering, vol. 6, no. 2, pp. 8-12, 2016.

[12] P. Indiramma, C. Sudharani, S. Needhidasan "Utilization of fly ash and lime to stabilize the expansive soil and to sustain pollution free environment–An experimental study" Materials Today: Proceedings, vol. 22: pp. 694-700, 2020.

[13] A. Malikzada, E. Arslan, İ. Develioğlu, H.F. Pulat "Determination of strength characteristics of natural and stabilized alluvial subgrades" Arabian Journal of Geosciences, vol. 15, no. 6, pp. 1-20, 2022.

[14] ASTM (American Society for Testing and Materials). 2012d. Standard specifcation for coal fy ash and raw or calcined natural pozzolan for use in concrete. ASTM C618–12a. West Conshohocken, PA: ASTM.

[15] S.C. Chu, H.S. Kao, "A study of engineering properties of a clay modified by fly ash and slag" In: SharpKD, editor. Fly ash for soil improvement–geotechnical special publication New York: ASCE; 1993, pp. 89–99.

[16] G. Inan, A. Sezer, "A review on soil stabilization techniques and materials used" MBGAK proceedings. pp. 369–377, 2003.

[17] ASTM D4318-17e1. Standard Test Methods for Liquid Limit, Plastic Limit, and Plasticity Index of Soils, ASTM International, West Conshohocken, PA, 2017.

[18] A.W. Skempton, "The Colloidal "Activity" of Clays" 3rd International Conference on Soil Mechanics and Foundation Engineering, Switzerland., 1953.

[19] ASTM D698-12. Standard Test Methods for Laboratory Compaction Characteristics of Soil Using Standard Effort, ASTM International, West Conshohocken, PA, 2021.

[20] ASTM D2166 / D2166M-16. Standard Test Method for Unconfined Compressive Strength of Cohesive Soil, ASTM

International, West Conshohocken, PA, 2016.

[21] ASTM D1883-16. Standard Test Method for California Bearing Ratio (CBR) of Laboratory-Compacted Soils, ASTM International, West Conshohocken, PA, 2016.

[22] AASTHO HB-12. Standard Specifications for Highway Bridges, 12th Edition, 1977.

[23] N.K. Sharma, S.K. Swain, U.C. Sahoo, "Stabilization of a clayey soil with fy ash and lime: a micro level investigation" Geotechnical and Geological Engineering, vol. 30, no. 5, pp. 1197–1205, 2012.

[24] S. Horpibulsuk, R. Runglawan, Y. Raksachon, "Role of fly ash on strength and microstructure development in blended cement stabilized silty clay" Soils and Foundations, vol. 49, no. 1, pp. 85-98, 2009.

SAKARYA ÜNİVERSİTESİ
FEN BİLİMLERİ ENSTİTÜSÜ DERGİSİ

Sakarya University Journal of Science
SAUJS

ISSN 1301-4048 e-ISSN 2147-835X Period Bimonthly Founded 1997 Publisher Sakarya University
http://www.saujs.sakarya.edu.tr/

Title: Investigation of The Effect of Design Variables on Slip Assembly: Spline Module and Slip Length

Authors: Onur ŞEN, Mert Can KAHYALAR, Hüseyin ÖZGÜRLER

Recieved: 2021-10-01 00:00:00

Accepted: 2022-04-13 00:00:00

Article Type: Research Article

Volume: 26
Issue: 3
Month: June
Year: 2022
Pages: 459-465

How to cite
Onur ŞEN, Mert Can KAHYALAR, Hüseyin ÖZGÜRLER; (2022), Investigation of The Effect of Design Variables on Slip Assembly: Spline Module and Slip Length. Sakarya University Journal of Science, 26(3), 459-465, DOI: 10.16984/saufenbilder.1003171
Access link
http://www.saujs.sakarya.edu.tr/tr/pub/issue/70993/1003171

Sakarya University Journal of Science 26(3), 459-465, 2022

Investigation of The Effect of Design Variables on Slip Assembly: Spline Module and Slip Length

Onur ŞEN*[1], Mert Can KAHYALAR[1], Hüseyin ÖZGÜRLER[1]

Abstract

The driveshaft which transmits the power from the engine to the wheels in the motor vehicles is one of the vital elements in the driveline. Driveshafts have two basic motions depending on the road conditions: angular and axial movements. Angular movement is provided by the universal joints while the axial movement is provided by the slip assembly which involves a group of sliding components. Therefore, the slip assembly is an important part of the drive shaft. Basically, a slip assembly consists of two parts which are connected to each other by means of their spline forms. The parts can move back and forth longitudinally while they transmit the torque thanks to the connection interface of their spline forms. And so, they can slide, and adjust the drive shaft lengths due to the changing position of the axles under road conditions.

During the motor vehicle movement, slip assembly are subjected to torsion like the other components on the driveshaft. In this context, spline size and magnitude of the length compensation are highly important in the design process of a slip assembly. In this study, the effect of the spline size and the slip length were investigated for the yoke shaft design, by using analytical and numerical methods in terms of shear stress. It has been observed that the analytical and the numerical methods give the similar results in shear stress on the pitch diameter of the spline. Thus, the analytical method can be preferred instead of the finite element analysis (FEA), especially considering that the FEA is a time consuming method compared to the analytical method in the design process.

Keywords: Driveshaft, spline, design, analytical method

1. INTRODUCTION

A driveline covers a large number of components which transmit the torque from engine to the driven wheels (Figure 1). Among these components, driveshaft which transmits the torque and the rotational motion is the most vital element because it is an intermediate element providing a connection between driveline components such as transmission and differential. In this sense, it allows relative movement between two adjacent components in driveline [1]. The basic facility of a driveshaft is that it has angular

* Corresponding author: osen4590@gmail.com
[1] Tirsan Kardan A.Ş.
E-mail: m.kahyalar@tirsankardan.com.tr, h.ozgurler@tirsankardan.com.tr
ORCID: https://orcid.org/0000-0001-8763-3246, https://orcid.org/0000-0001-6826-5310, https://orcid.org/0000-0002-5140-5070

and longitudinal plunging movement at the same time. And so, it can compensates the displacement of the axles depending on the road condition and maintains the connection between two other driveline components.

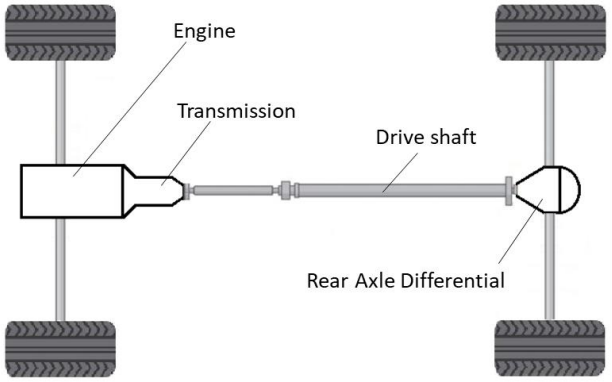

Figure 1 A classical driveline for the motor vehicle [2]

The abilities of angular and longitudinal plunging movements of a driveshaft are respectively provided by joint and slip assembly. A slip assembly totally involves two components which are connected to each other by means of the spline form (Figure 2). Spline form is a kind of profile with equally and circumferentially spaced teeth/grooves. They are used to make a contact between two mating pieces which transmit torque and rotation. The parts relatively exhibit a motion back and forth during transmitting the torque. They can slide and adjust the drive shaft length due to the position of the axle which changes depending on the road conditions.

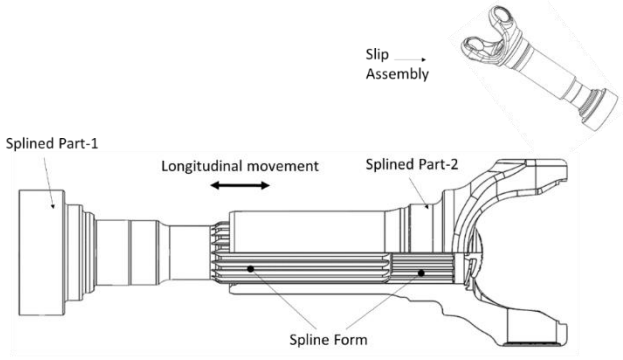

Figure 2 An illustration of slip assembly and yoke shaft

Driveshaft, and so slip assembly operate under torsion and shear stress between driving and driven components in a driveline. For this reason, they should be sufficiently durable against to the stress.

Spline module and slip length are the variables which should be taken into consideration in design process of slip assembly. There are many alternatives of spline modules for the design according to international standard DIN 5480 [3, 4]. The important point is to consider the longitudinal plunging motion of the splined parts composing the slip assembly.

The contact area between the teeth surfaces of mutual splined parts depends on the compensation length in a driveshaft, while the contact area between the teeth surfaces of mutual gears is steady during the operation in a gear system. In brief, the contact area between the teeth of the splined parts in a driveshaft changes, unlike the gears. Here, it should be taken into consideration that the splined parts move longitudinally and the contact area between the teeth of the mutual splines changes during the length compensation of driveshaft. In this study, the effect of the design variables spline module and slip length was investigated. Different spline modules and plunging length were considered and analyzed by using an analytical method.

As a result of the literature research, it has been observed that the studies on the slip assembly are highly limited. When these studies of limited numbers were examined, it was seen that they focused more on the load distributions along the spline teeth. As differing from these studies, Schäfer and Garzke [5] studied on the way to improve the load capacity of splines for various applications. They proposed some modifications on some features such as root geometry, radius and helix angle. It was reported that the stress concentration could be reduced by changing the root geometry and the root radius. And they added that a homogeneous load distribution could be reached by modifying the helix angle for the spline connections whose ratio of length to diameter was equal to 0,6 or greater.

Ding et al. [6] carried out a study on the wear strength of a spline tooth in a spline coupling by implementing a finite element based on simulating the effects of material removal with

fretting wear. They predicted that low frequency, torque, and axial loading induced wear reduced the fretting fatigue and, also increased the life while higher frequency, rotating moment, and fluctuating torque increased the fretting fatigue.

Barrot et al. [7] extended a model developed by Tatur [8] so as to consider different loading cases and geometries. The extended model was used to optimize the design. On the other hand, a finite element analysis was performed. The result showed that the extended model gave an excellent design. Thus, they suggested using the extended model.

Hong et al. [9] investigated the load distribution on the spline interfaces by applying a finite element analysis and surface integral contact analysis model. Finally, they proposed a model to determine the effects of the manufacturing tooth indexing error on the spline load distribution.

Pardhi and Khamankar [10] worked on the stress in the spline shaft under different load conditions from transmitted torque. They used finite element method along with experimental technique of photo elasticity. As a result, they observed that both results were highly close to each other, and maximum shear stress concentration was at the rot diameter of the spline teeth.

Barsoum et al. [11] determined the torsion strength of hardened involute splined shafts by regarding the spline geometry and the hardness profile together. They revealed that the transmitted torque causing distortion of induction hardened splined shafts was dependent on the hardness depth, by using the finite element method. Additionally, they reported that an optimum hardness depth improving the torsional strength could be reached by means of hardening the shafts through half radius.

In another study, Suresha and Mruthunjaya [12] studied to investigate the root cause of the yoke shaft failure in steering assembly. They implemented a fatigue analysis by means of finite element method. Finally, they suggested an improvement in the design/production process by evaluating the current model under various crack conditions in terms of life estimation.

In this study, the effect of the spline size and slip length on the yoke shaft design were investigated by using an analytical method. Most important part of the study is to consider the changes in the contact area of the spline couple during the length compensation of the drive shaft. The aim of the study is to determine the optimum values of the spline parameters by using an analytical method and according to international standard DIN5480 [3,4] as well.

2. METHODOLOGY

An optimum spline module has been analytically determined by considering the contact surfaces between the mutual splines. But it should be noticed that the contact surfaces change depending on the longitudinal plunging movement. In the analytical investigation, the combinations of the spline module and the length of engagement were handled in terms of stress at the pitch diameter of the teeth. For this purpose, different models were prepared for each combination of the spline module with the engagement length. The spline profiles of the models were involute spline according to DIN 5480. The splines in DIN 5480 are within a module range 0,5 to 10, having number of teeth ranging 6 to 32, and with a pressure angle of 30° [3, 4].

Basic dimensions for each combination were given in Table 1 below. In the combinations, the reference diameter has been kept stable while the length of engagement changes, and so the effect of the engagement length has been investigated (see combination 1 vs. 2) for a certain number of teeth. On the other hand, reference diameter and engagement length were kept stable while the module changed, and so the effect of the module was investigated (see combination 1, 3, 4 and 5). The investigation was carried out by using analytical method as well as numerical method. The numerical method FEA was applied for combination 1 to compare both methods with each other, and to prove the validation of the methods with respect to other one.

Table 1 The basic dimensions for the combination of spline module and engagement length

Combination	Reference Diameter (mm)	Module	Pitch diameter (mm)	Number of Teeth	Engagement Length
1	38	2	36	18	62
2	38	2	36	18	42
3	38	2,5	35	14	62
4	38	1,5	36	24	62
5	38	1,75	35	20	62

2.1. Analytical Method

Analytical method was applied to calculate the shear stress on the pitch diameter of the spline for each model. The calculation which was carried out for each combination given in Table 1 provided a comparison of the combinations. In this context, the shear stress on the pitch diameter was calculated by the following equation [13].

$$S_s = \frac{4\,T\,K_a\,K_d}{D\,z\,L_e\,s\,K_f} \quad (1)$$

where T, Ka, Kd, D, z, Le, s, Kf are respectively torque applied in Nmm, spline application factor, load distribution factor, pitch diameter in mm, number of teeth, engagement length of spline in mm, tooth thickness in mm and fatigue life factor. The factors of Ka, Kd and Kf for the calculations were given in the Table 2. It should be noticed that "torque cycle" term in Table 2 involves one start one stop, not the number of revolutions.

Table 2 Factors for calculation of shear stress [13]

Spline Application Factor, Ka	Load distribution factor, Km	Fatigue-Life Factor, Kf
2 for medium shock from engine	1 for flexible spline, according to the face width	0.4 for a fully reversed 100,000 torque cycles

The calculations were implemented by considering the applied torque of 4600 Nm on the splined part, for all combinations in the Table 1. The material of the splined parts, AISI 5140 is quenching and tempering steel, and so shear strength of the material is 809 MPa as hardened steel.

2.2. Numerical Method

Finite element method (FEM) was implemented to validate both methods (numerical and analytical) with another one. For this reason, FEAs were carried out for different engagement lengths (combination-1 and combination-2). In the analysis, it was assumed that splined part runs under a constant torque and it has a uniform geometry. The 3D models of splined part-1 and splined part-2 designed by computer aided design (CAD) software SolidWorks were transferred to computer aided engineering (CAE) software HyperWorks so as to carry out the finite element analysis.

In order to create a mesh structure which was the first step of the finite element analysis, the necessary geometric arrangements were carried out on the three-dimensional (3D) models. Considering the study implemented by Kahyalar and Sen [14], in which a proper element size was determined as a result of the correlation between test and finite element analysis, the mesh structure on which the boundary conditions and external loads were applied, were defined by using R-trias and 3D tetra elements with 1 mm element size respectively.In the next step, FREEZ contact definition was implemented to create a connection between splined part-1 and part-2. After this step, rigid elements were defined on the surface of the splined part-1 which was welded with the tube, while boundary conditions were defined by assigning fixing elements to the midpoints of these rigid elements. Thus, there was no freedom in translation with rotation.

The rigid elements of splined part-2 defined on the inner surface of the ear hole and a torque of

4600 Nm was defined at the midpoint of the rigid elements. Finally, the material definition was made by using the values given in Table 3 (yield strength of AISI 5140 is the final property after quenching and tempering) and the pre-processing step was completed. The 3D model after all these preparations was expressed in Figure 3. The analysis was carried out structurally in a linear static condition.

Table 3 Material properties of the AISI 5140

Part ID	Density	Young's Modulus	Poisson's Ratio	Yield Strength
Splined Part-1	7,85 g/cm^3	210 GPa	0,3	1402 MPa
Splined Part-2	7,85 g/cm^3	210 GPa	0,3	1402 MPa

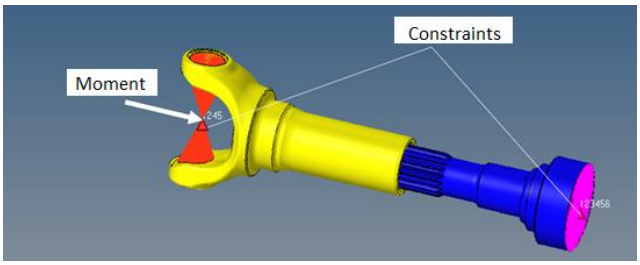

Figure 3 Pre-processing for FEA

3. RESULTS

The shear stress values on the pitch diameter were respectively calculated for all combinations given in Table 1, by using the analytical method. The results for each combination considering the engagement length and spline module were given in Table 4.

Table 4 The max. shear stress values on the pitch diameter of spline teeth for each combination of spline module and engagement length

Combination	Module	Engagement Length	Max. Shear Stress	Shear Stress Limit	Safety Factor
1	2	62 mm	729 MPa	809 MPa	1,11
2	2	42 mm	1076 MPa		0,75
3	2,5	62 mm	771 MPa		1,05
4	1,5	62 mm	729 MPa		1,11
5	1,75	62 mm	771 MPa		1,05

When the results for combination 1 and 2 are examined, it is obvious that the shear stress on the pitch diameter of the spline increases along with the decrease in the engagement length.

If combination 1 and 4 are examined as a couple, the results show that the splines with the same engagement length as well as pitch diameter show the same shear stress on the pitch diameter of the spline.

In addition to the analytical calculations, FEA were implemented for combination 1 and combination 2. And so, analytical and FEA methods were compared with each other.

In this context, the finite element model with 1398653 elements has been used for combination 1 and 2. The results of FEA for combination 1 and 2 showed that the max. shear stress values on the pitch diameter were respectively 718 MPa and 1059 MPa as seen in Figure 4. Similarly, the results of the analytical calculations for combination 1 and 2 gave respectively a max. shear stress value of 729 MPa and 1076 MPa on the pitch diameter (Table 4).

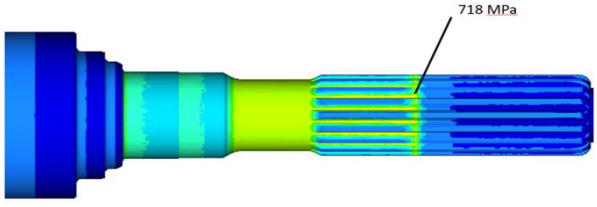

a) Maximum shear stress for combination 1

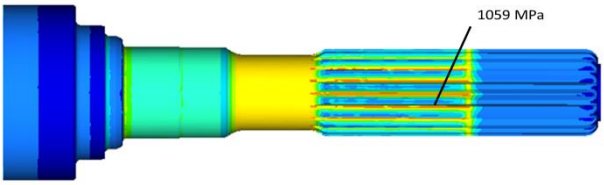

b) Maximum shear stress for combination 2

Figure 4 The maximum shear stress on the pitch diameter of the spline as a result of FEA

The percentage errors between the results of FEA and numerical analysis were calculated by means of Equation 2. The results for combination 1 and 2 are respectively %1,53 and %1,60.

$$E_{\%} = \frac{|FEA-NUM|}{NUM} \quad (2)$$

where $E_{\%}$, FEA, NUM are respectively percentage error, FEA result and numerical result.

4. CONCLUSION

In this study, five combinations including spline module and engagement length were considered in order to achieve the aim. In this context, the analytical studies were carried out to reveal the relationship between the shear stress and the design parameters such as spline module and engagement length while the numerical analysis was carried out to compare both methods (analytical and numerical) with each other.

The results from the study are as follows:

- The results from the analytical and the numerical studies, which have been implemented for combination 1 and combination 2 are similar each other with a percentage error of 1,53-1,60 respectively. The results point out that the analytical method can be preferred instead of finite element analysis, especially considering that the finite element analysis is time consuming.
- The spline parameters given in the combinations 1 and 4 gave the best results in terms of the shear strength on the spline teeth when compared to the other combinations in Table 1.
- The shear stress on the pitch diameter for the splines having the same reference diameter, pitch diameter and engagement length (see Table 1 for combination 1 and 4) is the same.

Funding

The authors have no received any financial support for the research, authorship or publication of this study.

The Declaration of Conflict of Interest/ Common Interest

No conflict of interest or common interest has been declared by the authors.

Authors' Contribution

The first and second authors contributed to study equally with 40% while the third author has contribution of 20%.

The Declaration of Ethics Committee Approval

This study does not require ethics committee permission or any special permission.

The Declaration of Research and Publication Ethics

The authors of the paper declare that they comply with the scientific, ethical and quotation rules of SAUJS in all processes of the paper and that they do not make any falsification on the data collected. In addition, they declare that Sakarya University Journal of Science and its editorial board have no responsibility for any ethical violations that may be encountered, and that this study has not been evaluated in any academic publication environment other than Sakarya University Journal of Science.

REFERENCES

[1] H.Chr. Seherr-Thoss, F. Schmelz and E. Aucktor, "Universal Joints and Driveshafts," Springer, Berlin, Heidelberg, pp. 249-344, 2006.

[2] O. Şen and M. Kahyalar, "Structural Analysis of Yoke Part in Design of Driveshaft," International Journal of Automotive Science and Technology, vol. 4, no. 4, pp. 248-252, 2020.

[3] DIN 5480-1:2006-03, "Involute splines based on reference diameters - Part 1: Generalities," DIN Deutsches Institut für Normung, Berlin, Germany, 2006.

[4] DIN 5480-2:2015-03, "Involute splines based on reference diameters - Part 2: Nominal and inspection dimensions," DIN Deutsches Institut für Normung, Berlin Germany, 2006.

[5] G. Schäfer and M. Garzke, "Increasing Load Capacity of Splines Due to Design," International Design Conference - Design 2002, Dubrovnik, pp. 695-700, 2002.

[6] J. Ding, S.B. Leen, E.J. Williams and P.H. Shipway, "Finite element simulation of fretting wear-fatigue interaction in spline couplings," Tribology - Materials, Surfaces & Interfaces, vol. 2, no. 1, pp. 10-24, 2008.

[7] A. Barrot, M. Paredes and M. Sartor, "Extended Equations of Load Distribution in The Axial Direction in A Spline Coupling," Engineering Failure Analysis, vol. 16, no. 1, pp. 200–211, 2009.

[8] G.K. Tatur, A.G. Vygonnyi, "Irregularity of Load Distribution Along a Splined Coupling," Russian Engineering Journal, 49 (4), 23–27, 1969.

[9] J. Hong, D. Talbot and A. Kahraman, "Load distribution analysis of clearance-fit spline joints using finite elements," Mechanism and Machine Theory, vol. 74, pp. 42-57, 2014.

[10] D.G. Pardhi and S.D. Khamankar, "Stress Analysis of Spline Shaft Using Finite Element Method and Its Experimental Verification by Photo Elasticity," International Journal of Mechanical Engineering and Robotics Research, vol. 3, no. 4, pp. 451-458, 2014.

[11] I. Barsoum, F. Khan and Z. Barsoum, "Analysis of The Torsional Strength of Hardened Splined Shafts," Materials and Design, vol. 54, pp. 130–136, 2014.

[12] P.M. Suresha and M. Mruthunjaya, "Root Cause Analysis of Forged Spline Yoke Shaft Using Finite Element Method," Materials Today: Proceedings, vol. 5, no. 11, pp. 23491-23498, 2018.

[13] E. OBERG and F.D. Jones, "Machinery's Handbook 29th Ed," Industrial Press Inc., NY, USA. 2638,2012.

[14] M.C. Kahyalar, O. Şen, "Kardan Milli İstavroz Gövdesinde Dayanıklılığın Arttırılması ve Yapısal Analiz ile Doğrulanması," Üçüncü Ulusal Üniversite Sanayi İş Birliği, Ar-Ge ve İnovasyon Kongresi, Manisa, Türkiye, 154-160, 2020.

SAKARYA ÜNİVERSİTESİ
FEN BİLİMLERİ ENSTİTÜSÜ DERGİSİ

Sakarya University Journal of Science
SAUJS

ISSN 1301-4048 e-ISSN 2147-835X Period Bimonthly Founded 1997 Publisher Sakarya University
http://www.saujs.sakarya.edu.tr/

Title: Using Locusta migratoria as a Nitrogen Source for the Growth and Development of Microorganisms

Authors: Perihan AKBAŞ, Esabi Başaran KURBANOĞLU

Recieved: 2021-12-21 00:00:00

Accepted: 2022-04-13 00:00:00

Article Type: Research Article

Volume: 26
Issue: 3
Month: June
Year: 2022
Pages: 466-473

How to cite
Perihan AKBAŞ, Esabi Başaran KURBANOĞLU; (2022), Using Locusta migratoria as a Nitrogen Source for the Growth and Development of Microorganisms. Sakarya University Journal of Science, 26(3), 466-473, DOI: 10.16984/saufenbilder.1037496
Access link
http://www.saujs.sakarya.edu.tr/tr/pub/issue/70993/1037496

Sakarya University Journal of Science 26(3), 466-473, 2022

Using *Locusta migratoria* as a Nitrogen Source for the Growth and Development of Microorganisms

Perihan AKBAŞ*[1], Esabi Başaran KURBANOĞLU[2]

Abstract

Characteristics and the use as culture media of protein hydrolysate from *Locusta migratoria* were determined in comparison with different peptones. After powdering, it was hydrolyzed chemically (acid hydrolysis) and obtained product Locust Peptone (LP). The contents of nitrogen, protein, fat, ash, total sugars, minerals and amino acids of LP were determined and it was seen that it has both organic and inorganic materials enough to use as a component of the medium. The effects of different concentrations added 20g/l glucose of LP on the growth of four test bacteria (*Staphylococcus aureus, Bacillus subtilis, Pseudomonas putida* and *Escherichia coli*) and test yeasts (*Rhodotorula glutinis, Candida albicans, Saccharomyces cerevisiae*) were investigated and it was found that the optimal concentration for bacteria and yeast are %0,6 and LP was compared with bacteriological peptone (BP), fish peptone (FP) and meat peptone (MP) .The obtained results with surface streaking and shaking culture procedures showed that LP yielded a little higher or equal FP and BP in both normal bacteria, but these values were lower than values obtained from MP. The results show that LP performed similar to or even better than commercial peptones as nitrogen sources for microorganisms growth. A new peptone has been developed from locust for microbiological media in the present study.

Keywords: Culture media, *Locusta migratoria*, Locust peptone, nitrogen source, peptone, protein hydrolysate

1. INTRODUCTION

A large number of microorganisms require organic nitrogen sources, which are incorporated into the commercial culture medium in the form of peptones, or protein hydrolysates, in varying degrees of hydrolysis [1-3]. There are many articles comparing various media to support the greatest number of bacterial growth from environmental samples [4].

Peptones are defined as protein hydrolysates that cannot be precipitated with heat, alkalis or ammonium sulfate, which are readily soluble in water. It is one of the important components of the bacterial culture medium. The biological properties of each peptone are different and no

* Corresponding author: perihanakbas36@gmail.com
[1] Ondokuz Mayıs University, Karadeniz Advanced Technology Research and Application Center, Samsun, Turkiye
ORCID: https://orcid.org/0000-0001-5977-7621
[2] Ataturk University, Faculty of Science, Biology Department, Erzurum, Turkiye
E-mail: ekurbanoglu@yahoo.com
ORCID: https://orcid.org/0000-0002-7434-6309

component can meet the needs of all microorganisms or cells in the culture medium. Many different sources of animal and plant origin are used for the production of valuable and expensive peptones [4-7].

Most part of microorganisms can not use proteins as a source of nitrogen. Therefore, nitrogen compounds with proteins are needed to convert more useful protein hydrolysate. For this reason peptones are obtained by breaking up with peptide bond of protein macromolecules consist of the chain of amino acids, either enzymatic way (pepsin, trypsin, papain ie.) or chemical hydrolysis using acid, alkali. [8, 9]. Peptone can be used as a medium without additives. Many bacteria can grow media having very low peptone rate, such as 1% [10-12]. Peptones have many macroelements and microelements, so it is used source of mineral nutrients [9, 10].

The Migratory Locust is a large insect, the Migratory Locust is mainly graminivorous cover near the ground occupying the grass. Sea banks, lake, river and with plantings of sedges and reeds. *Locusta migratoria* continue to occur on all continents except Antarctica, Solitary hoppers and adults can damage rice, cotton, various vegetable crops as well as plantations of volatile oil bearing plants in Tajikistan. During years of mass increases/outbreaks, crops are severely damaged as well as hayfields and pastures [13].

Locusta migratoria is a locust both cultured and sold as pet food in Turkey. In this study a peptone prepared from Migratory Locust by acid hydrolysis and it has been tested for the enumeration of aerobic bacteria and compared with standard peptones. Locust peptone (LP) has not been extensively investigated as a source of bacterial nitrogen not widely used for microbial production studies.

2. MATERIALS AND METHODS

The chemicals, culture media and test peptones employed in the present study were analytical grades and purchased from Oxoid (Basingstoke, UK), Merck (Darmstadt, Germany) and Difco (Detroit, MI, USA).

Locusta migratoria were bought from MIRA farm alive animal and insect Agricultural Tourism Company Antalya in Turkey. Bacteria: *Escherichia coli, Bacillus subtilis, Pseudomonas putida* and *Staphylococcus aureus*, yeast; *Rhodotorula glutinis, Candida albicans, Saccharomyces cerevisiae* obtained from Atatürk University Science Faculty Biology Department Microbiology Laboratory collection.

2.1. 1. Production of LP

Locusts were stored -20 degree in freezer and later dried in an furnace at 105 ºC. Dried locusts were cut into small pieces and then ground with a blender (Waring Products Corp., New York City, NY, USA). This material was termed as locust flour (LF). For the preparation of Locust Peptone were used an acid hydrolize method [10, 14, 15] and the production scheme of LP is shown in Figure 1.

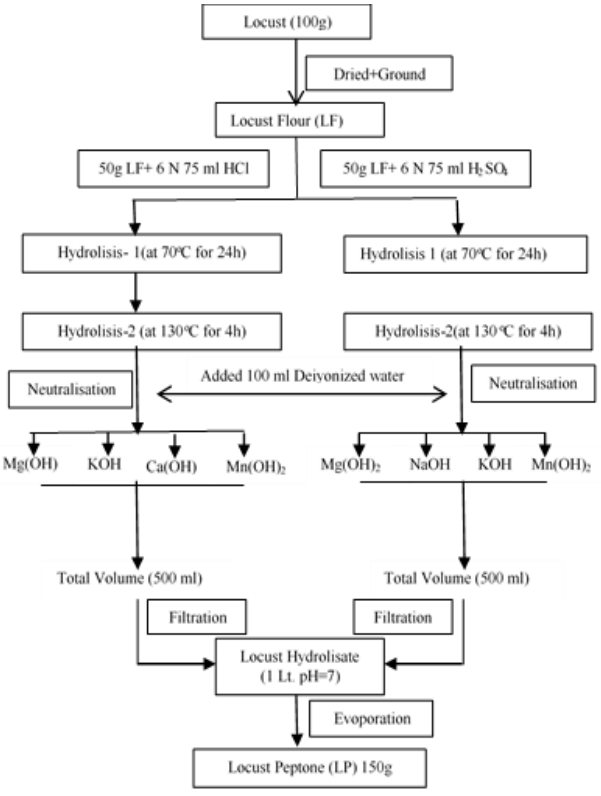

Figure 1 Production scheme of locust peptone

Analysis of LP; Dry matter and ash contents of the peptones were determined according to AOAC methods [16]. Amino acid (HPLC method) and total protein (Kjeldahl method) were estimated in

Duzen Norwest laboratory (Ankara, Turkey). Total sugar contents of LP were determined according to the anthrone method using glucose as a standard [17]. Fat analyses of the peptones were performed by Soxhlet extraction method, Ministry of Agriculture and Rural Affairs Directorate of Erzurum Provincial Control Laboratory [6, 18, 19].

2.2. Determination optimal concentration of peptone and Comparison with other peptones

Broth and agar medium prepared containing different concentrations of LP (%0.1, 0.2, 0.3, 0.4, 0.5, 0.6, 0.7, 0.8, 0.9 ve 1.0), %2 glucose and pure water and pH adjusted to 7. Test bacteria were incubated in Nutrient broth (NB) at 30 ^{o}C for 48 h and yeasts were incubated in Sabouraud Dextrose Broth (SDB) at 24 ^{o}C for 48 h 200 rev in the min. a shaking incubator (ROSI 1000 Thermolyne), the optical density (600 nm) of the cultures was spectrophotometrically adjusted to 2. 0, 1 ml of each culture was inoculated into each concentration of LP liquid medium. Growths of these microorganisms were investigated by two techniques, dry matter measurements and optical density. For agar culture studies, the inoculation cultures were diluted and 1ml of each dilution inoculated in each concentration of LP. After incubation broth cultures measured by the spectrophotometer and centrifuged at 5000 rpm 20 min and after twice washed distilled water, dried at 60 °C till they came to constant weight. Colonies counted on agar plates [10, 20]. LP was compared with three commercial peptones (fish peptone, bacteriological peptone and meat peptone) at the optimal concentration on agar and broth cultures.

2.3. Statistical analysis

The experiments for all chemical, physical, and microbiological analyses, the determinations were run in triplicate. Data were subjected to analysis of variance (ANOVA). Differences among means were tested for significance ($p < 0.05$). Statistical analysis was carried out using SPSS statistic program (Version 15.0) for Windows [21].

3. RESULTS

Locusta migratoria tested for its quality of ash, protein, fat, and element by Hannover Veterinary Foundation School. It is showed that Table 1. *Locusta migratoria* is an appropriate choice for peptone production.

Table 1 Some characteristics of *Loocusta miratoria*

Components	Original matter g/kg	Dry mater g/kg
Ash	15,2	40,4
Protein	230	612
Fat	0,30	0,92
Calsiyum (Ca)	1,23	3,27
Phosphor (P)	2,52	6,7
Magnesium (Mg)	0,47	1,25
Sodium (Na)	0,61	1,62
Potassium (K)	3,67	9,76
Clor(Cl)	1,81	4,81
Copper(Cu)	127	33,8
Zinco(Zn)	509	135
Manganese(Mn)	5,05	13,4
Iron (Fe)	39,3	105
Selenium (Se)	0,07	19

These data show that LP (Locust Peptone) is rich in organic materials. As an expected result, LP does have no methionine and threonine amino acids, because of the high-temperature application during acid hydrolisation process.

Table 2 Amino acid composition of LP.

Parameter	LP Result (g/100 g)	Parameter	LP Result (g/100 g)
Aspartic acid	2,220	Valine	2,571
Glutamic acid	3,742	Methionine	‹0,001
Asparagin	0,361	Tryptophane	0,192
Serine	0,590	Phenylalanine	1,234
Hystidine	0,686	Isoleucine	1,970
Glycine	2,123	Ornithine	1,031
Theronin	‹0,001	Leucine	3,227
Citruline	0,111	Lysine	1,796
Arginine	0,850	Hydroxyproline	1,974
Alanine	4,483	Sarcosine	1,015
Tyrosine	1,180	Proline	2,819
Cystine	0,198	Total aminoacids	33,10

According to Table 2. LP is rich in amino acid content. The essential amino acids are included, among them alanine (4.483 g/100 g) and glutamic acid (3.742 g/100 g) is the highest. Acid hydrolysis is very effective, but since the final

product contains a high amount of acid, the neutralization step is needed [10]. At the same time acidic conditions cause some amino acids to disappear such as tryptophan, basic hydrolysis does not lose amino acids, but the process is slow and sometimes cannot complete [22].

The effect of different concentrations of LP on the number of colonies of test bacteria and yeast growing on agar medium showed Table 3.

The effect of different concentrations of LP on the biomass yield of test bacteria and yeast growing in broth medium showed Table 4.

LP in different concentrations was tested for optimum microorganism production (Table 3, Table 4 According to the results obtained, the optimum LP concentration for bacterial and yeast reprocessing was determined to be 6 g/l, and comparisons between other standard peptones sold commercially and LP were made at this concentration. The results for bacterial growth with different peptones were given in Table 5.

Table 3 The effect of different concentrations of LP on the number of colonies of test bacteria and yeast growing on agar medium

	LP Concentration (g / l) / Number of Colonies (CFU / ml)									
Test Microorganisms	1	2	3	4	5	6	7	8	9	10
Bacteria(3 days 30ºC)										
E. coli	84 e	94 de	115 d	126 c	142 b	158 a	135 b	124 c	84 e	52 f
B. subtilis	31 f	51 e	102 c	115 c	123 bc	142 a	131 b	128 bc	76 d	68 d
P. putida	72 ef	78 e	89 d	105 c	112 b	128 a	104 b	86 de	84 de	36 g
S. aureus	35 g	38 g	49 f	72 e	110 c	146 a	128 b	96 d	84 de	51 f
Yeast (3 days 30ºC)										
S. cerevisieae	15 h	34 f	48 de	50 bc	56 b	64 a	52 bc	42 ef	38 ef	26 g
C. albicans	56 c	57 c	61 c	72 b	78 ab	85 a	77 b	75 b	59 c	53 c
S. boulardii	38 e	42 de	49 c	54 bc	58 ab	63 a	54 bc	51 bc	47 cd	36 e
R. glutinis	33 e	38 e	48 cd	52 cd	58 b	57 a	57 bc	51 cd	46 d	33 e

The difference between the values indicated by the same letters in the same lines is insignificant at $p<0.05$.

Table 4 The effect of different concentrations of LP on the biomass yield of test bacteria and yeast growing in broth medium

Test	LP Concentration (g / l) / Biomass (g / l)									
Microorganisms	1	2	3	4	5	6	7	8	9	10
Bacteria										
E. coli	1,25 g	1,61 f	2,06 e	2,13 de	2,25 bc	2,53 a	2,36 b	2,3 b	2,26 bc	1,8 g
B. subtilis	1,62 c	1,98 b	2,08 b	2,14 b	2,22 b	2,42 a	2,26 b	2,19 b	1,61 c	1,431 c
P. putida	0,9 e	1,06 d	1,23 cd	1,32 bc	1,34 b	1,57 a	1,44 ab	1,33 bc	1,18 cd	1,09 d
S. aureus	1,33 de	1,86 d	2,18 c	2,24 c	2,35 bc	2,64 a	2,47 b	2,31 bc	2,09 c	1,42 de
Yeast										
S. cerevisieae	1,13 e	1,4 d	1,65 c	1,91 bc	2,03 b	2,13 a	2,01 b	1,82 bc	1,66 c	1,16 e
C. albicans	1,44 f	2,14 e	2,86 d	3,64 c	3,82 c	4,38 a	4,12 b	3,63 c	2,94 d	2,36 e
S. boulardii	1,28 g	1,87 f	2,16 de	2,29 bc	2,40 b	2,68 a	2,24 bc	2,12 de	2,05 e	1,72 f
R. glutinis	1,89 e	2,09 d	2,20 cd	2,26 cd	2,44 b	2,62 a	2,43 b	2,37 bc	2,24 cd	2,22 cd

The difference between the values indicated by the same letters in the same lines is insignificant at $p<0.05$.

Table 5 The effect of the test bacteria on the biomass yields and colony counts of the cell and other test peptones developed in the liquid culture

Test Bacteria	Test Peptone (6 g/l)	Max. Biomass (g/l)	Max. Absorbace (600nm)	Colony Number (CFU/ml) (10^8)
B. subtilis	LP	2,46 a	6,05	142 ab
	FP	2,36 b	5,31	125 c
	MP	2,48 a	6,12	154 a
	BP	1,78 c	4,42	117 d
E. coli	LP	2,53 a	6,32	158 b
	FP	2,43 b	6,51	115 d
	MP	2,49 ab	6,11	169 a
	BP	2,37 b	6,42	130 c
S. aureus	LP	2,64 a	6,62	146 ab
	FP	2,10 b	5,21	120 c
	MP	2,72 a	6,84	164 a
	BP	2,19 b	5,42	121 c
P. putida	LP	1,46 a	3,67	130 a
	FP	1,32 b	3,40	132 a
	MP	1,41 ab	3,24	134 a
	BP	1,50 a	3,87	111 b

The difference between the values indicated by the same letters between the same columns is insignificant at $p<0.05$.

LP: Locust Peptone, FP: Fish Peptone, MP: Meat Peptone, BP: Bacteriologic Peptone.

The results for yeast growth were shown in Table 6.

Table 6 The effect of on the biomass yield of test bacteria and yeast growing in broth medium and other test peptones developed in the liquid culture.

Test Yeast	Test Peptone (6 g/l)	Max. Biomass (g/l)	Max. Abs. (600nm)	Colony Number (10^8)
S. cerevisiae	LP	2,13 b	5,36	64 b
	FP	2,04 bc	5,68	56 c
	MP	2,19 b	6,02	62 b
	BP	2,35 a	5,42	75 a
C. albicans	LP	4,38 b	10,03	85 a
	FP	4,13 c	11,52	78 ab
	MP	3,60 d	6,71	66 c
	BP	4,47 a	7,84	86 a
R. glutinis	LP	2,64 ab	6,75	68 b
	FP	2,33 d	5,94	57 c
	MP	2,55 c	6,43	61 bc
	BP	2,76 a	7,02	79 a

The difference between the values indicated by the same letters between the same columns is insignificant at $p<0.05$.

LP: Locust Peptone, FP: Fish Peptone, MP: Meat Peptone, BP: Bacteriologic Peptone.

The difference between the values indicated by the same letters between the same columns is insignificant at $p<0.05$.

According to tables 5 and 6, it is seen that the locust peptone has the potential to produce equivalent to bacteriological peptone and fish peptone.

4. DISCUSSION

Causes cause large-scale damage in agricultural areas with the reason that they are crowded. Grasshopper invasion is a difficult situation to avoid. There are also records at the end of summer that adult locusts have died in flocks and dead locusts have caused diseases [13]. In this case the dead locust can be regarded as a waste. Up to now for peptone production purposes has been benefited from different animal and plant sources or wastes [8, 23-25]. In this study, the use of peptone for microorganisms in the locus was investigated. In our work peptone has been produced from a locust and has been reported to be suitable for bacteria and yeast as a substrate for the produced peptone.

The media prepared with waste peptones and standard peptones are enriched with different carbon sources, especially glucose [6, 10, 20]. Addition of 20 g glucose per liter in addition to the standard nitrogen source on a medium resulted in a 67% increase in the amount of biomass [26, 27]. For this reason, in the medium 20 g of glucose, which is preferred primarily by most microorganisms as carbon source, is added.

All of the test yeasts were reproducible on all media. The highest biomass yield in LP was shown by C. albicans. This can be explained as the optimum level of carbon, nitrogen or minerals required for the development of a causative human pathogen, C. albicans. All the yeasts were best produced in BP after this LP. The number of colonies for the LP test bacteria is biodegradable and is suitable for use as a nutrient. Especially biomass yield of S. aureus was found to be bigger than other test peptones in LP. The maximum

number of colonies was E. coli while the lowest number of colonies was P. putida. Considering all these data, it is considered that LP is a suitable nutrient in terms of rich mineral content and nitrogen amount.

The presence of minerals, vitamins, amino acids, and amount of them in each peptone is a factor that affects the reproduction of microorganisms. The findings of this study show that when the selected raw materials were converted into hydrolyzed products, they were high yielding. In addition, all selected raw materials could be converted into peptones, which can strongly promote bacterial growth. This study showed that LP is suitable for microbiological peptone production when appropriate hydrolysis methods are used due to its high mineral and amino acid content. As a result, the use of these raw materials is an inexpensive and effective way to obtain a nitrogen source for microbial growth.

Funding

"The authors has no received any financial support for the research, authorship or publication of this study.

The Declaration of Conflict of Interest/ Common Interest

No conflict of interest or common interest has been declared by the authors.

Authors' Contribution

This publication was produced from Perihan Akbaş's doctoral thesis. The authors contributed equally to the study.

The Declaration of Ethics Committee Approval

This study does not require ethics committee permission or any special permission.

The Declaration of Research and Publication Ethics

The authors of the paper declare that they comply with the scientific, ethical and quotation rules of SAUJS in all processes of the paper and that they do not make any falsification on the data collected. In addition, they declare that Sakarya University Journal of Science and its editorial board have no responsibility for any ethical violations that may be encountered, and that this study has not been evaluated in any academic publication environment other than Sakarya University Journal of Science.

REFERENCES

[1] J. H. Green, S. L. Paskell, D. Goldmintz, “Fish peptones for microbial media developed from red hake and from a fishery by-product” Journal of Food Protection, vol. 40, no. 3, pp. 181-186, 1977.

[2] O. Villamil, H. Vaquiro, J. F. Solanilla, “Fish viscera protein hydrolysates: Production, potential applications and functional and bioactive properties” Food chemistry, vol. 224, pp. 160-171, 2017.

[3] M, Djellouli, O. Martínez-Alvarez, M. Y. Arancibia, D. Florez-Cuadrado, M. UgarteRuiz, “Effect of seafood peptones on biomass and metabolic activity by Enterococcus faecalis DM19” LWT-Food Science and Technology, vol. 81, pp. 94-100, 2017.

[4] J. A. Vazquez, A. Meduina, A. I. Duran, M. Nogueira, A. Fernandez-Compas, “Production of valuable compounds and bioactive metabolites from by-products of fish discards using chemical processing, enzymatic hydrolysis, and bacterial fermentation” Marine drugs, vol. 17, no. 3, pp. 139, 2019.

[5] A. Poernomo, K. A. Buckle, “Crude peptones from cowtail ray (Trygon sephen) viscera as microbial growth media” World Journal of Microbiology & Biotechnology, vol. 18, no. 4, pp. 333-340, 2002.

[6] E. Vasileva-Tonkova, M. Nustorova, A. Gushteroval, “New Protein Hydrolysates from Collagen Wastes Used as Peptone for Bacterial Growth” Current Microbiology, vol. 54, no. 1, pp. 54- 57, 2007.

[7] A. L. Valimaa, S. Makinen, P. Mattila, P. Marnila, A. Pihlanto, "Fish and fish side streams are valuable sources of high-value components" Food Quality and Safety, vol. 3, no. 4, pp. 209-226, 2019.

[8] E. B. Kurbanoglu, N. I. Kurbanoglu, "A new process for utilization as of ram horn waste" Journal of Bioscience and Bioengineering, vol. 94, no. 3, pp. 202-206, 2002.

[9] D. Dutta, M. D. Das, "Effect of C/N ratio and microelements on nutrient dynamics and cell morphology in submerged fermentation of Aspergillus giganteus MTCC 8408 using Taguchi DOE" 3 Biotech, vol. 7, no. 1, 34, 2017.

[10] E. B. Kurbanoglu, N. I. Kurbanoglu, "Utilization as peptone for glycerol production of ram horn waste with a new process" Energy Conversion and Management, vol. 45, no. 2, 225-234, 2004.

[11] S. Vaidya, K. Jain, D. Madamwar, "Metabolism of pyrene through phthalic acid pathway by enriched bacterial consortium composed of Pseudomonas, Burkholderia, and Rhodococcus (PBR)" 3 Biotech, vol. 7, no. 1, 29, 2017.

[12] T. Yao, Y. Asayama, "Animal-cell culture media: history, characteristics, and current issues" Reproductive medicine and biology, vol. 16, no. 2, pp. 99-117, 2017.

[13] M. G. Sergeev, "Regulahrities in distribution of orthopterous insects of Northern Asia (Novosibirsk Nauka)" 238, 1986.

[14] APHA, "Standard Methods for the Examination of water and Wastewater, 16th ed.," American Public Health Association, (Washington DC), 1985.

[15] J. Ferrer, G. Paez, Z. Marmol, E. Ramones, E. Garcia, "Acid Hydrolysis of Shrimp-Shell wastes and the production of single cell protein from the hydrolysate" Bioresource Technology," vol. 57, no. 1, 55-60, 1996.

[16] AOAC, "Official methods of analysis (15th ed.)," Association of Official Analytical Chemists (Washington DC), 1990.

[17] J. E. Hodge, B. T. Hofreiter, "Samogyi micro copper method. Methods in Carbohydrate Chemistry. (Academic Press. New York)" vol. 1, pp. 383-386, 1962.

[18] N. Bhaskar, V. K. Modi, K. Govindaraju, C. Radha, R. G. Lalitha, "Utilization of meat industry by products: Protein hydrolisate from sheep visceral mass" Biosource Technology, vol. 98, no. 2, pp. 388-394, 2007.

[19] S. N. Jamdar, P. Harikumar, "A rapid autolytic method fort he preperation of protein of protein hydrolisate from poultry viscera" Bioresource Technology, vol. 99, no. 15, pp. 6934-6940, 2008.

[20] L. J. Benedini, M. H. A. Santana, "Effects of soy peptone on inoculum preparation of Streptoccus zooepidemicus for production of hyaluronic acid" Bioresource Technology, vol. 130, pp. 798-800, 2013.

[21] M. Chamalaiah, G. Narsing, D. G. Rao, T. Jyothirmayi, "Protein hydrolisates from meriga (Cirrhinus mrigala) egg and evaluation" Food Chemistry, vol. 120, no. 3, pp. 652-657, 2010.

[22] G. Coward-Kelly, F. K. Agbogbo, M. T. Holtzapple, "Lime treatment of keratinous materials for the genaration of highly digestible animal feed 2. Animal hair" Bioresource Technology, vol. 97, no. 11, pp 1344-1352, 2006.

[23] R. Rossman, D. Giraud, J. A. Albrecht, "Misting effects of the microbial quality of retail leaf lettuce" RURALS, Review of Undergraduate Research in Agricultural and Life Sciences, vol. 7, no. 1, pp.1, 2012.

[24] I. De la Torre, M. Ladero, V. E. Santos, "Production of d-lactic acid by Lactobacillus delbrueckii ssp. delbrueckii from orange peel waste: techno-economical assessment of nitrogen sources" Applied Microbiology and Biotechnology, vol. 102, no. 24, pp. 10511-10521, 2018.

[25] G. Strazzera, F. Battista, N.H. Garcia, N. Frison, D. Bolzonella, "Volatile fatty acids production from food wastes for biorefinery platforms: A review" Journal of environmental management, vol. 226, pp. 278-288, 2018.

[26] S. J. Horn, S. I. Aspmo, V. G. H. Eijsink, "Growth of Lactobacillus plantarum in media containing hydrolisates of fish viscera" Journal of Applied Microbiology, vol. 99, no. 5, pp. 1082-108, 2005.

[27] M. Ozdal, E. B. Kurbanoglu, "Use of chicken feather peptone and sugar beet molasses as low cost substrates for xanthan production by Xanthomonas campestris MO-03" Fermentation, vol. 5, no.1, pp. 9, 2019.

SAKARYA ÜNİVERSİTESİ
FEN BİLİMLERİ ENSTİTÜSÜ DERGİSİ

Sakarya University Journal of Science
SAUJS

ISSN 1301-4048 e-ISSN 2147-835X Period Bimonthly Founded 1997 Publisher Sakarya University
http://www.saujs.sakarya.edu.tr/

Title: A Configurable Interface for Analog Sensor Outputs

Authors: Baran DEMİRER, Faik BAŞKAYA

Recieved: 2021-06-04 00:00:00

Accepted: 2022-04-17 00:00:00

Article Type: Research Article

Volume: 26
Issue: 3
Month: June
Year: 2022
Pages: 474-487

How to cite
Baran DEMİRER, Faik BAŞKAYA; (2022), A Configurable Interface for Analog Sensor Outputs. Sakarya University Journal of Science, 26(3), 474-487, DOI: 10.16984/saufenbilder.947632
Access link
http://www.saujs.sakarya.edu.tr/tr/pub/issue/70993/947632

Sakarya University Journal of Science 26(3), 474-487, 2022

A Configurable Interface for Analog Sensor Outputs

Baran DEMİRER[1], Faik BAŞKAYA*[1]

Abstract

Reading out analog sensor outputs can be a challenging task at low frequencies because of the low frequency noise. To obtain a sensor signal clearly, special interface circuits are required. By using such circuits, analog signals are cleaned from offset, drift and 1/f noise. Besides, if the interface circuitry is configurable, it can be possible to interface to inputs at different frequency ranges. At the interface block, analog sensor output signal is moved to a frequency band where low frequency noise effects are not dominant by using chopping modulation technique. The frequency-shifted signal is then filtered using various filter types. To remove the low frequency noise before moving the signal back to the original band, G_m-C filter is used. The entire topology can be configured by a 5-bit digital to analog converter (DAC) called Biasing DAC (BDAC). This allows us to digitally change the biasing current of operational transconductance amplifiers (OTA), so that OTA based amplifiers and filters can operate at different frequency ranges. As conclusion, a configurable analog sensor interface has been designed. The design and layouts have been realized and simulated in Cadence Virtuoso using UMC 130nm CMOS technology.

Keywords: Sensor, sensor interface, analog

1. INTRODUCTION

Importance of sensors and sensing devices has increased dramatically recently. As a definition, a sensor is an electronic device that detects or responds to changes and events in its environment. These events can be changes in temperature, pressure, illumination resistance or capacitance values etc. Thus, different types of sensors are needed. Measuring blood sugar, temperature [1], and reading biomedical signals [2], seismic signals [3], accelerometer data [4] are common examples of sensors used in our lives. Yet, it is not enough only to measure or sense but also important to transmit these signals faithfully to a circuit where they will be processed. To achieve this, interface circuits are needed to read, evaluate, modulate, clean, and amplify the output of analog sensors. They are also used to eliminate low frequency noise such as 1/f noise and DC offset of components. Otherwise, noise and offset interfere with the real signal and decrease the signal to noise ratio (SNR), resulting in false sensing or incorrect measurement. Today's technology has enabled us to measure a plethora of physical quantities utilizing as many sensors. These sensors have different requirements when it comes to their interfaces due to the fact that the underlying sensing mechanisms are quite

* Corresponding author: faik.baskaya@boun.edu.tr
[1] Boğaziçi University, Faculty of Engineering
E-mail: baran.demirer@boun.edu.tr
ORCID: https://orcid.org/0000-0003-3013-4782, https://orcid.org/0000-0001-6743-3992

different. Designing a new interface for each sensor type and application is an unnecessarily difficult and expensive task.

In this paper, we propose a configurable interface topology that can be used for a wide range of analog sensor outputs without requiring a new design. The proposed configurable interface circuit uses a variable frequency chopping modulation technique to eliminate the DC offset contributions of the amplifier, while a configurable Gm-C filter removes the high frequency artifacts added by the chopper to the signal. In addition, a fully differential design approach improves common mode signal and noise rejection. Although these techniques are known to be useful for reducing the low frequency noise as well, the main focus in this paper has been demonstrating the elimination of the offset voltage. The next section describes how chopping technique eliminates low frequency noise, drift, and offset. In section 3, the design and operation of each individual block has been explained. Section 4 presents the simulation results of the entire design, while section 5 concludes this paper.

2. BACKGROUND

Analog sensor interfaces may perform with various sensor outputs such as data from biological signals, accelerometers, seismic sensors, shock sensors, ultrasonic sensors, acoustic sensors, etc. However, noise, offset, and drift are major problems while reading out these sensor outputs. the most significant achievement of this sensor interface is reading and cleaning the outputs of different types of sensors up to 15kHz frequency effectively.

Threshold voltage (V_{TH}) of a transistor depends on various factors such as body effect, operating temperature, oxide thickness and dopant concentration in the channel region [5]. Since oxide thickness and dopant concentration cannot be uniform throughout the entire IC because of process variations, V_{TH} values deviate from typical values, resulting in unbalanced differential pairs. Offset voltage at the input of a differential pair can go up to 10mV in CMOS technology because of the mismatches in transistor V_{TH} values [6]. Increasing device dimensions might alleviate the offset problem at the cost of increased chip area and input capacitance [5].

Upper limit for offset voltage at the input of a differential pair can be 10mV in CMOS technology because of the mismatches in transistor threshold voltage values manufacturing variations or uncertainty [6]. Threshold voltage V_{TH} is a function of doping amount in the channel and gates in MOS devices. The reason why there might be mismatch in the V_{TH} is that these parameters may have different values depending on the device [5]. Besides, during fabrication of MOS transistors, mismatch might occur in micron level that result in the offset. Increasing device dimensions might solve offset problem but that occupies too much chip area [5].

1/f noise stems from the defects in the gate oxide and silicon substrate. Thus, 1/f noise depends on the purity of oxide-silicon interface. At low frequencies, 1/f noise is the dominant noise factor in CMOS technology, and it is modeled as in equation (1) below:

$$V_n^2 = \frac{K}{W.L.C_{ox}.f} \quad (1)$$

In the equation, K is a constant depending on process and it is in the order of 10^{-25} V^2F, W and L are the width and length of the MOS transistor, C_{ox} is the capacitance per unit area, and f is the frequency. 1/f noise performance of PMOS is better than NMOS in most technologies [5].

Drift is caused by the cross-sensitivity of some error sources to temperature or time. For high precision temperature measurement, it is very important that the drift has to be detected at the component level and must be kept low. Gain and offset drifts are the two main types of drift and have to be eliminated to decrease the overall drift level.

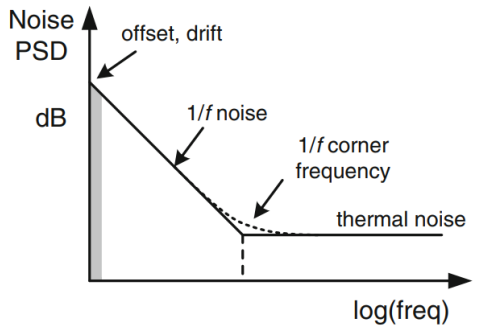

Figure 1 Low frequency noise spectrum of CMOS and 1/f noise [5]

To summarize, at low frequencies non-idealities are mainly caused by 1/f noise, offset, and drift in CMOS technology as illustrated in Figure 1. To eliminate these errors, some of the precision techniques that can be applied to the output signal of sensors are autozeroing, correlated double sampling, dynamic element matching, and chopping [5]. In this work, chopping technique is the preferred approach to eliminate the low frequency effects mentioned above.

2.1. Chopping Technique

Chopping is a continuous time modulation and precision technique which is used to obtain high precision signals from the analog sensor outputs, introduced with the vacuum tube amplifiers.

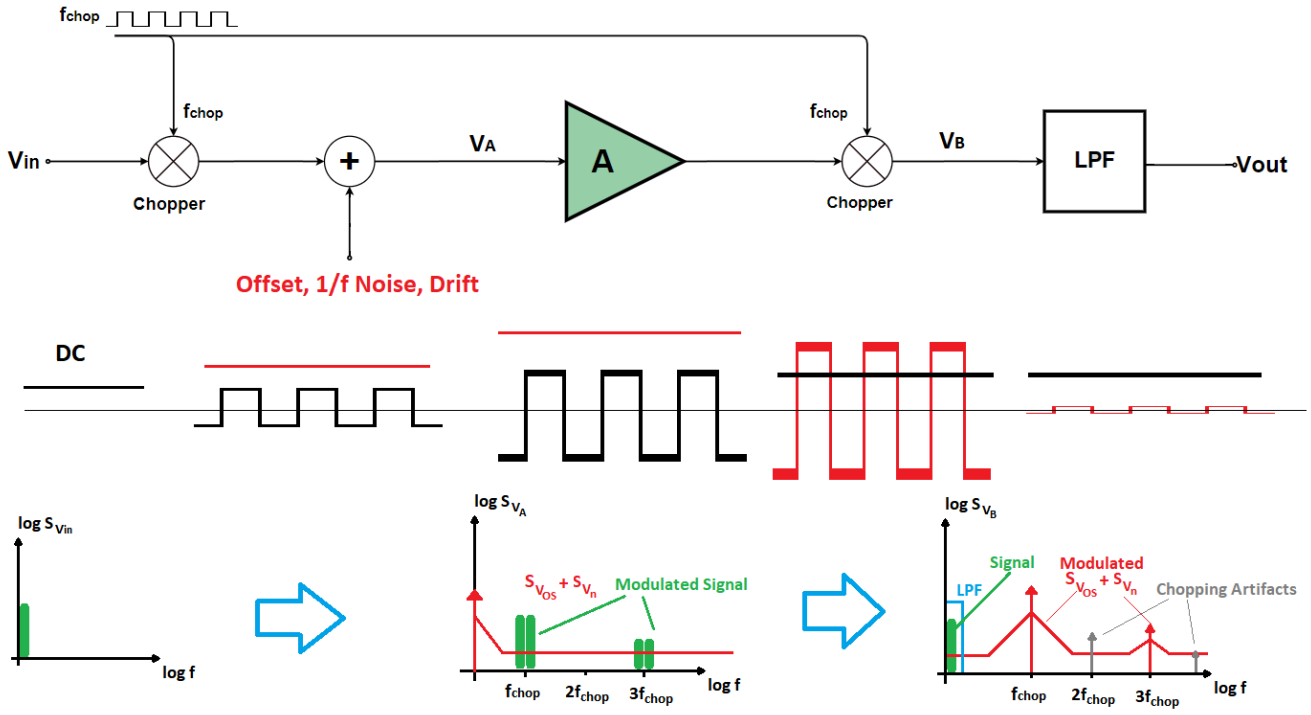

Figure 2 General scheme of chopping topology [5]

As depicted in Figure 2, input signal V_{in} is first modulated (chopped) at f_{chop} frequency, effectively shifting low frequency components of the sensor output signal to higher frequencies. When the modulated signal is amplified, DC offset and low frequency noise contributions from the amplifier will not affect the actual signal components since they remain at a higher frequency at this stage. Then the amplified signal is demodulated to DC level by another identical chopper. In the meantime, the low frequency components such as DC offset, the dominant low frequency components of 1/f noise and drift are shifted to odd harmonics of f_{chop}. Finally, the demodulated signal is filtered by a low-pass filter, which separates the input signal from low frequency non-idealities [5]. The remaining signal components from modulated offset and

noise as well as chopping artifacts appear as ripples in Figure 2. The amplitude of these ripples can be reduced by increasing the chopping frequency f_{chop}. To remove 1/f noise effectively, f_{chop} should be set to a frequency much higher than the noise corner frequency. The upper limit for f_{chop} is determined by the 3dB point of amplifier bandwidth.

3. DESIGN OF BLOCKS

In this section, circuit design for each block in the paper will be presented. Design properties and explanations are provided with references. The entire design has been implemented in UMC 130nm technology using Cadence Virtuoso CAD tool.

3.1. Biasing Circuit

The biasing circuit generates reference voltage and current values to bias OTAs and OPAMPs. All biasing voltages or currents are generated internally using a digital input value, making the whole design self-biased. The biasing circuitry of the interface system is a bandgap reference circuit which has complementary to absolute temperature (CTAT) and proportional to absolute temperature (PTAT) circuits as depicted in Figure 3 [7].

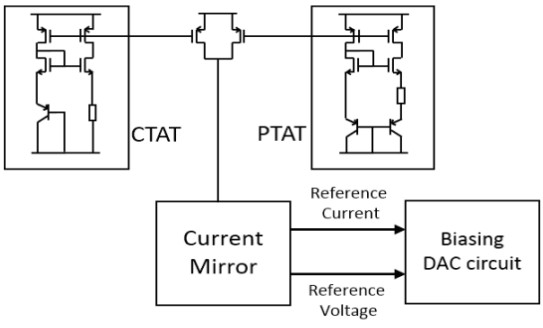

Figure 3 Biasing scheme of overall design [7]

3.1.1. Bandgap Reference Circuit

Bandgap reference circuit provides the constant voltage and current (V_R, V_B, and I_{bias}) required to bias various blocks independent from the variations in temperature [8]. The bandgap reference circuit consists of a CTAT circuit, a PTAT circuit, and a pair of transistors that mirror and add the currents from CTAT and PTAT. The currents obtained from CTAT and PTAT are mirrored to generate reference voltages and currents. As the temperature increases, the voltage and current values generated by CTAT circuit decreases while in the PTAT circuit, current and voltage values increase to compensate the loss from CTAT.

Figure 4 depicts the details of the bandgap reference circuit used in the proposed system. In CTAT, base-emitter voltage (V_{BE}) of the BJT, which is equal to the voltage on the resistor, decreases as the temperature increases, forcing the current through the resistor to decrease as well. In the PTAT part on the other hand, there are two BJT transistors, one of which is 5 times larger than the other one. The difference between the V_{BE} voltages of these two BJT transistors, which is equal to the voltage on the resistor used in the PTAT circuit (V_{Res}), varies proportionally to the temperature as shown in equation 2, forcing the current through the resistor to increase:

$$V_{Res} = V_{EB2} - V_{EB1} = \frac{kT}{q} \ln\left(\frac{I_2.A_{E1}}{I_1.A_{E2}}\right) \quad (2)$$

The currents flowing through CTAT and PTAT resistors are mirrored and summed to obtain a current that does not vary with temperature changes. The summed current then flows into a cascode current mirror to generate the reference and biasing voltages V_r and V_b. The bandgap reference circuit also generates the biasing current at I_{out} port with 1μA value. At the V_r and V_b nodes, voltage values of 623mV and 903mV are generated respectively.

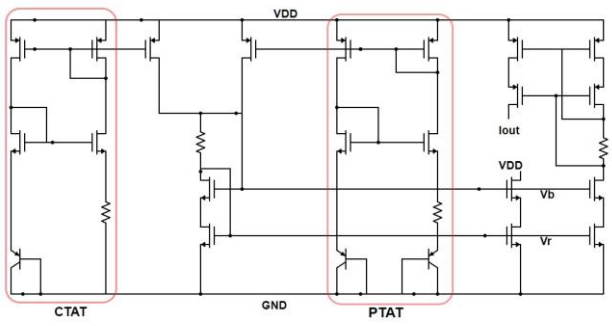

Figure 4 Bandgap reference circuit with CTAT and PTAT circuits

3.1.2. Biasing Digital to Analog Converter (BDAC)

BDAC is a digital to analog converter that is based on current steering topology and is used to bias OTAs and OPAMPs used in the system. Since voltage level at the output of BDAC will be used for only biasing and is not expected to change frequently while operating, conversion speed is not a priority.

Schematic of the BDAC is depicted in Figure 5. Switches are connected to 5-bit digital control word to set output current to desired value. The digital input word n determines the number of turned on cells that results in the output current $I_{out} = n.I_{ref}$. The value of I_{out} changes from 0 to 31μA. The 5-bit digital input is connected to BDAC via 5 transmission gate switches. Figure 6 displays the output characteristics of I_{out} current. Current values vary from 0 to 31μA and each bit combination corresponds to a current value. Differential non-linearity (DNL) error values of the used design vary between 0.01 and 0.03 LSB. Integral non-linearity (INL) is less than +/-1 LSB.

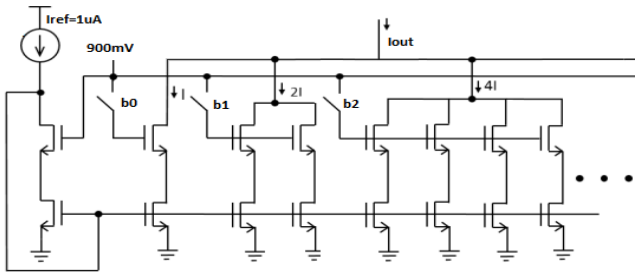

Figure 5 5-bit current mirror based BDAC [13]

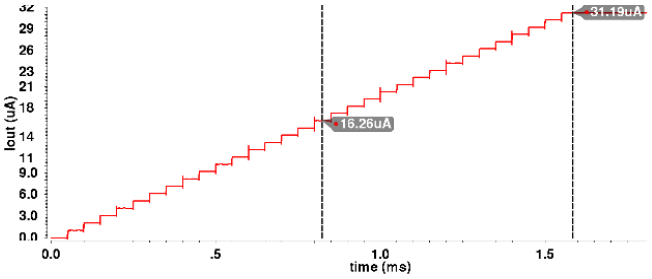

Figure 6 Output current of BDAC

3.2. Chopping Amplifier

3.2.1. Chopper

To make a chopping amplifier, choppers are connected to both input and output of an Operational Transconductance Amplifier (OTA). Each chopper has four switches driven by the complementary periodic signals CLK and $\overline{CLK}$ at chopping frequency f_{chop} as depicted in Figure 7. To prevent V_{TH} drop during switching, transmission gate switches are preferred rather than NMOS switches. Transmission gate switches also have better characteristics in terms of noise margin, less switching resistance, and less power dissipation [9].

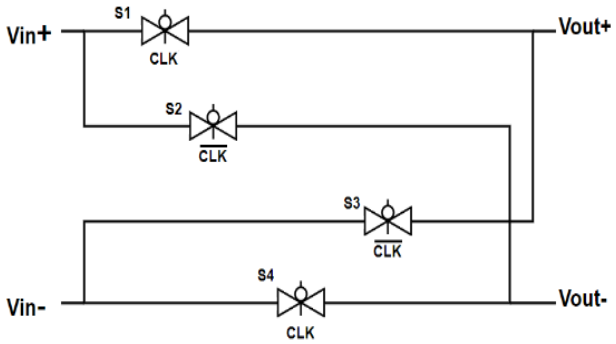

Figure 7 Chopper circuit schematic

3.2.2. Amplifier

In this part, amplifier of chopping topology and its operation with modulator chopper and demodulator chopper are explained. Amplifier block of chopping topology consists of a fully differential folded cascode OTA and it is depicted in Figure 8. The reason for preferring the folded cascode topology is its better output swing and common mode input range in comparison to the telescopic counterpart [10]. At the input of the folded cascode topology, PMOS differential pair is chosen due to its better noise performance than the NMOS pair.

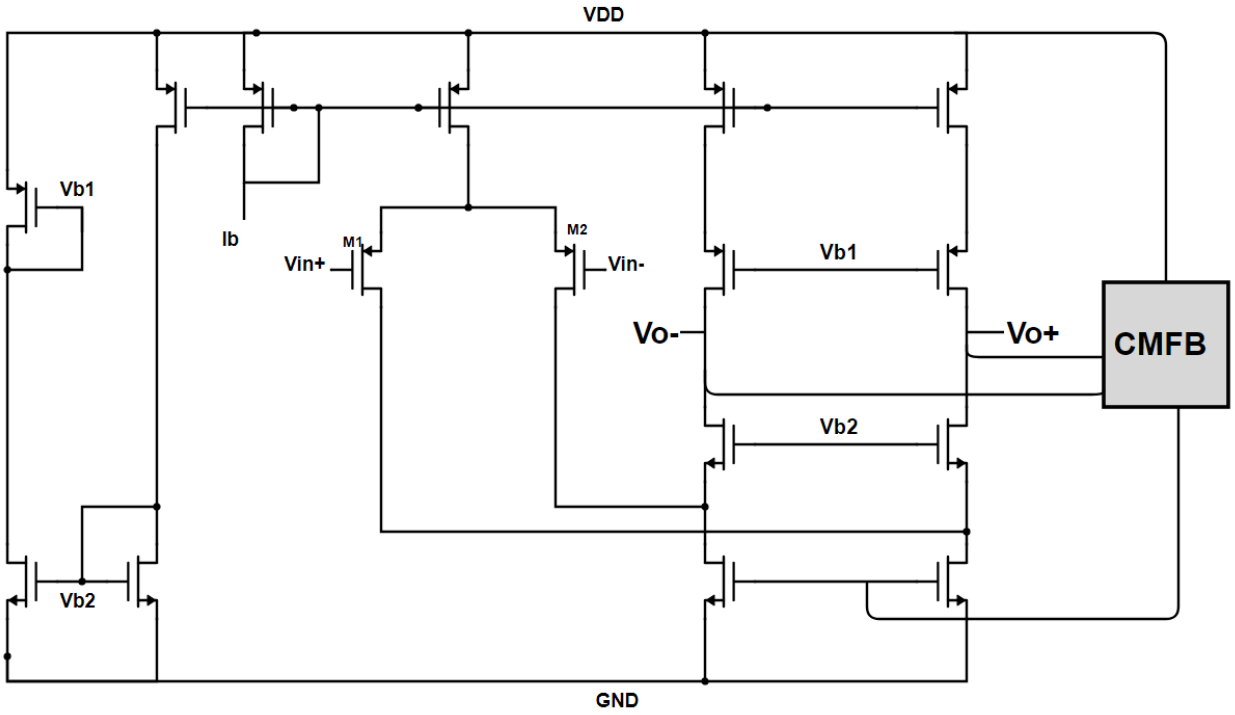

Figure 8 Amplifier of chopping topology with common mode feedback

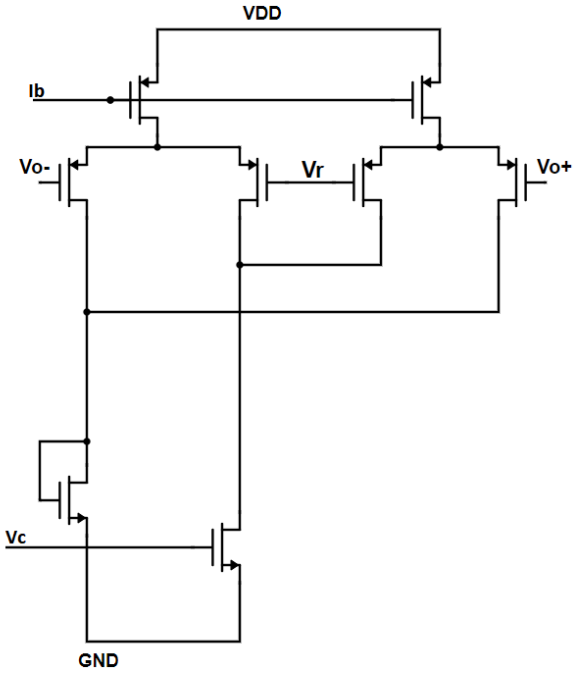

Figure 9 Common mode feedback circuit

Common mode feedback (CMFB) is used in order to control the output common mode voltage level and reject the common-mode activity of some components. To achieve these, CMFB with two differential pairs has been applied as depicted in Figure 9. As depicted in Figure 10, differential gain of the amplifier varies from 28dB to 32dB while its phase margin varies from 60 to 90 degrees when the biasing current is swept from 1µA to 31µA.

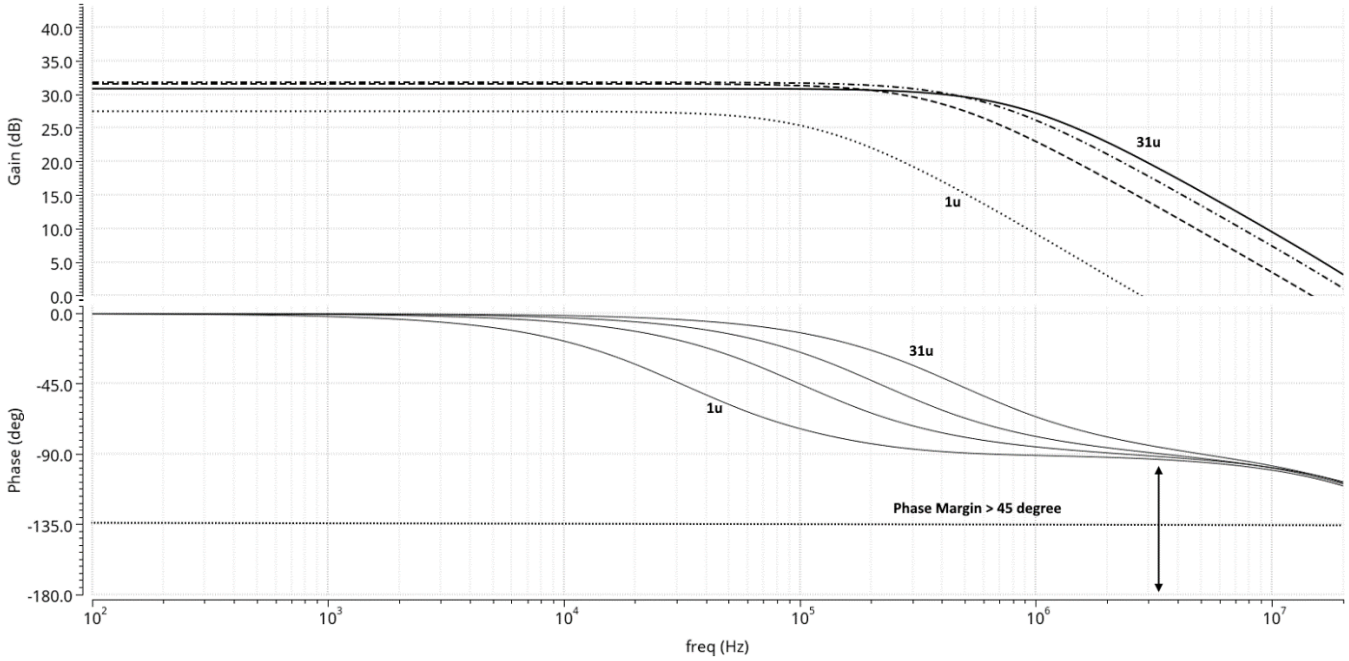

Figure 10 Amplifier gain and phase plots for bias currents of 1, 11, 21, and 31 µA

3.2.3. Low Pass Filter

In both industry and academic designs, G_m-C filters are the most tunable filter topology because G_m-c filters or OTA-C filters are easy to tune via the biasing current of OTAs. Besides, their power consumption is low and they have less phase shift than other filter types. Tuning the overall transconductance value of OTAs provides flexibility during filter design. However, in filter design, transconductance characteristics of the OTAs used in amplifiers are not as linear as desired. In order to achieve linear transconductance or G_m characteristics, linearization techniques such as current division [11] and source degeneration [12] are required. Transconductance of the OTA is the same as the transconductance of the differential PMOS transistors $g_{m1,2}$, which is equal to $\sqrt{2.K_{1,2}.I_b}$. The relationship between input differential voltage V_{id}, G_m, and output current I_o in the linear operating region of OTA is given in equation 3

$$I_o = G_m.V_{id}\sqrt{1-\left(\frac{V_{id}}{2V_{ov}}\right)^2} \quad (3)$$

The transconductance of OTAs can be tuned via biasing current I_{bias} under a vital constraint which is $V_{id} < 2V_{ov}$ for low voltage operations. To obtain more tunable and linear transconductance characteristics and to remove second harmonics, linearization techniques have been applied. So, the source degeneration resistors have been replaced by transistors which are operating in sub-threshold region [13]. Besides, current division method has been applied to linearize the transconductance characteristics of the OTA by adding two input pair transistors to the differential input of the OTA as shown in Figure 11.

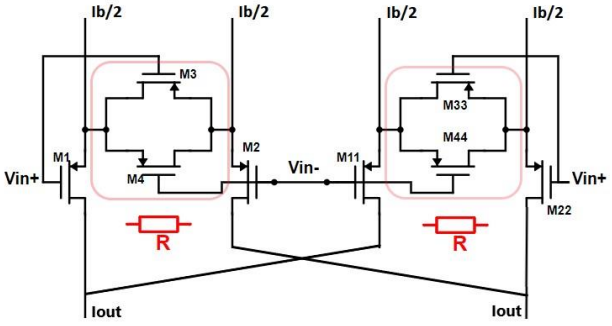

Figure 11 Current division and source degeneration method scheme [13]

$$\frac{G_{m1}}{(V_{ov1})^2} = \frac{G_{m2}}{(V_{ov2})^2} \quad (4)$$

The most important point in this step is to eliminate the third harmonic term of I_o. To achieve this, the transistors $M_{1,2,11,22}$ in Figure 11

have to satisfy the condition in Equation 4. This equation states that these particular transistors have to be matched as much as possible. Therefore, source degeneration method has also been applied to the OTAs because current division method alone is not sufficient to remove the third harmonic term. Unlike in the conventional approach, source degeneration method uses resistors; however, they are replaced by transistors operating in triode region because resistors add parasitics, cause thermal noise, occupy large area, and decrease individual and overall transconductance of OTAs [12]. As shown in Figure 11, when degeneration transistors M_3, M_4, M_{33}, and M_{44} are matched well, it is possible to obtain higher transconductance. The third harmonic term is further decreased after applying both current division and source degeneration methods [13].

The output current and transconductance characteristics of the linearized OTA have been simulated in Cadence and the results are shown in Figure 12. The biasing current from BDAC is tuned from 1 µA to 31 µA, V_{id} is tuned from -0.3 V to 0.3 V, and overall G_m of the linearized OTA varies from 330 µS to 690 µS. Similarly, simulation results for the output current I_{out} is shown in Figure 13. Between -0.3 V and 0.3 V V_{id}, the output current I_{out} has linear characteristics.

The designed OTAs are connected to implement fully differential 5th order Butterworth G_m-C filter as shown in Figure 14. 10 identical OTAs are used in G_m-C filter. All g_{mi} values are equal to each other and C = C_1 = C_2. The cut-off frequency of G_m-C filter can be found as $f = \frac{g_{mi}}{C}$ and the quality factor Q can be calculated as $Q = \frac{g_{mi}}{g_{mi2}}$. The transfer function of the filter is presented in Equation 5, which is the multiplication of a first order transfer function as in Equation 6 and two biquad sections as in Equations 7 and 8.

$$H(s) = H_{1st}(s).H_{2nd_1}(s).H_{2nd_2}(s) \quad (5)$$

$$H_{1st}(s) = \frac{G_{m1}}{G_{m2}+C_s} \quad (6)$$

$$H_{2nd_1}(s) = \frac{\frac{g_{m11}g_{m13}g_{m14}}{g_{m14}\quad C_1C_2}}{s^2+s\left(\frac{g_{m12}}{C_1}\right)+\frac{g_{m13}g_{m14}}{C_1C_2}} \quad (7)$$

$$H_{2nd_2}(s) = \frac{\frac{g_{m21}g_{m23}g_{m24}}{g_{m24}\quad C_1C_2}}{s^2+s\left(\frac{g_{m22}}{C_1}\right)+\frac{g_{m23}g_{m24}}{C_1C_2}} \quad (8)$$

This filter has been implemented and simulated in Cadence. In order to show its tunability, the biasing current from BDAC is swept from 1µA to 31µA to observe various cut-off frequencies. The 1µA biasing current corresponds to the cut-off frequency 15.6 kHz, 31µA bias current corresponds to cut-off frequency 56.7 kHz as shown in Figure 15.

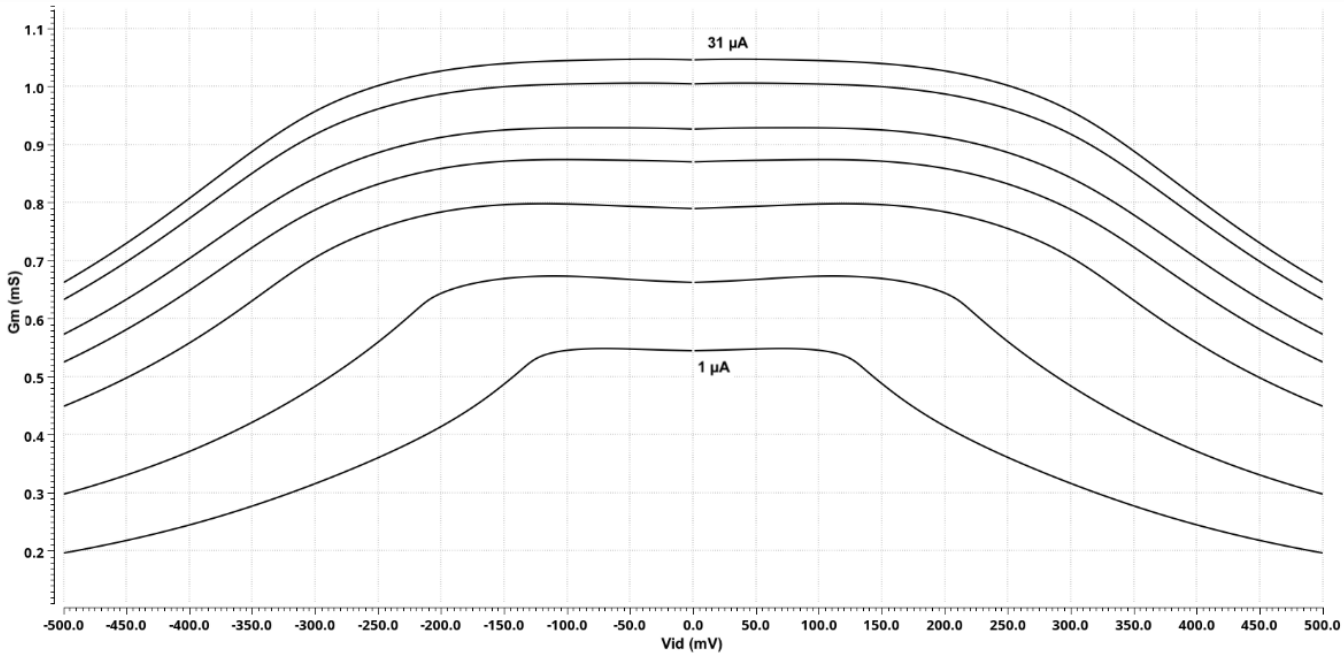

Figure 12 Overall transconductance G_m characteristics of the linearized OTA for bias currents 1, 6, 11, 16, 21, 26, and 31 µA

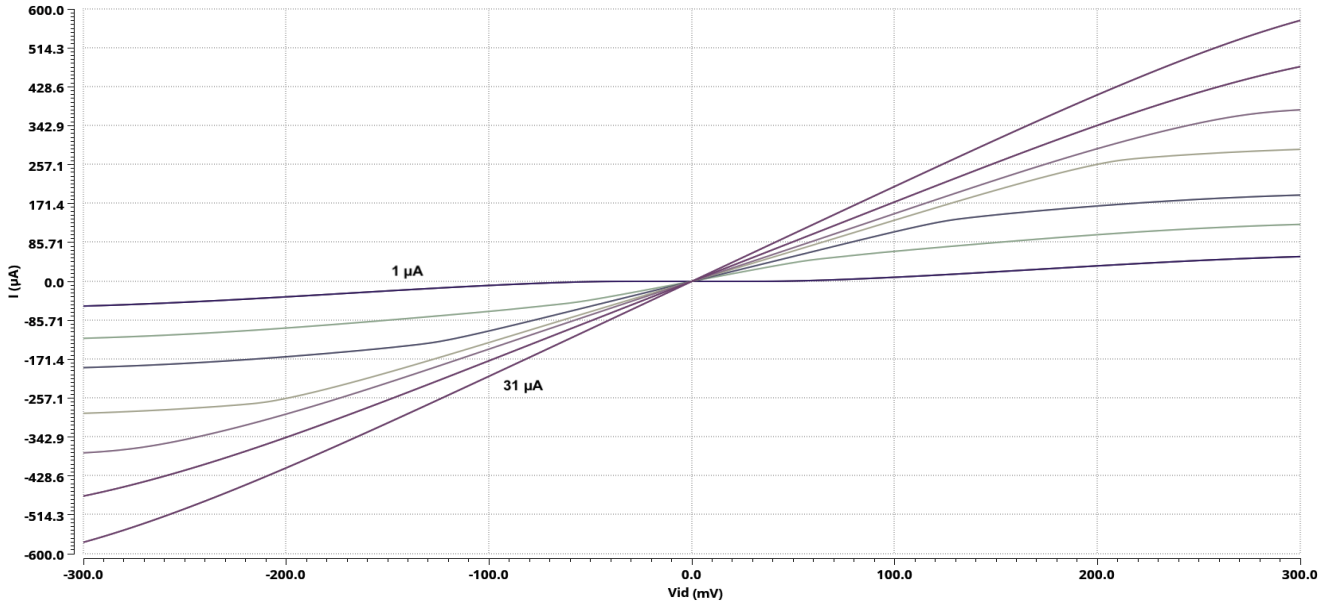

Figure 13 Output current I_{out} characteristic of the linearized OTA for bias currents 1, 6, 11, 16, 21, 26, and 31 µA

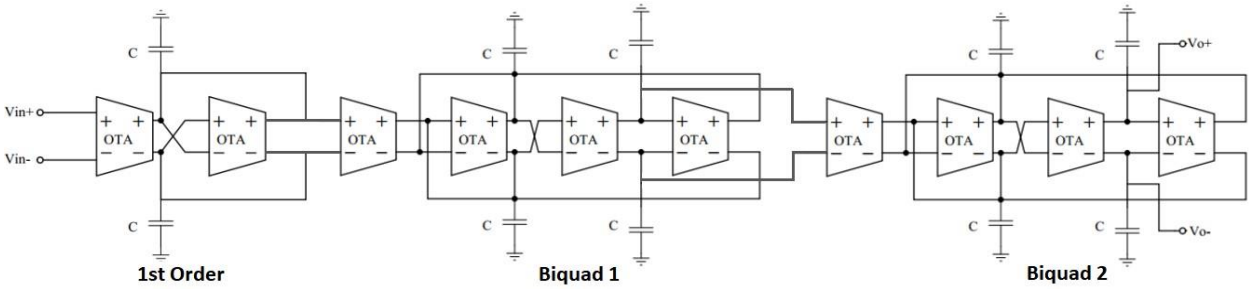

Figure 14 Fully differential 5th order Butterworth G_m-C filter

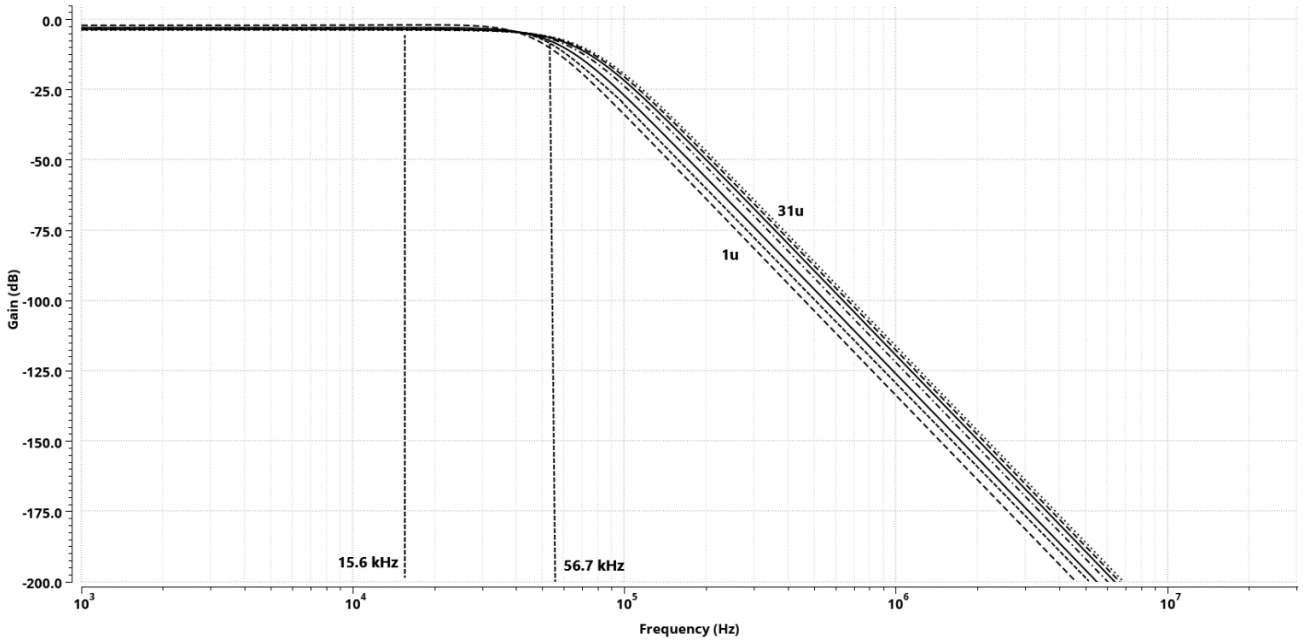

Figure 15 Fully differential 5th order Butterworth G_m-C filter after tuning I_{bias} at 1, 6, 11, 16, 21, 26, and 31 μA

4. SIMULATIONS AND RESULTS

A complete system is depicted in Figure 16, where the chopping amplifier and the fifth order G_m-C low-pass filter is at the center, and a clock signal generator for the choppers is placed to the left. To demonstrate the offset effects, a 1mV DC supply was added as V_{offset} to the positive input terminal of the OPAMP used in the amplifier. The bandgap reference circuit at the bottom left supplies biasing voltages and currents to the entire design via several digitally programmable BDACs. The BDAC below the amplifier generates biasing current for the amplifier, while the remaining 10 BDACs supply biasing currents for the OTAs in the G_m-C filter.

The chopping amplifier topology depicted in Figure 16 has been configured and simulated for three different frequencies, where the applied input signal frequencies are 10 Hz, 100 Hz, and 1 kHz as presented in Figures 17, 18, and 19, respectively; and chopper frequencies (f_{chop}) are selected as 100 times the signal frequencies. Filter cut-off frequencies (f_c) are selected as 500 Hz, 1 kHz, and 25 kHz for the configurations of simulation results in Figures 17, 18, and 19, respectively. The applied input signal is a 1 mV amplitude sine wave for each differential input, the overall signal gain is 25, and the input offset voltage is 1 mV DC in all configurations. All plots presented in Figures 17, 18, and 19 are differential voltages. In these figures, input signal V_{in} is plotted on the top, followed by the first chopper output, which is the input to the amplifier. The third, fourth and fifth plots present the amplifier output, the filter input (i.e., the second chopper output), and the filter output, respectively. This topology eliminates the offset contribution from the amplifier significantly as demonstrated by the fifth plot (i.e., filter output). Without the choppers in the system, the amplifier alone would amplify the input offset as well as the input signal, resulting in a significant DC level shift with respect to the signal amplitude, as demonstrated in the sixth plot. The difference between the fifth (i.e., filter output) and sixth (i.e., V_{out} without chopper) plots proves that the chopper helps amplification of a weak input signal without any DC offset, making the output signal ready for conversion to digital. The filter required by the chopper topology also serves as the anti-aliasing filter required by the analog to digital converters (ADC); thus, it is not really an additional cost to the system.

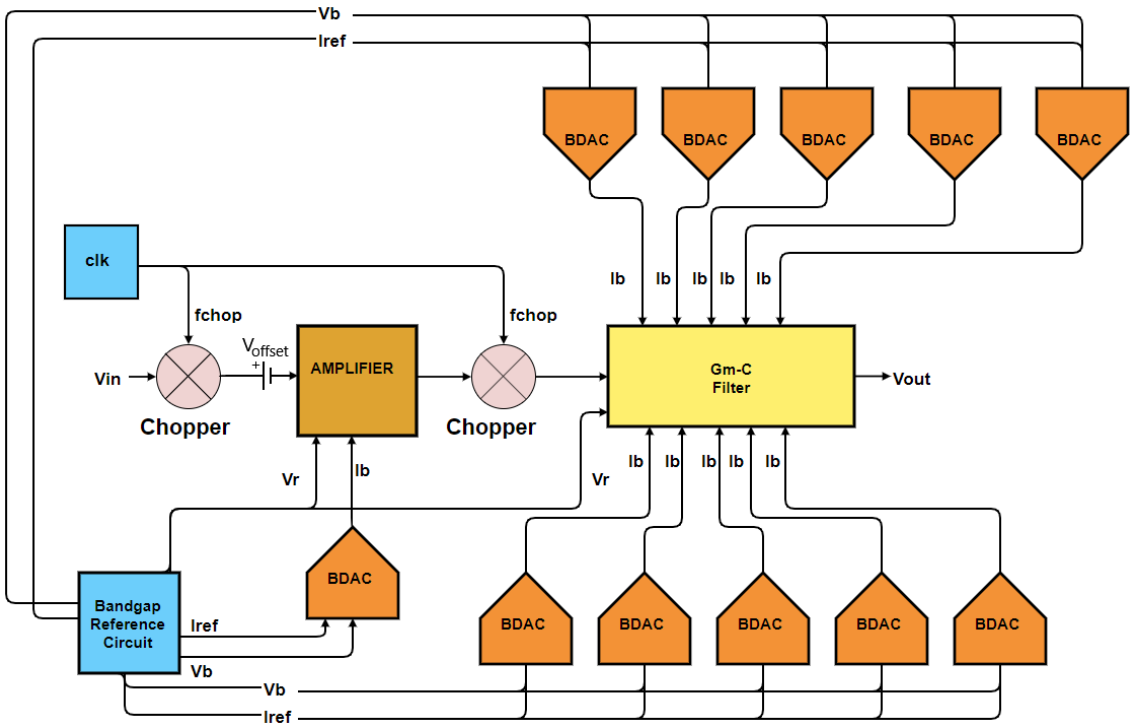

Figure 16 Chopping amplifier topology with tunable G_m-C filter

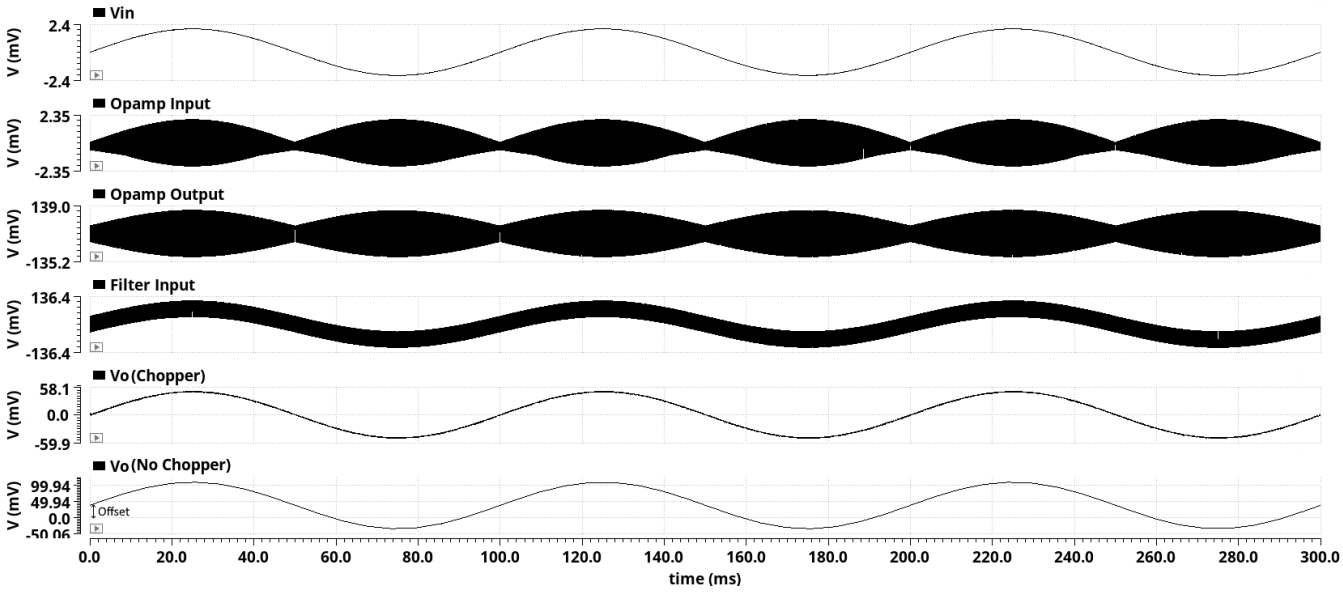

Figure 17 Simulation result of chopping topology with tunable G_m-C filter, f_{input}=10Hz, f_{chop}=1kHz and f_c=500Hz

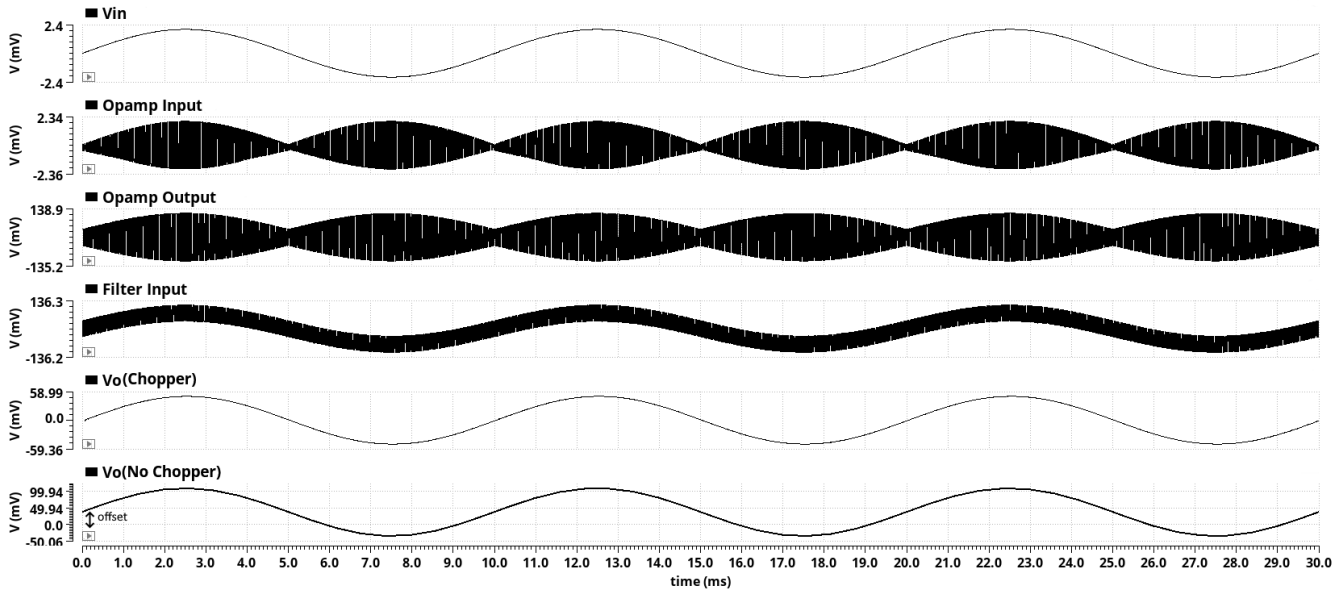

Figure 18 Simulation result of chopping topology with tunable G_m-C filter, f_{input}=100Hz, f_{chop}=10kHz and f_c=1kHz

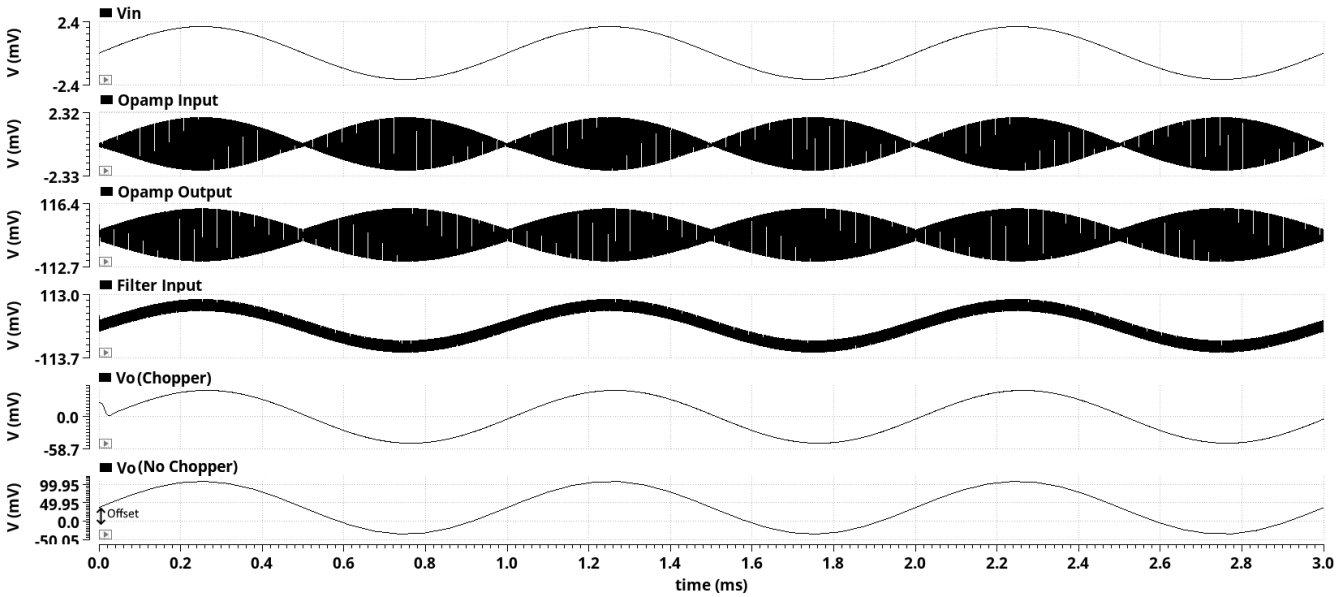

Figure 19 Simulation result of chopping topology with tunable G_m-C filter, f_{input}=1kHz, f_{chop}=100kHz and f_c=25kHz

5. CONCLUSION

There are many physical quantities to measure and as many sensors, which have different interfacing requirements. Designing a new interface for each sensor type and application is an unnecessarily difficult and expensive task. A configurable interface to be used for a wide range of analog sensor outputs has been designed and simulated in UMC 130nm CMOS technology. Chopping amplifier topology has been used as a precision technique to remove the DC offset, which can be a major problem in the processing of low frequency signals. As filter, a fully differential 5th order low pass Butterworth G_m-C filter has been designed from configurable OTAs and connected to the output of the chopping amplifier to obtain a clean signal. Both filter and amplifier are tunable via biasing current supplied from BDAC. The proposed design is self-biased so that all biasing voltages and currents are generated by a bandgap reference circuit. Operating frequency is up to 100 kHz while designed filters are able to operate in a wider range.

Funding

This study is supported by the research Grant of the Scientific and Technological Research Council of Turkey (TUBITAK) project under the Project Number 111E195.

The Declaration of Conflict of Interest/ Common Interest

No conflict of interest or common interest has been declared by the authors.

Authors' Contribution

The first author contributed 40%, the second author 60%.

The Declaration of Ethics Committee Approval

This study does not require ethics committee permission or any special permission.

The Declaration of Research and Publication Ethics

The authors of the paper declare that they comply with the scientific, ethical and quotation rules of SAUJS in all processes of the paper and that they do not make any falsification on the data collected. In addition, they declare that Sakarya University Journal of Science and its editorial board have no responsibility for any ethical violations that may be encountered, and that this study has not been evaluated in any academic publication environment other than Sakarya University Journal of Science.

REFERENCES

[1] F. Butti, P. Bruschi, M. Piotto, "A chopper modulated low noise instrumentation amplifier for MEMS thermal sensors interfacing", 2011 7th Conference on Ph. D. Research in Microelectronics and Electronics, Madonna di Campiglio, Italy, 2011, pp. 133–136.

[2] A. N. Mohamed, H. N. Ahmed, M. Elkhatib, K. A. Shehata, "A low power low noise capacitively coupled chopper instrumentation amplifier in 130 nm CMOS for portable biopotential acquisiton systems", 2013 International Conference on Computer Medical Applications (ICCMA), Sousse, Tunisia, 2013, pp. 1–5.

[3] Y. Ando, N. H. Fletcher, M. R. Schroeder, "Modern Acoustics and Signal Processing", pp. 12–13, 2007.

[4] J. Wu, G. K. Fedder, L. R. Carley, "A low-noise low-offset capacitive sensing amplifier for a 50-μg/√Hz monolithic CMOS MEMS accelerometer", IEEE Journal of Solid-State Circuits, vol. 39, no. 5, pp. 722–730, 2004.

[5] R. Wu,, J. H. Huijsing, K. A. Makinwa, "Precision instrumentation amplifiers and read-out integrated circuits", Springer Science & Business Media, 2012.

[6] J.F. Witte, "Dynamic offset compensated CMOS amplifiers" EEMCS, Delft University of Technology, 2008, p.178.

[7] A. Sarrafinazhad, I. Kara, F. Baskaya, "Design of blocks for a Field Programmable Mixed Array (FPMA)", 2015 IEEE East-West Design Test Symposium (EWDTS), 2015, pp. 1–6.

[8] P. E. Allen, D. R. Holberg, "CMOS analog circuit design", Elsevier, 2011.

[9] Q. Fan, K. A. Makinwa, J. H. Huijsing, "Capacitively-Coupled Chopper Amplifiers" Springer, 2017.

[10] P. R. Gray, P. J. Hurst, S. H. Lewis, R. G. Meyer, "Analysis and design of analog integrated circuits" John Wiley & Sons, 2009.

[11] A. Lewinski and J. Silva-Martinez, "OTA linearity enhancement technique for high frequency applications with IM3 below -

65dB", Proceedings of the IEEE 2003 Custom Integrated Circuits Conference, 2003, pp. 9–12.

[12] J. L. L. Ochoa, E. M. Guerrero, E. J. Hernandez, "A 3rd order OTA-C low pass filter for W-CDMA standard applications in zero-IF receiver", CONIELE-COMP 2013, 23rd International Conference on Electronics, Communications and Computing, 2013, pp. 249–253.

[13] A. Sarrafinazhad, I. Kara, F. Baskaya, "Design of a digitally tunable 5th order GM-C filter using linearized OTA in 90nm CMOS technology", 2015 International Symposium on Signals, Circuits and Systems (ISSCS), 2015, pp. 1–4.

SAKARYA ÜNİVERSİTESİ
FEN BİLİMLERİ ENSTİTÜSÜ DERGİSİ

Sakarya University Journal of Science
SAUJS

ISSN 1301-4048 e-ISSN 2147-835X Period Bimonthly Founded 1997 Publisher Sakarya University
http://www.saujs.sakarya.edu.tr/

Title: All solutions of the Diophantine equations 2F_n=3^s·y^b and F_n±1=3^s·y^b

Authors: İbrahim ERDURAN, Zafer ŞİAR

Recieved: 2022-02-10 00:00:00

Accepted: 2022-04-18 00:00:00

Article Type: Research Article

Volume: 26
Issue: 3
Month: June
Year: 2022
Pages: 488-492

How to cite
İbrahim ERDURAN, Zafer ŞİAR; (2022), All solutions of the Diophantine equations 2F_n=3^s·y^b and F_n±1=3^s·y^b. Sakarya University Journal of Science, 26(3), 488-492, DOI: 10.16984/saufenbilder.1069960
Access link
http://www.saujs.sakarya.edu.tr/tr/pub/issue/70993/1069960

Sakarya University Journal of Science 26(3), 488-492, 2022

All solutions of the Diophantine equations $2F_n = 3^s \cdot y^b$ and $F_n \pm 1 = 3^s \cdot y^b$

İbrahim ERDURAN*[1], Zafer ŞİAR[1]

Abstract

The Fibonacci sequence (F_n) is defined by $F_0 = 0$, $F_1 = 1$, and $F_n = F_{n-1} + F_{n-2}$ for $n \geq 2$. In this paper, we will give all solutions of the Diophantine equations $2F_n = 3^s \cdot y^b$ and $F_n \pm 1 = 3^s \cdot y^b$ in nonnegative integers $s \geq 0$, $y \geq 1$, $b \geq 2$, $n \geq 1$ and $(3, y) = 1$.

Keywords: Fibonacci and Lucas numbers, exponential Diophantine equations, elementary number theory

1. INTRODUCTION

The Fibonacci sequence (F_n) is defined by $F_0 = 0$, $F_1 = 1$, and $F_n = F_{n-1} + F_{n-2}$ for $n \geq 2$. The Lucas sequence (L_n), which is similar to the Fibonacci sequence, is defined by the same recursive pattern with initial conditions $L_0 = 2$, $L_1 = 1$. The terms of the Fibonacci and Lucas sequences are called Fibonacci and Lucas numbers, respectively. The Fibonacci and Lucas numbers for negative indices are defined by $F_{-n} = (-1)^{n+1}F_n$ and $L_{-n} = (-1)^n L_n$ for $n \geq 1$. For a brief history of Fibonacci and Lucas sequences one can consult [7]. The Fibonacci and Lucas sequences have many interesting properties and have been studied in the literature by many researchers. They specially have interested in square terms, perfect powers in these sequences and the exponential Diophantine equations including these sequences. Firstly, square terms and later perfect powers in the Fibonacci and Lucas sequences have attracted the attention of the researchers. As related these subjects, the authors gave the following theorems, which can be deduced from [4,5,6] and are useful to us.

Theorem 1. The only perfect powers in the Fibonacci sequence are $F_0 = 0, F_1 = 1, F_2 = 1, F_6 = 8$ and $F_{12} = 144$.

Theorem 2. The only perfect powers in the Lucas sequence are $L_1 = 1$ and $L_3 = 4$.

Theorem 3. If

$$F_n = 2^s \cdot y^b$$

for some integers $n \geq 1$, $y \geq 1$, $b \geq 2$ and $s \geq 0$ then $n \in \{1,2,3,6,12\}$. The solutions of the similar equation with F_n replaced by L_n have $n \in \{1,3,6\}$.

Theorem 4. If

$$F_n = 3^s \cdot y^b$$

* Corresponding author: ierduran01@gmail.com
[1] Bingöl University, Faculty of Science and Literature, Department of Mathematics
E-mail: zsiar@bingol.edu.tr
ORCID: https://orcid.org/0000-0003-3307-8181, https://orcid.org/0000-0002-6473-4754

for some integers $n \geq 1, y \geq 1, b \geq 2$ and $s \geq 0$ then $n \in \{1,2,4,6,12\}$. The solutions of the similar equation with F_n replaced by L_n have $n \in \{1,2,3\}$.

Recently, many mathematicians have dealth with exponential Diophantine equations concerning Fibonacci and Lucas numbers. For example, the Diophantine equation $L_n + L_m = 2^a$ has been tackled in [2] by Bravo and Luca. Two years later, the same authors solved Diophantine equation $F_n + F_m = 2^a$ in [3]. Besides, in [5], Bugeaud et al. showed that if

$$F_n \pm 1 = y^a \tag{1}$$

for some nonnegative integers (n, y, a) with $a \geq 2$, then $n \in \{0,1,2,3,4,5,6\}$. In [1], the authors proved that if

$$F_n \pm 2 = y^a \tag{2}$$

for some nonnegative integers (n, y, a) with $a \geq 2$, then $n \in \{1,2,3,4,9\}$. Later, in [10], Luca and Patel handled the equation

$$F_n \pm F_m = y^p, \ p \geq 2, \tag{3}$$

which is general form of the equations (1) and (2). They found that the Diophantine equation (3) in integers (n, m, y, p) has solution either $max\{|n|, |m|\} \leq 36$ or $y = 0$ and $|n| = |m|$ if $n \equiv m(mod 2)$. This problem remain open for the case $n \not\equiv m(mod 2)$. But, in [8], the authors solved this equation by fixing y in the interval [2,1000].

Motivated by the above mentioned studies, in this paper, we consider the Diophantine equations

$$F_n + F_n = 2F_n = 3^s \cdot y^b \tag{4}$$

and

$$F_n \pm 1 = 3^s \cdot y^b \tag{5}$$

in nonnegative integers $s \geq 0, y \geq 1, b \geq 2, n \geq 1$ and $(3, y) = 1$.

2. PRELIMINARIES

In this section, we will give some idendities including Fibonacci and Lucas numbers, which will be used in the proofs of the main theorems. The following identites can be found in [9].

$$F_{n+1} + F_{n-1} = L_n. \tag{6}$$

If $m \geq 3$, then $F_m | F_n \Leftrightarrow m | n$. (7)

If $m \geq 2$, then $L_m | L_n \Leftrightarrow m | n$ and $\frac{n}{m}$ is odd. (8)

$$F_{3n} = F_n\left(5{F_n}^2 + 3(-1)^n\right). \tag{9}$$

The following theorem is given in [9].

Theorem 5. ([9], $Theorem$ 10.9), *The following equalities hold.*

1. $F_{4k} + 1 = F_{2k-1} \cdot L_{2k+1}$,

2. $F_{4k+1} + 1 = F_{2k+1} \cdot L_{2k}$,

3. $F_{4k+2} + 1 = F_{2k+2} \cdot L_{2k}$,

4. $F_{4k+3} + 1 = F_{2k+1} \cdot L_{2k+2}$,

5. $F_{4k} - 1 = F_{2k+1} \cdot L_{2k-1}$,

6. $F_{4k+1} - 1 = F_{2k} \cdot L_{2k+1}$,

7. $F_{4k+2} - 1 = F_{2k} \cdot L_{2k+2}$,

8. $F_{4k+3} - 1 = F_{2k+2} \cdot L_{2k+1}$.

Using the property $(F_m, F_n) = F_{(m,n)}$ given in Theorem 10.3 of [9], it can be easily seen that the greatest common divisors of Fibonacci and Lucas numbers in the right side of the equalties in the above theorem are 1 or 3. Particularly,

$$\begin{aligned}(F_{2k-1}, L_{2k+1}) = (F_{2k+1}, L_{2k}) = (F_{2k+1}, L_{2k+2}) \\ = (F_{2k+1}, L_{2k-1}) = (F_{2k}, L_{2k+1}) \\ = (F_{2k+2}, L_{2k+1}) = 1\end{aligned} \tag{10}$$

and

$$(F_{2k+2}, L_{2k}) = (F_{2k}, L_{2k+2}) = 1 \text{ or } 3. \tag{11}$$

3. MAIN THEOREMS

Theorem 6. The only solutions of the Diophantine equation (4) in nonnegative integers $s \geq 0$, $y \geq 1$, $b \geq 2$, $n \geq 1$ and $(3, y) = 1$, are given by

$(n, s, y, b) =$
$(3,0,2,2), (6,0,2,4), (6,0,4,2), (12,2,2,5).$

Proof. Assume that (n, s, y, b) is a solution of the equation (4). If $s = 0$, then we get $2F_n = y^b$ and therefore $F_n = 2^{b-1} \cdot \left(\frac{y}{2}\right)^b$. This equation has solutions only for $n = 3$ or $n = 6$ by Theorem 3. Thus, we can see by a simple computation that $(n, s, y, b) = (3,0,2,2), (6,0,2,4), (6,0,4,2)$.
From now on, assume that $s \geq 1$. On the other hand, it is clear that y is an even number. Say $y = 2^r x$ for some positive integers x and r such that $(x, 2) = 1$. Then we have the equation

$$F_n = 3^s \cdot 2^{rb-1} \cdot x^b. \tag{12}$$

Let n be the smallest positive integer satisfying the equation (12). Since $b \geq 2$, it follows that 2^{rb-1} is an even number. Therefore $2|F_n$, which implies that $3|n$ by (7). Hence, $n = 3k$ for some positive integer k. Thus, we get the equation

$$F_n = F_{3k} = F_k\left(5{F_k}^2 + 3(-1)^k\right) = 3^s \cdot 2^{rb-1} \cdot x^b \tag{13}$$

by (9). Since $s \geq 1$, it follows that $3|F_n$ and thus it can be seen that $3|F_k$ and $3|\left(5{F_k}^2 + 3(-1)^k\right)$. Therefore, it should be $s \geq 2$. Then, the equation (13) can be written

$$\left(\frac{F_k}{3}\right)\left(\frac{5{F_k}^2+3(-1)^k}{3}\right) = 3^{s-2} \cdot 2^{rb-1} \cdot x^b. \tag{14}$$

Also, it is obvious that $\left(\frac{F_k}{3}, \frac{5{F_k}^2+3(-1)^k}{3}\right) = 1$ and thus $3 \nmid \left(\frac{5{F_k}^2+3(-1)^k}{3}\right)$. Hence, we have

$$\frac{F_k}{3} = 3^{s-2}u^b \text{ and } \frac{5{F_k}^2+3(-1)^k}{3} = 2^{rb-1}v^b$$

or

$$\frac{F_k}{3} = 3^{s-2} \cdot 2^{rb-1} \cdot u^b \text{ and } \frac{5{F_k}^2+3(-1)^k}{3} = v^b$$

for some positive integers u and v such that $(u, v) = 1$, $uv = x$. In the first case, the equation $F_k = 3^{s-1}u^b$ has solution only for $k = 4$ or $k = 12$ by Theorem 4 since $s \geq 2$. If $k = 4$, then we get $s = u = 1$ and $b = 5$, $r = v = 1$ from the equality

$$\frac{5{F_k}^2+3(-1)^k}{3} = \frac{5{F_4}^2+3(-1)^4}{3} = 16 = 2^{rb-1} \cdot v^b .$$

Thus $(n, s, y, b) = (12,2,2,5)$ is a solution. In the second case, we have the equation $F_k = 3^{s-1} \cdot 2^{rb-1} \cdot u^b$, which is in the form (12). But, since $k < n$, this contradicts our assumption that n is the smallest positive integer satisfiying the equation $F_k = 3^{s-1} \cdot 2^{rb-1} \cdot u^b$.

As a result, the solutions (n, s, y, b) satisfying (4) are $(3,0,2,2), (6,0,2,4), (6,0,4,2)$ and $(12,2,2,5)$. Thus, the proof is completed.

Theorem 7. Let $s \geq 0, y \geq 1, b \geq 2, n \geq 2$ and $(3, y) = 1$. Then all solutions of the equation

$$F_n \pm 1 = 3^s \cdot y^b \tag{15}$$

are

$F_4 + 1 = 4 = 3^0 \cdot 2^2$, $F_6 + 1 = 9 = 3^2 \cdot 1^b$,
$F_3 + 1 = 3 = 3^1 \cdot 1^b$

and

$F_5 - 1 = 4 = 3^0 \cdot 2^2$, $F_3 - 1 = 1 = 3^0 \cdot 1^b$,
$F_7 - 1 = 12 = 3^1 \cdot 2^2$.

Proof. Assume that (n, s, y, b) is a solution of the equation (15). If we divide n by 4, we can write $n = 4k + r$ with $0 \leq r \leq 3$ for some integers k, r. Thus, considering the equation (15) together with Theorem 5, we have the following cases:

i) $F_{4k} + 1 = F_{2k-1} \cdot L_{2k+1} = 3^s y^b$,

ii) $F_{4k+1} + 1 = F_{2k+1} \cdot L_{2k} = 3^s y^b$,

iii) $F_{4k+2} + 1 = F_{2k+2} \cdot L_{2k} = 3^s y^b$,

iv) $F_{4k+3} + 1 = F_{2k+1} \cdot L_{2k+2} = 3^s y^b$,

v) $F_{4k} - 1 = F_{2k+1} \cdot L_{2k-1} = 3^s y^b$,

vi) $F_{4k+1} - 1 = F_{2k} \cdot L_{2k+1} = 3^s y^b$,

vii) $F_{4k+2} - 1 = F_{2k} \cdot L_{2k+2} = 3^s y^b$,

viii) $F_{4k+3} - 1 = F_{2k+2} \cdot L_{2k+1} = 3^s y^b$.

Case i) In this case, since $3 \nmid F_{2k-1}$ and $3 \nmid L_{2k+1}$ by (7) and (8), it follows that $s = 0$. Then, using (10), we have the equations $F_{2k-1} = u^b$ and $L_{2k+1} = v^b$ for some integers u and v such that $(u, v) = 1$ and $y = uv$. By Theorem 1, it is seen that $k = 1, v = b = 2$ and therefore $u = 1$. Thus, $(n, s, y, b) = (4,0,2,2)$.

Case ii) Since $3 \nmid F_{2k+1}$ by (7), we have $F_{2k+1} = u^b, L_{2k} = 3^s v^b$ for some integers u and v such that $(u, v) = 1$ and $y = uv$. It can be seen that these equations have no solution by Theorem 1 and Theorem 4.

Case iii) We know that $(F_{2k+2}, L_{2k}) = 1$ or 3 by (11). Firstly, let $(F_{2k+2}, L_{2k}) = 1$. If k is odd, then $3 \mid F_{2k+2}$ and $3 \mid L_{2k}$ by (7) and (8) and thus $3 \mid (F_{2k+2}, L_{2k})$, which contradicts the fact that $(F_{2k+2}, L_{2k}) = 1$. Therefore k is even. Thus, since $3 \nmid F_{2k+2}$ and $3 \nmid L_{2k}$ by (7) and (8), it follows that $s = 0$. Then we have the equations $F_{2k+2} = u^b$ and $L_{2k} = v^b$ for some integers u and v such that $(u, v) = 1$ and $y = uv$. But, the equation $L_{2k} = v^b$ has no solutions by Theorem 2. Secondly, let $(F_{2k+2}, L_{2k}) = 3$. Then, it is obvious that $s \geq 2$, $\left(\frac{F_{2k+2}}{3}, \frac{L_{2k}}{3}\right) = 1$ and k is odd. In this case, we have the following equations

$$\frac{F_{2k+2}}{3} = u^b, \frac{L_{2k}}{3} = 3^{s-2} v^b$$

and

$$\frac{F_{2k+2}}{3} = 3^{s-2}, \frac{L_{2k}}{3} = v^b$$

for some integers u and v such that $(u, v) = 1$ and $y = uv$. In both cases, we get $k = 1$ by Theorem 4. Thus, making necessary calculation we obtain $(n, s, y, b) = (6,2,1, b)$.

Case iv) In this case, since $3 \nmid F_{2k+1}$ by (7), we have the equation $F_{2k+1} \cdot \frac{L_{2k+2}}{3^s} = y^b$. Using (10), this equation implies that there exist positive integers u and v such that $(u, v) = 1$, $y = uv$, $F_{2k+1} = u^b$ and $\frac{L_{2k+2}}{3^s} = v^b$. By Theorem 1, the equation $F_{2k+1} = u^b$ has a solution only for $k = 0$. Thus, we get $(n, s, y, b) = (3,1,1, b)$.

Since the proof of the last four cases is similar to that of the first four cases, we omit them. Considering a similar argument, we see that the solutions of the equation (15) is $(n, s, y, b) = (5,0,2,2), (3,0,1, b), (7,1,2,2)$. Thus, the proof is completed.

4. CONCLUDING REMARK

It is an open problem to find all solutions of the equation $F_n \pm F_m = 3^s \cdot y^b$ in nonnegative integers $s \geq 0, y \geq 1, b \geq 2, n \geq m \geq 1$ and $(3, y) = 1$. Theorem 6 and Theorem 7 can be useful to find the solutions of the equation $F_n \pm F_m = 3^s \cdot y^b$.

Acknowledgments

The authors wish to thank the editors and the anonymous referees for their contributions.

Funding

The authors has no received any financial support for the research, authorship or publication of this study.

The Declaration of Conflict of Interest/ Common Interest

No conflict of interest or common interest has been declared by the authors.

Authors' Contribution

The first author contributed 40%, the second author 60%.

The Declaration of Ethics Committee Approval

This study does not require ethics committee permission or any special permission

The Declaration of Research and Publication Ethics

"The authors of the paper declare that they comply with the scientific, ethical and quotation rules of SAUJS in all processes of the paper and that they do not make any falsification on the data collected. In addition, they declare that Sakarya University Journal of Science and its editorial board have no responsibility for any ethical violations that may be encountered, and that this study has not been evaluated in any academic publication environment other than Sakarya University Journal of Science.

REFERENCES

[1] M.A. Bennett, V. Patel, S. Siksek, "Shifted powers in Lucas-Lehmer sequences" Research in Number Theory, vol. 5, no. 1, pp. 1-27, 2019.

[2] J. J. Bravo, F. Luca, "Powers of Two as Sums of Two Lucas Numbers" Journal of Integer Sequences, vol. 17, no. 8, pp. 14-8, 2014.

[3] J. J. Bravo, F. Luca, "On the Diophantine Equation $F_n + F_m = 2^a$" Quaestiones Mathematicae, vol. 39, no. 3, pp. 391-400, 2016.

[4] Y. Bugeaud, M. Mignotte, S. Siksek, "Classical and modular approaches to exponential Diophantine equations I. Fibonacci and Lucas perfect Powers", Annals of mathematics, vol. 163, no. 3, pp. 969-1018, 2006.

[5] Y. Bugeaud, F. Luca, M. Mignotte, S. Siksek, "Fibonacci numbers at most one away from a perfect power" Elemente der Mathematik, vol. 63, pp. 65-75, 2008.

[6] Y. Bugeaud, F. Luca, M. Mignotte, S. Siksek, "Perfect powers from products of terms in Lucas sequences" Journal fur die Reine und Angewandte Mathematik, vol. 611, pp. 109-129, 2007.

[7] L. Debnath, "A short history of the Fibonacci and golden numbers with their applications" International Journal of Mathematical Education in Science and Technology, vol. 42, no. 3, pp. 337-367, 2011.

[8] S. Kebli, O. Kihel, J. Larone, F. Luca, "On the nonnegative integer solutions to the equation $F_n \pm F_m = y^a$" Journal of Number Theory, vol. 220, pp. 107-127, 2021.

[9] T. Koshy, "Fibonacci and Lucas Numbers with Applications", John Wiley and Sons, Proc., New York-Toronto, 2001.

[10] F. Luca, V. Patel, "On perfect powers that are sums of two Fibonacci numbers" Journal of Number Theory, vol. 189, pp. 90-96, 2018.

SAKARYA ÜNİVERSİTESİ
FEN BİLİMLERİ ENSTİTÜSÜ DERGİSİ

Sakarya University Journal of Science
SAUJS

ISSN 1301-4048 e-ISSN 2147-835X Period Bimonthly Founded 1997 Publisher Sakarya University
http://www.saujs.sakarya.edu.tr/

Title: Decolorization of Some Textile Dyes Using Phormidium sp. in Heterotrophıc Culture Conditions

Authors: Tuğba ŞENTÜRK

Recieved: 2021-12-30 00:00:00

Accepted: 2022-04-21 00:00:00

Article Type: Research Article

Volume: 26
Issue: 3
Month: June
Year: 2022
Pages: 493-500

How to cite
Tuğba ŞENTÜRK; (2022), Decolorization of Some Textile Dyes Using Phormidium sp. in Heterotrophıc Culture Conditions. Sakarya University Journal of Science, 26(3), 493-500, DOI: 10.16984/saufenbilder.1050981
Access link
http://www.saujs.sakarya.edu.tr/tr/pub/issue/70993/1050981

Sakarya University Journal of Science 26(3), 493-500, 2022

Decolorization of Some Textile Dyes Using *Phormidium* sp. in Heterotrophic Culture Conditions

Tugba SENTURK*[1]

Abstract

Cyanobacteria have gained interest in recent decades as intriguing potential bioresources candidates due to their potential applications in biotechnology. Under heterotrophic circumstances, the decolorization of Dianix Blue CC, Benazol Black Zn, and Dianix Yellow Brown CC by the low-cost biosorbent *Phormidium* (Cyanobacteria) with three different initial dye concentrations of 25, 50, and 100 mg/L was examined. For the best dye decolorization, the carbon source, incubation period, temperature, pH, and agitation rate were 10 g/L glucose, 168 h, 40 0C, 8.5, and 60 rpm, respectively. *Phormidium* showed high dye uptake, with maximum efficiency ranging from 20% to 40% (5.47 to 40.04 mgg^{-1}) for Dianix Blue, 22% to 52% (5.95 to-52.32 mgg^{-1}) for Benazol Black ZN and 20% to 68% (13.18 to 20.78 mgg^{-1}) for Dianix Yellow Brown under heterotrophic conditions at all dye concentrations tested. The best color decolorization in terms of maximum efficiency was obtained 57% (57.76 mgg^{-1}) for Dianix Blue, 74% (74.04 mgg^{-1}) for Benazol Black at 100 mg/L and 77% (19.42 mgg^{-1}) for Dianix Yellow Brown at 25 mg/L dye concentrations. The study reveals that the decolorization of dye process using *Phormidium* offers an efficient, quit of charges and environmentally friendly biosorbent for the remediation of textile effluents.

Keywords: *Phormidium*, Decolorization, Heterotrophic culture, Bioremediation.

1. INTRODUCTION

Synthetic dyes and pigments have been widely used for various industries like dying textile fibers, plastic, leather, paper industries etc., to colour their final products [1]. The effluents of these industries are discharged into receiving waters cause damages to the ecological balance, affecting photosynthetic activity in aquatic food web because of curtained light refraction [2-6]. Many investigations focused on different techniques including almost all the known physical (membran flotation), chemical (coagulation, precipitation) and biological techniques (inactivated or activated biosorbents) for removal of dye from wastewaters [7]. Each process alone may not meet the requirements. Therefore, these processes are could be a combination like chemical-biological, biological-chemical, chemical-physical, chemical-chemical etc. Besides, it is necessary to develop a low-cost

* Corresponding author: tugba_sen34@hotmail.com
[1] Manisa Celal Bayar University
ORCID: https://orcid.org/ 0000-0002-9882-0079

or cost-efficient sorbent or biosorbent that are easily accessible with lofty adsorption capacities. There are number of biosorbents for the treatment of various industrial effluents. Phytoremediation of wastewater from textile industry could be less expensive alternative techniques compared to the physical and chemical methods. Many microorganisms such as fungi, algae and bacteria etc., either in their living or dead cell, have been studied to decolorization methods from wastewaters [8-13]. However, there are few studies concerning the bioaccumulation of unwanted materials from wastewaters by living microalgae [14-16].

The potential synthetic dye uptake capability of a low-priced biosorbent *Phormidium* microalgae (cyanobacteria) is well recognized for its biosorption capacity [17]. *Phormidium* is prokaryotic blue green algae and its biomass can be easily and economically produced [18] and the results of this study supported that the algal biomass can be used as efficient biosorbent for treatment of textile wastewater. Therefore, utilization of living or dead biomass as a biosorbent could be one of the useful features for the regional communities. For this reason, *Phormidium* a cheap and low cost biosorbent has been chosen for this study.

The research objective was to determine decolorization potential of most widely used dyes Dianix Blue CC, Benazol Black Zn and Dianix Yellow Brown CC among textile producers by *Phormidium* cells grown in laboratory condition.

2. MATERIALS AND METHODS

2.1. Microorganism and growth conditions

Prokaryotic blue-green algae *Phormidium* (BDCC 002) cells, used in this study were obtained from Celal Bayar University Biology Department Culture Collection in Manisa, Turkey. The alga was grown in 250 mL erlenmeyer flasks containing 100 mL BG-11 medium, was like that described by Stanier et al. (1971) [19], and incubated under heterotrophic and autotrophic culture conditions.

The culture was incubated under 2.0-3.0 klux with measuring light meter continuous illumination using cool, white fluorescent lamps set on 16:8 h photoperiod. The carbon source, incubation time, temperature, pH and agitation rate were 10 g/L glucose (for heterotrophic culture), 168 h, 40 ^{o}C, 8.5 and 60 rpm, respectively, for the optimum dye decolorization. The pH of the culture medium was adjusted using concentrated (1 M) and dilute (0.01 M) sulfuric acid/sodium hydroxide solutions. The phenol-sulfuric acid method, a very widely used colorimetric method, was used to determine the glucose concentration [20].

Phormidium cells used in the experiment were harvested approximately on the 15th and 20th days of incubation. After completion of the logarithmic growth phase of algal cells, the biomass was settled by centrifugation (6000 rpm, 5 min, 25 °C) and dried in aluminum beakers at 70 °C for 24 hours, then homogenized and pulverized. The powdered biosorbent was passed through a sieve (0.5 mm) and used in biosorption experiments. Two types of culture of biosorbents were prepared and tested for removal of these dyes. One of them was heterotrophic culture (contain 10 g/L glucose) and the other one was autotrophic culture form (no glucose).

All measurements were repeated 3 times, and the results are reported as the average of these replicates.

2.2. Experimental procedures

The tests were performed by adding 0.1 g of biosorbent into 100 mL of dye solutions with the initial dye concentration ranging from 25 to 100 mg/L at pH 8.5 in incubatore (Biosan S 20/60) for 7 days. Initial pH of the dye solutions was adjusted with the addition of 0.1 M of NaOH or 0.1 M of HCl.

2.3. Dye uptake

The stock solution of Biological decolorization of Benazol Black, Dianix Blue and Dianix Yellow Brown, a reactive azo-type textile dyestuff, textile

dyes were obtained from the Ekoten Textile Factory in Turkey. The stock solution was prepared by dissolving of 0.1 g of dye in 100 mL deionized double distilled water.

The working solutions of dyes were prepared by diluting the stock solution to the desired concentrations (showed as 25-100 mg/L) in tables and figures) in each experiment. All of the dye removal experiments carried out in the laboratory were performed in Erlenmeyer flasks containing the desired amount of dye and 100 mL of working solution. Erlenmeyer flasks contained dye only and working solutions were used as controls. The Benazol Black, Dianix Blue and Dianix Yellow Brown concentrationswere determined at 590 nm, 624 nm and 550 nm, respectively using UV–Visible Spectrophotometer (Varian Carry).

The mixed dyes removal efficiency was demonstrated based on the following equation:

The amount of dyes uptake per unit weight of biosorbent (q_t, mg/g); were obtained by the following Eq. (1)

$$qt = \frac{(\mathrm{Co} - \mathrm{Ct}) * \mathrm{V}}{\mathrm{M}}$$

where, *Co* and *Ct* (mg L-1) represent at initial and at *t* time concentrations of dyes in the solution, respectively. *V* (L) is the volume of solution, *M* (g) is the mass of adsorbent.
The dyes removal efficiency was demonstrated based on the following equation: Eq. (2)

$$\text{Removal efficiency } \% = \frac{(\mathrm{C0} - \mathrm{Ce})}{\mathrm{C0}} X100$$

where Co, the concentration of the initial dyes, Ce, the final dyes concentration. All of the experiments were performed in triplicate [21].

3. RESULTS AND DISCUSSION

In this study carried out under laboratory conditions, the removal capacity of synthetic dyes such as azo and anthraquinone, one of the most used dyes in the textile industry, of *Phormidium* cells was investigated as a function of time (1,3,5 and 7d), initial dye concentration (25, 50 and 100 mg/L), and different growth culture conditions (heterotrophic and autotrophic).

Dianix Blue CC, Benazol Black ZN and Dianix Yellow Brown CC, which are widely preferred diazo type dyes, were used to determine the dye removal potential of *Phormidium*. The dye biosorption studies, published in the literature, were investigated the effect of dye concentration with different range of dye concentrations between 20 and 2500 mg/L [22-24]. The dye concentration between 25-100 mg/L was examined in order to reach the closest dye concentration of the real dye containing wastewater which was mentioned by Bilinska et al. (2016) [25].

It was determined that *Phormidium* cells grown in heterotrophic culture medium for 7 days removed the Dianix Blue dye at values ranging from 0.31 mgg^{-1} (min) to 57.76 mgg^{-1} (max) on average, and the determined values are shown in Figure 1. Cells grown in heterotrophic media performed dye removal at higher dye concentration (100 mg/L) rather than low dye concentration (25-50 mg/L). As the dye concentrations increased, the dye-absorbing capacity of *Phormidium* cells increased in direct proportion especially at 100 mg/L. At the end of the dye removal work carried out in a heterororthophic culture, 55% of the Dianix Blue textile dye was removed at 100 mg/L dye concentration at the end of 7 days of incubation.

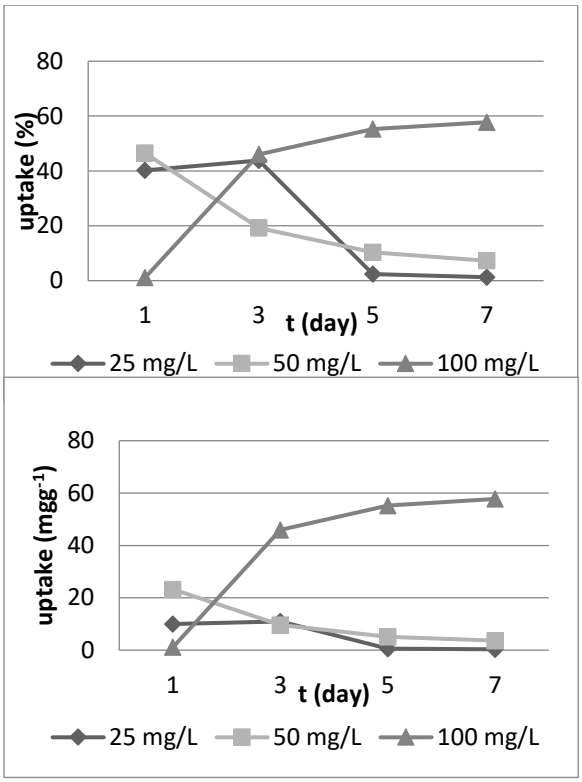

Figure 1 The effect of initial Dianix Blue CC dye concentration on the uptake yield (%, mgg^{-1}) of *Phormidium* sp. during the heterotrophic incubation period

In dye removal studies, the high initial dye concentration creates a significant driving force on the dye resistance between the aqueous and solid phases. As a result, dye uptake increases in parallel with higher concentration. The effect of the initial dye concentration on the biosorption capacity was found to be quite significant for the Dianix Blue CC azo dye used [26]. Ertugrul et al. (2008) [16] reported that, species of micro algae *Phormidium* are potential "biosorbent" for biological decontamination of Remazol Blue and Reactive Black B with maximum uptake yields ranging from 50% to 88% at all dye concentrations tested. In addition, Gul et al. (2019) [13] made research about the dye uptake of the dye acid red P-2BX by *Phormidium animale* (prokaryotic algae)and *Scenedesmus sp.* (eukaryotic algae). They reported that the maximum dye removal was performed by dried *P. animale* as 99.70±0.27% under thermophilic conditions in a batch system.

At high dye concentrations for the Benazol Black (100 mg/L, 1-3th days), uptake yield exceeded 70–75%. At the end of the dye removal study carried out in the laboratory condition, the dye uptake yield of *Phormidium* decreased especially at 25 and 50 dye concentrations; the highest dye removal was obtained in the samples having higher initial dye concentrations under the heterotrophic culture condition. At 100 mg/L dye concentration 74.04 mgg^{-1} of the initial dye was decolorized at the end of 3th day of incubation (Fig. 2).

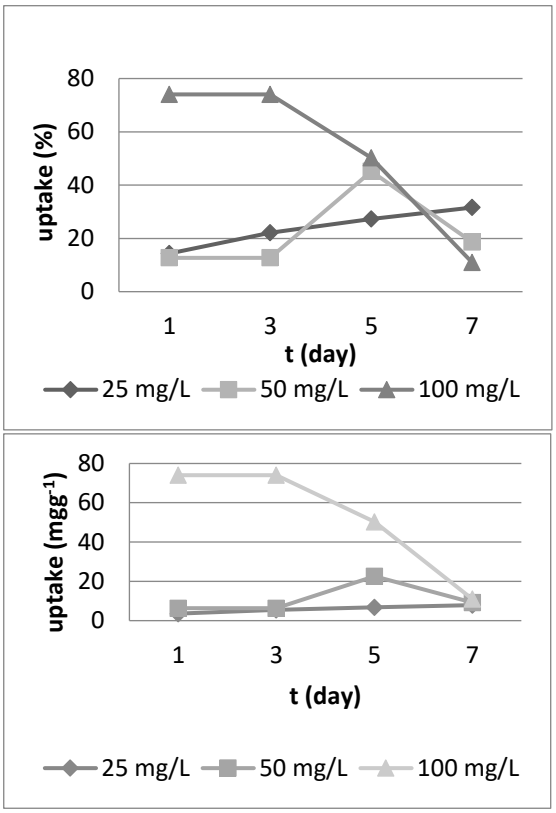

Figure 2 The effect of initial Benazol Black Zn dye concentration on the uptake yield(%, mgg^{-1}) of *Phormidium* sp. during the heterotrophic incubation period

In dye removal studies, the dye removal rate reaches maximum level (saturation) at the end of approximately 3 or 4 days. After that, the removal remains constant or the yield decreases.

In addition, the decrease in the dye removal concentration, especially after the 3rd day, may be due to the saturation (adsorption) of the surface

areas of the cells with the dye molecules and the lack of empty or unsaturated regions [27].

After mixing the microalgae with dye for 7 days at heterotrophic culture, the maximum uptake of Dianix Yellow dye was 77.69% and 69.10%, respectively, at about 25mg/L initial dye concentrations. At the end of the dye removal study, the maximum uptake level was obtained at lower initial dye concentrations at 5th and 7th days of incubation (Fig. 3).

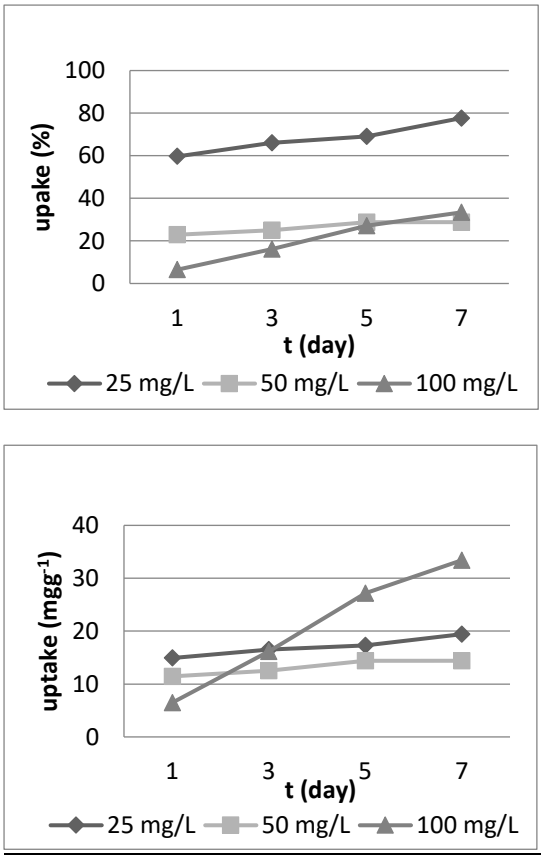

Figure 3 The effect of initial Dianix Yellow Brown CC dye concentration on the uptake yield (%, mgg^{-1}) of *Phormidium* sp. during the heterotrophic incubation period

In present study, *Phormidium* had average decolorization efficiency against both Dianix Blue and Benazol Black at 100 mg/L dye concentration. As the concentrations of the two textile dyes were decreased to 25 mg/L, the dye uptake capacity of cells was found to be decreased. Furthermore, *Phormidium* cells showed lower dye uptake efficiency against Dianix Yellow Brown at high dye concentration when it compared with Benazol Black and Dianix Blue. This may be due to changes in the chemical structures of substances. The decrease in dye removal rate may vary depending on its high molecular weight, structural complexity and the presence of inhibitor groups such as $-NO_2$ and $-SO_3Na$ in the dyes [28].

At the end of the 7 days dye removal, the mean dye uptake (%) value of *Phormidium* was calculated higher in the heterotrophic growth condition than autotrophic growth condition and the results are tabulated in Table 1.

Table 1 The comparison of the mean dye uptake (%) in the heterotrophic and autotrophic culture conditions of *Phormidium* sp.

mean uptake (%) under heterotrophic culture conditions				
	t (day)			
Dyes	1	3	5	7
Dianix Blue CC	29.26	36.33	22.68	22.09
Benazol Black Zn	33.68	36.28	40.89	76.08
Dianix Yellow Brown	29.68	35.72	41.67	46.64

mean uptake (%) under autotrophic culture conditions				
	t (day)			
Dyes	1	3	5	7
Dianix Blue CC	16.86	5.68	8.65	11.55
Benazol Black Zn	18.36	4.45	15.87	33.56
Dianix Yellow Brown	16.41	4.45	16.00	20.25

While the dye uptake concentrations were, in general, less than 34% in the effluent when no glucose was added, a significant increase in the dye uptake concentrations was observed in the heterotrophic growth media. Glucose or other carbon source which supplied an essential substrate for the production of enzyme and growth of the cell was previously shown to be crucial for dye decolorization studies [29].

Table 1 shows the dye uptake rates during the decolorization assays, including the condition where no glucose was added as the autotrophic culture assay. Zhang et al. (1999) [30] investigated that glucose concentration affected the dye uptake values and the most suitable concentration of glucose was about 5 g/L. Contrary to this, Mou et al. (1991) [31] studied the effects of glucose concentration on uptake of dyes by *Myrothecium verrucaria* and observed that the glucose concentration did not significantly influence the bio-dye uptake process.

Phormidium showed high dye decolorization, with maximum efficiency ranging from 20% to 40% (5.47 to 40.04 mgg^{-1}) for Dianix Blue, 22% to 52% (5.95 to-52.32 mgg^{-1}) for Benazol Black ZN and 20% to 68% (13.18 to-20.78 mgg^{-1}) for Dianix Yellow Brown under heterotrophic conditions at all dye concentrations tested. The best color decolorization in terms of maximum efficiency was obtained 57% (57.76 mgg^{-1}) for Dianix Blue, 74% (74.04 mgg^{-1}) for Benazol Black at 100 mg/L and 77% (19.42 mgg^{-1}) for Dianix Yellow Brown at 25 mg/L dye concentrations.

Results obtained in this study suggest that the biosorbent *Phormidium* a microalgae may provide a promising cost effective and environmentally friendly alternative to replace or supplement current treatment processes for the removal of very high concentrations of dyes in industrial wastewater effluents, as they are biodegradable and available for use and retainable.

Funding

The author (s) has no received any financial support for the research, authorship or publication of this study.

The Declaration of Conflict of Interest/ Common Interest

No conflict of interest or common interest has been declared by the authors.

Authors' Contribution

The first author contributed 100%.

The Declaration of Ethics Committee Approval

This study does not require ethics committee permission or any special permission.

The Declaration of Research and Publication Ethics

The authors of the paper declare that they comply with the scientific, ethical and quotation rules of SAUJS in all processes of the paper and that they do not make any falsification on the data collected. In addition, they declare that Sakarya University Journal of Science and its editorial board have no responsibility for any ethical violations that may be encountered, and that this study has not been evaluated in any academic publication environment other than Sakarya University Journal of Science.

REFERENCES

[1] J.L.C. Rowsell and O.M. Yaghi, “Metal–organic frameworks: a new class of porous materials”, Microporous and Mesoporous Materials, vol. 73, pp. 3-14, 2004.

[2] E.A. Clarke and R. Anliker, “Organic dyes and pigments. In: Hutzinger, O., (Eds), The handbook of environmental chemistry. Part a: Anthropogenic compounds. 3rd ed. New York: Springer, pp. 181–215, 1990.

[3] T. Robinson, G. McMullan, R. Marchant and P. Nigam, “Remediation of dyes in textile effluent: a critical review on current treatment technologies with a proposed alternative”, Bioresource Technology, vol. 77, pp. 247–255, 2001.

[4] C.I. Pearce, J.R. Lloyd and J.T. Guthric, “The removal of colour from textile

wastewater using whole bacterial cells: a review", Dyes and Pigments, vol. 58, pp. 179–196, 2003.

[5] Z. Aksu, "Application of Biosorption for the removal of organic pollutants: a review", Process Biochemistry, vol. 40, pp. 997–1026, 2005.

[6] E. Fourest and B. Volesky, "Contribution of sulfonate groups and alginate to heavy metal biosorption by the dry biomass of *Sargassum fluitans"*, Environmental Science Technology, vol. 30, pp. 277-282, 1996.

[7] J.H. Oliver, K. Hyunook and C. Pen-Chi. "Decolorization of wastewater", Critical Reviews in Environmental Science and Technology, vol. 30, pp. 449–505, 2000.

[8] E.A. Dil, M. Ghaedi, G.R. Ghezelbash and A. Asfaram, "Multi-responses optimization of simultaneous biosorption of cationic dyes by live yeast *Yarrowia lipolytica* 70562 from binary solution: application of first order derivative spectrophotometry", Ecotoxicology and Environmental Safety, vol. 139, pp. 158-164, 2017.

[9] E. Bagda, M.Tuzen and A. Sarı, "Equilibrium, thermodynamic and kinetic investigations for biosorption of uranium with green algae (*Cladophora hutchinsiae*)", Journal of Environmental Radioactivity, vol. 175-176, pp. 7-14, 2007.

[10] Y.A.R. Lebron, V.R. Moreira, L.V.S. Santos and R.S. Jacob, "Remediation of methylene blue from aqueous solution by *Chlorella pyrenoidosa* and *Spirulina maxima* biosorption: equilibrium, kinetics, thermodynamics and optimization studies", Journal of Environmental Chemical Engineering, vol. 6, pp. 6680-6690, 2008.

[11] M. Bilal, T. Rasheed, J.E. Sosa-Hernandez, A. Raza, F. Nabeel and H.M.N. Iqbal, "Biosorption: an interplay between marine Algae and potentially toxic elementsd-a review", Maine. Drugs, vol. 16, pp. 65-74, 2018.

[12] A. Saraeian, A. Hadi, F. Raji, A. Ghassemi and M. Johnson, "Cadmium removal from aqueous solution by low-cost native and surface modified *Sorghum drummondii* (Sudangrass)", Journal of Environmental Chemical Engineering, vol. 6, pp. 3322-3331, 2018.

[13] U.D. Gul, B.E. Tastan and G. Bayazit, "Assessment of algal biomasses having different cell structures for biosorption properties of acid red P-2BX dye", South African Journal of Botany, vol. 127, pp. 147-152, 2019.

[14] N, Rangsayatorn, E.S, Upatham, M. Kruatrachue, P. Pokethitiyook and G.R, Lanza, "Phytoremedition potential of *Spirulina* (Arthrospira) *platensis*: biosorption and toxicity studies of cadmium", Environmental Pollution, vol. 119, pp. 45-53, 2002.

[15] L. Pane, C. Solisio, A. Lodi, G.L. Mariottini and A. Converti, "Effect of extracts from *Spirulina platensis* bioaccumulating cadmium and zinc on L929 cells", Ecotoxicology and Environmental Safety, vol. 70, pp. 121–126, 2007.

[16] S. Ertugrul, M. Bakir and G. Donmez, "Treatment of dye-rich wastewater by an immobilized thermophilic cyanobacterial strain: *Phormidium* sp.", Ecological Engineering, vol. 32, pp. 244–248, 2008.

[17] G. Bayazit, B.E. Tastan and U.D. Gul, "Biosorption, isotherm and kinetic properties of common textile dye by *Phormidium animale"*, Global NEST Journal, vol. 22, pp. 1-7, 2020.

[18] S. Lage, Z. Gojkovic, C. Funk and F.G. Gentili, "Algal biomass from wastewater

and flue gases as a source of bioenergy", Energies, vol. 11, pp. 664-672, 2018.

[19] R.Y. Stanier, R. Kunisawa, M. Mandel and G. Cohen-Bazire, "Purification and properties of unicellular blue-green algae (order Chroococcales)", Bacteriological Reviews, vol. 35, pp. 171-205, 1971.

[20] M.K.A. DuBois, J.K. Gilles, H.P.A. Reber and F. Smith, "Colorimetric method for determination of sugars and related substances", Anaytical Chemistry, vol. 28, pp.350–356, 1959.

[21] Kenney J. F., Keeping E.S., Mathematics of Statistics. In: Nostrand D.V., (Eds). The handbook of Mathematics of Statistics. Part a: Statistics. 2nd ed. Princeton, (1951) 310-320.

[22] Z. Aksu, S. Tezer, "Biosorption of reactive dyes on the green alga *Chlorella vulgaris"*, Process Biochemistry, vol. 40, pp. 1347–1361, 2005.

[23] R. Maurya, T. Ghosh, C. Paliwal, A. Shrivastav and K. Chokshi, "Biosorption of methylene blue by de-oiled algal biomass: equilibrium, kinetics and artificial neural network modelling", PLoS One, vol. 9, pp. 109-545, 2014.

[24] S. Mona, A. Kaushik and C.P. Kaushik, "Biosorption of reactive dye by waste biomass of *Nostoc linckia"*, Ecological Engineering, vol. 37, pp. 1589–1594, 2011.

[25] L. Bilinska, M. Gmurek and S. Ledakowicz, "Comparison between Industrial and Simulated Textile Wastewater Treatment by AOPs–Biodegradability, Toxicity and Cost Assessment", Chemical Engineering Journal, vol. 306, pp. 550–559, 2016.

[26] A. Rathinam, R.R. Jonnalagadda and U.N. Balachandran, "Removal of basic yellow dye from aqueous solution by sorption ongreen alga *Caulerpa scalpelliformis*". Journal of Hazardous Materials, vol. 142, pp. 68–76, 2007.

[27] S. Venkata Mohan and J. Karthikeyan, "Removal of diazo dye from aqueous phase by algae *Spirogyra* species", Toxicological and Environmental Chemistry, vol.74, no. 3-4, pp. 147-154, 2000.

[28] T. Hu and S.C. Wu, "Assessment of the effect of azo dye Rp2B on the growth of nitrogen fixing Cyanobacterium, *Anabena* sp.", Bioresource Technology, vol. 77, pp. 95-104, 2001.

[29] J. Swamy and A. Ramsay, "Effects of glucose and NH_4^+ concentrations on sequential dye decolorization by *Trametes versicolor"*, Enzyme Microbial Technology, vol. 25, pp. 278–284, 1999.

[30] Q. Yang, T.A.O. Lingxia, M. Yang and H. Zhang, "Effects of glucose on the decolorization of reactive black 5 by yeast isolates", Journal of Environmental Sciences, vol. 20, pp. 105–108, 2008.

[31] D.G. Mou, K.K. Lim and H.P. Shen, "Microbial agents for decolorization of dye wastewater", Biotechnology Advances, vol. 9, pp. 613-622, 1991.

SAKARYA ÜNİVERSİTESİ
FEN BİLİMLERİ ENSTİTÜSÜ DERGİSİ

Sakarya University Journal of Science
SAUJS

ISSN 1301-4048 e-ISSN 2147-835X Period Bimonthly Founded 1997 Publisher Sakarya University
http://www.saujs.sakarya.edu.tr/

Title: GUP-corrected ΛCDM cosmology

Authors: Salih KİBAROĞLU

Recieved: 2021-12-07 00:00:00

Accepted: 2022-04-25 00:00:00

Article Type: Research Article

Volume: 26
Issue: 3
Month: June
Year: 2022
Pages: 501-509

How to cite
Salih KİBAROĞLU; (2022), GUP-corrected ΛCDM cosmology. Sakarya University Journal of Science, 26(3), 501-509, DOI: 10.16984/saufenbilder.1033550
Access link
http://www.saujs.sakarya.edu.tr/tr/pub/issue/70993/1033550

Sakarya University Journal of Science 26(3), 501-509, 2022

GUP-Corrected ΛCDM Cosmology

Salih KİBAROĞLU*[1]

Abstract

In this study, we investigate the effect of the generalized uncertainty principle on the ΛCDM cosmological model. Using quantum corrected Unruh effect and Verlinde's entropic gravity idea, we find Planck-scale corrected Friedmann equations with a cosmological constant. These results modify the ΛCDM cosmology.

Keywords: Generalized gravity theories, cosmology, uncertainty principle.

1. INTRODUCTION

In general, the dynamics of our Universe is explained by cosmological models. But there is no cosmological model that explains all phases of the evolution of the Universe. According to the Friedmann-Lemaitre-Robertson-Walker model, the Universe is assumed that it has a homogeneous and isotropic characteristic on a large scale. Furthermore, we know that this is an approximate theory and we should find more general cosmological models to explain our Universe more accurate.

In recent years, the Λ-cold dark matter (ΛCDM) cosmological model is known as the standard model of cosmology. According to this model, Einstein's theory of general relativity is a correct theory and the Universe has a characteristic like an Einstein-de Sitter space-time for the late time. This model provides well explanations from today to the radiation-dominated era such as the accelerated expansion of the Universe, cosmic microwave background. On the other hand, this theory is not successful to explain the early time period of the Universe such as the inflation era. For this reason, it is reasonable to extend/modify this theory to a more general form.

At this point, the extended theories of gravity help us to find generalized cosmological models. For instance, in 1998 it was discovered that the expansion rate of our Universe is accelerating [1-4]. To explain this acceleration, the main candidates are the cosmological constant and dark energy which can be obtained by adding extra source terms to the Einstein field equations [5, 6].

* Corresponding author: salihkibaroglu@maltepe.edu.tr
[1] Maltepe University, Faculty of Engineering and Natural Sciences
ORCID: https://orcid.org/ 0000-0002-8691-4959

There is another alternative approach for constructing an extended theory of gravity put forwarded by Verlinde [7, 8]. According to his theory, gravity is not a fundamental force but emerges as an entropic force. He formulated a thermodynamical description of gravity by considering the holographic principle and Bekenstein-Hawking entropy [9-11]. In the light of this idea, if one has modified/deformed thermodynamical quantity this leads to finding modified gravitational equations. This idea provides a very useful theoretical background to derive generalized versions of gravity theories [12-20] and cosmological models [21-30].

The quantum gravity studies show that Heisenberg's uncertainty principle should be modified [31]. In this context, one of the main studies is the Generalized Uncertainty Principle (GUP) [32-39] which provide a quantum gravitational correction to the Heisenberg relation as,

$$\Delta x \Delta p \geq \frac{\hbar}{2}\left[1+\beta l_p^2 (\Delta p)^2\right], \tag{1}$$

where l_p is the Planck length, β is a constant of order unity and dimensionless and $c=1$ is assumed. Furthermore, another study is the Extended Uncertainty Principle (EUP) have a position-uncertainty correction to the ordinary uncertainty relation,

$$\Delta x \Delta p \geq \frac{\hbar}{2}\left[1+\frac{\alpha}{l_H^2}(\Delta x)^2\right], \tag{2}$$

where α is taken to be of order unity and l_H is a large distance scale for instance the (anti)-de Sitter radius. Thus, EUP provides a way to introduce quantum effects on large scales [40-43].

In this paper, we investigate the possible effects of the GUP model on the ΛCDM cosmology. For this purpose, we use the entropic force approach and the GUP model that used in [39].

In Sec. 2, we summarize the GUP-corrected gravity model based on [39]. Then in Sec. 3, we give a brief description of the ΛCDM cosmology. In Sec. 4, we find a Planck-scale-corrected Friedmann equations based on the selected GUP model. We also note that this paper uses the natural units where the speed of light c and Boltzmann's constant k_B equal to one. The last section concludes the paper.

2. QUANTUM CORRECTED GRAVITY MODEL

One can derive the Unruh effect with the help of Heisenberg's uncertainty principle when we assume that a photon has crossed the Rindler event horizon [33, 38]. If we consider the Planck scale where the gravitational effect is neglected, we know that there are some modifications of HUP named as generalized uncertainty principle and extended uncertainty principle. So, these modified models affect the structure of thermodynamical quantities such as the Unruh effect. According to the paper [39] a GUP model is given as follows,

$$\Delta x \Delta p \geq \frac{\hbar}{2}\left[1+\beta\left(\frac{\Delta p}{m_p}\right)^2\right], \tag{3}$$

and

$$[\hat{x},\hat{p}] = i\hbar\left[1+\beta\left(\frac{\hat{p}}{m_p}\right)^2\right], \tag{4}$$

where the constant β is used as a dimensionless deformation parameter. By the help of this modified background, we can derive the modified Unruh temperature as follows,

$$T \cong T_U f(a). \tag{5}$$

Here $T_U = \hbar a/2\pi$ represents the ordinary Unruh temperature and the function $f(a)$ is defined as

$$f(a) = \left[1 + \frac{\beta}{2}\left(\frac{l_p a}{\pi}\right)^2\right]. \quad (6)$$

Here, a is the acceleration of the reference frame. According to this background and using the Verlinde's entropic gravity idea, a GUP-corrected gravitational field equation can be found as follows [30],

$$R_{ab} - \frac{1}{2} g_{ab} R + \frac{\Lambda}{f(a)} g_{ab} = \frac{8\pi G}{f(a)}\{T_{ab} + T_{ab}^{GUP}\}, \quad (7)$$

where Λ represents the cosmological constant, T_{ab} is originated from ordinary matter and T_{ab}^{GUP} comes from GUP modification and its form,

$$T_{ab}^{GUP} = \frac{1}{8\pi G}\left(\nabla_a \nabla_b f - \frac{1}{2} g_{ab} \nabla^2 f\right). \quad (8)$$

Moreover, in the concept of this GUP model, Newton's second law of gravity takes the following form,

$$F = maf(a), \quad (9)$$

where $f(a)$ is given by Eq.(6).

3. REVIEW OF ΛCDM COSMOLOGY

In this section, we present a brief review of the ΛCDM cosmological model which is also known as the standard model of cosmology [44]. According to this model, the Friedmann equation is given the following form,

$$H(t)^2 = \frac{8\pi G}{3}\rho(t) - \frac{k}{a^2} + \frac{\Lambda}{3}, \quad (10)$$

and the acceleration equation is,

$$\frac{\ddot{a}(t)}{a(t)} = -\frac{4\pi G}{3}(\rho + 3p) + \frac{\Lambda}{3}, \quad (11)$$

here $a(t)$ is a dimensionless arbitrary function of time, known as the scale factor, which is related to the expansion of the universe, $\rho(t)$ and $p(t)$ represents total energy density and the pressure of cosmological fluids, $H = \dot{a}(t)/a(t)$ is the Hubble parameter which describes the expansion rate of the universe and the dot represents the time derivative of the corresponding component. Moreover, the driving term $\Lambda/3$ is responsible for the acceleration. Besides, the continuity equation can be given as follows,

$$\dot{\rho} + 3H(\rho + p) = 0. \quad (12)$$

Using these equations, the Raychaudhuri equation can be written as follows,

$$\dot{H} = -4\pi G(\rho + p) + \frac{k}{a^2}. \quad (13)$$

4. GUP-CORRECTED FRIEDMANN EQUATIONS

We start with the Friedmann–Robertson–Walker universe with the metric

$$ds^2 = dt^2 - a(t)^2(dr^2 + r^2 d\Omega^2), \quad (14)$$

where $a(t)$ is the scale factor, and Ω denotes the line element of a unit sphere. According to Verlinde's paper, we have a spherical holographic screen with a spatial region which has the following physical radius,

$$\tilde{r} = a(t)r. \quad (15)$$

By assuming that our universe has homogeneity and isotropic form in a large scale, the matter

content of the universe forms a perfect fluid with the following stress-energy tensor,

$$T_{\mu\nu} = (\rho + p)u_\mu u_\nu + p g_{\mu\nu}, \tag{16}$$

and if we take the trace of this tensor we get,

$$T = T^{\mu}_{\mu} = \rho - 3p. \tag{17}$$

Here $u^\mu = (1,0,0,0)$ is the four-velocity and satisfies the relation $g_{\mu\nu}u^\mu u^\nu = 1$. Also $\rho(t)$ and $p(t)$ represents energy density and the pressure of cosmological fluids, respectively. By using the conservation of the energy–stress tensor, the continuity equation takes the following form,

$$\dot{\rho} + 3H(\rho + p) = 0. \tag{18}$$

The number of bits on the screen is defined as

$$N = \frac{A}{G\hbar}, \tag{19}$$

where $A = 4\pi\tilde{r}^2$ represents the area of the screen. According to the equipartition law of energy, the total energy on the screen can be written as follows,

$$E = \frac{1}{2}Nk_BT. \tag{20}$$

On the other hand, the energy can be represented as

$$E = M, \tag{21}$$

where the mass M represents the mass in the spatial region V. Using Eq.(16) and Eq.(21), the total mass in the spatial region can also be defined as

$$M = \int_V dV\left(T_{\mu\nu}u^\mu u^\nu\right), \tag{22}$$

where $T_{\mu\nu}u^\mu u^\nu$ is the energy density of the system. Moreover, the acceleration of the radial observer at r can be written,

$$a_r = -\frac{d^2\tilde{r}}{dt^2} = -\ddot{ar}. \tag{23}$$

By using this result the modified Unruh temperature should be the following form,

$$T = \frac{\hbar a_r}{2\pi}f(a_r) = T_U f(a_r). \tag{24}$$

From this background and by assuming the area as $A = 4\pi\tilde{r}^2$ and the volume as $V = \frac{4}{3}\pi\tilde{r}^3$, we get

$$\frac{\ddot{a}}{a} = -\frac{4\pi G}{3f}\rho, \tag{25}$$

This equation represents the dynamical equations for the Newtonian cosmology for the modified case. To obtain the Friedmann equations for the GUP-deformed general relativity, we use active gravitational mass (Tolman-Komar mass) $\mathcal{M}$ rather than total mass M in the spatial region V and it is defined as,

$$\mathcal{M} = 2\int_V dV\left(T_{\mu\nu} - \frac{1}{2}Tg_{\mu\nu} - \frac{\Lambda}{8\pi G}g_{\mu\nu}\right)u^\mu u^\nu, \tag{26}$$

After taking this integral, we get the active gravitational mass as

$$\mathcal{M} = \left(\rho + 3p - \frac{\Lambda}{4\pi G}\right)V. \quad (27)$$

Then using this new mass definition, we find the following equation,

$$\frac{\ddot{a}}{a} = -\frac{4\pi G}{3f}(\rho + 3p) + \frac{\Lambda}{3f}. \quad (28)$$

So, we find the acceleration equation including the cosmological term for the dynamical evolution of the FRW universe. Multiplying $\dot{a}a$ on both sides of the last equation and using the continuity equation in Eq.(16), we get

$$H^2 = \frac{8\pi G}{3f}\rho - \frac{k}{a^2} + \frac{\Lambda}{3f}, \quad (29)$$

Thus, we get the second Friedmann equation that is responsible for the time evolution of the FRW universe. Here, k is the integration constant and it can be interpreted as the spatial curvature of the region V in Einstein's theory of gravity. Here, $k = 1, 0, -1$ correspond to a closed, flat, and open FRW universe, respectively. The Eq.(29) can also be written as follows,

$$H^2 = \frac{8\pi G}{3f}(\rho - \rho_\Lambda) - \frac{k}{a^2}, \quad (30)$$

where an energy density corresponding to the cosmological constant is defined as,

$$\rho_\Lambda := -\frac{\Lambda}{8\pi G}. \quad (31)$$

In other words, it can be interpreted as an additional energy density to the universe. Moreover, time derivation of the Hubble parameter can be written as follows,

$$\dot{H} = \frac{\ddot{a}}{a} - H^2. \quad (32)$$

Using this equation together with Eqs.(28) and (29), we get,

$$\dot{H} = -\frac{4\pi G}{f}(\rho + p) + \frac{k}{a^2}. \quad (33)$$

Thus, we derive the GUP-corrected Raychaudhuri equation. With the help of Eq.(29), one can also write the matter density as follows,

$$\rho(t) = \rho_c + \rho_k + \rho_\Lambda, \quad (34)$$

where the critical density ρ_c and the energy density corresponding to the integration constant ρ_k are defined as follows,

$$\rho_c := \frac{3H^2}{8\pi G}f, \quad \rho_k := \frac{3k}{8\pi G a^2}f, \quad (35)$$

On the other hand, the density parameter is defined as $\Omega(t) = \rho/\rho_c$ and using this definition one can write,

$$\Omega(t) + \Omega_k(t) + \Omega_\Lambda(t) = 1, \quad (36)$$

where,

$$\Omega_k(t) = -\frac{k}{H^2 a^2}, \quad \Omega_\Lambda(t) = \frac{\Lambda}{3H^2 f}. \quad (37)$$

These expressions represent density parameters with respect to the integral constant and the cosmological constant, respectively. The density parameter contains information about the shape of our universe. If we suppose $\Omega(t) = 1$, this model describes a flat universe. The other conditions $\Omega(t) < 1$ and $\Omega(t) > 1$ corresponds to an open universe closed universe. Today it is known that

the value of the density parameter is close to one. From here, we can write the following expression,

$$\Lambda \cong \frac{3k}{a^2}\left[1+\frac{\beta}{2}\left(\frac{l_p a_r}{\pi}\right)^2\right]. \quad (38)$$

If we set the deformation parameter as $\beta = 0$ the modified equations go to their standard forms. Furthermore, some possible values of the deformation parameter β, both gravitational and non-gravitational cases, are summarized in [45]. According to this, for gravitational cases, the values of β change between $\beta < 10^{21}$ and $\beta < 10^{78}$. On the other hand, in some cases, β could get negative values [46-49]. This idea may lead to interesting results because a negative deformation parameter can change the sign of the cosmological constant in a special condition. If we consider very high acceleration values and at appropriate β values, the sign of Eq.(38) would be changed.

5. CONCLUSIONS

In this paper, we aimed to find the possible contribution of the generalized uncertainty principle on a cosmological model. We know that Verlinde's entropic gravity idea provides a useful theoretical background to extend/modify cosmological models.

From this background, we used GUP-corrected gravitational model in Eq.(7) (see also [30]) to derive modified Friedmann equations. Eventually, we derived quantum corrected Friedman equations Eq.(28) and Eq.(29). Also, these equations can be seen as quantum corrected ΛCDM model. In a certain condition, if the deformation parameter β in the function $f(a)$ in Eq.(6) goes to zero, the model reduces its conventional form.

According to the function $f(a)$ in Eq.(6) and modified Friedmann equations, the contribution that comes from GUP is very little because the function contains a square of the Planck length. In this condition, the corrections can be ignored when the Universe becomes large. But there may be a considerable contribution for the early universe such as the inflation phase. This is very important because the ΛCDM model is insufficient for the explanation the early Universe period.

In addition, $f(a)$ could have a negative sign when we chose negative deformation parameter and extreme acceleration conditions. This may lead to change some signs of the resulting Friedmann equations and the cosmological constant in Eq.(38). Thus, we can say that this kind of deformation could affect the evolution of the universe.

Consequently, one can say that modifications of the entropic gravity lead to derive extended cosmological models and these studies may provide a deeper understanding of our Universe.

Funding

The author has no received any financial support for the research, authorship or publication of this study.

The Declaration of Conflict of Interest/ Common Interest

No conflict of interest or common interest has been declared by the authors.

The Declaration of Ethics Committee Approval

This study does not require ethics committee permission or any special permission.

The Declaration of Research and Publication Ethics

The authors of the paper declare that they comply with the scientific, ethical and quotation rules of SAUJS in all processes of the paper and that they do not make any falsification on the data collected. In addition, they declare that Sakarya University Journal of Science and its editorial board have no responsibility for any ethical violations that may be encountered, and that this study has not been evaluated in any academic

publication environment other than Sakarya University Journal of Science.

REFERENCES

[1] S. Perlmutter et al., "Discovery of a supernova explosion at half the age of the Universe", Nature (London), vol. 391, pp. 51-54, 1998.

[2] S. Perlmutter et al., "Measurements of Ω and Λ from 42 High-Redshift Supernovae", The Astrophysical Journal, vol. 517, no. 2, pp. 565-586, 1999.

[3] G. Riess et al., "Observational Evidence from Supernovae for an Accelerating Universe and a Cosmological Constant", The Astrophysical Journal, vol. 116, no. 3, pp. 1009-1038, 1998.

[4] G. Riess et al., "Type Ia Supernova Discoveries at z > 1 from the Hubble Space Telescope: Evidence for Past Deceleration and Constraints on Dark Energy Evolution", The Astrophysical Journal, vol. 607, no. 2, pp. 665-687, 2004.

[5] J. Frieman, M. Turner, and D. Huterer, "Dark Energy and the Accelerating Universe", Annual Review of Astronomy and Astrophysics., vol. 46, pp. 385-432, 2008.

[6] T. Padmanabhan, "Dark Energy and its Implications for Gravity", Advanced Science Letters, vol. 2, no. 2, pp. 174-183, 2009.

[7] E. Verlinde, "On the origin of gravity and the laws of Newton", Journal of High Energy Physics, vol. 04, pp. 029, 2011.

[8] E. Verlinde, "Emergent Gravity and the Dark Universe", SciPost Physics, vol. 2, pp. 016, 2017.

[9] J. D. Bekenstein, "Black Holes and Entropy", Physical Review D, vol. 7, no. 8, pp. 2333-2346, 1973.

[10] S. W. Hawking, "Black hole explosions?", Nature, vol. 248, pp. 30-31, 1974.

[11] S. W. Hawking, "Particle creation by black holes", Communications in Mathematical Physics, vol. 43, pp. 199-220, 1975.

[12] M. Ho, D. Minic, and Y. J. Ng, "Cold dark matter with MOND scaling", Physics Letters B, vol. 693, pp. 567-570, 2010.

[13] T. Wang, "Modified entropic gravity revisited", Science China Physics, Mechanics & Astronomy, vol. 57, pp. 1623–1629, 2014.

[14] A. Sheykhi and S. H. Hendi, "Power-law entropic corrections to Newton's law and Friedmann equations", Physical Review D, vol. 84, pp. 44023, 2011.

[15] A. Sheykhi and S. K. Rezazadeh, "Einstein Equations and MOND Theory from Debye Entropic Gravity", Journal of Cosmology and Astroparticle Physics, vol. 10, pp. 012, 2012.

[16] E. Dil, "q-Deformed Einstein equations", Canadian Journal of Physics, vol. 93, pp. 1274-1278, 2015.

[17] H. Moradpour and A. Sheykhi, "From the Komar Mass and Entropic Force Scenarios to the Einstein Field Equations on the Ads Brane", International Journal of Theoretical Physics, vol. 55, pp. 1145-1155, 2016.

[18] M. Senay and S. Kibaroğlu, "q-deformed Einstein equations from entropic force", International Journal of Modern Physics A, vol. 33, no. 36, pp. 1850218, 2018.

[19] S. Kibaroğlu and M. Senay, "Effects of bosonic and fermionic q-deformation on the entropic gravity", Modern Physics Letters A, vol. 34, no. 31, pp. 1950249, 2019.

[20] S. Kibaroğlu, "Generalized entropic gravity from modified Unruh temperature", International Journal of Modern Physics A, vol. 34, no. 22, pp. 1950119, 2019.

[21] R. G. Cai, L. M. Cao, and N. Ohta, "Friedmann equations from entropic force", Physical Review D, vol. 81, pp. 61501, 2010.

[22] Y. F. Cai, J. Liu, and H. Li, "Entropic cosmology: A unified model of inflation and late-time acceleration", Physics Letters B, vol. 690, pp. 213-219, 2010.

[23] A. Sheykhi, "Entropic corrections to Friedmann equations", Physical Review D, vol. 81, pp. 104011, 2010.

[24] H. Wei, "Cosmological constraints on the modified entropic force model", Physics Letters B, vol. 692, pp. 167-175, 2010.

[25] Y. F. Cai and E. N. Saridakis, "Inflation in entropic cosmology: Primordial perturbations and non-Gaussianities", Physics Letters B, vol. 697, pp. 280-287, 2011.

[26] N. Komatsu and S. Kimura, "Non-adiabatic-like accelerated expansion of the late universe in entropic cosmology", Physical Review D, vol. 87, pp. 43531, 2013.

[27] N. Komatsu and S. Kimura, "Entropic cosmology for a generalized black-hole entropy", Physical Review D, vol. 88, pp. 83534, 2013.

[28] A. Awad and A. F. Ali, "Planck-scale corrections to Friedmann equation", Central European Journal of Physics, vol. 12, pp. 245-255, 2014.

[29] A. Sheykhi, "Modified Friedmann equations from Tsallis entropy", Physics Letters B, vol. 785, pp. 118-126, 2018.

[30] S. Kibaroğlu and M. Senay, "Friedmann equations for deformed entropic gravity", International Journal of Modern Physics D, vol. 29, no. 06, pp. 2050042, 2020.

[31] A. Kempf, G. Mangano, and R. B. Mann, "Hilbert space representation of the minimal length uncertainty relation", Physical Review D, vol. 52, no. 2, pp. 1108-1118, 1995.

[32] L. J. Garay, "Quantum gravity and minimum length", International Journal of Modern Physics A, vol. 10, no. 02, pp. 145-165, 1995.

[33] F. Scardigli, "Some heuristic semi-classical derivations of the Planck length, the Hawking effect and the Unruh effect", Nuovo Cimento B, vol. 110, pp. 1029-1034, 1995.

[34] F. Scardigli, "Generalized uncertainty principle in quantum gravity from micro-black hole gedanken experiment", Physics Letters B, vol. 452, pp. 39-44, 1999.

[35] S. Kalyana Rama, "Some consequences of the generalised uncertainty principle: statistical mechanical, cosmological, and varying speed of light", Physics Letters B, vol. 519, pp. 103-110, 2001.

[36] L. N. Chang, D. Minic, N. Okamura, and T. Takeuchi, "Effect of the minimal length uncertainty relation on the density of states and the cosmological constant problem", Physical Review D, vol. 65, pp. 125028, 2002.

[37] S. Hossenfelder, "Minimal Length Scale Scenarios for Quantum Gravity", Living Reviews in Relativity., vol. 16, pp. 2, 2013.

[38] J. Gine, "Hawking effect and Unruh effect from the uncertainty principle", Europhysics Letters., vol. 121, no. 1, pp. 10001, 2018.

[39] F. Scardigli, M. Blasone, G. Luciano, and R. Casadio, "Modified Unruh effect from generalized uncertainty principle", The European Physical Journal C, vol. 78, pp. 728, 2018.

[40] B. Bolen and M. Cavaglia, "(anti-)de Sitter black hole thermodynamics and the generalized uncertainty principle", General Relativity and Gravitation, vol. 37, pp. 1255-1262, 2005.

[41] C. Bambi and F.R. Urban, "Natural extension of the generalized uncertainty

principle", Classical and Quantum Gravity, vol. 25, no. 9, pp. 095006, 2008.

[42] S. Mignemi, "Extended Uncertainty Principle and The Geometry of (anti)-de Sitter Space", Modern Physics Letters A, vol. 25, no. 20, pp. 1697-1703, 2010.

[43] W. S. Chung and H. Hassanabadi, "Quantum mechanics on (anti)-de Sitter background", Modern Physics Letters A, vol. 32, no. 26, pp. 1750138, 2017.

[44] L. Bergström and A. Goobar, Cosmology and Particle Astrophysics, 2nd ed., Berlin, Springer, 2006.

[45] G. Lambiase and F. Scardigli, "Lorentz violation and generalized uncertainty principle", Physical Review D, vol. 97, pp. 075003, 2018.

[46] Y. C. Ong, "Generalized uncertainty principle, black holes, and white dwarfs: a tale of two infinities", Journal of Cosmology and Astroparticle Physics, vol. 2018, pp. 015, 2018.

[47] T. Kanazawa, G. Lambiase, G. Vilasi, and A. Yoshioka, "Noncommutative Schwarzschild geometry and generalized uncertainty principle", The European Physical Journal C, vol. 79, pp. 95, 2019.

[48] L. Buoninfante, G. G. Luciano, and L. Petruzziello, "Generalized uncertainty principle and corpuscular gravity", The European Physical Journal C, vol. 79, pp. 663, 2019.

[49] L. Buoninfante, G. G. Luciano, and L. Petruzziello, F. Scardigli, "Bekenstein bound and uncertainty relations", Physics Letters B, vol. 824, pp. 136818, 2022.

SAKARYA ÜNİVERSİTESİ
FEN BİLİMLERİ ENSTİTÜSÜ DERGİSİ

Sakarya University Journal of Science
SAUJS

ISSN 1301-4048 e-ISSN 2147-835X Period Bimonthly Founded 1997 Publisher Sakarya University
http://www.saujs.sakarya.edu.tr/

Title: Determination of Nutrition Habits and Food Supply Changes During Covid-19 Pandemic

Authors: Nilgün BUDAK

Recieved: 2022-01-17 00:00:00

Accepted: 2022-04-25 00:00:00

Article Type: Research Article

Volume: 26
Issue: 3
Month: June
Year: 2022
Pages: 510-522

How to cite
Nilgün BUDAK; (2022), Determination of Nutrition Habits and Food Supply Changes During Covid-19 Pandemic . Sakarya University Journal of Science, 26(3), 510-522, DOI: 10.16984/saufenbilder.1059231
Access link
http://www.saujs.sakarya.edu.tr/tr/pub/issue/70993/1059231

Sakarya University Journal of Science 26(3), 510-522, 2022

Determination of Nutrition Habits and Food Supply Changes During Covid-19 Pandemic

Havva Nilgün BUDAK*[1]

Abstract

The research aims to determine the changes that took place in the lifestyles and dietary and food purchasing habits of the Turkish population during the Covid-19 pandemic by considering regional distribution and age factors. A survey was applied in this study. The survey evaluated the participants' sociodemographic and anthropometric characteristics, dietary habits, food purchasing habits, and their daily, weekly, and monthly consumption of 22 different food items in terms of both the pre- and during-pandemic periods. The study enrolled 725 participants' between the ages 15-80, living in Turkey. The answers to the online questionnaire showed that there was an increase in their frequency of taking vitamin C and D, zinc, complex vitamins, fish oil, food supplements, buying packaged products, dairy products, probiotic supplements, fruits, seafood. While there was a decrease in the participants' smoking and alcohol consumption frequency, an increase in their daily sleep duration and gaining weight. Also, it was determined that online shopping increased by 166%, while local food market decreased by 41.12%. It has been determined that people should eat healthy and strengthen their immune system in epidemics. For this reason, it has been determined that the infrastructures of producers, carriers and sellers in the food supply chain should be improved in order to meet the needs of people.

Keywords: Covid-19 pandemic, nutritional habits, food supply, lifestyle, physical activity.

1. INTRODUCTION

Coronaviruses (CoV), discovered in the 21st century and understood to cause mild respiratory diseases in humans, were common viruses all over the world [1]. The severe acute respiratory syndrome Covid-19 (coronavirus) was defined as a virus. The World Health Organization (WHO) declared the Covid-19 pandemic to be a rapidly spreading epidemic worldwide [2]. Most people infected with coronavirus experience mild to moderate respiratory illness and recover without requiring special treatment. However, it had been reported that elderly people or those with medical problems such as diabetes, cardiovascular diseases, chronic respiratory disease, and cancer

* Corresponding author: nilgunbudak@isparta.edu.tr
[1] Isparta University of Applied Sciences, Egirdir Vocational School, Department of Food Processing
ORCID: https://orcid.org/0000-0003-2494-6370

are more likely to experience more severe symptoms [3].

According to WHO data, 5.518.343 people died and 318.648.834 infected from this disease [4] while according to the data of the Ministry of Health of the Republic of Turkey, 82.361 people died and 9.482.550 cases detected in Turkey as of 14 January 2022. On January 10, 2020, the Coronavirus Scientific Advisory Board was set up by the Ministry of Health to develop measures in the fight against the Covid-19 pandemic in Turkey. Wearing masks, maintaining social distance, and maintaining personal hygiene were suggested to the whole country and these suggestions became mandatory in the following days. With the advisory decision of the Scientific Board, all flights to and from Wuhan were suspended on January 23, 2020, all flights between China and Turkey were suspended on February 05, and all flights between Turkey and Italy, South Korea, and Iraq were suspended on February 29, 2020. On March 1, 2020, people from abroad were allowed to enter the country in a controlled manner, in line with Covid-19 measures and the recommendations of the Scientific Board. The first case in Turkey was detected on March 11, 2020, and all education (high school, undergraduate, postgraduate) / training activities (pilates/yoga, volleyball, basketball, running, swimming, walking) were suspended on March 12, 2020. Certain restrictions were applied in certain periods from March to November, 2020 [5].

Physical/social isolation and self-quarantine due to the pandemic strongly affected people's lives, especially their eating habits and other daily behaviors. The need for stocking up on food increased due to the changes in our living conditions such as online education, limitation of physical activity in closed areas, and restrictions on grocery shopping. In addition, interruption of work routine due to quarantines and lockdowns caused boredom and monotony at home, which caused an increase in individuals' food consumption and energy intake [6, 7]. Additionally, continuous exposure to news about Covid-19 on social media and other press channels caused a significant increase in people's stress levels. Stress urged people to overeat and have "food cravings," especially for "comfort food," which rich in sugar [8]. Food rich in simple carbohydrates reduced stress, as they stimulated the production of serotonin, which positively affect mood [9]. Fewer visited by people to grocery stores or supermarkets to avoid the Covid-19 led to an increase in the consumption of highly processed foods such as convenience foods, snacks, and ready-to-eat cereals. Psychological effects of compulsory quarantine and restrictions predicted to cause some changes in people's lifestyles such as physical activity, sleep patterns, smoking or alcohol consumption, as well as in their eating habits. The decline in income for many people during the Covid-19 pandemic caused people to limit their kitchen shopping [10].

In the present study, it was aimed to determine the changes that took place in lifestyles and dietary and food purchasing habits of the Turkish population during the Covid-19 pandemic by considering age factors and changes observed in different regions of the country

2. MATERIALS AND METHODS

2.1. Survey methodology

The population of the study consisted of people between the ages of 15-80 living with internet access in Turkey. The reason for choosing this age range was that they were thought to be able to respond to the online survey to be sent to them. The web-based survey form was sent to Turkish residents selected by snowball sampling via social media accounts and e-mails between October 7, 2020, and October 30, 2020. According to the formula given by Adam [11], it was calculated that if the size of the population was 45 million, the sample size (α=0.05, sampling error H=$\pm$0.05, and the ratios p=0.5; q=0.5) should be at least 384. The survey results of 725 participants were evaluated in the study. Accordingly, the sample size was considered to be large enough. The questionnaire consisted of a total of 45 questions, consisting of a set of verified questions [12]. Since the online survey did not allow multiple answers to the questions or skipping any questions, all the obtained data were included in

the study. It is estimated that the participants take 8-10 minutes to answer the questionnaire questions.

2.2. Data collection on Covid-19

The survey developed within the scope of the research consisted of three parts. The first part included questions about some socio demographic and anthropometric characteristics (height, weight before and during Covid-19) of the participants. The second part included questions about their habits (working conditions, smoking, alcohol consumption, use of supplements such as vitamins and minerals that strengthen the immune system, whether they were following a special diet, the number of meals per day, daily sleep duration, whether they do any exercises) and about the changes that took place in their habits after the pandemic (their demands for packaged products, food products stocked up at home in case of staying home for a long time, whether they have had a Covid-19 or antibody test). Finally, the third part included questions about their daily, weekly, and monthly consumption frequencies of 22 different food products in the pre- and post-pandemic periods [5, 12, 13]. The survey was web-based, so it did not allow multiple answers to the questions or skipping any questions.

For the survey, the permission was obtained from the Ministry of Health, General Directorate of Health Services, and Isparta University of Applied Sciences Scientific Research Publication Ethics Committee (Decision Date: 07.10.2020 and Decision No: 31/1).

2.3. Statistical analyses

In the study, the data collected by the survey method were analyzed. The data were analyzed with the SPSS 23 software. The "One-Sample Kolmogorov Smirnov" test was used to check the normality of the data. It was observed that the data was not normally distributed. A chi-square test was used to evaluate the relationship between categorical variables, and McNemar-Bowker analysis was used to investigate the relationship between categorical variables in the pre- and post-pandemic periods. Wilcoxon, Kruskal-Wallis, and Post-hoc/Tamhane tests were performed for intergroup comparisons of continuous variables. Statistical significance was set at $p<0.05$. It was examined whether any changes took place in the habits of the respondents after the pandemic broke out. The information about the sample and the scales used in the study were given below.

3. RESULT AND DISCUSSION

The data were represented as the number of respondents (n) and percentage (%) for categorical variables (Table 1).

Table 1 Demographic characteristics of the participants'

Demographic characteristics	Gender	Age/Education level/ Occupation	Metropolitan		Other cities	
			n	%	n	%
Gender	**Female**		273	38	214	30
	Male		106	14	132	18
Age	**Female**	<18	15	6	5	2
		18-30	72	26	61	29
		31-45	109	40	92	43
		45-65	63	23	46	21
		>65	14	5	10	5
	Male	<18	5	5	7	5

		18-30	22	21	17	13
		31-45	36	34	62	47
		45-65	41	40	40	30
		>65	1	1	6	5
Education level	**Female**	High school	36	13	29	14
		Undergraduate	172	63	134	63
		Postgraduate	65	24	51	24
	Male	High school	18	17	15	11
		Undergraduate	64	60	83	63
		Postgraduate	24	23	34	26
Occupation	**Female**	Government wage personnel	94	34	84	39
		Academician	23	9	11	5
		Self-employment	26	10	26	12
		Unemployed (student. retired. housewife)	129	47	93	44
	Male	Government wage personnel	54	51	52	40
		Academician	3	3	12	9
		Self-employment	21	20	41	31
		Unemployed (student. retired. housewife)	28	26	27	20

Values are expressed as n (participants' number) and % (percentage) for categorical variables. Government wage personnel (1000$ or less). Academician (1000-1500 $) are monthyl income group of Turkey.

Proportion of the participants, 68 % were female and 32% were male, 52% lived in metropolitan cities (cities with more than 750.000 inhabitants), and 48% lived in other cities (cities with less than 750.000 inhabitants). Different restrictions was applied depending on the density of population at pandemic in Turkey. The Covid-19 epidemic, which affects the whole world, poses a significant threated not only to our health but also to our economic well-being. In addition, changes in income levels caused changes in people's consumption habits during the pandemic process [14].

The participants were 39% (284) government wage personnel, 8% (49) academics, 14% (100) self-employed, and 39% (277) students/housewives/retired. Government wage personnel (1000$ or less), Academician (1000-1500 $) are monthyl income group of Turkey.

As regards the participants body mass index (BMI) values in both the pre- and post-pandemic periods, there was no statistically significant difference between big cities (cities with more than 750.000 inhabitants) and smaller cities while there was a statistically significant difference between males and females ($p<0.05$).

On the other hand, there was a decrease in the participants smoking and alcohol consumption frequency ($p<0.05$) but an increase in their daily sleep duration ($p<0.05$) in the during pandemic period. The increase rate of those who give up smoking during the pandemic was 80.76%. The rate of those who slept 9-12 hours in a day increased by 124% (Table 2).

According to the results of the survey research, an increase was observed in those who quit smoking and in their daily sleep hours during the pandemic. This high rate of those who give up smoking during the pandemic can be explained by the fear of respiratory distress and death risk in smokers [15]. The increase in the duration people stay at home was associated with increased daily sleep duration.

Table 2 Smoking and sleep times of the participants'

	Pre Covid-19		During Covid-19	
Smoking	**n**	**%**	n	**%**
No	418	58	418	58
<5 cigarettes/week	46	6	40	5
<5 cigarettes/day	132	18	114	17
1 package/day	103	14	106	14
Give up smoking	26	4	47	6
Sleeping	**n**	**%**	**n**	**%**
<3 hours	2	1	4	1
3-6 hours	139	19	111	15
7-8 hours	527	72	479	67
9-12 hours	50	7	112	16
>12 hours	5	1	7	1

Values are expressed as n (participant's number) and % (percentage) for categorical variables.

Among the parameters investigated, those that showed significant changes after the pandemic are described in the results section. Considering vitamin and mineral use before and during the Covid-19 pandemic, an increase was observed in the use of vitamin C (82%), vitamin D (17%), vitamin C and vitamin D combined (120%), zinc (300%), mineral complex (113%) and fish oil (32%) ($p<0.05$) In addition, it had also been observed that people increased their daily intake of vitamins and mineral. It was stated that vitamins and minerals play an active role in the formation of a healthy immune system, protect the body against infections and increase body resistance [16]. In order to protect people from the Covid-19 virus during the pandemic process, explanations had made on different social media channels. One of these explanations was taken vitamins and minerals [17]. In this research, 20% of the respondents reported having started to use food supplements ($p<0.05$) 342 of the participants (47%) gained weight, while 207 (29%) individuals' weight remained the same. The rate of those who diet to lose weight increased by 29% during pandemic. According to the results of survey data applied in this research, while there was no statistically significant difference between cities ($p>0.05$) and gender in presence of chronic diseases in Turkey; there was a statistically significant difference at the ages. There was a statistically significant difference in the rate of chronic disease among different age groups. The age range with the highest rate of chronic disease presence was 31-45 (299 people; 41%). and a statistically significant difference was found ($p<0.05$). The change in the participants working conditions before and during the Covid-19 pandemic was found to be significant ($p<0.05$) (Table 3).

Table 3 Change in the working conditions of the participants'

	Pre Covid -19		During Covid -19	
	n	%	n	%
Work from Office	468	65	274	37
Work from home	32	4	186	26
Short-Term Employment Allowance	0	0	32	5
Quit work	9	1	11	2
Not working	216	30	222	30

Values are expressed as n (participant's number) and % (percentage) for categorical variables.

38% (274 people) reported that they were still working in the workplace, whereas the percentage of those working from home increased from 4% to 26%. Also, 4% (32 individuals) began to benefit from the short-term employment allowance. The respondents were asked. "Will diet have an effect on recovery from Covid -19 with mild symptoms?" Individuals between the ages of 31-45 and 45-65 who participated in the

questionnaire thought that the diet had a significant effect on overcoming the disease ($p < 0.05$). While compared to individuals living in big cities and other cities, it was stated that the diet would not affect the disease ($p > 0.05$).

Demand for packaged products due to the Covid-19 pandemic was significantly higher in females (67%; 486 person) than in males (33%; 238 person), and in the 31-45 and 45-65 age ranges than in the other age ranges ($p<0.05$). Regarding the question about stocking up for the risk of staying home for a long time due to the Covid-19 pandemic, they stated stocked up 59% on food, 4% on cleaning materials, 1% on masks and gloves. 35% of individuals stated that they thought stocking up was unnecessary. At the end of the research, it was determined that different substances were stocked. However, a group of people did not feel the need to stock up. The reason why they think that there was no need to stock up on food may be the food storage traditions of Turkish food and cuisine culture [18]. The reduction of frequency of takeaway was observed during the Covid-19 pandemic in Turkey. Since the risk of catching Covid-19 from eating out or from food packaging causes anxiety in people, the frequency of consuming food cooked outside has decreased [19]. There was no significant change in exercise habits of the respondents in both the pre- and post-pandemic periods ($p>0.05$). As regards the physical exercises performed during the pandemic, 45% reported walking outdoors, 9-10% reported doing pilates, yoga, etc. while 18-20% reported engagement in both outdoor walking and doing yoga, pilates, etc. (Figure 1).

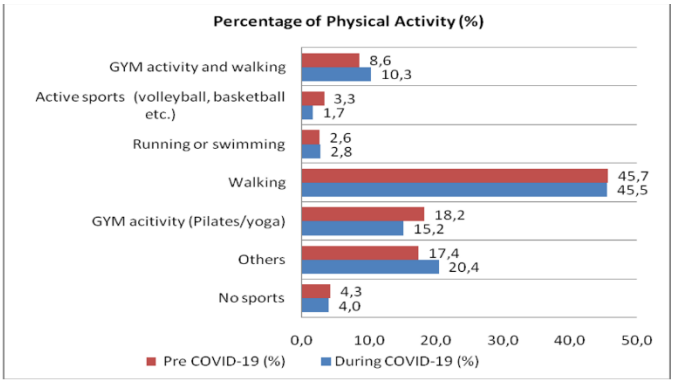

Figure 1 Physical activity changes of the participants before and during the pandemic

The physical activity most frequently stated by the respondents was outdoor walking: 35% reported going for a walk several times a week, 13% once a week, and 12% several times a month during the pandemic (Figure 2).

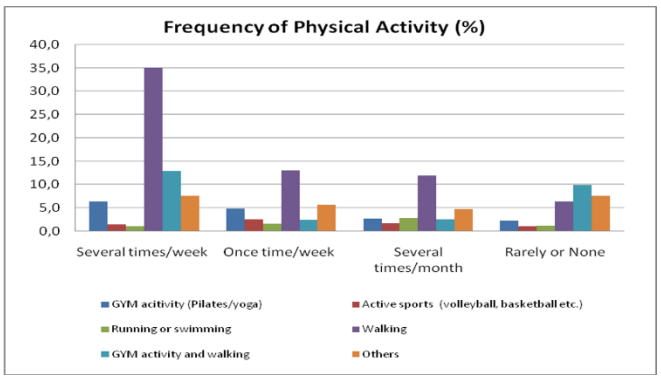

Figure 2 Physical activity frequency of the participants during the pandemic

The participant food purchasing habits and shopping frequencies before and during the pandemic were also evaluated (Figure 3, Figure 4).

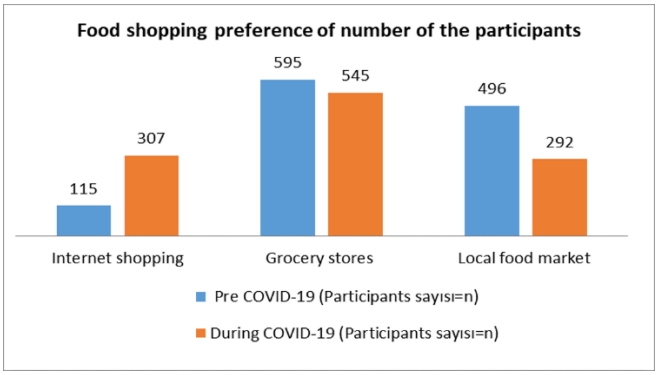

Figure 3 Food shopping preference of the participants before and during the pandemic

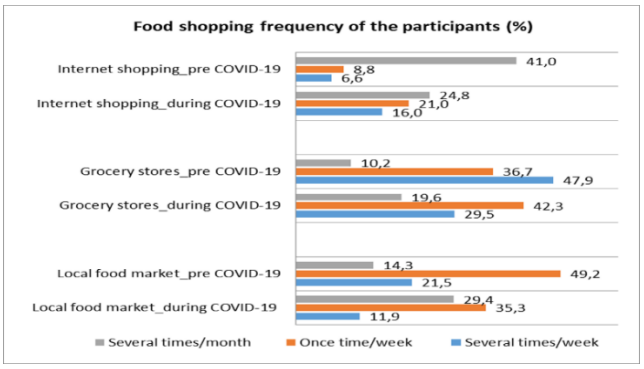

Figure 4 Food shopping frequencies of the participants before and during the pandemic

While online shopping increased by 166%, local food market shopping decreased by 41% ($p<0.05$). Shopping from grocery stores decreased by 8%, which was not statistically significant ($p>0.05$).

The percentage of those who did online shopping once to three times a week increased from 7% to 16% and once a week increased from 9% to 21%, while the percentage of those who did online shopping once to three times a month decreased from 41% to 25% ($p<0.05$). In general, the number of people who did online shopping at least once a week increased. While the frequency of local food market and grocery shopping decreased in participants with undergraduate and graduate education, the frequency of internet shopping increased in the Covid-19 pandemic process ($p<0.05$). On the other hand, the percentage of those who visited grocery stores once to three times a week decreased from 48% to 30%, the percentage of those who visited grocery stores once a week increased from 37% to 42%, and the percentage of those who visited grocery stores once to three times a month increased from 10% to 20%. These data show that people visit grocery stores less often. The habit of visiting local food market was quite common in Turkish society. The percentage of those who visited local food markets once to three times a week decreased from 22% to 12% and once a week decreased from 49% to 35% whereas the percentage of those who visited local food markets once to three times a month increased from 14 % to 29%. The participant frequency of visiting local food markets was determined as once a week or several times a month. Especially, the academicians showed a decrease in the local food market shopping frequency during the Covid-19 pandemic process ($p <0.05$). In other words, it was found that individuals visited local food markets as few times as possible.

3.1. Changes in eating and consumption habits during the pandemic

As regards the frequency of takeaway in both the before and during pandemic periods there was no significant difference between big cities and other cities in terms of both periods ($p>0.05$). While there was no significant difference between men and women in terms of the frequency of takeaway food before the pandemic ($p>0.05$), a statistically significant difference was observed between women and men during the pandemic process ($p<0.05$). It has been determined that women order take-away meals more frequently than men, since women are more organized in meeting their family food needs (Figure 5).

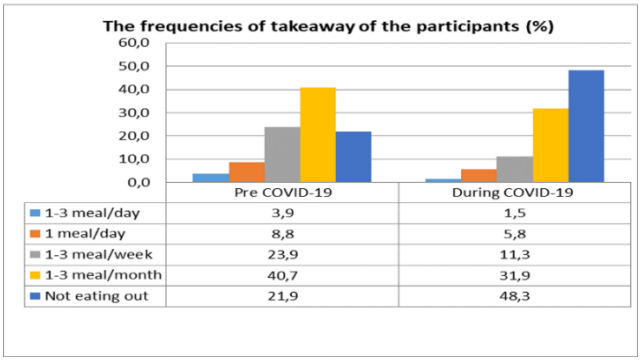

Figure 5 The frequencies of takeaway of the participants during

Furthermore, it was determined that there was a difference between <18, 18-30, 31-45 age ranges and 45-65 and >65 age ranges in terms of the frequency of takeaway food ($p<0.05$): Individuals over the age of 45 did not prefer takeaway food.

In fact, the overall frequency of takeaway decreased in Turkey after the Covid-19 pandemic. The percentage of those who not preferred takeaway increased by 120% in total from 22% to 48%. In addition, the frequency of eating out has decreased significantly.

The frequency of purchasing unpackaged food products decreased during the pandemic ($p<0.05$). Moreover, the demand for packaged products increased by 43% during the pandemic. This is because the risk of catching Covid-19 from unpackaged food products creates fear and anxiety in people.

The consumption of dairy products, probiotic product and supplements, vitamin C source foods such as oranges, other fruits, and seafood increased during the pandemic ($p<0.05$) (Table 4).

Table 4 Foods consumption frequency (n=725) and percentages (%) of the participants pre and during pandemic (Covid-19)

	3 portion/day		1 portion/day		3-4 portion/week		Never consume	
	n	%	n	%	n	%	n	%
Milk and milk products_pre Covid-19	124	17.1	412	56.8	173	23.9	16	2.2
Milk and milk products_during Covid-19	163	22.5	405	55.9	147	20.3	10	1.4
Probiotic products_pre Covid-19	35	4.8	242	33.4	228	31.4	220	30.3
Probiotic products_during Covid-19	52	7.2	283	39.0	188	25.9	202	27.9
Orange etc._pre Covid-19	68	9.4	295	40.7	314	43.3	48	6.6
Orange etc._during Covid-19	112	15.4	298	41.1	280	38.6	48	6.6
Other fruits_pre Covid-19	69	9.5	349	48.1	283	39.0	24	3.3
Other fruits_during Covid-19	102	14.1	370	51.0	234	32.3	19	2.6
Carbonated beverage_pre Covid-19	30	4.1	93	12.8	266	36.7	334	46.1
Carbonated beverage_during Covid-19	32	4.4	87	12.0	260	35.9	342	47.2

On the other hand, no change was observed in the frequency of consumption of fizzy drinks. Probiotic product consumption increased significantly in participants at all education levels during the pandemic process ($p<0.05$) (Table 4). The participants daily consumption of legumes, vegetables, and pastries increased, but the increase was not significant ($p>0.05$) (Table 5).

Table 5 Some foods consumption frequency (n=725) and percentages (%) of the participants pre and during pandemic (Covid-19)

	1 portion/day		1-3portion/week		1-3portion/month		Never consume	
	n	**%**	**n**	**%**	**n**	**%**	**n**	**%**
Red meat _pre Covid-19	121	16.7	465	64.1	127	17.5	12	1.7
Red meat_during Covid-19	118	16.3	474	65.4	116	16.0	17	2.3
White meat _pre Covid-19	83	11.4	413	57.0	179	24.7	50	6.9
White meat _during Covid-19	81	11.2	418	57.7	167	23.0	59	8.1
Sea food_pre Covid-19	46	6.3	245	33.8	381	52.6	53	7.3
Sea food_during Covid-19	44	6.1	276	38.1	349	48.1	56	7.7

Legumes_pre Covid-19	68	9.4	429	59.2	217	29.9	11	1.5
Legumes_during Covid-19	76	10.5	440	60.7	197	27.2	12	1.7
Dessert_pre Covid-19	100	13.8	314	43.3	249	34.3	62	8.6
Dessert_during Covid-19	89	12.3	319	44.0	250	34.5	67	9.2
Dried nuts_pre Covid-19	169	23.3	353	48.7	185	25.5	18	2.5
Dried nuts_during Covid-19	217	29.9	348	48.0	142	19.6	18	2.5
Vegetables_pre Covid-19	161	22.2	418	57.7	120	16.6	20	2.8
Vegetables_during Covid-19	177	24.4	417	57.5	113	15.6	10	1.4
Pasta_pre Covid-19	110	15.2	435	60.0	158	21.8	22	3.0
Pasta_during Covid-19	114	15.7	439	60.6	145	20.0	27	3.7
Pastries_pre Covid-19	66	9.1	340	46.9	282	38.9	34	4.7
Pastries_during Covid-19	71	9.8	351	48.4	248	34.2	46	6.3
Junk food_pre Covid-19	43	5.9	118	16.3	338	46.6	222	30.6
Junk food_during Covid-19	49	6.8	125	17.2	310	42.8	239	33.0

Daily consumption of dried nuts (28%) and junk food (14%) increased ($p<0.05$). Junk food is unhealthy food that is high in calories from sugar or fat, with little dietary fiber, protein, vitamins, minerals, or other important forms of nutritional value [9]. While no change was observed in the consumption of sweets, pasta, and bread, the consumption of red meat and white meat decreased during the pandemic ($p>0.05$). The daily water consumption of individuals during the pandemic was 2L and over 2L. As experts often advise people to strengthen their immune systems [20], the daily consumption of fermented products such as probiotic yogurt, vinegar, pickles, and kefir has increased. According to the findings of our survey research, consumption of dairy products, probiotic supplements, seafood, other fruits, and vitamin C-based foods such as oranges, increased during the pandemic. During the pandemic, milk, canned fruit, and flour sales increased by 3.5 times, 3 times, and 6 times, respectively, in the UK. In another study conducted with 2.933 people in England, America, Germany, and China, it was determined that the food and beverage expenditures of consumers increased by 43% in China, 22% in

Germany, 27% in the UK, and 27% in the USA [21, 22]. It was stated that sixty-five percent of the consumers have tried to con-sume more food that boosts the immune system since the COVID-19 pandemic started in Turkey [23].

Furthermore, they have had a proper eating habit regarding fruit and vegetable consumption. The increase in working from home and the length of staying home led to an increase particularly in the consumption of snacks such as nuts and junk food. In a survey study conducted in Spain, they stated that people increased their consumption of snacks such as chocolate, coffee, tea and nuts for combat stress during the Covid-19 pandemic [24]. In the studies conducted in different countries (including Turkey) during the Covid-19 process, it has been determined that people prefer chocolate, nuts, and snack foods to reduce boredom. In a study conducted in Spain, it was observed that while the consumption of vegetables, fruits, legumes, vegetables and fish changed towards healthier habits, there was an increase in the consumption of alcoholic and sugary drinks and processed products with high fat and salt or sugar content [25].

Studies were examined the effects of natural disasters such as storms, tornadoes, hurricanes, and earthquakes, and health crises such as pandemics on consumers' shopping and spending behaviors. According to a study by Elmore [26], both fuel spending and market spending a week before Hurricane Irma struck Florida increased by 63% and 41%, respectively, compared to the previous year. Also, it is seen that online purchases of durable consumer goods have increased significantly in the USA. Sales of rice, flour, canned vegetables, and canned legumes increased (+ 433%) in March compared to January 2020 in the USA [27]. A study carried out in Vietnam reported that the tendency to stock up on food during the pandemic increased by 45%, online shopping increased by 25%, and the frequency of visiting supermarkets/grocery stores and fresh food markets decreased by 50% [21]. Turkish restaurants, cafes and etc. catering businesses were adversely affected due to reduced frequency of eating out and restrictions on leaving the street in Turkey.

The working systems of people have also changed in the during Covid-19 pandemic. The percentage of those working from home increased while 4% began to benefit from the short-term employment allowance. Short-term employment can be defined as a compulsory reduction in working time or complete or partial cessation of work in case of compelling reasons such as general economic crisis, or sectoral and regional crisis in Turkey. On the other hand, the short-time employment allowance is payment support provided by the government to employees during short-term employment [28].

The habit of visiting the local food market is quite common in Turkish society. However, a significant decrease in local food market habits was observed during the pandemic process. Because the spread rate of the disease is stated to be more in places where there is collective communication.

The change in people's food purchasing habits has affected many industries and distribution channels. The Covid-19 pandemic has increased the need for reliable supply chains, demonstrating the vital importance of supply chains and logistics, as well as the disadvantages of international trade. During the pandemic, the necessity to ensure the smooth functioning of all supply chain and logistics operations from supply to production, from warehouse operations to shipping, from e-commerce to cargo and courier services was strongly felt [29].

The workload of the courier or distribution personnel required for the delivery of products purchased online has increased. In addition, restructuring and updating of the requirements of the market or the online sales channel of supermarkets in Turkey has emerged once again. In the event of a health crisis that may require people to use only online channels for shopping, the online shopping infrastructure should be strengthened to make shopping faster and safer in the future.

4. CONCLUSION

This study was attempt to provide data related to the changes that took place in Turkish consumers'

lifestyles. eating habits, and food purchasing habits during the Covid-19 pandemic. Compared to the pre-pandemic period, in the post-pandemic period, an increase was observed in the participants daily sleeping duration (especially 9-12 hours, 124%) in vitamin C consumption (82%), vitamin D consumption (17%), weight gain (47%), working from home (481%), and food supplement consumption (150%), but there was no change in their preferences for physical activity. As regards the BMI values of participants there was a statistically significant difference between males and females in terms of pre-pandemic and post-pandemic BMI values.

Also, it was determined that online shopping increased by 166%, while street market shopping decreased by 41%. Therefore, the necessity of restructuring or updating the online sales channels of markets or supermarkets in Turkey has emerged once more. The preference for ordering food delivery was found to be quite common in individuals under 45 years of age. It has been stated that the rate of those who do not prefer takeaway meals in all age groups has increased by 120 percent. Since the risk of catching Covid-19 from eating out or from food packaging causes anxiety in people, the frequency of consuming food cooked outside has decreased. The consumption of dairy products, probiotic supplements, vitamin C source foods such as oranges, other fruits, and seafood increased during the pandemic. Another promising data was the reduction in smoking and alcohol addiction during the Covid-19 pandemic.

4.1. Implications for Research and Practice

Experience with Covid-19 has shown that a pandemic requires an emergency plan with unique challenge. This study was the first attempt to provide data related to the changes that took place in Turkish consumers' lifestyles, eating habits, and food purchasing habits after the Covid-19 pandemic. The current study identified changes in people's diet and habits and behaviors during the pandemic period. Emergency plans should be made in countries to investigate the long-term effects and to prepare for the "new normality". During the Covid-19 pandemic, awareness has been raised for detecting the changes in nutrition in unexpected conditions, evaluating the production rate of food companies in this process, government officials to create appropriate resources and guidelines while preparing for the current pandemic conditions and other future emergencies.

An emergency plan should be created for those working in infectious disease outbreaks. Changes in diet patterns of individuals living in Turkey during the outbreak was identified by this research. However, this trend should be determined for all countries and emergency plans should be created in the future. Given that the Covid-19 pandemic is still ongoing, the obtained data should be investigated in larger population groups in the future. In addition, if the pandemic continues further, it will be important to focus on organizing, planning and improving the infrastructures of manufacturers, carriers, and sellers in the food supply chain.

Acknowledgements

I also thanks Assoc. Prof. Fikriye Yılmaz and Prof. İsmail Tokmak.

The Declaration of Conflict of Interest/Common Interest

No conflict of interest or common interest has been declared by the authors.

The Declaration of Ethics Committee Approval

For the survey, the permission was obtained from the Ministry of Health, General Directorate of Health Services, and Isparta University of Applied Sciences Scientific Research Publication Ethics Committee (Decision Date: 07.10.2020 and Decision, Count: 96714346-044-E, No: 31/1).

The Declaration of Research and Publication Ethics

During the writing process of my study, international scientific, ethical and citation rules have been followed, no falsification has been made on the data collected, and Sakarya University Journal of Science and its editorial

board have no responsibility for any ethical violations that may be encountered. I undertake that I have full responsibility and that this study has not been evaluated in any academic environment other than Sakarya University Journal of Science.

REFERENCES

[1] K. McIntosh and S. Perlman, "Coronaviruses, including Severe Acute Respiratory Syndrome (SARS) and Middle East Respiratory Syndrome (MERS) In: Bennett JE, Dolin R, Blaser MJ (eds). Principles and Practice of Infectious Diseases", 8th edition, Philadelphia: Elsevier-Saunders, 1928-1936, 2015.

[2] WHO (World Health Organization), "Rolling update on coronavirus (COVID-19)",https://www.who.int/emergencies/diseases/novel-coronavirus-2019/events-as-they-happen, (11.03.2020).

[3] WHO (World Health Organization), "Coronavirus disease (COVID-19)", https://www.who.int/health-topics/coronavirus#tab=tab_1, (9.12.2020).

[4] WHO (World Health Organization), "WHO Coronavirus Disease (COVID-19) Dashboard. https://covid19.who.int/ (29.12.2020).

[5] Anonymous, Republic of Turkey, Ministry of Health. "Covid-19 Information Page". https://covid19.saglik.gov.tr/ 01.01.2022.

[6] L. Di Renzo, P. Gualtieri, F. Pivari, L. Soldati, A. Attinà, G. Cinelli, C. Leggeri, G. Caparello, L. Barrea, F. Scerbo, E. Esposito and A. De Lorenzo, "Eating habits and lifestyle changes during COVID-19 lockdown: an Italian survey", Journal of Translational Medicine, vol: 18, no,229. Pp. 1-15, 2020.

[7] A. B. Moynihan, W. A. P. Van Tilburg, E. R. Igou, A. Wisman, A. E. Donnelly and J. B. Mulcaire, "Eaten up by boredom: consuming food to escape awareness of the bored self". Frontiers in Physiology, vol:6, pp.369, 2015.

[8] C. Yılmaz and V. Gökmen, "Neuroactive compounds in foods: occurrence. mechanism and potential health effects", Food Research International, vol:128, pp.108744-108748, 2020.

[9] Y. Ma, R. Ratnasabapathy and J. Gardiner, "Carbohydrate craving: not everything is sweet", Current Opinion in Clinical Nutrition & Metabolic Care, vol:20 pp.261–265, 2017.

[10] M. Adıgüzel, "Macro Economic Analysis of The Effect of The Covid-19 Pandemic in Turkey". Istanbul Commerce University, Journal of Social Sciences, Covid-19 Social Sciences Special Issue, vol:19, no:37, pp.191-221, 2020.

[11] A. M. Adam, "Sample Size Determination in Survey Research". Journal of Scientific Research & Reports, vol:26 no:5 pp.90-97, 2020.

[12] A. Uncu-Soykan, "Reliability and Validity of Food-Frequency Questionnaires". Cukurova University, Health Sciences Institute, Biostatistics Department. Adana. Turkey. 101s, 2007.

[13] S. Sood, "Impact of COVID-19 on Consumer Behavior in India". Conference: Sustainable Management Practices and Economic Slowdown in India At: Delhi, India. Project: Marketing and Consumer Behavior. https://www.researchgate.net/publication/343153169_Impact_of_COVID_19_on_Consumer_Behavior_in_India. Conference paper, 2020.

[14] B. K. Tetik, I. G. Tekinemre and S. Taş. "The Effect of the COVID-19 Pandemic on Smoking Cessation Success". Journal of Community Health, vol:8, pp.1–5, 2020.

[15] Y. Karaağaç and E. B. Koyu. "Vitamins and Minerals in Viral Infections: A Review Focusing on COVID-19". İzmir Kâtip Celebi

University, Journal of Health Sciences Faculty. vol:5, no:2 pp.165-173, 2020.

[16] U. S. Pharmacist, "Impact of Vitamins on Immune Function in COVID-19 Patients". https://www.uspharmacist.com/article/impact-of-vitamins-on-immune-function-in-covid19-patients, (09.01.2021).

[17] M. Güllü and Ş. Karagöz, "Traditional food storage methods in Turkish culinary culture". ISBN: 978-605-254-175-3. Page:181. Turkey, 2019.

[18] T. B. Hassen, H. E. Bilali and M. S. Allahyari, "Impact of COVID-19 on Food Behavior and Consumption in Qatar". Sustainability, vol:12, no:6973, pp.1-18, 2020.

[19] M. Alagawany, Y.A. Attia, M. R. Farag, S. S. Elsner, S. A. Nagadi, M. E. Shafi, A. F. Khafaga, H. Ohran, A. A. Alaqil, and M. E. Abd El-Hack, "The Strategy of Boosting the Immune System Under the COVID-19 Pandemic". Frontiers in Veterinary Science, vol:7, no:570748, pp.1-17, 2021.

[20] Statista, "Impact on consumer behavior due to COVID-19 among urban citizens in Vietnam 2020". https://www.statista.com/statistics/1102863/vietnam-impact-on-shoppingafter-covid-19-outbreak/, 30.03.2020.

[21] Statista, "Perishable Food Consumption Report",https://www.statista.com/chart/21109/sales-growth-of-non-perishablefood-items-in-the-us/, 28.03.2020.

[22] Bolek, S. "Food purchasing, preservation, and eating behavior during COVID-19 pandemic: A consumer analysis". Italian Journal of Food Science, vol:33 no:3 pp: 14–24, 2021.

[23] L. Laguna, S. Fiszman, P. Puerta, C. Chaya and A. Tárrega, "The impact of COVID-19 lockdown on food priorities. Results from a preliminary study using social media and an online survey with Spanish consumers". Food Quality and Preference. Vol:86, no:104028, pp.1-9, 2020.

[24] C. Pérez-Rodrigo, M. G. Citores, G. H. Bárbara, F. Ruiz-Litago, L. C. Sáenz, V. Arija, A. M. López-Sobaler E. M.Victori, R. M. Ortega, T. Partearroyo, J. Quiles-Izquierdo, L. Ribas-Barba, A. Rodríguez-Martín, G. S. Castell, J. A. Tur, G. Varela-Moreiras, L. Serra-Majem, and J. Aranceta-Bartrina. "Patterns of Change in Dietary Habits and Physical Activity during Lockdown in Spain Due to the COVID-19 Pandemic". Nutrients, vol:13, no:300, pp:1-16, 2021.

[25] C. Elmore, "Irma: Frenzied buying in Palm Beach. St. Lucie regions led state". Palm Beach Post. Retrieved from http://www.palmbeachpost.com/business/irma-frenzied-buying-palm-beach-lucie-regions-led-state/LIDVXIL3qlqJGLlaosfSiL/, 2017.

[26] Criteo, "5 ways the coronavirus is affecting consumer behavior". https://www.criteo.com/blog/coronavirus-consumer-behavior/, 19.12.2020.

[27] M. A. Ozdemir, "What are the Economic, Psychological and Social Consequences of the Covid-19 Crisis on Tourism Employees?" International Journal of Social, Political and Economic Research, vol:7, no:4, pp.1137-1163, 2020.

[28] G. Senir and A. Büyükkeklik. "Effects of the COVID-19 Outbreak on Supply Chains and Logistics Activities. In: Anatomy of the Global Epidemic Future of Man and Society". Ed: Şeker. M.. Özer. A.. Korkut. C.. First Edition. Turkey Academy of Sciences. TDV Publication Printing Facilities. Ankara. Turkey. Page:628-643, 2020.

SAKARYA ÜNİVERSİTESİ
FEN BİLİMLERİ ENSTİTÜSÜ DERGİSİ

Sakarya University Journal of Science
SAUJS

ISSN 1301-4048 e-ISSN 2147-835X Period Bimonthly Founded 1997 Publisher Sakarya University
http://www.saujs.sakarya.edu.tr/

Title: Quasi-Focal Curves of Spacelike Adjoint Curves in 3D Minkowski Space

Authors: Talat KÖRPINAR, Ahmet SAZAK

Recieved: 2022-01-26 00:00:00

Accepted: 2022-04-25 00:00:00

Article Type: Research Article

Volume: 26
Issue: 3
Month: June
Year: 2022
Pages: 523-529

How to cite
Talat KÖRPINAR, Ahmet SAZAK; (2022), Quasi-Focal Curves of Spacelike Adjoint Curves in 3D Minkowski Space. Sakarya University Journal of Science, 26(3), 523-529, DOI: 10.16984/saufenbilder.1063526
Access link
http://www.saujs.sakarya.edu.tr/tr/pub/issue/70993/1063526

Sakarya University Journal of Science 26(3), 523-529, 2022

Quasi-Focal Curves of Spacelike Adjoint Curves in 3D Minkowski Space

Talat KÖRPINAR*[1], Ahmet SAZAK[1]

Abstract

Associated curves bring meaningful geometric expression to the physics and mathematics fields in the characterization of curves and surfaces created by those curves, their behavior, and the study of particle motion in space-time. In this work, we examine the relationship between adjoint curves and focal curves, which are two important examples of associated curves. We do this review for spacelike curves under quasi(q)-frame in 3D Minkowski space. To put it more clearly, we obtain some new characterizations by defining the focal curve of the adjoint curve of a spacelike curve in this space.

Keywords: Quasi-frame, spacelike curve, focal curve, adjoint curve.

1. INTRODUCTION

Associated curves provide meaningful mathematical expressions in the study of the characterization of curves and surfaces, their behavior, and the particle motion defined by such curves. Fundamentally, it allows a second curve geometrically related to a curve to be defined with the help of the main curve. One of the most obvious examples of associated curves is integral curves, which is a superscript of adjoint curves [1-6]. Integral curves are important in terms of the possibilities they provide for the solution of some differential equations that we encounter in geometric problems. The adjoint curves that we will consider in our study are the curves determined by the integral of the binormal vector field of a curve. For more information on such curves, see [7-13].

Another curve that we will consider in our study is the focal curve. The focal curve is determined by the center points of the imaginary spheres that oscillate tangentially along a selected curve with arc length parameters. Let this chosen curve be denoted by ϑ. In this case, the focal curve of ϑ is given as

$$\vartheta_F(s) = (\vartheta + \omega_1 \boldsymbol{N} + \omega_2 \boldsymbol{B})(s), \qquad (1)$$

* Corresponding author: talatkorpinar@gmail.com
[1] Muş Alparslan University
E-mail: a.sazak@alparslan.edu.tr
ORCID: https://orcid.org/0000-0003-4000-0892, https://orcid.org/0000-0002-5620-6441

where $\boldsymbol{B}$ and $\boldsymbol{N}$ are the vector fields that are binormal and normal elements for the Frenet-Serret (F-S) frame, s is the arc-length parameter and, ω_1 and ω_2 are focal curvatures of the curve ψ [7].

Based on these considerations, the goal of our article is to describe and characterize a new curve created by the center points of an imaginary sphere that oscillates tangential to a curve adjoining the principal curve. In this study, we are doing this analysis for a spacelike curve that we have chosen under the quasi(q)-frame in M_1^3 space. First of all, we define the adjoint curve of the curve we have chosen and calculate the expressions of the q-frame elements of these two curves in terms of each other. Then, we define the focal curve of the adjoint curve by obtaining the focal curvatures of the focal curve. Finally, with the help of this definition and other obtained equations, we obtain some characterizations related to curvatures and curves.

2. PRELIMINARIES

In this part, we remind the q-frame equations and some related fundamental information for the spacelike curves we will choose in the 3-dimensional Minkowski (M_1^3) space, which we will base our study on.

The F-S frame formulas for an arbitrary curve ψ with arc length parameters are given as follows:

$$\begin{bmatrix} \boldsymbol{T}^s \\ \boldsymbol{N}^s \\ \boldsymbol{B}^s \end{bmatrix} = \begin{bmatrix} 0 & \kappa & 0 \\ -\kappa & 0 & \tau \\ 0 & -\tau & 0 \end{bmatrix} \begin{bmatrix} \boldsymbol{T} \\ \boldsymbol{N} \\ \boldsymbol{B} \end{bmatrix}. \tag{2}$$

Also, the F-S frame elements are given by these equations

$$\boldsymbol{T} = \partial\psi/\partial s, \quad \boldsymbol{N} = \frac{\partial^2\psi/\partial s^2}{\|\partial^2\psi/\partial s^2\|}, \quad \boldsymbol{B} = \boldsymbol{T} \times \boldsymbol{N}. \tag{3}$$

Here, τ and κ are torsion and curvature of ψ, and the vector fields $\boldsymbol{T}, \boldsymbol{N}, \boldsymbol{B}$ are tangent, unit normal, and binormal vector fields of the F-S frame [12].

In addition, the expressions of q-frame elements in terms of F-S frame elements are written as

$$\begin{aligned} \boldsymbol{T}_{q_\psi} &= \boldsymbol{T}, \\ \boldsymbol{N}_{q_\psi} &= (\boldsymbol{T} \times \rho)/\|\boldsymbol{T} \times \rho\|, \\ \boldsymbol{B}_{q_\psi} &= \boldsymbol{T}_{q_\psi} \times \boldsymbol{N}_{q_\psi}. \end{aligned} \tag{4}$$

Here $\rho = (0,1,0)$ is the projection vector. Let ψ be a spacelike curve and quasi(q)-normal vector field $\boldsymbol{N}_{q_\psi}$ be timelike. Then, the F-S frame formulas in M_1^3 are given as

$$\begin{bmatrix} \boldsymbol{T}_\psi^s \\ \boldsymbol{N}_\psi^s \\ \boldsymbol{B}_\psi^s \end{bmatrix} = \begin{bmatrix} 0 & \kappa_\psi & 0 \\ \kappa_\psi & 0 & \tau_\psi \\ 0 & \tau_\psi & 0 \end{bmatrix} \begin{bmatrix} \boldsymbol{T}_\psi \\ \boldsymbol{N}_\psi \\ \boldsymbol{B}_\psi \end{bmatrix}, \tag{5}$$

and the relationship between the F-S frame and the q-frame is given as

$$\begin{bmatrix} \boldsymbol{T}_{q_\psi} \\ \boldsymbol{N}_{q_\psi} \\ \boldsymbol{B}_{q_\psi} \end{bmatrix} = \begin{bmatrix} 1 & 0 & 0 \\ 0 & ch\theta & sh\theta \\ 0 & sh\theta & ch\theta \end{bmatrix} \begin{bmatrix} \boldsymbol{T}_\psi \\ \boldsymbol{N}_\psi \\ \boldsymbol{B}_\psi \end{bmatrix}, \tag{6}$$

$$\psi_1 = -\kappa_\psi ch\theta, \qquad \psi_2 = -\kappa_\psi sh\theta, \qquad \psi_3 = d\theta + \tau_\psi.$$

where ψ_1, ψ_2, ψ_3 are curvatures of ψ, and θ is the hyperbolic angle between $\boldsymbol{N}_{q_\psi}$ and $\boldsymbol{N}_\psi$. Then, the q-frame formulas in M_1^3 are given by

$$\begin{bmatrix} \boldsymbol{T}_{q_\psi}^s \\ \boldsymbol{N}_{q_\psi}^s \\ \boldsymbol{B}_{q_\psi}^s \end{bmatrix} = \begin{bmatrix} 0 & -\psi_1 & \psi_2 \\ -\psi_1 & 0 & \psi_3 \\ -\psi_2 & \psi_3 & 0 \end{bmatrix} \begin{bmatrix} \boldsymbol{T}_{q_\psi} \\ \boldsymbol{N}_{q_\psi} \\ \boldsymbol{B}_{q_\psi} \end{bmatrix}, \tag{7}$$

and vector products of q-frame elements with each other are written as

$$\begin{aligned} \boldsymbol{T}_{q_\psi} \times \boldsymbol{N}_{q_\psi} &= -\boldsymbol{B}_{q_\psi}, \\ \boldsymbol{N}_{q_\psi} \times \boldsymbol{B}_{q_\psi} &= -\boldsymbol{T}_{q_\psi}, \\ \boldsymbol{B}_{q_\psi} \times \boldsymbol{T}_{q_\psi} &= \boldsymbol{N}_{q_\psi}, \end{aligned} \tag{8}$$

Let ψ be a spacelike curve and q-binormal vector field $\boldsymbol{B}_{q_\psi}$ be timelike. Then, the F-S frame formulas in M_1^3 are given as

$$\begin{bmatrix} \boldsymbol{T}_{\psi}^{s} \\ \boldsymbol{N}_{\psi}^{s} \\ \boldsymbol{B}_{\psi}^{s} \end{bmatrix} = \begin{bmatrix} 0 & \kappa_{\psi} & 0 \\ -\kappa_{\psi} & 0 & \tau_{\psi} \\ 0 & \tau_{\psi} & 0 \end{bmatrix} \begin{bmatrix} \boldsymbol{T}_{\psi} \\ \boldsymbol{N}_{\psi} \\ \boldsymbol{B}_{\psi} \end{bmatrix}, \tag{9}$$

and the relationship between the F-S frame and the q-frame is given as

$$\begin{bmatrix} \boldsymbol{T}_{q_\psi} \\ \boldsymbol{N}_{q_\psi} \\ \boldsymbol{B}_{q_\psi} \end{bmatrix} = \begin{bmatrix} 1 & 0 & 0 \\ 0 & sh\theta & ch\theta \\ 0 & -ch\theta & -sh\theta \end{bmatrix} \begin{bmatrix} \boldsymbol{T}_{\psi} \\ \boldsymbol{N}_{\psi} \\ \boldsymbol{B}_{\psi} \end{bmatrix}, \tag{10}$$

$\psi_1 = \kappa_\psi sh\theta, \quad \psi_2 = -\kappa_\psi ch\theta, \quad \psi_3 = -d\theta - \tau_\psi.$

Then, the q-frame formulas in M_1^3 are given by

$$\begin{bmatrix} \boldsymbol{T}_{q_\psi}^{s} \\ \boldsymbol{N}_{q_\psi}^{s} \\ \boldsymbol{B}_{q_\psi}^{s} \end{bmatrix} = \begin{bmatrix} 0 & -\psi_1 & \psi_2 \\ -\psi_1 & 0 & \psi_3 \\ -\psi_2 & \psi_3 & 0 \end{bmatrix} \begin{bmatrix} \boldsymbol{T}_{q_\psi} \\ \boldsymbol{N}_{q_\psi} \\ \boldsymbol{B}_{q_\psi} \end{bmatrix}, \tag{11}$$

and vector products of q-frame elements with each other are written as [13]

$$\begin{aligned} &\boldsymbol{T}_{q_\psi} \times \boldsymbol{N}_{q_\psi} = \boldsymbol{B}_{q_\psi}, \\ &\boldsymbol{N}_{q_\psi} \times \boldsymbol{B}_{q_\psi} = -\boldsymbol{T}_{q_\psi}, \\ &\boldsymbol{B}_{q_\psi} \times \boldsymbol{T}_{q_\psi} = -\boldsymbol{N}_{q_\psi}. \end{aligned} \tag{12}$$

3. THE QUASI-FOCAL CURVES OF SPACELIKE ADJOINT CURVES

Definition 1. Let ψ be an arc-length parametrised curve and $\boldsymbol{B}_\psi$ be the binormal (unit) vector field of ψ. Then, the adjoint of curve ψ is defined by the equation [9]

$$\vartheta(s) = \int_{s_0}^{s} \boldsymbol{B}_\psi(s) ds. \tag{13}$$

Theorem 2. Let ψ be a spacelike curve, $\boldsymbol{T}_{q_\psi}, \boldsymbol{N}_{q_\psi}, \boldsymbol{B}_{q_\psi}$ be q-frame elements of ψ, ϑ be adjoint of ψ and $\boldsymbol{T}_{q_\vartheta}, \boldsymbol{N}_{q_\vartheta}, \boldsymbol{B}_{q_\vartheta}$ be q-frame elements of ϑ. If the q-normal vector field $\boldsymbol{N}_{q_\psi}$ is timelike, then the equations related to the curve ψ of q-frame elements of ϑ are given in

$$\begin{aligned} \boldsymbol{T}_{q_\vartheta} &= \frac{\psi_2}{\kappa_\psi} \boldsymbol{N}_{q_\psi} - \frac{\psi_1}{\kappa_\psi} \boldsymbol{B}_\psi, \\ \boldsymbol{N}_{q_\vartheta} &= \frac{\vartheta_2}{\kappa_\vartheta} \boldsymbol{T}_{q_\psi} + \frac{\psi_1 \vartheta_1}{\kappa_\psi \kappa_\vartheta} \boldsymbol{N}_{q_\psi} - \frac{\psi_2 \vartheta_1}{\kappa_\psi \kappa_\vartheta} \boldsymbol{B}_{q_\psi}, \\ \boldsymbol{B}_{q_\vartheta} &= \frac{\vartheta_1}{\kappa_\vartheta} \boldsymbol{T}_{q_\psi} + \frac{\psi_1 \vartheta_2}{\kappa_\psi \kappa_\vartheta} \boldsymbol{N}_{q_\psi} - \frac{\psi_2 \vartheta_2}{\kappa_\psi \kappa_\vartheta} \boldsymbol{B}_{q_\psi}, \end{aligned} \tag{14}$$

and, If the q-binormal vector field $\boldsymbol{B}_{q_\psi}$ is timelike, then the equations related to the curve ψ of q-frame elements of ϑ are given in

$$\begin{aligned} \boldsymbol{T}_{q_\vartheta} &= -\frac{\psi_2}{\kappa_\psi} \boldsymbol{N}_{q_\psi} + \frac{\psi_1}{\kappa_\psi} \boldsymbol{B}_\psi, \\ \boldsymbol{N}_{q_\vartheta} &= -\frac{\vartheta_2}{\kappa_\vartheta} \boldsymbol{T}_{q_\psi} - \frac{\psi_1 \vartheta_1}{\kappa_\psi \kappa_\vartheta} \boldsymbol{N}_{q_\psi} + \frac{\psi_2 \vartheta_1}{\kappa_\psi \kappa_\vartheta} \boldsymbol{B}_{q_\psi}, \\ \boldsymbol{B}_{q_\vartheta} &= -\frac{\vartheta_1}{\kappa_\vartheta} \boldsymbol{T}_{q_\psi} - \frac{\psi_1 \vartheta_2}{\kappa_\psi \kappa_\vartheta} \boldsymbol{N}_{q_\psi} + \frac{\psi_2 \vartheta_2}{\kappa_\psi \kappa_\vartheta} \boldsymbol{B}_{q_\psi}, \end{aligned} \tag{15}$$

Proof. From (13), we can easily obtain the equations $\boldsymbol{T}_\vartheta = \boldsymbol{B}_\psi$. In the case of $\boldsymbol{N}_{q_\psi}$ is timelike, from (3) and (5), we obtain

$$\boldsymbol{N}_\vartheta = \frac{\partial^2 \vartheta / \partial s^2}{\|\partial^2 \vartheta / \partial s^2\|} = \frac{\boldsymbol{B}_\psi^s}{\|\boldsymbol{B}_\psi^s\|} = \boldsymbol{N}_\psi, \tag{16}$$

$$\boldsymbol{B}_\vartheta = -\boldsymbol{T}_\vartheta \times \boldsymbol{N}_\vartheta = -\boldsymbol{B}_\psi \times \boldsymbol{N}_\psi = -\boldsymbol{T}_\psi. \tag{17}$$

Let φ be the hyperbolic angle between $\boldsymbol{N}_{q_\vartheta}$ and $\boldsymbol{N}_\vartheta$. Then, from (6), we get

$$\begin{aligned} \boldsymbol{T}_{q_\vartheta} = \boldsymbol{T}_\vartheta = \boldsymbol{B}_\psi &= -sh\theta \boldsymbol{N}_{q_\psi} + ch\theta \boldsymbol{B}_{q_\psi} \\ &= \frac{\psi_2}{\kappa_\psi} \boldsymbol{N}_{q_\psi} - \frac{\psi_1}{\kappa_\psi} \boldsymbol{B}_{q_\psi}, \end{aligned}$$

$$\begin{aligned} \boldsymbol{N}_{q_\vartheta} &= ch\varphi \boldsymbol{N}_\vartheta + sh\varphi \boldsymbol{B}_\vartheta = ch\varphi \boldsymbol{N}_\psi - sh\varphi \boldsymbol{T}_\psi \\ &= ch\varphi \left(ch\theta \boldsymbol{N}_{q_\psi} - sh\theta \boldsymbol{B}_{q_\psi} \right) - sh\varphi \boldsymbol{T}_{q_\psi} \\ &= \frac{\vartheta_2}{\kappa_\vartheta} \boldsymbol{T}_{q_\psi} + \frac{\psi_1 \vartheta_1}{\kappa_\psi \kappa_\vartheta} \boldsymbol{N}_{q_\psi} - \frac{\psi_2 \vartheta_1}{\kappa_\psi \kappa_\vartheta} \boldsymbol{B}_{q_\psi}, \end{aligned}$$

$$\begin{aligned} \boldsymbol{B}_{q_\vartheta} &= sh\varphi \boldsymbol{N}_\vartheta + ch\varphi \boldsymbol{B}_\vartheta = sh\varphi \boldsymbol{N}_\psi - ch\varphi \boldsymbol{T}_\psi \\ &= sh\varphi (ch\theta \boldsymbol{N}_{q_\psi} - sh\theta \boldsymbol{B}_{q_\psi}) - ch\varphi \boldsymbol{T}_{q_\psi} \\ &= \frac{\vartheta_1}{\kappa_\vartheta} \boldsymbol{T}_{q_\psi} + \frac{\psi_1 \vartheta_2}{\kappa_\psi \kappa_\vartheta} \boldsymbol{N}_{q_\psi} - \frac{\psi_2 \vartheta_2}{\kappa_\psi \kappa_\vartheta} \boldsymbol{B}_{q_\psi}, \end{aligned}$$

In case of $\boldsymbol{B}_{q_\psi}$ is timelike, we similarly obtain the other equations.

Definition 3. Let $\boldsymbol{T}_{q_\vartheta}, \boldsymbol{N}_{q_\vartheta}, \boldsymbol{B}_{q_\vartheta}$ be q-frame elements of a regular space curve ϑ. The focal curve of ϑ is expressed as

$$\vartheta_F = \vartheta + \omega_1 \boldsymbol{N}_{q_\vartheta} + \omega_2 \boldsymbol{B}_{q_\vartheta}. \tag{18}$$

Here ω_1, ω_2 are the coefficients describing focal curvatures of ϑ [10].

Theorem 4. Let ψ be a spacelike curve, ϑ be adjoint curve of ψ, ϑ_F its focal curve in M_1^3 and ϑ_i and ψ_i $(i = 1,2,3)$ be, respectively, the curvatures of ϑ and ψ according to q-frame. If the q-normal vector field $\boldsymbol{N}_{q_\psi}$ is timelike, the focal curve of ϑ is

$$\begin{aligned}\vartheta_F = \vartheta - e^{\int \frac{\vartheta_1\vartheta_3}{\vartheta_2}ds}\Big(\int e^{-\int \frac{\vartheta_1\vartheta_3}{\vartheta_2}ds}\frac{\vartheta_3}{\vartheta_2}ds - C\Big)\Big(\frac{\vartheta_2}{\kappa_\vartheta}\boldsymbol{T}_{q_\psi} \\ + \frac{\psi_1\vartheta_1}{\kappa_\psi\kappa_\vartheta}\boldsymbol{N}_{q_\psi} - \frac{\psi_2\vartheta_1}{\kappa_\psi\kappa_\vartheta}\boldsymbol{B}_{q_\psi}\Big) + \Big(\frac{1}{\vartheta_2} - \frac{\vartheta_1}{\vartheta_2}e^{\int \frac{\vartheta_1\vartheta_3}{\vartheta_2}ds}\Big(C - \\ \int e^{-\int \frac{\vartheta_1\vartheta_3}{\vartheta_2}ds}\frac{\vartheta_3}{\vartheta_2}ds\Big)\Big)\Big(\frac{\vartheta_1}{\kappa_\vartheta}\boldsymbol{T}_{q_\psi} + \frac{\psi_1\vartheta_2}{\kappa_\psi\kappa_\vartheta}\boldsymbol{N}_{q_\psi} - \frac{\psi_2\vartheta_2}{\kappa_\psi\kappa_\vartheta}\boldsymbol{B}_{q_\psi}\Big).\end{aligned} \tag{19}$$

and, if the q-binormal vector field $\boldsymbol{B}_{q_\psi}$ is timelike, the focal curve of ϑ is

$$\begin{aligned}\vartheta_F = \vartheta + e^{-\int \frac{\vartheta_1\vartheta_3}{\vartheta_2}ds}\Big(\int e^{\int \frac{\vartheta_1\vartheta_3}{\vartheta_2}ds}\frac{\vartheta_3}{\vartheta_2}ds + C\Big)\Big(\frac{\vartheta_2}{\kappa_\vartheta}\boldsymbol{T}_{q_\psi} \\ + \frac{\psi_1\vartheta_1}{\kappa_\psi\kappa_\vartheta}\boldsymbol{N}_{q_\psi} - \frac{\psi_2\vartheta_1}{\kappa_\psi\kappa_\vartheta}\boldsymbol{B}_{q_\psi}\Big) + \Big(\frac{1}{\vartheta_2} - \frac{\vartheta_1}{\vartheta_2}e^{-\int \frac{\vartheta_1\vartheta_3}{\vartheta_2}ds}\Big(C + \\ \int e^{\int \frac{\vartheta_1\vartheta_3}{\vartheta_2}ds}\frac{\vartheta_3}{\vartheta_2}ds\Big)\Big)\Big(\frac{\vartheta_1}{\kappa_\vartheta}\boldsymbol{T}_{q_\psi} + \frac{\psi_1\vartheta_2}{\kappa_\psi\kappa_\vartheta}\boldsymbol{N}_{q_\psi} - \frac{\psi_2\vartheta_2}{\kappa_\psi\kappa_\vartheta}\boldsymbol{B}_{q_\psi}\Big).\end{aligned} \tag{20}$$

Proof. Let ψ be a spacelike curve, ϑ be adjoint curve of ψ, ϑ_F its focal curve in M_1^3 and ϑ_i and ψ_i $(i = 1,2,3)$ be respectively curvatures of ϑ and ψ according to q-frame. Let q-normal vector field $\boldsymbol{N}_{q_\psi}$ be timelike. Applying derivative to the equation (18), we get

$$\begin{aligned}\vartheta_F^s = (1 - \vartheta_1\omega_1 - \vartheta_2\omega_2)\boldsymbol{T}_{q_\vartheta} + (\vartheta_3\omega_2 \\ + \omega_1^s)\boldsymbol{N}_{q_\vartheta} + (\omega_2^s + \vartheta_3\omega_1)\boldsymbol{B}_{q_\vartheta}.\end{aligned}$$

Since the focal curve expresses the centers of tangential oscillating spheres, the components of $\boldsymbol{T}_{q_\vartheta}$ and $\boldsymbol{N}_{q_\vartheta}$ vanish when applying the derivative based on the spring parameter to the curve. Hence, it's obtained

$$1 - \vartheta_1\omega_1 - \vartheta_2\omega_2 = 0, \tag{21}$$

$$\omega_1^s + \vartheta_3\omega_2 = 0. \tag{22}$$

From these equations, for $\vartheta_2 \neq 0$, we get

$$\omega_2 = \frac{\omega_1\vartheta_1 - 1}{\vartheta_2},$$

$$\omega_1^s - \frac{\vartheta_1\vartheta_3}{\vartheta_2}\omega_1 = -\frac{\vartheta_3}{\vartheta_2}.$$

By solving the above differential equation, it's found

$$\omega_1 = e^{\int \frac{\vartheta_1\vartheta_3}{\vartheta_2}ds}\Big(-\int e^{-\int \frac{\vartheta_1\vartheta_3}{\vartheta_2}ds}\frac{\vartheta_3}{\vartheta_2}ds + C\Big),$$

$$\omega_2 = \frac{1}{\vartheta_2} - \frac{\vartheta_1}{\vartheta_2}e^{\int \frac{\vartheta_1\vartheta_3}{\vartheta_2}ds}\Big(-\int e^{-\int \frac{\vartheta_1\vartheta_3}{\vartheta_2}ds}\frac{\vartheta_3}{\vartheta_2}ds + C\Big).$$

Also, from (14), we obtain

$$\begin{aligned}\vartheta_F = \vartheta - \omega_1\Big(\frac{\vartheta_2}{\kappa_\vartheta}\boldsymbol{T}_{q_\psi} + \frac{\psi_1\vartheta_1}{\kappa_\psi\kappa_\vartheta}\boldsymbol{N}_{q_\psi} - \frac{\psi_2\vartheta_1}{\kappa_\psi\kappa_\vartheta}\boldsymbol{B}_{q_\psi}\Big) \\ -\omega_2\Big(\frac{\vartheta_1}{\kappa_\vartheta}\boldsymbol{T}_{q_\psi} + \frac{\psi_1\vartheta_2}{\kappa_\psi\kappa_\vartheta}\boldsymbol{N}_{q_\psi} - \frac{\psi_2\vartheta_2}{\kappa_\psi\kappa_\vartheta}\boldsymbol{B}_{q_\psi}\Big).\end{aligned}$$

Hence, the first statement of the theorem is obtained as

$$\begin{aligned}\vartheta_F = \vartheta - e^{\int \frac{\vartheta_1\vartheta_3}{\vartheta_2}ds}\Big(\int e^{-\int \frac{\vartheta_1\vartheta_3}{\vartheta_2}ds}\frac{\vartheta_3}{\vartheta_2}ds - C\Big)\Big(\frac{\vartheta_2}{\kappa_\vartheta}\boldsymbol{T}_{q_\psi} \\ + \frac{\psi_1\vartheta_1}{\kappa_\psi\kappa_\vartheta}\boldsymbol{N}_{q_\psi} - \frac{\psi_2\vartheta_1}{\kappa_\psi\kappa_\vartheta}\boldsymbol{B}_{q_\psi}\Big) + \Big(\frac{1}{\vartheta_2} - \frac{\vartheta_1}{\vartheta_2}e^{\int \frac{\vartheta_1\vartheta_3}{\vartheta_2}ds}\Big(C - \\ \int e^{-\int \frac{\vartheta_1\vartheta_3}{\vartheta_2}ds}\frac{\vartheta_3}{\vartheta_2}ds\Big)\Big)\Big(\frac{\vartheta_1}{\kappa_\vartheta}\boldsymbol{T}_{q_\psi} + \frac{\psi_1\vartheta_2}{\kappa_\psi\kappa_\vartheta}\boldsymbol{N}_{q_\psi} - \frac{\psi_2\vartheta_2}{\kappa_\psi\kappa_\vartheta}\boldsymbol{B}_{q_\psi}\Big).\end{aligned}$$

On the other hand, let the q-binormal vector field $\boldsymbol{B}_{q_\psi}$ be timelike. Similarly, the focal curvatures of ϑ_F are computed as

$$\omega_1 = e^{-\int \frac{\vartheta_1\vartheta_3}{\vartheta_2}ds}\left(\int e^{\int \frac{\vartheta_1\vartheta_3}{\vartheta_2}ds}\frac{\vartheta_3}{\vartheta_2}ds + C\right),$$

$$\omega_2 = \frac{1}{\vartheta_2} - \frac{\vartheta_1}{\vartheta_2}e^{-\int \frac{\vartheta_1\vartheta_3}{\vartheta_2}ds}\left(\int e^{\int \frac{\vartheta_1\vartheta_3}{\vartheta_2}ds}\frac{\vartheta_3}{\vartheta_2}ds + C\right).$$

Therefore, from (15), we obtain the second statement of the theorem.

The following result is a consequence of Theorem 4.

Corollary 5. Let ψ be a spacelike curve, ϑ be adjoint curve of ψ, ϑ_F its focal curve in M_1^3 and ϑ_i and ψ_i $(i = 1,2,3)$ be respectively curvatures of ϑ and ψ according to q-frame. In the case of q-normal vector field $\boldsymbol{N}_{q_\psi}$ is timelike, the focal curvatures of curve ϑ are

$$\omega_1 = e^{\int \frac{\vartheta_1\vartheta_3}{\vartheta_2}ds}\left(-\int e^{-\int \frac{\vartheta_1\vartheta_3}{\vartheta_2}ds}\frac{\vartheta_3}{\vartheta_2}ds + C\right), \tag{23}$$

$$\omega_2 = \frac{1}{\vartheta_2} + \frac{\vartheta_1}{\vartheta_2}e^{\int \frac{\vartheta_1\vartheta_3}{\vartheta_2}ds}\left(\int e^{-\int \frac{\vartheta_1\vartheta_3}{\vartheta_2}ds}\frac{\vartheta_3}{\vartheta_2}ds - C\right), \tag{24}$$

and, in the case of q -binormal vector field $\boldsymbol{B}_{q_\psi}$ is timelike, the focal curvatures of curve ϑ are

$$\omega_1 = e^{-\int \frac{\vartheta_1\vartheta_3}{\vartheta_2}ds}\left(\int e^{\int \frac{\vartheta_1\vartheta_3}{\vartheta_2}ds}\frac{\vartheta_3}{\vartheta_2}ds + C\right), \tag{25}$$

$$\omega_2 = \frac{1}{\vartheta_2} - \frac{\vartheta_1}{\vartheta_2}e^{-\int \frac{\vartheta_1\vartheta_3}{\vartheta_2}ds}\left(\int e^{\int \frac{\vartheta_1\vartheta_3}{\vartheta_2}ds}\frac{\vartheta_3}{\vartheta_2}ds + C\right). \tag{26}$$

As a result of Theorem 4 and Corollary 5, we obtain Corollary 6.

Corollary 6. Let ψ be a spacelike curve, ϑ be adjoint curve of ψ, ϑ_F its focal curve in M_1^3 and ϑ_i and ψ_i $(i = 1,2,3)$ be respectively curvatures of ϑ and ψ according to q-frame. Suppose curvatures of ϑ are constant. In this case, if q-normal vector field is timelike, the focal curve ϑ_F is obtained as

$$\begin{aligned}\vartheta_F = \vartheta &+ \frac{\vartheta_1}{\vartheta_2}e^{\frac{\vartheta_1\vartheta_3}{\vartheta_2}s}C\left(\frac{\vartheta_1}{\kappa_\vartheta}\boldsymbol{T}_{q_\psi} + \frac{\psi_1\vartheta_2}{\kappa_\psi\kappa_\vartheta}\boldsymbol{N}_{q_\psi} - \frac{\psi_2\vartheta_2}{\kappa_\psi\kappa_\vartheta}\boldsymbol{B}_{q_\psi}\right)\\ &+\left(\frac{1}{\vartheta_1} + e^{\frac{\vartheta_1\vartheta_3}{\vartheta_2}s}C\right)\left(\frac{\vartheta_2}{\kappa_\vartheta}\boldsymbol{T}_{q_\psi} + \frac{\psi_1\vartheta_1}{\kappa_\psi\kappa_\vartheta}\boldsymbol{N}_{q_\psi} - \frac{\psi_2\vartheta_1}{\kappa_\psi\kappa_\vartheta}\boldsymbol{B}_{q_\psi}\right).\end{aligned} \tag{27}$$

and, if q-binormal vector field is timelike, the focal curve ϑ_F is obtained as

$$\begin{aligned}\vartheta_F = \vartheta &+ \frac{\vartheta_1}{\vartheta_2}e^{-\frac{\vartheta_1\vartheta_3}{\vartheta_2}s}C\left(\frac{\vartheta_1}{\kappa_\vartheta}\boldsymbol{T}_{q_\psi} + \frac{\psi_1\vartheta_2}{\kappa_\psi\kappa_\vartheta}\boldsymbol{N}_{q_\psi} - \frac{\psi_2\vartheta_2}{\kappa_\psi\kappa_\vartheta}\boldsymbol{B}_{q_\psi}\right)\\ &+\left(\frac{1}{\vartheta_1} + e^{-\frac{\vartheta_1\vartheta_3}{\vartheta_2}s}C\right)\left(\frac{\vartheta_2}{\kappa_\vartheta}\boldsymbol{T}_{q_\psi} + \frac{\psi_1\vartheta_1}{\kappa_\psi\kappa_\vartheta}\boldsymbol{N}_{q_\psi} - \frac{\psi_2\vartheta_1}{\kappa_\psi\kappa_\vartheta}\boldsymbol{B}_{q_\psi}\right).\end{aligned} \tag{28}$$

Example. Let us consider the unit speed spacelike curve $\psi(s) = \left(\frac{1}{\sqrt{2}}sh(s), \frac{s}{\sqrt{2}}, \frac{1}{\sqrt{2}}ch(s)\right)$.

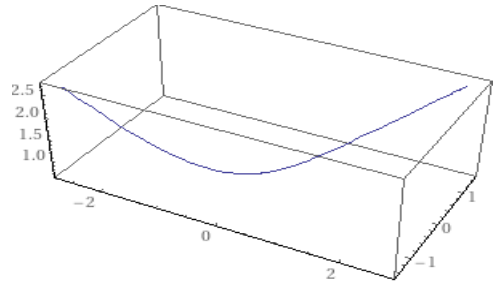

Figure 1 The unit speed spacelike curve ψ

Then, the F-S vectors of ψ are obtained as

$$\boldsymbol{T}_\psi = \frac{\partial\psi}{\partial s} = \left(\frac{1}{\sqrt{2}}ch(s), \frac{1}{\sqrt{2}}, \frac{1}{\sqrt{2}}sh(s)\right),$$

$$\boldsymbol{N}_\psi = \frac{\partial^2\psi/\partial s^2}{\|\partial^2\psi/\partial s^2\|} = (sh(s), 0, ch(s)),$$

$$\boldsymbol{B}_\psi = -\boldsymbol{T}_\psi \times \boldsymbol{N}_\psi = \left(\frac{-1}{\sqrt{2}}ch(s), \frac{-1}{\sqrt{2}}, \frac{-1}{\sqrt{2}}sh(s)\right).$$

Here, it can be easily seen that $\boldsymbol{N}_\psi$ is timelike and $\boldsymbol{B}_\psi$ is spacelike. Let ϑ be the adjoint curve of ψ. From (13), we obtain

$$\vartheta(s) = \int \boldsymbol{B}_\psi ds = \left(\frac{-1}{\sqrt{2}}sh(s), \frac{-s}{\sqrt{2}}, \frac{-1}{\sqrt{2}}ch(s)\right) + c.$$

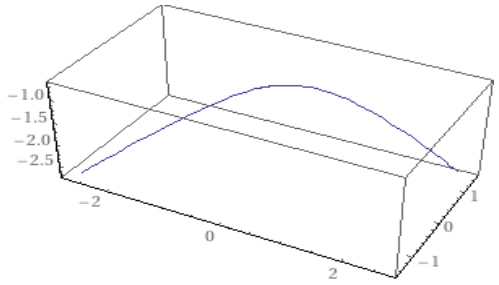

Figure 2 For $c = 0$, the curve ϑ, the adjoint of ψ

Here c is the integration constant. The F-S vectors of ϑ are obtained as

$$\boldsymbol{T}_{\vartheta} = \frac{\partial \vartheta}{\partial s} = \left(\frac{-1}{\sqrt{2}}ch(s), \frac{-1}{\sqrt{2}}, \frac{-1}{\sqrt{2}}sh(s)\right),$$

$$\boldsymbol{N}_{\vartheta} = \frac{\partial^2 \vartheta / \partial s^2}{\|\partial^2 \vartheta / \partial s^2\|} = (-sh(s), 0, -ch(s)),$$

$$\boldsymbol{B}_{\vartheta} = -\boldsymbol{T}_{\vartheta} \times \boldsymbol{N}_{\vartheta} = \left(\frac{-1}{\sqrt{2}}ch(s), \frac{-1}{\sqrt{2}}, \frac{-1}{\sqrt{2}}sh(s)\right).$$

For the spacelike projection vector $\rho = (0,1,0)$, from (4), The q-frame elements and the curvatures of ϑ are obtained as

$$\boldsymbol{T}_{q_{\vartheta}} = \boldsymbol{T}_{\vartheta} = \left(\frac{-1}{\sqrt{2}}ch(s), \frac{-1}{\sqrt{2}}, \frac{-1}{\sqrt{2}}sh(s)\right),$$

$$\boldsymbol{N}_{q_{\vartheta}} = \frac{\boldsymbol{T}_{\vartheta} \times \rho}{\|\boldsymbol{T}_{\vartheta} \times \rho\|} = \left(\frac{1}{\sqrt{2}}sh(s), 0, \frac{1}{\sqrt{2}}ch(s)\right),$$

$$\boldsymbol{B}_{q_{\vartheta}} = -\boldsymbol{T}_{\vartheta} \times \boldsymbol{N}_{q_{\vartheta}} = \left(\frac{1}{2}ch(s), \frac{1}{2}, \frac{1}{2}sh(s)\right),$$

$$\vartheta_1 = < \boldsymbol{T}_{\vartheta}^{s}, \boldsymbol{N}_{q_{\vartheta}} > = \frac{1}{2},$$

$$\vartheta_2 = < \boldsymbol{T}_{\vartheta}^{s}, \boldsymbol{B}_{q_{\vartheta}} > = 0,$$

$$\vartheta_3 = < \boldsymbol{N}_{q_{\vartheta}}^{s}, \boldsymbol{B}_{q_{\vartheta}} > = \frac{1}{2\sqrt{2}}.$$

On the other hand, the q-focal curve of ϑ is given by

$$\vartheta_F = \vartheta + \omega_1 \boldsymbol{N}_{q_{\vartheta}} + \omega_2 \boldsymbol{B}_{q_{\vartheta}}.$$

By using (21) and (22), we get

$$1 - \frac{1}{2}\omega_1 = 0,$$

$$\omega_1^s + \frac{1}{2\sqrt{2}}\omega_2 = 0.$$

Then, we obtain $\omega_1 = 2$, $\omega_2 = 0$. Therefore, for $c=0$, the q-focal curve of ϑ is obtained as

$$\vartheta_F = \vartheta + 2\boldsymbol{N}_{q_{\vartheta}} = \left(\frac{1}{\sqrt{2}}sh(s), -s, \frac{1}{\sqrt{2}}ch(s)\right).$$

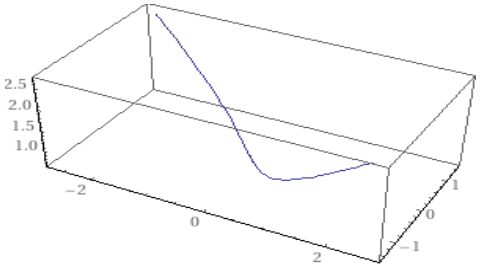

Figure 3 The q-focal curve of the adjoint curve ϑ

4. CONCLUSION

In this study, we aimed to obtain the equations characterizing the focal curve of the adjoint of a spacelike curve under the quasi frame in M_1^3. Here we obtained different equations for the two cases where the q-normal vector field is timelike, and the q-binormal vector field is timelike. Consequently, these equations showed that the q-focal curve of the adjoint curve of a main curve can be obtained depending on the curvatures of the main curve and the adjoint curve. Finally, as an example, we presented the q-focal curve of the adjoint curve of a spacelike curve with a timelike q-normal vector field and gave 3D plots of the main curve, the adjoint curve, and the q-focal curve.

The results we have obtained will help us to give characterizations of such curves and surfaces to be formed with these curves, their behavior and geometric expressions of particle motions that can be expressed by these curves. Therefore, we think that this study will bring a new perspective to the subject of associated, focal, and adjoint curves. In our next study, we are thinking of working on some special surfaces that such curves will create.

The Declaration of Conflict of Interest/ Common Interest

No conflict of interest or common interest has been declared by the authors.

Authors' Contribution

The authors contributed equally to the study.

The Declaration of Ethics Committee Approval

This study does not require ethics committee permission or any special permission.

The Declaration of Research and Publication Ethics

The authors of the paper declare that they comply with the scientific, ethical and quotation rules of SAUJS in all processes of the paper and that they do not make any falsification on the data collected. In addition, they declare that Sakarya University Journal of Science and its editorial board have no responsibility for any ethical violations that may be encountered, and that this study has not been evaluated in any academic publication environment other than Sakarya University Journal of Science.

REFERENCES

[1] J. M. Lee, "Introduction to Smooth Manifolds", Graduate Texts in Math., New York, 2003.

[2] J. H. Choi and Y. H. Kim, "Associated curves of a Frenet curve and their applications", Appl. Math. Comput., vol. 218, no. 18, pp. 9116-9124, 2012.

[3] T. Körpınar, M. T. Sarıaydın, and E. Turhan, "Associated curves according to Bishop frame in Euclidean 3-space", Adv. Model. Optim., vol. 15, no. 3, pp. 713-717, 2013.

[4] N. Macit and M. Düldül, "Some new associated curves of a Frenet curve in E3 and E4", Turkish J. Math., vol. 38, pp. 1023-1037, 2014.

[5] S. Enghardt, J. Bauch, "Application of Focal Curves to the Evaluation of Conic Diffraction Lines", Journal of Applied Mathematics and Physics, vol. 3, pp. 1386-1390, 2015.

[6] S. Yılmaz, "Characterizations of some associated and special curves to type-2 Bishop frame in E^3", Kırklareli University J. Eng. Sci., vol. 1, pp. 66-77, 2015.

[7] R. Uribe-Vargas, "On vertices, focal curvatures and differential geometry of space curves", Bull. Brazilian Math. Soc. vol. 36, no. 3, pp. 285-307, 2005.

[8] S. Desmukh, B. Y. Chen and A. Alghanemi, "Natural mates of Frenet curves in Euclidean 3-space", Turk. J. Math, vol. 42, pp. 2826-2840, 2018.

[9] S. K. Nurkan, I. A. Güven and M. K. Karacan, "Characterizations of adjoint curves in Euclidean 3-space", Proc Natl Acad Sci. India Sect A Phys Sci., vol. 89, pp. 155-161, 2019.

[10] P. Alegre, K. Arslan, A. Carriazo, C. Murathan and G. Öztürk, "Some Special Types of Developable Ruled Surface", Hacettepe Journal of Mathematics and Statistics, vol. 39, no. 3, pp. 319-325, 2010.

[11] T. Körpinar, H. Öztekin, "A Note on Quasi Biharmonic Curves According to Quasi Frame in the Minkowski Space", Journal of Advanced Physics, vol. 7, pp. 1-3, 2018.

[12] M. Dede, C. Ekici, and A. Görgülü, "Directional q-frame Along a Space Curve", IJARCSSE, vol. 5, no. 12, pp. 775-780, 2015.

[13] G. Tarım, "Minkowski Uzayında Yönlü Eğriler Üzerine", Postgraduate Thesis, Eskişehir Osmangazi University, December 2016.

SAKARYA ÜNİVERSİTESİ
FEN BİLİMLERİ ENSTİTÜSÜ DERGİSİ

Sakarya University Journal of Science
SAUJS

ISSN 1301-4048 e-ISSN 2147-835X Period Bimonthly Founded 1997 Publisher Sakarya University
http://www.saujs.sakarya.edu.tr/

Title: The Attitudes of the Telecommunication Customers in the COVID-19 Outbreak: The Effect of the Feature Selection Approach in Churn Analysis

Authors: Handan DONAT, Saliha KARADAYI USTA

Recieved: 2022-02-22 00:00:00

Accepted: 2022-04-27 00:00:00

Article Type: Research Article

Volume: 26
Issue: 3
Month: June
Year: 2022
Pages: 530-544

How to cite
Handan DONAT, Saliha KARADAYI USTA; (2022), The Attitudes of the Telecommunication Customers in the COVID-19 Outbreak: The Effect of the Feature Selection Approach in Churn Analysis. Sakarya University Journal of Science, 26(3), 530-544, DOI: 10.16984/saufenbilder.1077229
Access link
http://www.saujs.sakarya.edu.tr/tr/pub/issue/70993/1077229

Sakarya University Journal of Science 26(3), 530-544, 2022

The Attitudes of the Telecommunication Customers in the COVID-19 Outbreak: The Effect of the Feature Selection Approach in Churn Analysis

Handan DONAT[1], Saliha KARADAYI USTA*[1]

Abstract

Today's rising cutting-edge technology requirements and competitive environment in telecommunication industry has gained a remarkable importance due to the COVID-19 pandemics in terms of high need of information sharing and remote communication necessity. Telecommunication companies conduct significant analyses by highlighting that the customer data is the most valuable information. Besides, they obtain results emphasizing that acquiring new customers is costlier than retaining the existing ones. Therefore, the companies are willing to determine the important customer features in order to understand why they shift to the other telecommunication service providers. Hence, this study aims to conduct a churn analysis by feature selection approach with large volumes of telecommunication customer data in order to present what kind of customer behaviors and qualifications exist. Since there is a huge amount of data in this field, data mining is a vital requirement. The performance outputs were observed, and the features carrying these outputs to the highest value were identified. The data collection and analysis were carried out in mid-2019, and the same data collection and analysis were carried out again at the beginning of 2021, and these before and after results were compared. In addition, a comparison was made with the results obtained by the other churn analysis studies. This paper contributes to the practitioners by presenting the most important customer features in telecom customer churn, and a new approach in performance evaluation have been proposed specific to the telecommunication market with the industry experts' guidance as a theoretical contribution.

Keywords: Telecommunication, customer churn, churn analysis, data mining, machine learning

1. INTRODUCTION

Communication is a need for human beings, and it has gained different dimensions with the development of technology day by day [1-3]. Especially with the COVID-19 pandemics, remote access and online communication have been the only option to conduct business, and sharing the same environment was forbidden occasionally. Therefore, digitalization has quickly entered to the individuals' lives, and especially for the companies,

* Corresponding author: salihakaradayiusta@gmail.com
[1] İstinye University, Industrial Engineering Department,
E-mail: handanakterazi@gmail.com
ORCID: https://orcid.org/0000-0002-8348-4033, https://orcid.org/ 0000-0002-8006-0606

it has been inevitable to adapt to the digital environment.

The sector reports of the post-COVID-19 telecom supply chains have announced that the telecom industry has come to the fore with the digital technologies as the most used management tool of goods and services with a rate of 61%. Compared to other sectors, it has been effective in determining the impacts of the pandemics, and according to the customer surveys, 67% of the customers have stated that the telecom sector showed high performance during the pandemics [4]. In order to eliminate the negative effects of the COVID-19 pandemics on the telecom industry, companies have focused in workforce, operations and supply chain, communication strategies, customer data and revenue management [5]. Customer data has been significant as it is of vital importance for the telecom industry [6]. Since the customer information modeling creates an important competitive advantage [7, 8], the new researches discussed the impact of the pandemics in order to observe the changing customers' behaviors in detail.

The level of competition has increased with the technical progress and increasing number of operators in the telecommunications sector. The main strategies that the companies employ to generate more revenue are: acquiring new customers, retaining existing customers, and increasing the time duration and the loyalty of the customers by keeping them in the existing company. The third strategy has been found to be the most profitable strategy. For these reasons, companies should reduce the customer movement from one service provider to another which stands for the "customer churn" [9].

Customer churn is addressed in many industries such as telecommunication [10-13], peer-to-peer lending market [14], retail industry [15, 16], and banking [17, 18]. As it is obvious, the telecom industry mostly conducts churn analysis in order to keep the customers in the existing company by analyzing the customer specifications and behaviors.

The telecom churn analysis techniques are decision trees [19-21], logistics regression [22, 23], Bayesian networks [24], artificial neural networks [25-28], support vector machine [29, 30], K-means clustering [31, 32], machine learning [10, 12, 13, 18]. Here, the literature review points out to the artificial intelligence algorithms that are needed in processing the big data. Moreover, the telecommunication industry provides services like local and long distance calls, voice, fax, e-mail and other data traffic services. Due to globalization and market conditions, customer relationship management is becoming more and more important. Hence, due to the big amount of customer data, data mining is a requirement to understand business needs, to define the telecommunication model, to use resources efficiently and to increase service quality [33].

The purpose of this paper is implementing a churn analysis by feature selection approach with large amount of customer data in order to illustrate changing direction of customer behaviors. Owing to the existing big data, the machine learning techniques were applied. The performance outputs were recorded, and the customer features bringing these outputs to the highest value were determined. The data collection and analysis were carried out separately in both mid-2019 and at the beginning of 2021, and these two before and after COVID-19 results were compared. Additionally, a comparison was made with the results obtained by the other churn analysis studies as a discussion. Following sections include the methodology part with literature review, classification algorithms, feature selection, performance measurements, application, findings, discussion and conclusion parts.

2. METHODOLOGY

2.1. Literature Review

Data and techniques used in the telecom customer churn analysis vary in the literature. In case of analyzing the payment information, the monthly invoice amount [20, 34, 35] has been the mostly focused factor, while there were a few studies analyzing the billing trend [24]. In addition, call frequency [34], additional service payment information [20], and SMS cost [34] were also taken into consideration. On the other hand, the studies analyzing usage information has been focused on the use of minute [30, 35, 36], usage time intervals [37], usage frequency [38], SMS usage [36], evening and night usage frequency, vocal message

usage, the amount paid for services that require a monthly subscription, internet usage, the amount paid for the internet [38], and the time spent on the internet for international calls [36].

Metrics applied in the studies looking at the line information have been subscription age of the customer [38], payment type (with / without contract) [20, 39], line shifting information, deactivation date, activation date, line opening date, line closing date [37], whether it is 3G or 4G [35], the package used [24].

In the demographic analysis, age and gender [21, 40, 41], income [34], child info and customer profession [21], place of residence (rural / city) [42], education level [39], marital status [40] have been investigated.

In the analysis of customer internal information; billing institution, invoice complaints, weekly number of calls (call center), national and international invoicing [34], customer contact information with the operator [37], customer general complaint information [40] have been addressed. Additionally, customer present value data, customer potential value data, trust, perception, satisfaction, expectation [21], and the device used [30, 39] have been also examined.

2.2. Brief Information about Classification Algorithms

2.2.1. Naive Bayes Classification

In case of deciding whether a given x (x = [x (1), x (2), …, x (L)]$^T \in R^L$) belongs to class S_i or not, and if the independence proposition of Bayes decision theorem is used, then this type of classification is called NB classification. According to the NB decision theory, x belongs to S_i if $P(S_i)\prod_{k=1}^{L} P(x_k|S_i) > P(S_j)\prod_{k=1}^{L} P(x_k|S_j)$ where $P(S_i)$ and $P(S_j)$ are prior possibilities of classes i and j. Thus, the values can be easily calculated from the data set [43]. NB classification conducts good analysis in terms of both accuracy and computation time as a simple and quick statistical prediction algorithm. The NB classifier may be trained to categorize patterns with thousands of attributes and then used to classify thousands of patterns. As a result, NB is the algorithm of choice for data mining and other large classification challenges [44]. The existence (or lack) of a given property of a class (client mix) is assumed to be unrelated to the presence (or absence) of any other property by an NB classifier. The NB classifier outperformed other widely used algorithms in the prediction challenge for the wireless telecommunications industry, and it also increased prediction rates [45].

2.2.2. Logistics Regression

For discriminative probabilistic classification, logistic regression is a frequently used statistical modeling technique [46]. When the dependent variable is binary, this is the predictive regression strategy to use. It's used to describe data and explain the link between one dependent binary variable and one or more independent nominal, ordinal, interval, or ratio-level variables [47]. It estimates the probability of a particular event that occurs, and the probability calculation as $prob\,(y=1) = \frac{e^{\beta_0+\sum_{k=1}^{k}\beta_k x_k}}{1-e^{\beta_0+\sum_{k=1}^{k}\beta_k x_k}}$. Here y is the dependent variable that indicates whether the event occurred or not (when the event happens y = 1, otherwise y = 0). $x_1, x_2, \ldots, x_k$ are independent inputs. $\beta_0, \beta_1, \ldots, \beta_k$ are the regression coefficients that can be computed using the maximum likelihood technique using the training data [48].

2.2.3. Support Vector Machines

Support Vector Machines (SVM) is a highly preferred algorithm for machine learning by producing significant accuracy with less computation power for the classification duties. The SVM algorithm uses a linear combination of subsets (support vectors) of a training set to discover a hyperplane in an N-dimensional space (N is the number of features) [49]. If input vectors can be non-linearly separated, the support vector machines first map data into a high-resolution (possibly infinite) size feature area that uses a kernel number, and next classify the data by maximum margin. Equation used is $f(\vec{x}) = sgn(\sum_i^M y_i x_i \emptyset(\vec{x}_i, \vec{x}) + \delta)$. While the number of samples in the set of training is M, $\vec{x}_i$ is the vector with support $\vec{x}_i > 0$, ϕ is the kernel function, $\vec{x}_i$ is a sample feature vector that is unknown, and δ is threshold. Parameters $\vec{x}_i$ can be obtained by applying linear constraints to a

convex quadratic programming problem. Kernel functions are frequently used in practice with the polynomial kernel and Gaussian radial elementary functions. Consider the Karush - Kuhn - Tucker case for further information, and selecting any i with $\vec{x}_i > 0$ (supports vectors). In practice, it is, however, safer to use the average value of all support vectors [48].

2.2.4. Artificial Neural Networks

Artificial Neural Networks (ANN) are one of the information processing technology's artificial intelligence applications. It imitates the structure of the human brain and analyzes the existing data and generates new information from the data [50]. The advantages of ANN are being non-linear, ability to design with input and output mappings, possibility of adapt, being tolerant to fault [51]. The input, hidden, and output layers of a feed forward neural network are usually present. A sigmoid function is used to activate artificial neural networks. If an ANN has a hidden layer, the network outputs receive the hidden unit's activation functions by transforming it into a second layer of process components as an $output_{net}(j) = f\left(\sum_{l=1}^{L} w_{jl} f(\sum_{i}^{D} w_{li} x_i)\right), j_1, \dots \dots J.$ f is an activation function, while *D*, *l*, and *j* are the total number of units in the input, hidden, and output layers, respectively. To train ANNs, back propagation or fast back propagation learning techniques are used. [48].

2.3. Feature Selection

While establishing the customer churn model, it is checked how much the variables affect the algorithm on each customer base in order to create the best model. After running the algorithm, one should select the variables that have a greater impact and that provide higher accuracy results. In this study, the variables that affect the algorithm most with the information gain, gain ratio, Gini coefficient and correlation were sorted and the algorithms were run one by one in an order. Moreover, there is a clear advantage of feature selection by reducing the data size and the computational burden, being an easier analysis for the data with smaller data size, by decreasing data complexity, and by increasing class / numerical performance [52, 53]. In the following part, the feature selection metrics will be explained in brief.

2.3.1. Information Gain

Information gain is a method based on entropy having values between 0 and 1 by showing the disorder or uncertainty of the system. If the entropy value approaches 1, it indicates that the system is more regular and specific. Entropy value is calculated by $E = -\sum_{i=1}^{n} \left(log_2 \frac{ns(i)}{N}\right) * \frac{\mathrm{ns}(i)}{N}$ formula where E is entropy, N is the total sample size, n is number of classes, and *ns (i)* is the sample for the i^{th} class [54].

2.3.2. Gain Ratio

At each node of the decision tree, the gain ratio metric is used to select the test feature. This is a variation of information gain that lowers bias by considering the number and size of branches when selecting a feature and adjusting the information gain with the intrinsic information of a split [55]. It favours characteristics with a high number of possible values. C4.5 created the fundamental decision tree induction technique ID3, which employs a known extension of information gain to address this bias [56]. The gain ratio formula is based on the “gain = new ratio – old ratio” equation [57].

2.3.3. Gini Index

The Gini index is a strategy for separating pollution that works with binary, continuous numerical values. Breiman first introduced it in 1984 [58] and it is widely used in algorithms. As in the information gain and gain ratio, gain is calculated for each individual variables for ranking The Gini index is a scale that ranges from 0 to 1, with 0 denoting that all elements belong to one class or that there is only one class, and 1 denoting that the elements are randomly distributed across all classes. A Gini value of 0.5 indicates that items in some classes are evenly distributed. $Gini = 1 - \sum_{i=1}^{n} (p_i)^2$ is the Gini index formula where p_i is the likelihood of an object being categorized into a specific class. When constructing the decision tree, the root node should be the feature with the lowest Gini index. [59].

2.3.4. Correlation

The state of a linear relationship between two random variables is depicted by correlation in statistics. The correlation coefficient is used to determine whether or not there is a linear relationship and, if so, how strong it is. It ranges from -1 to +1 [60]. 1 indicates that for every positive increase in one variable, a fixed proportion increases in the other, whereas -1 indicates that for every positive increase in one variable, a fixed proportion decreases in the other. There is no positive or negative rise for every increase of zero. There is no connection between the two. Furthermore, the correlation coefficient's absolute value indicates the strength of the association. The stronger the association, the higher the number. $r = \frac{n(\sum xy) - (\sum x)(\sum y)}{\sqrt{[n(\sum x^2) - (\sum x)^2][n(\sum y^2) - (\sum y)^2]}}$ is the correlation formula [61].

2.4. Performance Measurements

Following the classification, success is evaluated according to the complexity matrix stated in Table 1.

Here, TP stands for true positive number, correctly defined positive samples, FP stands for false positives (incorrectly recognized negative samples), FN for false negatives (incorrectly identified positive samples), and TN for true negatives (incorrectly identified positive samples), correctly identified negative samples [62].

Table 1
Class Confusion Matrix

		Predicted		Total
		Churn Customer	*Non Churn Customer*	
Actual	*Churn Customer*	TP - True Positive	FN - False Negative	Actual Positive Number
	Non Churn Customer	FP - False Positive	TN - True Negative	Actual Negative Number
Total		Predicted Positive Number	Predicted Negative Number	Total Customer Number

There are many defined performance measurement metrics in the literature. Specificity is the ratio of correctly defined mixed negatives and defined as Specificity = (TN) / (TN+FP). Accuracy measures the overall sampling rate of the number of correctly predicted samples that are either positive or negative by the Accuracy = (TP + TN) / (TP + FP + FN + TN) formula. Sensitivity is the ratio of correctly defined mixed positives. It is also called the true positive rate and defined as Sensitivity = TP / (TP + FN). Precision is defined as the ratio of accurately recognized failures to all positive predictions, and it equals to Precision = TP / (TP + FP). Error Rate is the measure of 1 – Accuracy. Moreover, the widely used measure that integrates the balance between precision and sensitivity is the F measure by F Measure = 2* Sensitivity * Precision / (Sensitivity + Precision) [62, 63].

This paper develops a novel approach in performance evaluation specific to the telecommunication industry customers. The details will be stated in the modeling part.

3. APPLICATION

In the telecom industry, customer churn is very critical for the operators. For companies in the telecom industry, churn rates of prepaid customers are higher than the churn rates of postpaid customers. The reason for this is the density of periodic users mainly in prepaid customers. Therefore, the tendency of prepaid line users to leave the current company, which is critical and problematic for companies in the telecom sector, is analyzed.

Within the scope of this analysis, it is aimed that the algorithms frequently used in the literature will result in the shortest time and with the most accurate performance criteria, and the methods detailed in the previous sections are tried for this. The variables to be included in the modeling were tested for each performance criterion according to different feature selection methods and the highest output rate was determined. Modeling was done using the Rapid Miner software. It is used for statistical modeling, data preprocessing, business analysis, optimization and predictive analysis [64]. Rapid Miner data processing stages are defining the problem, designing the data requirement, data pre-processing, analytical processing on data and visualization of the data [65].

3.1. Data Definition

The study was conducted using a sample of data telecom company in Turkey. Company name is not shared due to confidentiality. "Ethics Committee Approval document no 12.10.2020-2020/17" was issued for the research. In accordance with the law on protection of personal data, the analysis was carried out on the computers of the company in the working environment of the relevant company, only the results were recorded and no customer data was recorded. The data set to be studied includes 16152 records. 1152 of 16152 customer data are customer data allocated. The customer churn rate has been 7% in mid-2019. There are a total of 27 variables in this data set. The variables used, types of variables and their explanations are shown in Table 2.

Table 2
Variables Used in This Study

	Variables	**Data type**
1	Subscription duration	Numeric
2	Last 6 months balance (rest of pay amount)	Numeric
3	Last 6 months average internet usage	Numeric
4	Customer age	Numeric
5	Days after last device change	Numeric
6	Number of complaints in the last 1 month	Numeric
7	Profit for the last 1 month	Numeric
8	Device group	Text
9	Billing province	Text
10	Internet usage for the last 1 month	Numeric
11	Young segment	Numeric
12	Total number of payments in the last 6 months	Numeric
13	Last 1 month cost	Numeric
14	The average number of calls outside, except abroad, for the last 6 months	Numeric
15	Average usage per person for the last 6 months, in terms of TL	Numeric
16	Average dial-out minutes in the last 6 months	Numeric
17	The average number of incoming calls except abroad for the last 6 months	Numeric
18	Average number of base station cell changes in the last 3 months	Numeric
19	Days since last pay	Numeric
20	Average incoming call minutes in the last 6 months	Numeric
21	Incoming voice call minutes, except abroad, on average in the last 6 months	Numeric
22	Customer gender	Text
23	Total number of lines	Numeric
24	Excess of package	Numeric
25	Excess of package, in terms of TL	Numeric
26	Mobil TV usage	Numeric

The 27th variable indicates whether the customer has left or not, and this variable takes the value 1 if the customer is gone and 0 if the customer is not. Since the text values in the data do not work in support vector machines and artificial neural networks algorithms, they have been made numerical.

3.2. Modeling

Four algorithms selected in modeling were studied; Logistic Regression, Artificial Neural Networks, Simple Bayes Classifier and Support Vector Machines. In these algorithms, 80% -20% training test data were used. In the data set, feature selection was weighted according to information gain, gain ratio, Gini index and correlation, and the resulting results were added in order of variables and algorithms were run.

The aim here is to reduce the noise in the data set. In other words, the purpose here is to determine "what is ineffective" in reaching the most accurate result without including variables having little or no effect. The previously performance criteria were compared, and the results were evaluated. In addition to these performance criteria, which are frequently used in the literature, new performance criteria have been added to measure customer churn in the telecom sector.

The reason for developing a new performance criterion is to ensure that high rate of predicting the customers churn, and ensure that the rate of correctly predicting the customers staying and leaving the company in the total model. Most of the studies are based only on the high rate of accuracy, i.e. customer churn rate. Besides, the sensitivity is not enough for the estimation, the rate of "keeping customers in the existing company" should be predicted well too. By doing so, the customer loss can be understood well and the company can offer them focused campaigns. In most of the studies, sensitivity and accuracy rate can be inversely proportional [66]. This study adopts "Accuracy * Sensitivity = the closest value to 1" measure since the closest and highest values of accuracy and precision ratio will give the best result.

4. FINDINGS

The outputs of the algorithms have been analyzed according to their performance outputs. First, 26 variables are listed according to information gain, gain ratio, Gini index and correlation. Accordingly, when the algorithms are run, the results are very close according to the first 6 variables. Differentiation starts after 6 variables. In Table 3, the results of the selected classification methods are given together with the number of variables that achieve the highest accuracy and sensitivity rates.

According to the interpretation of the Table 3, the results analysis runs with fewer variables have provided higher results. This also has enabled the model to run in a shorter time. Especially since large amount of data is used in the telecom sector, the data density determines the working performance and duration of the model. Fewer variables remove the noise of the model

According to the results in the Table 3, although very close values were reached in other algorithms, the highest accuracy and precision multiplication ratio has been obtained in the Artificial Neural Networks algorithm with the 7th variable as "profit for the last 1 month" set in the feature selection. This is an important result of the churn analysis. When the company's profit is high from that customer, then the churn is inevitable. People noticing that there are many packages with lower cost in other service providers, are tend to change the operator immediately. Also the 9th variable "billing province" has been attracted the attention by addressing that the people locating at the same province affects each other in the operator changing decision. In addition, as a result of the analysis, the 11st "young segment" variable says that young people are more in tendency to change the telecom server, the 17th "the average number of incoming calls, except abroad, for the last 6 months" variable emphasizes that the people having frequent phone calls shift to another operator more, and the 22nd variable "customer gender" is the another factor affecting the mobile service provider leaving decision.

Table 3
Highest Performance Outputs

	Logistics Regression	Support Vector Machines	Naive Bayes	Artificial Neural Networks
Information Gain	12nd, 13rd variables Accuracy:%98,30 Sensitivity: %78,24 Multiplication: 0,769	18 th variable Accuracy: %98,30 Sensitivity: %77,82 Multiplication: 0,778	13. variable Accuracy: %82,54 Sensitivity: %85,36 Multiplication: 0,705	7 th, 9th, 11st, 17th, 22nd variables Accuracy: %98,67 Sensitivity: %84,94 Multiplication: **0,849**
Gain Ratio	6th, 7 th variables Accuracy: %98,27 Sensitivity: %77,41 Multiplication: 0,774	6 th, 22nd, 23rd, 24th, 25th, 26th variables Accuracy: %98,27 Sensitivity: %77,41 Multiplication: 0,760	7 th variable Accuracy: %87,93 Sensitivity: %84,52 Multiplication: 0,743	7 th variable Accuracy: %98,67 Sensitivity: %84,94 Multiplication: **0,849**
Correlation	7 th variable Accuracy: %98,30 Sensitivity: %84,94 Multiplication: **0,835**	12 nd variable Accuracy: %98,33 Sensitivity: %78,24 Multiplication: 0,782	25th variable Accuracy: %81,64 Sensitivity: %84,52 Multiplication: 0,690	7 th , 9th variables Accuracy: %98,67 Sensitivity: %84,94 Multiplication: **0,849**
Gini Index	7 th variable Accuracy: %98,27 Sensitivity: %77,41 Multiplication: 0,774	23rd, 24th, 25th, 26th variables Accuracy: %98,27 Sensitivity: %77,41 Multiplication: 0,760	6 th variable Accuracy: %91,33 Sensitivity: %85,36 Multiplication: 0,779	7 th variable Accuracy: %98,67 Sensitivity: %84,94 Multiplication: **0,849**

Furthermore, the gain ratio and Gini index have produced same results in general. Naive Bayes has been the one giving lowest results. Correlation is the feature giving the highest performance measures in all classification algorithms.

The same analysis has conducted with the updated data in 2021, and the same results have been observed again. Therefore, it is clear that COVID-19 pandemics has not changed the churn behavior of the customers.

5. DISCUSSION

5.1. What happened after the COVID-19 pandemics?

During the COVID-19 period, while many countries around the world experienced serious problems in telecom services, companies with strong digital infrastructure successfully overcame this process and increased the number of customers significantly. It was determined that video calls increased by 50 percent, group video calls by 650 percent, and the use of other digital services increased by 50-60 percent [67]. Network occupancy rates have increased significantly, with mobile traffic increasing by 10 percent and constant 60 percent [68].

The effects of the pandemics on the telecom industry in the short and medium term required adaptation to changing customer habits. With the effect of COVID-19, people spent more time at their homes, increased the frequency of video conversations with their loved ones, and continued their education from home by working from home. These new habits have made the telecom industry one of the most important intermediaries connecting people to each other and the world during the struggle against the pandemics. In the short and medium term, COVID-19 has had both good and bad impacts on the industry in terms of changes in customer demands, supply chain and production-based activities, and operational responsibilities [69].

Despite the positive effects of customer behavior on the telecom industry, the operators experienced delays and decreases in "gaining new customers" due to the fact that customers are in a period of avoiding changes. However, there has been a decrease in the interest of customers, whose most basic needs are to stay connected and in communication, in other telecom products [69].

It has been observed that the most important customer data identified in this study that should be taken into account did not change with the COVID-19 outbreak. The analysis has been done in mid-2019 and has been repeated with the updated data in 2021, and almost the same results as in Table 3 have been observed again. The analysis highlights that only the usage amount has been changed, the customer behavior has remained same.

5.2. Comparison with other telecommunication sector customer churn analysis researches

Özdemir et al. [70] uses machine learning classification algorithms (k-Nearest Neighbors, ANN, NB and Random Forests Algorithm) in Python for the churn analysis in a telecom company, and achieves the maximum accuracy rate with ANN. Although the paper applies similar customer data, it does not underline the most important feature in classification. Pamina et al. [71] conducts a similar study in telecom for churn analysis by using the performance measures as accuracy, recall, precision, F-score, etc. with the aim of producing the highest recall value, and resulted in that the Decision Tree model outperforming all other models. Hooda and Mittal [72] present an exposition of data mining techniques for customer churn in telecom sector, and defines possible factors for churn as price, width of service area, service quality, prepaid packages, curiosity and advertisement. They applied Genetic Programming and Fast Fuzzy C-Means in order to find the expected maximum profit measure for the customer churn. Sharm et al. [73] uses logistic regression and SVM with accuracy, sensitivity, specificity and precision performance metrics. No clear factor is available in the study. Eria and Marikannan [74] apply Random Forest and Logistic Regression, identifies that demographics and customer lifestyles are the most important factors. Gaur and Dubey [75] use Logistic Regression, SVM, Random Forest and Gradient boosted tree algorithms, and emphasizes that Gradient boosting is best in among four models. Al-Shboul et al. [76] plans the churn prediction structure by predicting customers who are likely to churn with

2 heuristic approaches as Fast Fuzzy C-Means and Genetic Programming. Brandusoiu and Toderean [77] urge a complicated technique for predicting the churn in the mobile telecommunications sector by using SVM. Gain measure is in comparisons as performance measurement metric. As a result, the findings of this paper comply with the other researches.

The genuine value of this work hinges upon *(i)* creating a comprehensive feature selection framework as a list based on real customer data from telecommunication industry, *(ii)* providing a comparative study by evaluating the findings of before and after pandemics customer attitudes, *(iii)* presenting applications of different artificial intelligent techniques in telecommunication and indicating these techniques' influence on the findings, *(iv)* specifying the similarities and differences of the findings of this study in comparison with the other existing researches.

While the existing literature presents partial telecommunication customer data (see literature review section), this study takes the advantage of having real telecommunication customer data in order to select the features of the customers. This paper examines the literature in detail, and points out that there are studies focusing on some specific features of the customer. However, this paper utilizes a real telecommunication company's in-use customer feature framework to state the real business management insights of the sector.

6. CONCLUSION

Competition is the main problem facing almost all telecommunications industries around the world. Customer churn in telecommunications is defined as the dissatisfaction of the customers who are leaving the company, or the customer shifting to the other companies that offering reasonable prices. This causes a potential loss of revenue / profit to the companies. Moreover, retaining customers has become a difficult task in the industry. Hence, the companies continue to develop new technologies and applications so that they can provide the best services to their customers. It is necessary to identify customers who are likely to leave the company in the near future, because losing them will result in significant profit loss for the company.

Time management is paramount of importance for the telecommunication companies. In the period of aggressive competition, companies are required to create a quick response according to changing needs. Besides, running big data analysis is both tiring and time consuming for the existing system. In this study, a research was carried out to transform big data into effective data. In other words, the result with big data actually gives the same result when it is done with the specific variables that affect the model. One can reach the same results when they first found the main variables affecting the model and compared the results with both the input variables and the effective variables. As a result, we obtained fewer and more effective variables and proceeded with those variables in future studies. Since it is not working with large data, a great saving was achieved in terms of time.

In this study, the machine learning classification techniques in customer churn analysis have been applied to thousands of customer data, an approach as a new performance criteria have been developed specific to the telecommunication market in order to evaluate the performances of the algorithms, and the most important customer features have been selected in both mid-2019 before the pandemics, and in 2021. Accordingly, the profit amount per customer is the most important criteria in customers' decision of leaving the existing mobile service provider. Secondly, the people in the same location affect each other towards shifting an another operator. Next, young people are more in tendency to change the telecom server. Also the people having frequent phone calls shift to another operator more, while the customer gender is the another factor affecting the mobile service provider leaving decision. Additionally, ANN is the algorithm giving the best results with correlation in feature selection.

Although the rising importance of the telecommunication sector, the customer behaviors have been not altered during the COVID-19 pandemics. The mid-2019 analysis

results, and the newly conducted 2021 results are nearly the same. Only the usage amounts in phone calls, internet and the other services have been increased. The customer churn results have remained the same. Besides, the other current telecom customer churn results support the findings of this paper. Furthermore, as is it seen in the discussion part, the existing researches only groups the customers in terms of some variables. However, they do not clearly illustrate what are these features shaping the customer churn. Hence, this paper contributes to the practitioners by presenting the most important factors. In addition, a new approach in performance evaluation have been proposed specific to the telecommunication market with the industry experts' guidance as a theoretical contribution.

The study is limited only in terms of reflecting a telecom company in one country and representing just one company. However, due to the having a huge amount of data, the sample size is big enough to demonstrate the population's general situation. The paper presents a real-life application, and emphasizes which customer features and which performance metrics should be focused on. Future studies may use different data mining methods with changing data and achieve different results with changing customer profile.

Funding

The authors have no received any financial support for the research, authorship or publication of this study.

The Declaration of Conflict of Interest/ Common Interest

No conflict of interest or common interest has been declared by the authors.

Authors' Contribution

The authors contributed equally to the study.

The Declaration of Ethics Committee Approval

Ethics Committee Approval document no 12.10.2020-2020/17 is taken for the study.

The Declaration of Research and Publication Ethics

The authors of the paper declare that they comply with the scientific, ethical and quotation rules of SAUJS in all processes of the paper and that they do not make any falsification on the data collected. In addition, they declare that Sakarya University Journal of Science and its editorial board have no responsibility for any ethical violations that may be encountered, and that this study has not been evaluated in any academic publication environment other than Sakarya University Journal of Science.

REFERENCES

[1] P.J. Nesse, S.W. Svaet, D. Strasunskas, and A.A. Gaivoronski, "Assessment and optimisation of business opportunities for telecom operators in the cloud value network", Transactions on emerging telecommunications technologies, vol.24, no.5, pp. 503-516, 2013.

[2] T.-H. Chou, J.-L. Seng, "Telecommunication e-services orchestration enabling business process management", Transactions on emerging telecommunications technologies, vol.23, no.7, pp. 646-659, 2012.

[3] Y. Atlı, N. Yücel, "Hibrit iletişim teknolojileri", Süleyman Demirel Üniversitesi İktisadi ve İdari Bilimler Fakültesi Dergisi, vol.21, no.3, pp. 785-797, 2016.

[4] Deloitte. "Covid-19 sonrası tedarik zincirlerinde kazananlar ve kaybedenler." https://www2.deloitte.com/tr/tr/pages/consumer-business/articles/Covid-19-sonrasi-tedarik-zinciri.html 2021.

[5] PwC. "COVID-19 salgınının telekom sektörü üzerinde olası etkileri".

https://www.pwc.com.tr/covid-19-telekom-sektoru 2020.

[6] S. Tabassum, M.A. Azad, and J. Gama, "Profiling high leverage points for detecting anomalous users in telecom data networks", Annals of Telecommunications, vol.75, no.9-10, pp. 573-581, 2020.

[7] U. T. Şimşek Gürsoy, "Customer churn analysis in telecommunication sector". Istanbul University Journal of the School of Business Administration, vol.39, no.1, pp.35–49, 2010.

[8] García, D. L., Nebot, À., & Vellido, A. Intelligent data analysis approaches to churn as a business problem: a survey. Knowledge and Information Systems, 2017, 51(3), 719–774.

[9] A. K. Ahmad, A. Jafar, & K. Aljoumaa, "Customer churn prediction in telecom using machine learning in big data platform". Journal of Big Data, pp. 6-28, 2019.

[10] M. Al-Mashraie, S.H. Chung, H.W. Jeon, "Customer switching behavior analysis in the telecommunication industry via push-pull-mooring framework: A machine learning approach", Computers and Industrial Engineering, vol.144, 106476, 2020.

[11] N. Alboukaey, A. Joukhadar, N. Ghneim, "Dynamic behavior based churn prediction in mobile telecom", Expert Systems with Applications, 162, 2020.

[12] M. Ahmed, H. Afzal, I. Siddiqi, M.F. Amjad, K. Khurshid, "Exploring nested ensemble learners using overproduction and choose approach for churn prediction in telecom industry", Neural Computing and Applications, vol. 32, no.8, pp. 3237-3251, 2020.

[13] M. Hemalatha, S. Mahalakshmi, "Customer churns prediction in telecom using adaptive logitboost learning approach", International Journal of Scientific and Technology Research, vol.9 no. 2, pp. 5703-5713, 2020.

[14] D. Kim, "Investor churn analysis in a P2P lending market", Applied Economics, vol. 52 no. 52, pp. 5745-5755, 2020.

[15] J. Kaur, V. Arora, S. Bali, "Influence of technological advances and change in marketing strategies using analytics in retail industry", International Journal of Systems Assurance Engineering and Management, vol.11 no. 5, pp. 953-961, 2020.

[16] M.A. De la Llave Montiel, F. López, "Spatial models for online retail churn: Evidence from an online grocery delivery service in Madrid", Papers in Regional Science, vol. 99 no.6, pp. 1643-1665, 2020.

[17] W. Jiang, Y. Luo, Y. Cao, G. Sun, C. Gong, "On the build and application of bank customer churn warning model", International Journal of Computational Science and Engineering, vol.22 no.4, pp. 404-419, 2020.

[18] P. Verma, "Churn prediction for savings bank customers: A machine learning approach", Journal of Statistics Applications and Probability, vol.9 no.3, pp. 535-547, 2020.

[19] S. Höppner, E. Stripling, B. Baesens, S.V. Broucke, T. Verdonck, "Profit driven decision trees for churn prediction", European Journal of Operational Research, vol.284 no.3, pp. 920-933, 2020.

[20] H. Li, D. Wu, G. X. Li, Y. H. Ke, W. J. Liu, Y. H. Zheng, & X. Lin, "Enhancing telco service quality with big data enabled churn analysis: infrastructure, model, and deployment". Journal of Computer Science and Technology, vol.30 no.6, pp.1201–1214, 2015.

[21] W. Hengliang, & W. Zhang, "A customer churn analysis model in e-business environment". International Journal of Digital Content Technology and Its

Applications, vol. 6 no.9, pp.296–302, 2012.

[22] K. Dahiya, "Customer Churn Analysis in Telecom Industry". 4th International Conference on Reliability, Infocom Technologies and Optimization, pp.1–6, 2015.

[23] M. Günay, "Makine öğrenmesi yöntemleri ile kayıp müşteri analizi", 26th Signal Processing and Communications Applications Conference, pp.1–4, 2018.

[24] P. Kisioglu, & Y. I. Topcu, "Applying Bayesian belief network approach to customer churn analysis : A case study on the telecom industry of Turkey". Expert Systems with Applications, vol.38, pp.7151–7157, 2010.

[25] A. Chouiekh, E.H.I. El Haj, "Deep convolutional neural networks for customer churn prediction analysis", International Journal of Cognitive Informatics and Natural Intelligence, vol.14 no.1, pp. 1-16, 2020.

[26] T. Mandhula, S. Pabboju, N. Gugulotu, "Predicting the customer's opinion on amazon products using selective memory architecture-based convolutional neural network", Journal of Supercomputing, vol.76 no.8, pp. 5923-5947, 2020.

[27] A. De Caigny, K. Coussement, K.W. De Bock, S. Lessmann, "Incorporating textual information in customer churn prediction models based on a convolutional neural network", International Journal of Forecasting, vol.36 no.4, pp. 1563-1578, 2020.

[28] F. Napitu, "Twitter opinion mining predicts broadband internet's customer churn rate". IEEE International Conference on Cybernetics and Computational Intelligence, pp.141–146, 2010.

[29] I. Amali, R. Arunkumar, "Particle swarm optimization with kernel support vector machine for churn prediction in telecommunication industry", International Journal of Scientific and Technology Research, vol.9 no.4, pp. 253-257, 2020.

[30] R. Dong, F. Su, S. Yang, & X. Cheng, "Customer Churn Analysis for Telecom Operators Based on SVM". In: Sun S., Chen N., Tian T. (eds) Signal and Information Processing, Networking and Computer, vol.473, pp.327-333. Springer, Singapore. 2018.

[31] N.N.A. Sjarif, M.R.M. Yusof, D.H.-T. Wong, S. Yakob, R. Ibrahim, M.Z. Osman, "A customer Churn prediction using Pearson correlation function and K nearest neighbor algorithm for telecommunication industry", International Journal of Advances in Soft Computing and its Applications, vol.11 no. 2, pp. 46-59, 2019.

[32] X. Long, Y. Wenjing, A. Le, N. Haiying, L. Huang, Q. Luo, & Y. Chen. "Churn analysis of online social network users using data mining techniques", Lecture Notes in Engineering and Computer Science, vol.2195, pp.551-556, 2012.

[33] F. Fessant, J. François, F. Clérot, "Characterizing ADSL customer behaviours by network traffic data-mining", Annals of Telecommunications, vol.62 no.3-4, pp. 350-368, 2007.

[34] V. Mahajan & Misra. "Review of data mining techniques for churn prediction in telecom", Journal of Information and Organizational Sciences, vol.39 no.2, pp.183–197, 2015.

[35] A. Rodan, A. Fayyoumi, H. Faris, J. Alsakran, & O. Al-kadi, "Negative correlation learning for customer churn prediction : a comparison study". The Scientific World Journal, 1-7, 2015.

[36] Y. Gao, G. Zhang, J. Lu, & J. Ma, "A bi-level decision model for customer churn analysis", Computational Intelligence, vol.30 no.3, pp. 583-599, 2014.

[37] Ç.K. Kontacı, O. Çetintürk, G. G. Polat, K. C. Özkısacık & A. A. Salah, "A simulator for generating realistic simulations of telecom customer behaviors", 24th Signal Processing and Communication Application Conference (SIU), pp. 537-540, 2016.

[38] P. Wanchai, "Customer churn analysis : a case study on the telecommunication ındustry of Thailand". 12th International Conference for Internet Technology and Secured Transactions, pp.325–331, 2017.

[39] V. Gülpınar, & D. Altaş, "Customer churn analysis through artificial neural networks in Turkish telecommunications market", International Journal of Economic Perspectives, vol.7 no.4, pp.63–80, 2013.

[40] N. Forhad, S. Hussain, R. M. Rahman, "Churn Analysis : Predicting Churners". Ninth International Conference on Digital Information Management, pp.237–241, 2014.

[41] Y. Zhao, B. Li, X. Li, W. Liu, S. Ren, "Customer Churn Prediction using improved one-class Support Vector Machine", Lecture Notes in Computer Science, Editör: Li X, Wang S, Yang-Dong Z. 3584, Springer, Berlin, 300–306, 2005.

[42] S. Jamil, & M. S. Cs, "Churn comprehension analysis for telecommunication ındustry using ALBA". International Conference on Emerging Technologies, 1–5, 2016.

[43] K. M. Leung, "Naive Bayesian Classifier".https://web.archive.org/web/20160311202321/http://cis.poly.edu/~mleung/FRE7851/f07/naiveBayesianClassifier.pdf. 2007.

[44] C. Budak, M. Türk, A. Toprak, "Removal of impulse noise in digital images with Naive Bayes classifier method". Turkish Journal of Electrical Engineering and Computer Science, vol.24 no.4, pp.2717-2729, 2016.

[45] T. Vafeiadis, K. I. Diamantaras, G. Sarigiannidis & K. C. Chatzisavvas, "A comparison of machine learning techniques for customer churn prediction". Simulation Modelling Practice and Theory, vol.55, 1–9, 2015.

[46] D.W. Hosmer & S. Lemeshow, "Applied logistic regressions", RX Sturdivant, John Wiley & Sons, 1996.

[47] StatisticsSolutions, "What is Logistic Regression?"https://www.statisticssolutions.com/what-is-logistic-regression/ 2021.

[48] B. Huang, M. T. Kechadi, & B. Buckley, "Customer churn prediction in telecommunications". Expert Systems with Applications, vol.39 no.1, pp.1414–1425, 2011.

[49] R. Gandhi, "Support Vector Machine — Introduction to Machine Learning Algorithms".https://towardsdatascience.com/support-vector-machine-introduction-to-machine-learning-algorithms-934a444fca47 2018.

[50] F. Filiz, "Artificial neural networks". https://medium.com/@fahrettinf/4-1-1-artificial-neural-networks-6257a7a54bb3 2017.

[51] S. Haykin, "Neural Networks and Learning Machines". Pearson Education, New Jersey, 1999.

[52] Y. Miche, P. Bas, A. Lendasse, C. Jutten, O. Simula, "Advantages of Using Feature Selection Techniques on Steganalysis Schemes". F. Sandoval et al. (Eds.) Springer-Verlag Berlin Heidelberg, pp. 606–613, 2007.

[53] J. Brownlee, "Feature Selection to Improve Accuracy and Decrease Training Time". https://machinelearningmastery.com/feature-selection-to-improve-accuracy-and-decrease-training-time/ 2021.

[54] O. Kaynar, H. Arslan, Y. Görmez, & Y. E. Işık, "Makine öğrenmesi ve öznitelik seçim

yöntemleriyle saldırı tespiti". Bilişim Teknolojileri Dergisi, pp.175–185, 2018.

[55] M. Santini, "Decision Trees: Entropy, Information Gain, Gain Ratio". https://www.slideshare.net/marinasantini1/lecture-4-decision-trees-2-entropy-information-gain-gain-ratio-55241087?from_action=save 2015.

[56] A. G. Karegowda, A. S. Manjunath, M.A. Jayaram, "Comparative study of attribute selection using gain ratio". International Journal of Information Technology and Knowledge and Knowledge Management, vol.2 no.2, pp.271–277, 2010.

[57] Toppr "Calculation of Gaining Ratio". https://www.toppr.com/guides/principles-and-practices-of-accounting/retirement-of-a-partner/calculation-of-gaining-ratio/ 2021.

[58] L. Breiman, "Classification and regression trees", Chapman & Hall/CRC, 1984.

[59] S. Tahsildar, "Gini Index for Decision Trees".https://blog.quantinsti.com/gini-index/ 2019.

[60] F. Kayaalp, M. S. Başarslan, & K. Polat, "TSCBAS: A novel correlation based attribute selection method and application on telecommunications churn analysis". International Conference on Artificial Intelligence and Data Processing, 2019.

[61] S. Glen, "How to Calculate Pearson's Correlation Coefficient". https://www.statisticshowto.com/probability-and-statistics/correlation-coefficient-formula/#Pearson 2020.

[62] M. Yıldız & S. Albayrak, "Customer churn prediction in telecommunication", 23nd Signal Processing and Communications Applications Conference, pp.256-259, 2015.

[63] F. Salfner, M. Schieschke, & M. Malek, "Predicting failures of computer systems: A case study for a telecommunication system". 20th International Parallel and Distributed Processing Symposium, 2006.

[64] A. K. Yadav, H. Malik, & S. S. Chandel, "Application of rapid miner in ANN based prediction of solar radiation for assessment of solar energy resource potential of 76 sites in Northwestern India". Renewable and Sustainable Energy Reviews, vol.52, pp.1093–1106, 2015.

[65] S. Dwivedi, P. Kasliwal, & S. Soni, "Comprehensive study of data analytics tools (RapidMiner, Weka, R tool, Knime)". Symposium on Colossal Data Analysis and Networking, 1-8, 2016.

[66] A. Tharwat, "Classification assessment methods". Applied Computing and Informatics.doi:10.1016/j.aci.2018.08.003 2018.

[67] M. Erkan, "Koronavirüs sürecinde telekom operatörleri nasıl çalıştı?" https://www.hurriyet.com.tr/teknoloji/koronavirus-surecinde-telekom-operatorleri-nasil-calisti-41539689 2020.

[68] C. Deegan, "Koronavirüs sürecinde telekom operatörleri nasıl çalıştı?". https://www.hurriyet.com.tr/teknoloji/koronavirus-surecinde-telekom-operatorleri-nasil-calisti-41539689 2020.

[69] KocDigital. "Covid-19 Telekom sektörü etkileri",https://www.kocdigital.com/blog/covid-19-telekom-sektoru-etkileri 2020.

[70] O. Özdemir, M. Batar, A.H. Işık, "Churn Analysis with Machine Learning Classification Algorithms in Python", Lecture Notes on Data Engineering and Communications Technologies, vol.43, pp. 844-852, 2020.

[71] J. Pamina, J. Beschi Raja, S. Sam Peter, S. Soundarya, S. Sathya Bama, M.S. Sruthi, "Inferring machine learning based parameter estimation for telecom churn prediction", Advances in Intelligent Systems and Computing, 1108 AISC, pp. 257-267, 2020.

[72] P. Hooda, P. Mittal, "An exposition of data mining techniques for customer churn in telecom sector", International Journal of Emerging Trends in Engineering Research, vol.7 no.11, pp. 506-511, 2019.

[73] S. Sharm, S. S. Sushasukhanya "Prediction of customer churn in telecom industries", International Journal of Recent Technology and Engineering, vol.8 no.1, pp. 369-372, 2019.

[74] K. Eria, B.P. Marikannan, "Significance-based feature extraction for customer churn prediction data in the telecom sector", Journal of Computational and Theoretical Nanoscience, vol.16 no.8, pp. 3428-3431, 2019.

[75] A. Gaur, R. Dubey, "Predicting Customer Churn Prediction in Telecom Sector Using Various Machine Learning Techniques", International Conference on Advanced Computation and Telecommunication, 8933783, 2018.

[76] B. Al-Shboul, H. Faris, N. Ghatasheh, "Initializing Genetic Programming using Fuzzy Clustering and its Application in Churn Prediction in the Telecom Industry", Malaysian Journal of Computer Science, vol.28 no.3, 213-22, 2015.

[77] I. Brandusoiu, G. Toderean, "Churn Prediction in the Telecommunications Sector Using Support Vector Machines", Annals of the Oradea University, Fascicle of Management and Technological Engineering, vol.1, pp. 19-22, 2013.

SAKARYA ÜNİVERSİTESİ
FEN BİLİMLERİ ENSTİTÜSÜ DERGİSİ

Sakarya University Journal of Science
SAUJS

ISSN 1301-4048 e-ISSN 2147-835X Period Bimonthly Founded 1997 Publisher Sakarya University
http://www.saujs.sakarya.edu.tr/

Title: The Evaluations Of Taxonomic Classifications In The Genus Trifolium L. Based On ITS Sequences

Authors: Aykut YILMAZ, Yudum YELTEKİN

Recieved: 2022-02-16 00:00:00

Accepted: 2022-04-28 00:00:00

Article Type: Research Article

Volume: 26
Issue: 3
Month: June
Year: 2022
Pages: 545-553

How to cite
Aykut YILMAZ, Yudum YELTEKİN; (2022), The Evaluations Of Taxonomic Classifications In The Genus Trifolium L. Based On ITS Sequences. Sakarya University Journal of Science, 26(3), 545-553, DOI: 10.16984/saufenbilder.1074625
Access link
http://www.saujs.sakarya.edu.tr/tr/pub/issue/70993/1074625

Sakarya University Journal of Science 26(3), 545-553, 2022

The Evaluations Of Taxonomic Classifications In The Genus *Trifolium* L. Based On ITS Sequences

Aykut YILMAZ*[1], Yudum YELTEKİN[1]

Abstract

The genus *Trifolium* L. belonging to family Fabaceae is represented by about 255 species in the world. Two classifications based on the sections or subgenus are commonly used by the researchers in the taxonomically evaluation of the genus *Trifolium*. However, there are still some confusing and complex situations about the taxonomy of the genus. For this reason, internal transcribed spacer (ITS) regions between rDNA genes in nrDNA were examined for 139 *Trifolium* taxa with the Maximum Parsimony (MP) method. Furthermore MP tree were evaluated based on two classification used commonly in the genus to provide contributions to taxonomic classification of the *Trifolium* species and to evaluate phylogenetic relationships of the *Trifolium* species. Study results support the status of subgenus proposed by new infrageneric classification. Also it can be stated that it is rationale to divide the section *Lotoidea* into several sections according to phylogenetic relationships of the taxa examined. Finally, this study reveals the importance of sequence information and problems in the barcoding.

Keywords: *Trifolium*, Fabaceae, Internal transcribed spacer, Maximum parsimony, *Lotoidea*

1. INTRODUCTION

The genus *Trifolium* L. (clover) belongs to the Fabaceae that are the third largest angiosperm family with approximately 20,000 species [1, 2]. *Trifolium* is one of the largest and important genus as forage crops for animals in the family Fabaceae. Besides the members of the genus have great importance for animals, the most of species belonging to the genus *Trifolium* are popular as ornamental plants [3, 4].

Trifolium taxa have cosmopolitan distribution. However, the greatest species diversity is found in the Mediterranean region and its periphery [3, 5]. The genus is represented by about 255 species which consist of herbaceous perennials or annuals commonly called clover [2, 6]. There are some confusing and complex situations about the taxonomy of the genus, especially in the

* Corresponding author: aykut.yilmaz@usak.edu.tr
[1] Uşak University
E-mail: yudum_yeltekin01@hotmail.com
ORCID: https://orcid.org/ 0000-0002-0327-8388, https://orcid.org/0000-0003-3891-8717

classification of the species based on the sections or subgenus. While some researchers use the classification proposed by Zohary and Heller [3, 6, 7], some researchers use the classification proposed by Ellison *et al.* [2, 5]. In the classification of *Trifolium* taxa based on Zohary and Heller [6], the taxa are evaluated into 8 sections as *Lotoidea*, *Paramesus* (C.Presl), *Mistyllus* (C.Presl), *Vesicaria*, *Chronosemium*, *Trifolium*, *Trichocephalum* Koch, and Involucrarium Hooker. In the classification of *Trifolium* taxa based on Ellison *et al.* [5], taxa belonging to the genus *Trifolium* firstly are classified into two subgenus as *Trifolium* L. and *Chronosemium* (Ser.) Reichenb. The most of taxa are placed to subgenus *Trifolium* in this classification. Thereafter, these taxa which belong to subgenus *Trifolium* are grouped within 8 sections as *Glycyrrhizum* Bertol., *Paramesus* (C. Presl), *Lupinaster* (Fabricius) Ser., *Trifolium*, *Trichocephalum* Koch, *Vesicastrum* Ser., *Trifoliastrum* S.F. Gray, *Involucrarium* Hooker.

Especially molecular techniques based on the polymerase chain reaction (PCR) methods or DNA sequence information's are frequently used to solve taxonomic problems, to explain the genetic status and phylogenetic relationships of taxa in the genus *Trifolium* [4,5,7,8], because of morphological variations caused by ecological factors, genetic drift, gene flow, hybridization, and epigenetic mechanisms in plants. However, molecular studies show that there are still taxonomic problems and some species are not grouped together with other species belonging to the same section [8]. Furthermore it is observed in some studies that the taxa belonging to section *Chronosemium* are found together with the taxa belonging to other sections (*Vesicaria* and *Lotoidea*) [7], unlike the new infrageneric classification proposed by Ellison *et al*. [5].

In this study, 139 *Trifolium* taxa were examined based on ITS1 and ITS2 sequences informations between rRNA genes provided from NCBI (National Center of Biotechnology Information) [9]. The objective of this study is to evaluate phylogenetic relationships of the *Trifolium* species, to compare the taxonomic classifications suggested by Zohary and Heller [6] and Ellison *et al*. [5] using the results obtained from this study separately for both taxonomic classifications and finally to provide important contributions to taxonomic classification of the *Trifolium* species.

2. MATERIAL AND METHODS

Internal transcribed spacer (ITS) regions between rDNA genes in nrDNA are commonly used in plant molecular systematic studies, due to these regions have high variable sites to determine the status and phylogenetic relationships of species. Furthermore, both regions (ITS1 and ITS2) appropriate for resolving taxonomic problems and understanding relationships within the genus. All sequence informations for ITS1 and ITS2 regions were provided from NCBI [9] and later these regions were analysed in point of compatibility of sequence information. All regions belonging to ITS1 and ITS2 whose sequence information is compatible were determined and used in this study (Appendix).

A total of 139 *Trifolium* taxa that is compatible were detected and examined based on sequence informations belonging to ITS1 and ITS2 regions of nrDNA in this study.

Sequences of the ITS1 and ITS2 regions which were analysed separately for the same plant samples in NCBI were taken and combined [8, 10]. Furthermore, the sequence informations of regions such as ITS1- 5,8SrRNA- ITS2 [11, 12], 18SrRNA Partial- ITS1- 5,8SrRNA- ITS2- 26SrRNA Partial [4, 13, 14, 15] and finally 18SrRNA Partial- ITS1- 5,8SrRNA- ITS2- 28SrRNA Partial [5, 16] were provided, the sequences belonging to ITS1 and ITS2 from these regions were extracted and then sequence informations of these two regions were combined for effective analysis.

Genbank codes for ITS1 and ITS2 sequences provided from NCBI are presented in Appendix. After the ITS1 and ITS2 sequence informations separately provided and combined with each other, multiple sequence alignments for 139 taxa belonging to the genus *Trifolium* were performed by using Molecular Evolutionary Genetics Analysis (MEGA X) [17]. Variable sites,

conserved sites and parsim-info sites were computed by using alignment sequences that were edited. Transitional and transversional substitutions (%) were determined in addition to transition/transversion ratios for purines-pyrimidines. Furthermore, nucleotide frequencies of the regions containing ITS1 and ITS2 for *Trifolium* taxa examined were computed by using alignment sequences. Finally, dendrogram showing the evolutionary history was inferred using the Maximum Parsimony method. The percentage of replicate trees in which the associated taxa clustered together in the bootstrap test (500 replicates) are shown next to the branches [18]. This analysis involved 139 sequences belonging to *Trifolium* taxa and all datas stated were computed by MEGA X. Gaps analyzed in comparison of these sequences were treated as missing data. In other words, the positions containing gaps and missing data were eliminated with complete deletion option for effective analysis.

3. RESULTS AND DISCUSSIONS

The sequences which belong ITS1 and ITS2 were combined for each taxa and aligned to determine the sequence similarities and variations for each *Trifolium* taxa. Alignment length of the taxa examined was determined as 558 bp with 328 variable sites and 231 parsimony informative sites. It was observed that the rate of transitional substitutions with 58.92 % is higher than transversional substitutions. Furthermore, transition/transversion ratios are 2.01 for purines and 3.64 for pyrimidines (Table 1). The overall transition/transversion ratio is 1.44 (Table 1). Nucleotide frequencies of ITS1 and ITS2 sequences were also analysed for *Trifolium* taxa and determined as 51.83 % for A+T/U and for 48.17 G+C (Table 1).

Table 1

The informations of taxa examined based on ITS1-ITS2 sequences

DNA regions	Taxon (number)	Alignment lenght (bp)	Variable site	Parsim-info site	Transitional substitutions (%)	Transversional substitutions (%)	Transition/Transversion rate Purines (k_1)	Pyrimidines (k_2)	Overall (R)	Nucleotide freq. (%) A+T/U	G+C
ITS1-ITS2	139	558	328	231	58.92	41.08	2.01	3.64	1.44	51.83	48.17

Furthermore, phylogenetic tree provided from Maximum Parsimony analysis were used in the comparisons of the taxonomic classifications based on Zohary and Heller [6] (Figure 1) and Ellison *et al*. [5] (Figure 2). In this way, it was aimed to understand the taxonomy of the genus better, besides determination of problems in taxonomic classification within the genus *Trifolium*.

Trifolium taxa based on Zohary and Heller [6] are evaluated into 8 sections. All sections were represented by the taxa examined in this study. Taxa belonging to section *Chronosemium* were grouped in same clade and formed a distinct group with outmost species in phylogenetic tree. The most of the taxa belonging to the section *Trifolium* (26 taxa) were grouped in two close clade and formed the outmost groups after section *Chronosemium*. However, other taxa from the section *Trifolium* were separated from these two out groups and formed distinct clade in phylogenetic tree. While some of these taxa such as *T. alexandrinum*, *T. clypeatum*, *T. echinatum*, *T. pallidum* and *T. pannonicum* were grouped in

same clade, other taxa (*T. hirtum*, *T. scabrum*, *T. cherleri* and *T. scutatum*) showed unexpected positions in phylogenetic tree. The *Lotoidea* with 76 taxa is the section represented by the highest species number in this study. These taxa were grouped in many clades according to MP tree. It can be stated that relationships of species within the section *Lotoidea* are very complex and confusing. While some species from section *Lotoidea* formed the wide clades which consist of many species, some clades contained a few species from section *Lotoidea*. Section *Paramesus* represented by *Trifolium strictum* was embedded among *Lotoidea* clusters. This situation show similarity with the result of Watson *et al*. [8] and supports the suggestion of Zohary and Heller [6] that section *Paramesus* needs to be included within section *Lotoidea* [8].

The species belonging to sections *Mistyllus* and *Vesicaria* were grouped together in two separate clades. It is reported by Badr [19] that these sections have the same chromosome number with 2n = 16. The result is consistent in this aspect. Section *Trichocephalum* was represented by two species in this study (*T. subterraneum* and *T. eriosphaerum*). These two species were grouped together in same clade with a few species from section *Lotoidea*. Section *Involucrarium* was represented by *T. depauperatum* and *T. buckwestiorum*. These species were grouped together and embedded within wide clade which consist of many species belonging to section *Lotoidea*.

In addition to classification based on Zohary and Heller [6], *Trifolium* taxa in this study was evaluated based on classification of Ellison *et al*. [5]. The 15 taxa belonging to subgenus *Chronosemium* formed a distinct group with outmost species in MP tree and clearly separated from other taxa examined. This result show similarity with Ellison *et al*. [5]. It can be said that the most of taxa from section *Trifolium* (26 from 37 taxa) were grouped together into two close clade. Furthermore, these taxa consist of outmost species within subgenus *Trifolium*. In other words, *Trifolium* is a section showing the most differences in comparison to others. However, other taxa from the section *Trifolium* were grouped separately from these two clades in unexpected positions in phylogenetic tree. These discrepancies can be caused by the situations such as labelling errors in accessions or misidentifications of the taxa. Consequently, it can be stated that there are similarity with the results of Ellison *et al*. [5] in point of the problematic taxa within the section *Trifolium*. The section *Vesicastrum* was represented by 27 taxa in this study. The taxa from section *Vesicastrum* were grouped together and formed three clades. Four taxa: *T. semipilosum*, *T. resupinatum*, *T. vesiculosum* and *T. clusii* showed differences from other taxa within the section and grouped with the taxa belonging to other sections. The section *Involucrarium* was represented by 27 taxa and all taxa were grouped in same clade. It is observed that the section *Involucrarium* is close to section *Vesicastrum*, unlike Ellison *et al*. [5] classification. The section *Trifoliastrum* was represented by 20 taxa and all taxa were closely grouped with each other. These taxa were previously classified within the section *Lotoidea* based on Zohary and Heller [6] and formed the problematic species belonging to the *Lotoidea* section in phylogenetic tree. As a result, it can be stated that it is rationale to divide the largest section *Lotoidea* into several sections like Ellison *et al*. [5]. The section *Lupinaster* were represented by 9 taxa in this study. Wide geographical distribution and variations observed due to theirs distribution is the basic reason of issues related to the *Lupinaster* [4].

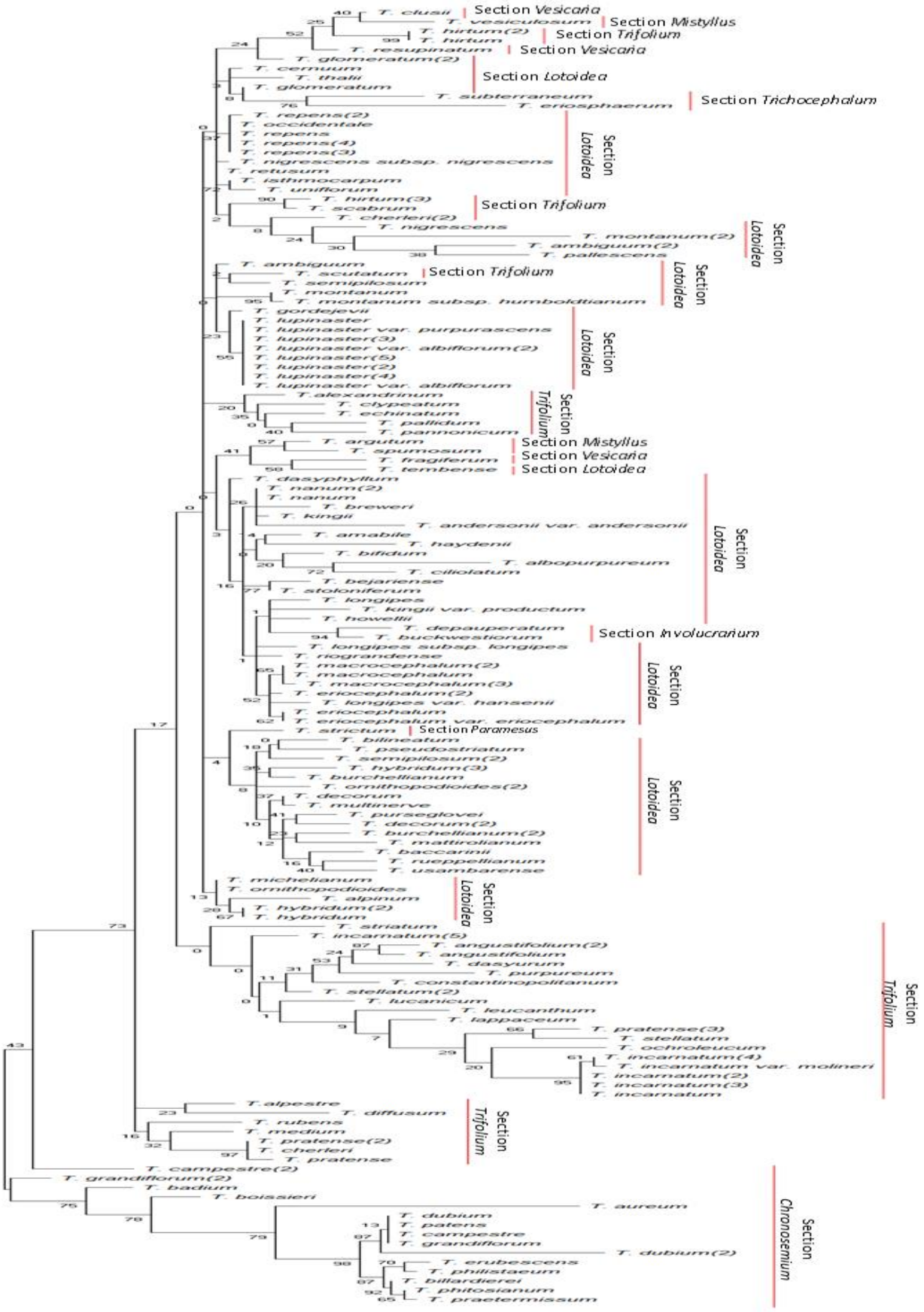

Figure 1 Phylogenetic relationships based on Zohary and Heller (1984)

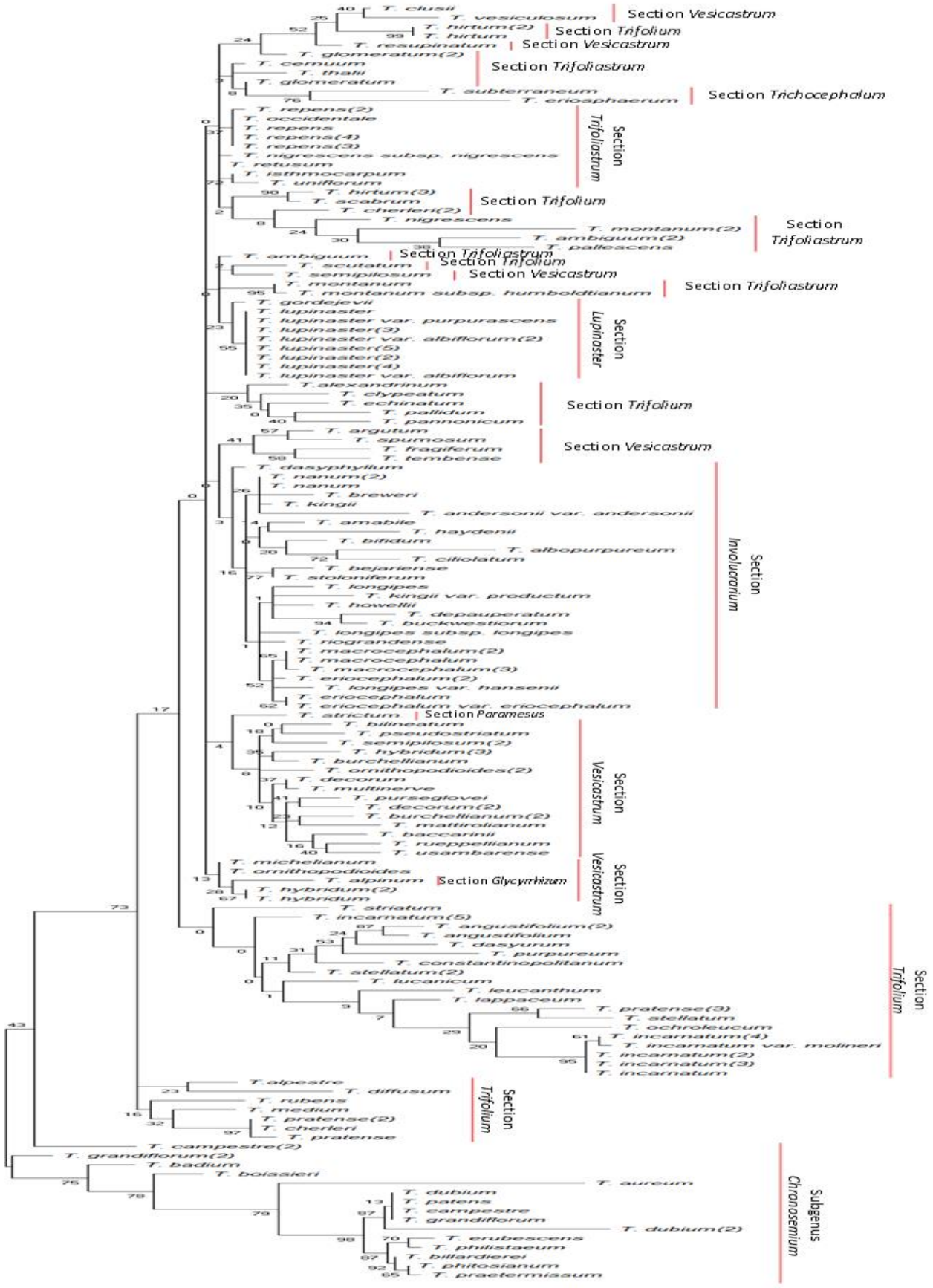

Figure 2 Phylogenetic relationships based on Ellison *et al.* (2006)

The taxa from section *Lupinaster* were grouped together in same clade and the relationships among taxa were observed to be quite similar. Section *Trichocephalum* was represented by two species in this study (*T. subterraneum* and *T. eriosphaerum*). These two species were grouped together in same clade with a few species from section *Trifoliastrum.* Section *Glycyrrhizum* was represented by *T. alpinum* and it was embedded within the clade which consist of *Vesicastrum* species. Section *Paramesus* was represented by *T. strictum*. This taxon merged from outermost to the clade which consist of *Vesicastrum* species.

4. CONCLUSIONS

When sequence information of ITS1 and ITS2 regions added by many researchers to NCBI were examined, it was observed that sequence lengths for *Trifolium* species are quite compatible, although the sequence determinations were made at different times by many researchers. However, ITS sequences of Ellison *et al*. [5] did not match with other researches. Therefore, sequence informations of only 15 taxa were used in this study with other sequence informations.

As a result of this study, firstly it can be said that the taxa belonging to *Chronosemium* formed outmost clade in MP tree and showed the highest differences in the comparison of other taxa. In other words, study result supports the classification in the status of subgenus proposed by Ellison *et al*. [5]. Second highest variations were observed in the section *Trifolium*. While the most of taxa from the section *Trifolium* were grouped in two clades with outmost species, a group exhibited irregular distribution in MP tree. In the study of Vizintin *et al*. [20] based on genetic characterization of selected *Trifolium* species, it is stated that there is quite a high variation within the section *Trifolium*. Similar results are stated by Uslu and Babaç [3] in their studies based on pollen and seed characteristics. The section *Lotoidea* based on Zohary and Heller [6] was represented by highest taxa in this study. It was observed that the taxa from the section *Lotoidea* were grouped together but in many distinct clades (see Figure 1). Consequently, it can be stated that it is rationale to divide the largest section *Lotoidea* into several sections like Ellison *et al*. [5]. However, when the relationships between the sections are examined in terms of phylogenetic, it is observed some differences with the results of the Ellison *et al*. [5].

It was determined that some species represented by a few taxa were not grouped together in same clade or some species from same section formed distinct clade in far distance. These discrepancies can be caused by the situations such as labelling errors in accessions, missing data caused by sequencing or misidentifications of the taxa.

Appendix

AF154381.1, AF154605.1, AF154400.1, AF154624.1, AF154379.1, AF154603.1, AF154353.1, AF154578.1, AF154388.1, AF154612.1, AF154365.1, AF154589.1, AF154370.1, AF154594.1, AF154405.1, AF154629.1, AF154373.1, AF154597.1, AF154406.1, AF154630.1, AF154372.1, AF154596.1, AF154403.1, AF154627.1, AF154357.1, AF154582.1, AF154362.1, AF154586.1, AF154383.1, AF154607.1, AF154386.1, AF154610.1, AF154387.1, AF154611.1, AF154401.1, AF154625.1, AF154382.1, AF154606.1, AF154366.1, AF154590.1, AF154360.1, AF154584.1, AF154404.1, AF154628.1, AF154359.1, AF154932.1, AF154376.1, AF154600.1, AF154392.1, AF154616.1, AF154395.1, AF154619.1, AF154394.1, AF154618.1, U56017.1, U56018.1, AF154390.1, AF154614.1, AF154399.1, AF154623.1, AF154352.1, AF154577.1, U50859.1, U50860.1, AF154356.1, AF154581.1, AF154397.1, AF154621.1, AF154377.1, AF154601.1, AF154354.1, AF154579.1, AF154385.1, AF154609.1, AF154384.1, AF154608.1, AF154396.1, AF154620.1, AF154375.1, AF154599.1, AF154389.1, AF154613.1, AF154371.1, AF154595.1, AF154361.1, AF154585.1, AF154398.1, AF154622.1, AF154369.1, AF154593.1, AF154358.1, AF154583.1, AF154380.1, AF154604.1, AF154374.1, AF154598.1, AF154364.1, AF154588.1, AF154393.1, AF154617.1, AF154391.1, AF154615.1, AF154378.1, AF154602.1, AF154367.1, AF154591.1, AF154368.1, AF154592.1, AF154363.1, AF154587.1, AF004305.1, JX506163.1, AF004304.1, AF004302.1, AF004303.1, AF004301.1, AF004300.1, AF053143.1, AF053144.1, AF053145.1, MF963884.1, EF667004.1, AF053147.2, AF053156.1, MF963868.1, AF053148.1, AF053149.1, AF053150.1, AF053151.1, AF053152.1, KX254378.1, AF053153.1, AF053154.1, MF964020.1, MF963886.1, AF053155.1, KX254380.1, AF053157.1, AF053158.1, MF963885.1, AF053159.1, EU348779.1, AF053160.1, AF053161.1, KX254379.1, MF963869.1, AF053162.1, MF963887.1, KX254386.1, KX254385.1, KX254384.1, KX254375.1, AF053163.1, KX254376.1, KX254373.1, KX254383.1, KX254372.1, MF964097.1, MF963870.1, AF053164.1, AF053165.1, AF053146.1, AF053166.1, KX254374.1,

AF053167.1, AF053168.1, AF053169.1, AF053171.1, EU348780.1, AF053172.1, KY968960.1, AF053173.1, AF053174.1, AF053175.1, AF053176.1, AF053177.1, AF053178.1, AF053179.1, DQ312005.1, DQ312015.1, DQ312025.1, DQ312041.1, DQ312047.1, DQ312050.1, DQ312051.1, DQ312062.1, DQ312098.1, DQ312116.1, DQ312121.1, DQ312122.1, DQ312137.1, KC572140.1, DQ311962.1, DQ312165.1

Acknowledgments

The authors would like to thank to NCBI for sequence informations used in this study and the authors sharing the sequence informations in NCBI.

Funding

The author has no received any financial support for the research, authorship or publication of this study.

The Declaration of Conflict of Interest/ Common Interest

No conflict of interest or common interest has been declared by the authors.

Authors' Contribution

The authors contributed equally to the study. A.Y: Data collection, literature research, writing the article, Y.Y: data collection, literature research.

The Declaration of Ethics Committee Approval

This study does not require ethics committee permission or any special permission.

The Declaration of Research and Publication Ethics

The authors of the paper declare that they comply with the scientific, ethical and quotation rules of SAUJS in all processes of the paper and that they do not make any falsification on the data collected. In addition, they declare that Sakarya University Journal of Science and its editorial board have no responsibility for any ethical violations that may be encountered, and that this study has not been evaluated in any academic publication environment other than Sakarya University Journal of Science.

REFERENCES

[1] LPWG, Legume Phylogeny Working Group, "A new subfamily classification of the Leguminosae based on a taxonomically comprehensive phylogeny," Taxon, vol. 66, no. 1, pp. 44–77, 2017.

[2] I. Choi, T. A. Ruhlman, and R. K. Jansen, "Comparative Mitogenome Analysis of the Genus *Trifolium* Reveals Independent Gene Fission of ccmFn and Intracellular Gene Transfers in Fabaceae," International Journal of Molecular Sciences, vol. 21, no. 6, pp. 1959, 2020.

[3] E. Uslu and M. T. Babaç, "A descriptive study of some *Trifolium* L. (Clover) taxa grown in Bolu Province," Turkish Journal of Botany, vol. 43, pp. 673–686, 2019.

[4] V. A. Kalinkina, V. M. Yulia, and E. K. Dmitry, "Diversity and taxonomy of the *Trifolium lupinaster* polymorphic complex in Eastern Europe and Asia," Flora, vol. 267, pp. 151597, 2020.

[5] N. W. Ellison, A. Liston, J. J. Steiner, W. M. Williams, and N. L. Taylor, "Molecular phylogenetics of the clover genus (*Trifolium*—Leguminosae)," Molecular Phylogenetics and Evolution, vol. 39, no. 3, pp. 688–705, 2006.

[6] M. Zohary and D. Heller, "The Genus *Trifolium*," The Israel Academy of Science and Humanities, Jerusalem, 1984.

[7] E. Uslu, G. D. Ertuğrul, and M.T. Babaç, "Assessment of genetic diversity in naturally growing 29 *Trifolium* L. taxa from Bolu Province using RAPD and SSR markers," Turkish Journal of Biology, vol. 37, pp. 479–490, 2013.

[8] L. E. Watson, H. Sayed-Ahmed, and A. Badr, "Molecular phylogeny of Old World

Trifolium (Fabaceae), based on plastid and nuclear markers," Plant Systematics and Evolution, vol. 224, pp. 153–171, 2000.

[9] NCBI, National Centre of Biotechnology Information,https://www.ncbi.nlm.nih.gov/genbank.

[10] M.J. Sanderson and M. F. Wojciechowski, "Diversification rates in a temperate legume clade: Are there ''so many species'' of *Astragalus* (Fabaceae)?," American Journal of Botany, vol. 83, no. 11, pp. 1488–1502, 1996.

[11] J. Steiner, E. Piccioni, M. Falcinelli, and A. Liston, "Germplasm Diversity among Cultivars and the NPGS Crimson Clover Collection," Crop Science, vol. 38, no. 1, pp. 263–271, 1998.

[12] H. Schaefer, P. Hechenleitner, A. Santos-Guerra, M. M. de Sequeira, R. T. Pennington, G. Kenicer, and M. A. Carine, "Systematics, biogeography, and character evolution of the legume tribe Fabeae with special focus on the middle-Atlantic island lineages," BMC Evolutionary Biology, vol. 12, no. 1, pp. 250, 2012.

[13] L. Vizintin and B. Bohanec, "Measurement of nuclear DNA content of the genus *Trifolium* L. as a measure of genebank accession identity," Genetic Resources and Crop Evolution, vol. 55, pp. 1323–1334, 2008.

[14] A. H. Thornhill, B. G. Baldwin, W. A. Freyman, S. Nosratinia, M. M. Kling, N. Morueta-Holme, T. P. Madsen, D. D. Ackerly and B. D. Mishler, "Spatial phylogenetics of the native California flora," BMC Biology, vol. 15, no. 1, pp. 96, 2017.

[15] S. Z. Xu, Z.Y. Li, and X. H. Jin, "DNA barcoding of invasive plants in China: a resource for identifying invasive plants," Molecular Ecology Resources, vol. 18, no. 1, pp. 128–136, 2017.

[16] Q. R. Bai, X. Y. Jiang, Y. Y. Xie, H. Y. Sun, and J. Gao, "Summer Blight of White Clover (*Trifolium repens*) Caused by *Rhizoctonia solani* AG-1-IB in China," Plant Disease, vol. 98, no. 8, pp. 1153, 2014.

[17] S. Kumar, G. Stecher, M. Li, C. Knyaz, and K. Tamura, "MEGA X: Molecular Evolutionary Genetics Analysis across computing platforms," Molecular Biology and Evolution, vol. 35, pp. 1547–1549, 2018.

[18] J. Felsenstein, "Confidence limits on phylogenies: An approach using the bootstrap," Evolution, vol. 39, pp. 783–791, 1985.

[19] A. Badr, "Electrophoretic studies of seed proteins in relation to chromosomal criteria and the relationships of some taxa of *Trifolium*," Taxon, vol. 44, pp. 183–191, 1995.

[20] L. Vizintin, B. Javornik, and B. Bohanec, "Genetic characterization of selected *Trifolium* species as revealed by nuclear DNA content and ITS rDNA region analysis," Plant Science, vol. 170, no. 4, pp. 859–866, 2006.

SAKARYA ÜNİVERSİTESİ
FEN BİLİMLERİ ENSTİTÜSÜ DERGİSİ

Sakarya University Journal of Science
SAUJS

ISSN 1301-4048 e-ISSN 2147-835X Period Bimonthly Founded 1997 Publisher Sakarya University
http://www.saujs.sakarya.edu.tr/

Title: Evaluation of Statistical Power in Random Effect Meta Analyses for Correlation Effect Size

Authors: Burçin ÖNER

Recieved: 2022-03-18 00:00:00

Accepted: 2022-05-05 00:00:00

Article Type: Research Article

Volume: 26
Issue: 3
Month: June
Year: 2022
Pages: 554-567

How to cite
Burçin ÖNER; (2022), Evaluation of Statistical Power in Random Effect Meta Analyses for Correlation Effect Size. Sakarya University Journal of Science, 26(3), 554-567, DOI: 10.16984/saufenbilder.1089793
Access link
http://www.saujs.sakarya.edu.tr/tr/pub/issue/70993/1089793

Sakarya University Journal of Science 26(3), 554-567, 2022

Evaluation of Statistical Power in Random Effect Meta Analyses for Correlation Effect Size

Burçin ÖNER*[1]

Abstract

In meta-analysis, numerical index is used as an estimate of effect size to describe the results of each study and thereafter these estimates of across studies are combined to obtain summary of results.

It should be known that calculations of the power of statistical tests are important in planning research studies and for interpreting situations in which a result has not proven to be statistically significant. Although statistical power is often considered in the design of primary research studies, it is rarely considered in meta-analysis. Despite the importance of statistical power, few studies have been examined the performance of simulated power in meta-analysis. (In this study, calculations of statistical power for statistical tests that are used for unequal sample size on random effects model in meta-analysis using correlation coefficient as effect size were conducted.)

The power of the test for the overall effect size was calculated by using both analytical method and simulation method. Thus, it was investigated whether there was any difference between the simulation power and analytical power in random effects meta-analysis by using correlation coefficient as an effect size.

Keywords: Meta-analysis, simulation power, correlation, analytical power

1. INTRODUCTION

Meta-analysis is a statistical method helpful for qualitatively and quantitatively combining the results of the studies conducted in the same subject in different place, time and centers, as well as reaching a general result in that issue [1].

Today, more research is needed for the number of the studies conducted on the same subject in different areas and for the related subject in every study. The research results with quantitatively

* Corresponding author: burcin.oner@bilecik.edu.tr
[1] Bilecik Şeyh Edebali University, Bozüyük Vocational School,
ORCID: https://orcid.org/0000-0001-9550-0435

large sample size give reliability to the researchers in reaching the judgment that the study is definitely correct. In this meaning, there could be no need for conducting additional studies regarding the subject. Besides; conduction of wide-scope studies will be very challenging for the researcher due to the fact that they are expensive, time-consuming and have complex applications. However; the usage of an alternative method like meta-analysis is important in terms of overcoming these hardships for the researcher.

Meta-analysis is a method frequently applied in the fields such as health and social sciences. It combines the summary results of various studies previously conducted on the interested research subject by joining them together under the convenient conditions. In this way, it could be asserted that it is an efficient way in reaching a general result in the related subject.

Meta-analysis is a very popular method in today's scientific world. When an inference is desired to be made with this analysis method, the metrics called "effect size" are used to define the result of each study to be used in the meta-analysis. These scales could be the numeric values representing the means, ratios or relations. Thanks to the combination of these used effect sizes, general effect size will also be able to be calculated. In this way; the hypothesis tests belonging to the query that "whether general effect is existent or not" being one of the main objectives of meta-analysis will also be able to be conducted.

Although the inference procedures belonging to the significance tests of the effect sizes are existent for long years in meta-analysis, relatively fewer studies have been conducted in the issue of the calculation of the power of the statistical tests. Power calculations related to the statistical tests are always an important part of the sound statistical planning [2]. The requirement for the attainment of statistical power estimations is an issue showing an increase in the meta-analysis studies in recent years.

First, Field conducted studies on different effect sizes for the models in meta-analysis under various conditions, and showed under which conditions effect sizes yield stronger results [3]. Hedges and Pigott presented procedures for analytical power calculations for fixed and random effect models [2]. Analytical power is the power calculated with the help of the sampling distribution of the statistics used as the effect size. Cohn and Becker emphasized that one of the frequently encountered problems in meta-analysis is the low statistical power and they sought ways to increase the power [4]. Hedges and Pigott also dealt with statistical power calculations of fixed and mixed effects moderator tests in their meta-analysis [5]. Cafri and Kromrey developed a software for these calculations, since regular applications of statistical power calculations in the meta-analysis in the literature require technical expertise and take a long time [6]. Valentine, Pigott and Rothstein tried to determine the required sample size to achieve high statistical power in meta-analysis [7]. Liu investigated the differences between analytical power and simulated power for standardized mean difference effect size in fixed and random effects meta-analysis models, and the effect of unbalanced design and unequal sample sizes on statistical power [8]. Simulated power is the calculated power with the help of software programs under conditions such as number of studies, sample sizes, effect size, type 1 error and number of simulations. Liu and Pan argued that there is not enough evidence for the accuracy of the formulas in the literature for statistical power in meta-analysis and they used simulation studies as an alternative way to calculate the power of the test [9].

It is seen in the studies conducted regarding the statistical power in meta-analysis that the power calculations are generally conducted with analytical way and sometimes with Monte Carlo simulation studies [2, 10]. The information and related formula regarding how the analytic process will be for the statistical power calculations in meta-analysis have been given by Hedges and Pigott [2] the information regarding how the statistical software items (SAS, R etc.) will be carried out for these calculations have been given by Liu [8].

The sampling distribution of the statistics belonging to the effect size used in the related

meta-analysis is benefited while calculating the power in analytic way. Depending on the effect size preferred in meta-analysis; the sampling distribution of the statistics being the estimation of this effect size is affected from: (i) the study patterns applied in the combination of the studies (such as one-sample, independent or dependent two samples and the independent samples with two values), (ii) assumptions regarding the distribution of the group or groups according to the interested variable/variables, (iii) degree of the effect size (especially the correlation coefficient and odds ratio) and (iv) the size of the sample sizes in the study.

It is also an inevitable result that the analytic power of the test related to the statistical test used in the meta-analysis will also be affected due to these conditions efficient on the sampling distribution of the statistics. Especially in the meta-analyses in which relation scales (correlation coefficient, odds ratio etc.) are used as the effect size, the result may occur that the calculated analytic power does not reflect the real power sometimes due to the relation degree and sometimes due to the small sample [2, 8]. Because the sampling distribution of the statistics used as the effect size in the large samples converges to a known theoretical probability distribution, the usage of this probability distribution becomes possible in the calculation of the analytic power. However; the analytic power that will be calculated with the same probability distribution also in small samples will not show the real power. This is because the formulas for the sampling distribution of the relevant effect size statistics are not valid for small sample sizes. At this situation; it will be more convenient to prefer the way of simulation in the calculation of the power of the test on condition that the conditions necessary for the power calculation will remain the same. Because; when the conditions are the same, the power value attained with the simulation way comes out higher than the value attained with analytic power way.

In the literature, considering this feature of the correlation coefficient effect size, it has been determined that there is no comparison of analytical and simulation-based studies of statistical power in the meta-analysis. For this reason, in this study, the power of test calculations belonging to the statistical tests used for the situation of an unequal sample size in random effects model have been handled in a meta-analysis in which the correlation coefficient has been taken as the effect size. The power of test calculations belonging to the general effect size from them have been attained with the use of analytic methods and simulation method. In this way; the issue that whether there is a difference between the statistical power simulation and analytic power in a meta-analysis in which the correlation coefficient has been used as the effect size metrics has been examined for both models.

Required encodings were/has been written in R program for the analytic power and simulation power calculations. Analytic power and simulation power methods have been used in the power calculation. Within the scope of the study, the research question “Is there any difference between the analytic power and simulation power calculated for the random effects model in meta-analyses in which correlation coefficient has been used in effect size?” has been addressed.

2. MATERIAL AND METHOD

For a meta-analysis study to be conducted, the aim of the relevant study, study design, and data format are to be guide in the selection of the effect size. The effect size to be used in the studies assessing the relation among the variables without conducting causal direction inferences could be the relation scales like correlation coefficient. In this study, correlation coefficient has been used as the effect size. For this reason; correlation coefficient statistics and its sampling distribution have been focused in this part.

If the correlation coefficient is used as the effect size in a meta-analysis, the study pattern is the one-group studies. In the studies in which correlation coefficient expressing the direction and degree of the linear relation between two continuous variables is used, correlation parameter is shown with θ for the population and the sample correlation coefficient statistics which is the estimation of this parameter is shown with

r. This statistic takes a value within the range of [-1, +1] and is defined as follows:

$$r = \frac{\sum_{i=1}^{n}(x_i - \overline{x})(y_i - \overline{y})}{\sqrt{\sum_{i=1}^{n}(x_i - \overline{x})^2 \sum_{i=1}^{n}(y_i - \overline{y})^2}} \quad (1)$$

The sampling distribution of this statistics does not show a normal distribution. Especially on condition that $\theta_0 \epsilon [-1, +1]$; the sampling distribution of r statistics shows a skew distribution towards right ($\theta_0 > 0$) or left ($\theta_0 < 0$) while $H_0: \theta = \theta_0$. Also; the expected value of r statistics is equal to the parameter (namely θ), but its variance is a function of itself and the sample size [11].

For the sample correlation coefficient r statistics; the expected value and variance is given with the following equation respectively:

$$E(r) = \theta \text{ and } V_r = \frac{(1 - r^2)^2}{n - 2} \quad (2)$$

For this reason; in the meta-analysis studies in which the correlation coefficient is used as the effect size, r statistics is not directly used for the statistical inferences such as especially the hypothesis test and the power of test. At this situation, processes are conducted by applying Fisher Z transformation on the correlation coefficient. Fisher Z transformation is the following equation:

$$Z = \frac{1}{2} \times \ln\left(\frac{1 + r}{1 - r}\right) \quad (3)$$

and the sampling distribution of this Z statistics shows a normal distribution [12, 13] whose parameters are respectively;

$$E(Z) = \frac{1}{2} ln\left(\frac{1 + \theta}{1 - \theta}\right) \text{ and } V(Z) = \frac{1}{n - 3} \quad (4)$$

Consequently; correlation values could be attained again by applying inverse transformation on Eq. (3).

Let's assume that there are k independent studies on a particular topic has been handled. Let θ_i be the population effect size parameter belonging to i^{th} study. Let effect size estimations be attained from these studies and let us show the estimator of θ_i parameter with T_i. In this situation; an assumption belonging to T_i is as follows;

$$T_i \sim N(\theta_i, v_i); \quad i = 1,2, \dots, k \quad (5)$$

In the case where the correlation coefficient is used as an estimation of the effect size, vi is a known variance and dependent on the sample size. According to Hedges and Olkin [14], this assumption is always valid for effect sizes such as the correlation coefficient transformed with Fisher's Z transformation. However; correlation coefficient which has not been transformed is not completely valid for the effect size; it is only accepted to be correct for large samples [2]. Thus; for i[th] study, $i = 1,2, \dots, k$; $T_i = Z_i$ from (3) and $v_i = \frac{1}{n_i - 3}$ from (4).

2.1. Analytic Power in Random Effect Model

When the studies are combined in meta-analysis according to the random effect model and the correlation coefficient belonging to the studies are taken as the effect size parameter, the model equation defined under Fisher Z transformation is given with the following equation;

$$Z_i = \xi_i + \varepsilon_i = \mu + \eta_i + \varepsilon_i \ ; \ i = 1,2, \dots , \ k \quad (6)$$

In this model; for $i = 1,2, \dots , k$; the effect size ξ_i belonging to i^{th} study (correlation coefficient transformed for the population) is a random variable.

According to the related model; ε_i is the random error of $Z_i$and η_i is the random error of ξ_i, these are both random errors. For these random errors; it is assumed that these are distributed as; $\varepsilon_i \sim N(0, v_i)$ and $\eta_i \sim N(0, \tau^2)$, $(i = 1, 2, \dots , k)$ and independent. In this situation; as the linear functions of the normals, both Z_i being the sample effect size estimation attained with Fisher Z transformation of the correlation coefficient belonging to i[th] study and ξ_i being the effect size belonging to i[th] study (correlation coefficient transformed for the population) have normal distribution. Such that; for $i = 1, 2, \dots , k$; $\xi_i \sim N(\mu , \tau^2)$ while $Z_i \sim N(\xi_i , v_i)$. Here; v_i is the

conditional sampling variance of Z_i and it is calculated with $v_i = \frac{1}{n_i - 3}$, $i = 1, 2, \dots, k$.

Also; τ^2 known as the component of variance between studies could be estimated with $\hat{\tau}^2 = \frac{Q-(k-1)}{c}, Q > (k-1)$. Here; Q is Cochran Q test statistic and c is a constant that is a function of the weights. Thus; statistical analyses could be conducted in the meta-analysis on the mean effect size parameter (μ) belonging to the random effect model, the variance of the random effect size or the component of variance (τ^2) between studies. In these analyses, both the hypotheses about parameters could be tested and the power calculations for these tests could also be conducted.

When the combination of the studies in meta-analysis is conducted according to the random effect model, the effect size has a unique distribution due to the fact that it is a random variable.

When the population correlation coefficient $(\theta_i, i = 1, 2, \dots, k)$ is taken as random effect size for the studies, the effect size transformed under Fisher Z transformation is $\xi_i = \frac{1}{2}\left\{\ln\left[\frac{1+\theta_i}{1-\theta_i}\right]\right\}, i = 1, 2, \dots, k$ random variable and $\xi_i \sim N(\mu, \tau^2)$.

Here; μ is the mean of the effect size distribution and it is known as the mean effect size parameter. Statistical inferences could be made about the effect size with a hypothesis test related to the mean effect size parameter.

The hypotheses to be tested in this test process are formed as follows:

$$\begin{aligned} &\textbf{a)}\ H_0: \mu = \mu_0 \ ;\ H_1: \mu \neq \mu_0 \\ &\textbf{b)}\ H_0: \mu = \mu_0 \ ;\ H_1: \mu < \mu_0 \\ &\textbf{c)}\ H_0: \mu = \mu_0 \ ;\ H_1: \mu > \mu_0 \end{aligned} \qquad (7)$$

Here; μ_0 is a known real number. $\bar{Z}_.^* = \frac{\sum_{i=1}^{k} w_i^* Z_i}{\sum_{i=1}^{k} w_i^*}$ that is an unbiased estimator of the mean effect size parameter and it also is the weighed mean statistic of random effects estimations. The sampling distribution of this statistic is shown with $\bar{Z}_.^*$ and has a normal distribution with mean μ and variance $v_.^*$ for the large samples. Such that, here $v_.^*$ is the unconditional sampling variance of Z_i and is calculated with $v_.^* = v_i + \tau^2$. In this case, the test statistic to test the H_0 hypothesis will be the Z statistics which has standard normal distribution and given by the following;

$$Z = \frac{\bar{Z}_.^* - \mu}{\sqrt{v_.^*}} \sim N(0,1) \qquad (8)$$

The value of the test statistics is $Z = \frac{\bar{Z}_.^* - \mu_0}{\sqrt{v_.^*}}$ when H_0 is correct. Regarding the decision to be reached as a result of the test process; H_0 is rejected if $|Z| > C_{\alpha/2}$ for the two-sided test and H_0 is rejected if $|Z| > C_\alpha$ for the one-sided tests.

The calculation of the power of test will be able to be a matter in the conditions in which H_0 hypothesis is rejected. In this situation, the distribution of Z test statistics according to the alternative hypothesis will show a normal distribution whose mean is λ^* and variance is 1. Here; the real value of the mean effect size according to the H_1 is $\mu_G = E(\bar{Z}_.^*)$, and parameter λ^* is calculated with the following equation;

$$\lambda^* = \frac{\mu_G - \mu_0}{\sqrt{v_.^*}} \qquad (9)$$

The power function which will occur as a result of the rejection of H_0 hypothesis at a given significance level at α will be

$$1 - \beta = 1 - \emptyset(C_\alpha - \lambda^*) \qquad (10)$$

for the one-sided tests; and

$$1 - \beta = 1 - \emptyset\left(C_{\alpha/2} - \lambda^*\right) + \emptyset(-C_{\alpha/2} - \lambda^*) \qquad (11)$$

for the two-sided test. Here; $\emptyset(x)$ shows the cumulative standard normal distribution function.

2.2. Simulation Power in Meta-Analysis

In the meta-analyses in which some effect sizes such as correlation coefficient and odds ratio have been used, the sampling distributions of the sample effect size statistics could be calculated approximately and asymptotically for the large

samples. For this reason; the analytic power calculations are made using these approximate distributions under the alternative hypotheses for the statistical power related to the tests in meta-analysis. Thereof; it is thought that considering the analytic power values attained regarding the mentioned statistical tests not as the real power, but as the approximate value will be more correct.

According to Liu [8]; it is not known whether the accuracy of the analytic power formulas taking place in the literature is certain or not. The fact that there are some assumptions in the application of the formulas may cause to some biases in the results. Some of the mentioned assumptions could be given as; (i) accepting the within study variances as equal, (ii) preference of the smallest sample size among groups in which small sample sizes are intensive for the purpose of determining a more consistent within study sample size in the combined studies and (iii) preference of the smallest study number among the study numbers to determine a more consistent study number etc. [2, 8].

However; when the correlation coefficient is used as the effect size, the sampling distributions of the test statistics related to the statistical tests may be formed asymptotically for the large samples and the analytic power calculation could also be made with the help of these formed distributions. Therefore; it is highly likely that the analytic power values attained from especially small samples are the biased when compared to the real values.

In this study; statistical power calculation with simulation is suggested as an alternative method in the meta-analyses in which correlation coefficient is taken as the effect size in terms of being able to eliminate the problems in the analytic power calculations for the statistical power related to the statistical tests in meta-analysis.

The formulas used in the analytic power calculations are dependent on the parameters of the population effect size, statistical significance level, sample size, number of studies to be included in the analysis and the component of variance between studies. For this reason; these parameters should be taken into consideration also in the simulation power calculations.

Sample size may show difference from one to the other study included in the meta-analysis. As in the primary studies, the population effect size and statistical power are correlated within the same direction also in the meta-analysis. In other words; as the population effect size increases, statistical power also increases. Generally, the standardized or transformed effect size values are used to combine the measurement scales between studies in meta-analysis; because these operations make the measurement units of the variables independent from each other.

The number of studies to be included in meta-analysis is also in a positive relation with the statistical power when other parameters are equal. Namely; as the number of studies included in meta-analysis increases, statistical power will also increase.

In addition; a simulation study is a very advantageous method both in terms of checking the correctness of the statistical power in a real meta-analysis study and emphasizing its relation with the analytic power. While calculating the population variance in power formulas, the variance of every study is accepted to be equal to one another. This approach is not a correct method in practice although it is frequently used in the power calculation process. So; it could be said that simulation power will give more correct results when compared to the analytic power. Also; the comparison of these two calculated powers provides the opportunity of being able to check the correctness of the calculation findings. In addition, the differences between analytical power and simulation power provide the opportunity for defining a potential bias existent in the power formulas [8].

As in the analytic power calculation, same conditions will be taken into consideration also in the simulation power calculation. These are the sample size, number of studies, population effect size, type I error ratio and model type. In addition to these conditions, also the number of simulations will be considered in the calculation of the simulation power.

3. RESULTS

In this study; the power of test calculations belonging to the statistical tests used in random effects model have been focused in a meta-analysis in which correlation coefficient is considered as the effect size. For this; the examination of both the simulation power and analytic power of a meta-analysis planned on a simulation data have been conducted and the results attained according to two methods have been compared.

The focused research question has been determined as "Is there any difference between the calculated analytic power and simulation power for the random effect models in meta-analysis?"

Power simulation has been conducted under various conditions by taking into account the factors affecting the statistical power and the simulation status and afterwards, analytic power has been calculated using the existent power formulas and the attained two statistical power results have been compared. R programming language has been benefited for these processes. Simulation conditions have been based on similar studies [8].

The conditions have been determined as follows:

Average sample size: The condition showing variability in different meta-analysis studies changes between 20 and 100 (20, 30, 40, 50, 75, 100) in this study. In a real meta-analysis study, the mean sample size is expected to be rather large. However; when the other parameter values are equal, the sample sizes larger than 100 have been neglected in this study due to the fact that the large sample sizes have a statistical power enhancing effect. Besides; the study concerns with the impact of small sample sizes on statistical power.

In reality, the sample sizes among the primary studies are not equal to one another. Thereof; the truncated binomial distribution has been used to meet the sample sizes and to be able to produce positive integer numbers in the simulation study. The maximum value taking place in the distribution has been changed and the variety of the sample size has been ensured. The sample size of each study has been diversified based on different ratios [8].

Population effect sizes: In this study, correlation coefficient (r) has been discussed as the population effect size. Respectively $r = 0$ (no effect), $r = 0{,}1; 0{,}2$ (little effect), $r = 0{,}5$ (medium effect) and $r = 0{,}8$ (high effect) values have been determined for these selected effect sizes and included in the study.

The principles of Cohen [15] and the values taking place in the study of Field [16] who determined as the low, medium and high degree correlation coefficients have been taken into consideration for the determination of these effect sizes.

The sampling distribution of the correlation coefficient shows a distribution which is both not normal and dependent on the unknown population correlation coefficient. Therefore; correlation coefficient is not directly used in the meta-analysis and power calculations.

In this situation, Fisher Z transformation being a logarithmic transformation is applied on the correlation coefficient. This transformation extends $[-1\,;\,+1]$ interval being the interval of values that could be taken by the correlation coefficient into the interval of $(-\infty\,;\,+\infty)$. Also; the sample distribution of the new statistics defined with Fisher Z transformation will approach to the normal distribution [2, 14, 17].

Number of Studies: The numbers of studies determined for this condition shows varieties between 5 and 75 (5, 10, 20, 30, 45, 60, 75). These numbers have been selected by basing them to the real meta-analysis studies.

Moreover; the fact that there is a positive relation between the number of studies and the statistical power when other parameters are equal gives rise to reaching a satisfying power in the numbers of studies higher than 75. For this reason; the numbers of studies higher than 75 have not been included in the power calculation conditions.

Number of Repetitions: Meta-analysis study has been repeated for 10 000 times for the purpose of attaining a constant simulation result.

Type I error ratio: As the related ratio, the ratio of $0{,}01$ used commonly in the literature has been determined in terms of the reliability of the statistical hypothesis test for this study.

According to all these, total simulation scenario is dependent on 3 different factors. These are 5 population effect sizes (0; $0{,}1$; $0{,}2$; $0{,}5$; $0{,}8$), 7 sample sizes ($20, 30, 40, 50, 60, 75, 100$) and 7 numbers of studies ($5, 10, 20, 30, 45, 60, 75$). Sample size and number of studies have 49 combinations. 10 000 Monte Carlo tests have been conducted for each combination

3.1. Type I Error Ratio Control

What is necessary to be conducted before performing the processes for the research question is type I error control. In the condition where the population effect size is zero in the model, the probability of rejecting the zero hypothesis gives the real type I error ratio. This control is necessary, because type I error ratio may affect the type II error ratio, therefore, the statistical power [8]. Related results are given in Table 1 for $0{,}01$ significance level.

Table 1
Type I error control in random effects model (for $\alpha = 0{,}01$)

	Number of Studies						
ASS*	5	10	20	30	45	60	75
20	0,006	0,007	0,007	0,007	0,008	0,007	0,009
30	0,005	0,007	0,007	0,007	0,009	0,007	0,008
40	0,007	0,008	0,007	0,008	0,008	0,009	0,009
50	0,005	0,007	0,008	0,006	0,007	0,008	0,008
60	0,009	0,008	0,009	0,009	0,007	0,008	0,009
75	0,007	0,008	0,009	0,008	0,009	0,008	0,007
100	0,006	0,006	0,009	0,009	0,008	0,008	0,009

* Average Sample Size

3.2. Statistical Power and Simulation under Random Effects Model

When the situation in which the sample size among studies is not equal to one another is taken into consideration, the requirement that the sample sizes to be produced to calculate the simulation power should be positive integer numbers occurs.

In this situation, truncated binomial distribution is benefited to produce various sample sizes between studies. The sample sizes produced thanks to this distribution have turned to the positive integer numbers with a certain mean and standard deviation.

As the standard deviation of the binomial distribution changes, maximum sample size has also been changed. Maximum sample size is attained by multiplying the mean sample size with a certain number.

In this study, it has been selected as" the mean sample size *3". Different tests have been conducted for a larger maximum sample size, but similar results have been attained. For this reason; only the condition "$maximum\ sample\ size = mean\ sample\ size * 3$" has been adopted in the study.

The simulation power and analytic power values calculated by considering the criteria of the number of studies, sample size and different population effect sizes for the random effects model under the design of the inequality of the sample sizes are given in Table 2.

The results related to the power calculations have been attained by coding them in R program.

Table 2
Statistical power in random effects model while type I error ratio is 0,01 ($Maximum\ sample\ size = average\ sample\ size * 3$)

ASS[1]	Simulation Power							Analytical Power						
	Number of Studies													
	5	10	20	30	45	60	75	5	10	20	30	45	60	75
Population Effect Size=0,1														
20	0.036	0.079	0.194	0.332	0.528	0.703	0.824	0.040	0.085	0.202	0.337	0.535	0.698	0.815
30	0.056	0.140	0.359	0.554	0.787	0.924	0.968	0.062	0.144	0.353	0.556	0.782	0.907	0.964
40	0.081	0.208	0.500	0.734	0.926	0.976	0.994	0.086	0.211	0.497	0.728	0.913	0.976	0.994
50	0.109	0.283	0.635	0.849	0.973	0.997	0.999	0.113	0.280	0.624	0.843	0.968	0.994	0.999
60	0.153	0.349	0.743	0.924	0.991	0.999	0.999	0.141	0.352	0.729	0.915	0.989	0.999	0.999
75	0.191	0.474	0.847	0.972	0.998	1.000	1.000	0.187	0.459	0.842	0.968	0.998	0.999	1.000
100	0.289	0.634	0.949	0.996	1.000	1.000	1.000	0.268	0.616	0.943	0.995	0.999	1.000	1.000
Population Effect Size=0,2														
20	0.186	0.450	0.838	0.967	0.998	0.999	1.000	0.178	0.442	0.826	0.962	0.997	0.999	1.000
30	0.326	0.698	0.972	0.998	1.000	1.000	1.000	0.313	0.684	0.968	0.998	1.000	1.000	1.000
40	0.475	0.848	0.996	1.000	1.000	1.000	1.000	0.447	0.842	0.995	0.999	1.000	1.000	1.000
50	0.593	0.931	0.999	1.000	1.000	1.000	1.000	0.571	0.927	0.999	1.000	1.000	1.000	1.000
60	0.703	0.970	0.999	1.000	1.000	1.000	1.000	0.677	0.969	0.999	1.000	1.000	1.000	1.000
75	0.817	0.992	1.000	1.000	1.000	1.000	1.000	0.798	0.992	1.000	1.000	1.000	1.000	1.000
100	0.921	0.9993	1.000	1.000	1.000	1.000	1.000	0.916	0.999	1.000	1.000	1.000	1.000	1.000
Population Effect Size =0,5														
20	0.969	1.000	1.000	1.000	1.000	1.000	1.000	0.972	1.000	1.000	1.000	1.000	1.000	1.000
30	0.997	1.000	1.000	1.000	1.000	1.000	1.000	0.999	1.000	1.000	1.000	1.000	1.000	1.000
40	0.999	1.000	1.000	1.000	1.000	1.000	1.000	1.000	1.000	1.000	1.000	1.000	1.000	1.000
50	0.999	1.000	1.000	1.000	1.000	1.000	1.000	1.000	1.000	1.000	1.000	1.000	1.000	1.000
60	0.999	1.000	1.000	1.000	1.000	1.000	1.000	1.000	1.000	1.000	1.000	1.000	1.000	1.000
75	1.000	1.000	1.000	1.000	1.000	1.000	1.000	1.000	1.000	1.000	1.000	1.000	1.000	1.000
100	1.000	1.000	1.000	1.000	1.000	1.000	1.000	1.000	1.000	1.000	1.000	1.000	1.000	1.000
Population Effect Size=0,8														
20	1.000	1.000	1.000	1.000	1.000	1.000	1.000	1.000	1.000	1.000	1.000	1.000	1.000	1.000
30	1.000	1.000	1.000	1.000	1.000	1.000	1.000	1.000	1.000	1.000	1.000	1.000	1.000	1.000
40	1.000	1.000	1.000	1.000	1.000	1.000	1.000	1.000	1.000	1.000	1.000	1.000	1.000	1.000
50	1.000	1.000	1.000	1.000	1.000	1.000	1.000	1.000	1.000	1.000	1.000	1.000	1.000	1.000
60	1.000	1.000	1.000	1.000	1.000	1.000	1.000	1.000	1.000	1.000	1.000	1.000	1.000	1.000
75	1.000	1.000	1.000	1.000	1.000	1.000	1.000	1.000	1.000	1.000	1.000	1.000	1.000	1.000
100	1.000	1.000	1.000	1.000	1.000	1.000	1.000	1.000	1.000	1.000	1.000	1.000	1.000	1.000

Furthermore; the graphical demonstration of these attained simulation and analytic power results have been drawn in MATLAB R2018b program and the attained curve is given in Figure 1.

The straight lines in the graphics show the analytic power values and the dashed lines shows the simulation power values and the colors of red, yellow, blue, green, black, purple and light blue respectively express the numbers of studies (5, 10, 20, 30, 45, 60, 75).

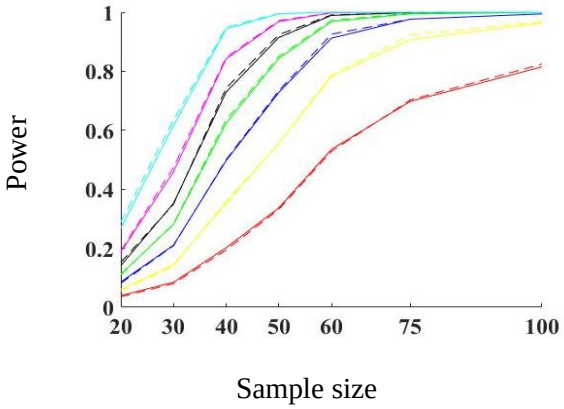

Figure 1 Statistical power in random effects model when type I error ratio is 0,01

Figure 1 shows the power curve in the situation of the inequality of the sample sizes in the random effects model when the type I error ratio is 0,01. It has been observed in the graphics that there are differences between the two power values although the simulation power and analytic power values are very close to each other. The graphics has been drawn only for this effect size due to the fact that the widest differences could be determined for 0,1 population effect size and very close values have been attained for the other designs.

3.3. Differences between the Analytic Power and Simulation Power

In this part, firstly the differences of between analytical power and simulation power under different conditions in random effects model have been examined. As it could be seen from Table 2, simulation power and analytic power have taken values very close to each other under all conditions. So; it cannot be said that there is a systematic difference between them, namely power has underestimation or overestimation different conditions.

It could be theoretically said that statistical power increases as the number of studies, population effect size and average sample size expanded. Also; when the population effect size is 0,8; it has been observed that the power has taken the value of 1 for two random effects model. It is understood here that when the population effect size is very high, other parameters affecting the statistical power become unimportant. However; it cannot be said that the reverse situation is correct. For instance; power could take very low values when the average sample size starts from the value of 100 and number of studies and population effect size take very low values.

The differences in the random effects model have been checked by comparing the power estimations attained from Table 2 for the significance level of 0,01 in the event of the unequal sample size and these comparison results are given in Table 3.

Table 3
Differences between analytic power and simulation power in random effects model ($\alpha = 0{,}01$)

Average Sample Size	Number of Studies						
	5	10	20	30	45	60	75
	Population Effect Size=0,1						
20	-0,004	-0,006	-0,008	-0,005	-0,007	0,005	0,009
30	-0,006	-0,004	0,006	-0,002	0,005	0,017	0,004
40	-0,005	-0,003	0,003	0,006	0,013	0	0
50	-0,004	0,003	0,011	0,006	0,005	0,003	0
60	0,012	-0,003	0,014	0,009	0,002	0	0
75	0,004	0,015	0,005	0,004	0	0,001	0
100	0,021	0,018	0,006	0,001	0,001	0	0

In the case of sample size is not equal, the number of studies, the average sample size and the values of population effect size required to reach a desired statistical power, for the level of Type I

error rate at 0.01, according to the model type are given in Table 4.

Table 4
Average sample size amount necessary for a statistical power at the level of 0,80 and above in random effects model while type I error ratio is 0,01.

	Random Effect Model ($\alpha = 0{,}01$ için)						
Population Effect Size	Number of Studies						
	5	10	20	30	45	60	75
0,1	>100	>100	75	50	>30	30	20
0,2	75	40	20	20	20	20	20
0,5	20	20	20	20	20	20	20
0,8	20	20	20	20	20	20	20

4. CONCLUSION AND DISCUSSION

As seen in Table 1; type 1 error ratio has been kept under control using 0,01 significance level and limited to 1% level for the random effects model. It means that the model has an error ratio at 1% level. In other words; β is one (1), $1-\beta$ is zero (0). Because the population effect size takes the value of zero (0) here, H_0 hypothesis is not wrong and therefore, it requires no rejection. Also; if an examination is conducted according to the average sample size when the numbers of studies are kept stable and according to the number of studies when the average sample size is kept stable, it has been observed that there have been increases and decreases in the values. This could be interpreted as the fact that there is no systematic increase or decrease in the random effects model.

When the situation in which population effect size is 0,1 is considered according to Table 2, the number of studies necessary to attain a power at a level of 80% and above is sufficient to be around 75 according to both simulation and analytic calculations for the average sample size of 20 units is used. When the sample size of 30 units is used, the number of studies necessary to attain a power at a level of 80% and above should approach 60 according to both the simulation and analytic calculations. When the sample size of 40 units is used, the number of studies necessary to attain a power at a level of 80% and above should approach 45 according to both the simulation and analytic calculations. When the sample size of 50 and 60 units is used, the number of studies necessary to attain a power at a level of 80% and above should be around 30 according to both the simulation and analytic calculations. When the sample size of 75 and 100 units is used, the number of studies necessary to attain a power at a level of 80% and above should approach 20 according to both the simulation and analytic calculations.

When the population effect size is 0,2; while the sample size amount necessary to attain a power at a level of 80% and above is sufficient to be 75 in a meta-analysis in which there are 5 studies according to the simulation calculations, the sample size necessary to attain a power at a level of 80% and above should approach to 100 according to the analytic calculations. The sample size necessary to attain a power at a level of 80% and above is around 40 according to both the simulation and analytic calculations in a meta-analysis in which there are 10 studies. The sample size necessary to attain a power at a level of 80% and above is sufficient to be around 20 according to both the simulation and analytic calculations in a meta-analysis in which there are 20, 30, 45, 60 and 75 studies.

When the population effect size is 0,5 and 0,8; sample sizes and numbers of studies with very little size are sufficient for the statistical power to come out very high.

When Figure 1 is examined; while the difference between the simulation power and analytic power is very little in the places in which the sample size is between 60 and 75 for the number of studies is 5, the differences have been observed to have become clearer in other sample size values. It has been seen that the differences have become clearer when the sample size has taken values higher than 60 in the places in which the number of studies is 10, but the power values have come so much closer to each other in the sample size at a level of 100 and higher. The differences have been observed to come closer to each other very much in the event that the sample size has taken a value between 50 and 75 in the places in which the number of studies is 20. No clear difference has been observed between two powers in the places in which the number of studies is 30. While

the differences have become clearer when the sample size has taken a value between 40 and 60 in the places in which the number of studies is 45, it has been monitored that the clear differences have occurred in the sample sizes less than 40 in the meta-analyses to which 60 and 75 studies have been included. When examination has been conducted on the values in which the sample size has increased on the Figure, it has been observed that the two power values have come closer to each other and even reached the integer value of 1.

When Table 3 has been examined; it has been seen that the difference between the simulation power and analytic power is too little at the significance level of 0,01 and it has also been observed that these differences become clearer when the population effect size is 0,1 and 0,2.

For the numbers of studies are respectively 60, 45, 20 and 10 while the population effect size is 0,1 and the average sample size is 30, 40, 50, 75 and 100; also, for the numbers of studies are respectively 5 and 20 and the average sample size is 60; differences exceeding 0,01 have been observed. It has been seen that especially for the number of studies is 10 and average sample size is 100, this difference has approached 0,02 and it has exceeded 0,02 for the number of studies is 5 and the average sample size is 100. It has been determined that there have been differences exceeding 0,01 in the event that the number of studies is 5 while the population effect size is 0,2 in all average sample sizes except for the sample sizes of 20 and 100 units; and for the average sample size has been respectively 30 and 20 in the situations in which the numbers of studies are 10 and 20. It has been observed that the difference has approached 0,03 for the sample sizes are respectively 40, 50 and 60 while especially the number of studies is 5.

It has been seen while the population effect size is 0,5 and 0,8 that the difference between the simulation power and analytic power has remain at a very little level in the random effects model in the unequal sample size. The interpretations belonging to the impact of the unequal sample sizes among studies on the statistical power have been made upon the simulation power although the analytic power and simulation power have given results close to each other. As it could be seen from the power tables, the unequal sample size among studies and the population effect size have had an increasing impact on the statistical power. Because the situation in which population effect size is 0,8 presents 1 integer power, it has been kept out of observation and interpretations have been made upon the other effect sizes.

The results expected to be attained from this study could be sequenced as follows: (a) What the parameters of average sample size, number of studies and population effect size necessary for a meta-analysis study to be conducted to have a statistical power at the desired level at a certain type I error level will be should be decidable, (b) Some differences could be found between the results of analytic power and simulation power attained within the frame of the statistical power calculation in meta-analysis. This difference may stem from the fact that analytic power is based on certain formulas and the differences at or below the level of type I error ratio which has been determined are assumed to be acceptable and (c) Because the differences may show underestimations or overestimations, it cannot be said that there is a systematic increase or decrease in the analytic power.

This study presents the results attained along the simulation conditions that could affect the power belonging to random effects meta-analysis method. The study has provided a wider point of view about the power estimations of the meta-analysis procedures. Two estimations have been supported. These are: (1) Very few differences have been observed to be existent between simulation power and analytic power calculated by taking the determined criteria into consideration. The differences lower than type I error ratio are the neglectable differences. In this situation, it could be said that simulation power and analytic power calculations complete each other. In contrast; in the situation in which type I error ratio is 0,01; it has been observed that the differences are a little higher than this error ratio for some scenarios. Here; it could be inferred that the analytic power estimation will estimate the real power more deficiently as the difference

between the two powers increases. In addition; as the related parameters (mean sample additional volume, population effect size and number of studies) are changed, the differences between analytic power and simulation power have decreased to an acceptable level. (2) As it could be understood from the power tables, no systematic bias has been observed. Both underestimations and overestimations have been detected.

Consequently; in this study it is aimed to determine which method gives better results in the analytical and simulation-based comparison of statistical power in meta-analysis, considering the characteristics of the sampling distribution of the correlation coefficient effect size. Also, it gives researchers an idea about the sample size, the number of studies and the population effect size required for a meta-analysis study in which correlation coefficient will be used as the effect size to have a statistical power at the level of 80% and above.

Funding

The author has no received any financial support for the research, authorship or publication of this study.

The Declaration of Conflict of Interest/ Common Interest

No conflict of interest or common interest has been declared by the authors.

The Declaration of Ethics Committee Approval

This study does not require ethics committee permission or any special permission.

The Declaration of Research and Publication Ethics

The authors of the paper declare that they comply with the scientific, ethical and quotation rules of SAUJS in all processes of the paper and that they do not make any falsification on the data collected. In addition, they declare that Sakarya University Journal of Science and its editorial board have no responsibility for any ethical violations that may be encountered, and that this study has not been evaluated in any academic publication environment other than Sakarya University Journal of Science.

REFERENCES

[1] Mosteller, F. and Colditz, G.A., "Understanding research synthesis (Meta–analysis)", Annu. Rev. Public Health, 17, 1 – 23, 1996.

[2] Hedges, L. V. and Pigott, T. D., "The power of statistical tests in meta-Analysis", The American Psychological Association, 6 (3), 203-217, 2001.

[3] Field. A. P., "Meta-analysis of correlation coefficients: A Monte Carlo comparison of fixed- and random-effects methods", Psychological Methods, 6(2), 161–180, 2001.

[4] Cohn, L. D. and Backer, B. J., "How meta-analysis increases statistical power", The American Psychological Assosiation, 8(3), 243-253, 2003.

[5] Hedges, L. V. and Pigott, T. D., "The power of statistical tests for moderators in meta-analysis", The American Psychological Association, 9(4), 426–445, 2004.

[6] Cafri, G., Kromrey, J. D. and Brannick, M. T., "A SAS macro for statistical power calculations in meta-analysis" Behavior Research Methods, 41 (1), 35-46, 2009.

[7] Valentine, J. C., Pigott, T. D. and Rothstein, H. R., "How many studies do you need? A primer on statistical power for meta-analysis", Journal of Educational and Behavioral Statistics, 35(2), 215–247, 2010.

[8] Liu, J., "Statistical power in meta-analysis", Ph.D. dissertation, Dept. Educational Studies, South Carolina University, Carolina, USA, 2015.

[9] Liu, J. and Pan, F., "A SAS Macro to investigate statistical power in meta-analysis", in Paper presented at the Southeast SAS Users Group, Savannah, GA, 2015-September, 109-114.

[10] Field. A. P., "Meta-analysis of correlation coefficients: A Monte Carlo comparison of fixed- and random-effects methods", Psychological Methods, 6(2), 161–180, 2001.

[11] Gamgam, H, Ünver, Ö. ve Atunkaynak, B., Temel istatistik yöntemler, Seçkin Yayıncılık, Ankara, 2011.

[12] Chow, S. C., Shao, J. and Wang H., "Considerations Prior to Sample Size Calculation" in Sample size calculations in clinical research, Second ed., New York, USA, Boca Raton: Taylor & Francis, 2008, 25-49.

[13] Schmidt, F., "What do data really mean? Research findings, meta-analysis, and cumulative knowledge in psychology", American Psychologist, 47(10), 1173-1181, 1992.

[14] Hedges, L. and Olkin, I., Statistical methods for meta-analysis, San Diego, CA, USA, Academic Press, 1985, 224-237.

[15] Cohen, J., Statistical power analysis for the behavioral sciences, Hillsdale, NJ, USA, Erlbaum, 1988, 47-51.

[16] Field. A.P., "The problems of using fixed-effects models of meta-analysis on real-world data", Psychological Methods, 6(2), 161–18, 2003.

[17] Borenstein, M., Hedges, L. V., Higgins, J. P. T., Rothstein, H. R., "Effect Sizes Based on Correlations" in Introduction to meta-analysis, First ed., United Kingdom, John Wiley & Sons, Ltd, 41-44, 2009.

SAKARYA ÜNİVERSİTESİ
FEN BİLİMLERİ ENSTİTÜSÜ DERGİSİ

Sakarya University Journal of Science
SAUJS

ISSN 1301-4048 e-ISSN 2147-835X Period Bimonthly Founded 1997 Publisher Sakarya University
http://www.saujs.sakarya.edu.tr/

Title: A Conformal Fractional Derivative-based Leaky Integrate-and-Fire Neuron Model

Authors: İsmail DEVECİOĞLU, Reşat MUTLU

Recieved: 2021-12-24 00:00:00

Accepted: 2022-05-06 00:00:00

Article Type: Research Article

Volume: 26
Issue: 3
Month: June
Year: 2022
Pages: 568-578

How to cite
İsmail DEVECİOĞLU, Reşat MUTLU; (2022), A Conformal Fractional Derivative-based Leaky Integrate-and-Fire Neuron Model. Sakarya University Journal of Science, 26(3), 568-578, DOI: 10.16984/saufenbilder.1041088
Access link
http://www.saujs.sakarya.edu.tr/tr/pub/issue/70993/1041088

Sakarya University Journal of Science 26(3), 568-578, 2022

A Conformal Fractional Derivative-based Leaky Integrate-and-Fire Neuron Model

İsmail DEVECİOĞLU*[1], Reşat MUTLU[1]

Abstract

Neuron model have been extensively studied and different models have been proposed. Nobel laureate Hodgkin-Huxley model is physiologically relevant and can demonstrate different neural behaviors, but it is mathematically complex. For this reason, simplified neuron models such as integrate-and-fire model and its derivatives are more popular in the literature to study neural populations. Lapicque's integrate-and-fire model is proposed in 1907 and its leaky integrate-and-fire version is very popular due to its simplicity. In order to improve this simple model and capture different aspects of neurons, a variety of it have been proposed. Fractional order derivative-based neuron models are one of those varieties, which can show adaptation without necessitating additional differential equations. However, fractional-order derivatives could be computationally costly. Recently, a conformal fractional derivative (CFD) is suggested in literature. It is easy to understand and implement compared to the other methods. In this study, a CFD-based leaky integrate-and-fire neuron model is proposed. The model captures the adaptation in firing rate under sustained current injection. Results suggest that it could be used to easily and efficiently implement network models as well as to model different sensory afferents.

Keywords: Fractional order derivatives, conformal fractional derivative, leaky integrate-and-fire, neuron model

1. INTRODUCTION

Integrate-and-fire (IF) model of a neuron, which is first suggested by Louis Lapicque [1], has influenced many studies in neuroscience [2]. Even today, it is still used in solution of many different neuroscience problems thanks to its simplicity [2]. Lapique's neuron model paved the way for a more complex neuron model by Hodgkin-Huxley [3]. Although Hodgkin-Huxley neuron model is physiologically consistent and can interpret different behaviors of a real neuron,

* Corresponding author: idevecioglu@nku.edu.tr
[1] Tekirdağ Namık Kemal University
E-mail: rmutlu@nku.edu.tr
ORCID: https://orcid.org/ 0000-0003-4119-617X, https://orcid.org/ 0000-0003-0030-7136

it is mathematically complex. For this reason, simplified neuron models are usually preferred where the behavior of individual neurons is not that critical. A variety of IF-models has been published in the literature. The most popular one is the leaky IF (LIF) model, in which the membrane potential decreases if the input is ceased. The non-linear models such as Fitzhugh-Nagumo model [4-6] and Izhikevich neuron model [7-10] are also popular since they can capture different neural behaviors. However, implementation of a simple LIF is still easier and efficient compared to these models. The drawback of a LIF neuron is the lack of adaptation term (i.e., the decrement of firing rate of the neuron with elongated stimulation). In order to implement adaptation in LIF, an additional equation which increases the threshold to generate an action potential (hereafter called spike) with every spike is used. On the other hand, if the change of membrane potential is defined with a fractional order derivative, a LIF model can capture the adaptive behavior without addition of a second differential equation.

Fractional order derivatives (FD) have emerged as a hot research area especially in the half century [11-15]. Their application areas in engineering and applied science have been rising continuously [12-15]. They are also used to model biological systems [16]. Since the suggestion of their existence in 1695 [17], different types of fractional derivatives are found [11-15, 18]. The conformal fractional derivative (CFD) has been one of the recently found fractional order derivatives [19]. It has been a major interest since it is easier to understand and implement compared to other types of the fractional derivatives [19-20]. The CFD is the multiplication of the ordinary derivative with $t^{(1-\alpha)}$ (i.e., time (t) to the $(1-\alpha)$th power). Furthermore, it has a valid physical interpretation that the other fractional derivative types lack [21]. More on the usage of fractional derivatives in electrical circuits can be found in [22]. The CFD has also been used to model supercapacitors [23-29]. The CFD capacitors and analysis of their usage with other circuit elements have also come out as a popular topic [22, 27-31]. Some circuits which have been analyzed with the CFD can be found in [32-34].

Fractional order capacitors have already been used to model neurons in the literature [16, 35-36]. FD-based leaky integrate and fire neuron models can be found in [35-36]. Additionally, a CFD-based FitzHugh–Nagumo neuron model was presented recently [37]. To the best of our knowledge a CFD-based leaky integrate and fire neuron model has not been examined in literature yet. In this study, a CFD-based leaky integrate and fire neuron model is made, and its spiking pattern is inspected.

The remainder of the paper is organized as follows; In the second section, a brief introduction to the IF neuron model is given. In the third section, the conformal fractional derivative and CFD capacitor model are briefly explained. In the fourth section, the CFD capacitor neuron model and its differential equation are given, and its spiking pattern was inspected under a constant current input. The paper is concluded with the last section.

2. A SHORT REVIEW OF INTEGRATE-AND-FIRE NEURON MODELS

Lapicque's IF model demonstrates a neuron in its very basic form, and it can be considered as the fundamental component of other models. LIF model is widely known and used in different studies, and it includes another fundamental component for neurons which is "forgetting" (i.e., decrement of membrane potential if the current input is ceased). Fractional order model introduces the adaptation behavior of neurons in the same equation that is used to calculate neuron's membrane potential. Therefore, we briefly explained IF, LIF and fractional-order neuron models in this section.

2.1. Lapicque's Integrate-and-Fire Model

After his work on frog nerves, Louis Lapicque introduced the IF model in 1907 [1,2]. Actually, he realized that the time to excite a nerve with a constant current stimulation can be estimated with a capacitor's current-voltage equation:

$$\frac{dV(t)}{dt} = \frac{1}{C} I(t) \qquad (1)$$

where V is the membrane potential of the neuron and C is the membrane capacitance. If a current, $I(t)$, flows through the membrane of the neuron, the membrane potential increases as the integral of the current flowing. When the membrane potential reaches a certain value (e.g., a spike threshold, V_{TH}), it generates a spike which is modelled as a Dirac delta function, and the membrane potential returns to its resting state (V_r). Then, the neuron continues to integrate and fire periodically until the current stimulation is ceased. The firing rate (i.e., frequency of spike generation) of IF model, r, is proportional to the input current:

$$r = \frac{I}{CV_{TH}} \tag{2}$$

r linearly increases without any limits as the current amplitude increases. However, physiological neurons do not do so, their firing rate is limited by their refractory period, t_{ref}. Therefore, a $t_{ref}>0$ is used to limit the firing rate of IF neuron:

$$r = \frac{I}{CV_{TH}+t_{ref}I} \tag{3}$$

When the input current is ceased, however, IF neuron keeps its membrane potential indefinitely. If the stimulation is continued at a late time, then the neuron's membrane potential starts to increase from where it remained. This behavior is inconsistent with physiological neurons which return to their resting state with a time constant when the input current is ceased. This shortcoming is solved by introducing a leakage term in the equation as in LIF model.

2.2. Leaky Integrate-and-Fire Model

LIF model consists of a capacitor connected in parallel with a resistor. The resistor, R, introduced in the model represents the leakage resistance for ions diffusing through the cell membrane, and hence, it acts to reduce the membrane potential towards its resting state. The model equation is given as following:

$$\frac{dV(t)}{dt} = \frac{1}{RC}(I(t)R - V(t)) \tag{4}$$

where V is the membrane potential and R is the resistance of leakage channels on the membrane. The membrane potential increases until a threshold, V_{TH}, is reached, then, a spike is generated, and the membrane potential is reset to its resting value.

For a constant current input, the minimum current amplitude to generate a spike is defined as $I_{TH}=V_{TH}/R$. Assuming a reset to zero, the firing rate can be estimated as following:

$$r = \begin{cases} 0, & I \le I_{TH} \\ \left[t_{ref} - RC\log(RI - V_{TH})\right]^{-1}, & I > I_{TH} \end{cases} \tag{5}$$

LIF model, as well as IF model, fires at a constant rate for a given constant current input. However, physiological neurons fires with increasing intervals as the current input is sustained. This behavior is called adaptation. Nonlinear generalized IF models show adaptation by including an adaptation term which is also defined with a differential equation [38].

2.3. Fractional-Order Leaky Integrate-and-Fire Model

Unlike LIF and other generalized IF models, fractional-order LIF model can demonstrate adaptation in firing rate in a single equation. The model equation is defined as [36]:

$$\frac{d^{\alpha}V(t)}{dt^{\alpha}} = \frac{1}{RC}(I(t)R - V(t)) \tag{6}$$

In [36], the change of membrane potential is also rewritten as:

$$\frac{dV(t)}{dt} = \frac{1}{RC}\frac{d^{1-\alpha}}{dt^{1-\alpha}}(I(t)R - V(t)) \tag{7}$$

The Caputo fractional derivative is used to solve the differential equation in [36]. Spike generation progresses as in IF and LIF models explained in previous sections.

3. THE CONFORMAL FRACTIONAL DERIVATIVE AND THE CFD CAPACITOR MODEL

The fractional calculus is used to explain and model the fractional order elements [14, 16]. The CFD has been becoming more prominent fractional derivative method although it is developed in the recent decade [19-21]. It is easy to use and to understand compared to the other types of fractional derivatives [19-21]. In [17], The CFD is described as:

$$\frac{d^{\alpha}f(t)}{dt^{\alpha}} = \frac{df(t)}{dt}t^{1-\alpha} \tag{8}$$

This FD is easy and efficient to implement compared to other fractional derivatives.

Some capacitors can be modeled using fractional order derivatives [23-29]. The symbol of a CFD capacitor is shown in Figure 1. The constitutional law of a capacitor modeled using the CFD is given as:

$$i_C(t) = C_{\alpha}\frac{d^{\alpha}v_C(t)}{dt^{\alpha}} = C_{\alpha}\frac{dv_C(t)}{dt}t^{1-\alpha} \tag{9}$$

where C_{α} is the CFD capacitor coefficient, $i_C(t)$ is the CFD capacitor current, and $v_C(t)$ is the CFD capacitor voltage.

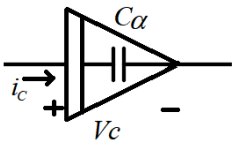

Figure 1 The CFD capacitor symbol

4. THE PROPOSED CFD-BASED NEURON MODEL

4.1. Theoretical Analysis of the Model

In this section, we propose a novel CFD-based neuron model. The neuron's electrical circuit is shown in Figure 2. It consists of a switch (S), a current source (I_S), a leakage resistor (R), and the CFD capacitor (C_{α}). R and C_{α} shares the current injected into the model, which prevents C_{α} to charge too quickly. The charging time of C_{α} depends on the constant $\tau=RC_{\alpha}$. The switch S is used to discharge C_{α} when it reaches a certain threshold voltage, VTH. This event is registered as a spike. As soon as the discharge occurs, the switch is open again. Then, the integrate and fire operation of the neuron continues until the current injection is ceased.

When an input current (I_S) flows through the neuron, the following differential equation can be written using Kirchhoff's laws:

$$I_S = i_C(t) + i_R(t) \tag{10}$$

$$I_S = C_{\alpha}\frac{d^{\alpha}v_C(t)}{dt^{\alpha}} + \frac{v_C(t)}{R} \tag{11}$$

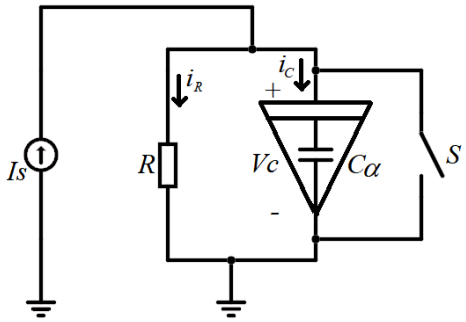

Figure 2 The proposed CFD-based neuron model

$$I_S = C_{\alpha}\frac{dv_C(t)}{dt}t^{1-\alpha} + \frac{v_C(t)}{R} \tag{12}$$

After multiplying each term with R and rearranging terms, derivative of the capacitor voltage (v_C; called membrane potential hereafter) can be found as following:

$$RI_S = RC_{\alpha}\frac{dv_C(t)}{dt}t^{1-\alpha} + v_C(t) \tag{13}$$

$$RI_S - v_C(t) = RC_{\alpha}\frac{dv_C(t)}{dt}t^{1-\alpha} \tag{14}$$

$$\frac{dv_C(t)}{dt} = \frac{1}{RC_{\alpha}t^{1-\alpha}}(RI_S - v_C(t)) \tag{15}$$

If the terms are rearranged, a solution for $v_C(t)$ can also be found:

$$\frac{dt}{t^{1-\alpha}} = RC_{\alpha}\frac{dv_C(t)}{RI_S - v_C(t)} \tag{16}$$

$$\frac{dt}{t^{1-\alpha}} = -RC_{\alpha}\frac{dv_C(t)}{v_C(t) - RI_S} \tag{17}$$

Taking indefinite integration of each side:

$$\int \frac{dt}{t^{1-\alpha}} = -RC_\alpha \int \frac{dv_C(t)}{v_C(t) - RI_S} \quad (18)$$

$$-\frac{1}{RC_\alpha}\int t^{\alpha-1}dt = \int \frac{dv_C(t)}{v_C(t) - RI_S} \quad (19)$$

$$-\frac{t^\alpha}{\alpha RC_\alpha} + K = \ln\left(v_C(t) - RI_S\right) \quad (20)$$

where K is the integration constant. Rearranging the last equation, the membrane potential is found as:

$$v_C(t) - RI_S = e^{-t^\alpha/\alpha RC_\alpha + K} = e^K e^{-t^\alpha/\alpha RC_\alpha} \quad (21)$$

$$v_C(t) = RI_S + e^K e^{-t^\alpha/\alpha RC_\alpha} \quad (22)$$

Assuming the CFD neuron's membrane potential is zero at t=0 s ($v_C(0)$ = 0 V), the integration constant e^K can be found as:

$$v_C(0) = RI_S + e^K e^0 = RI_S + e^K = 0 \quad (23)$$

$$e^K = -RI_S \quad (24)$$

By substituting e^K back into the equation (22), the neuron's membrane potential is found as:

$$v_C(t) = RI_S - RI_S e^{-\frac{t^\alpha}{\alpha RC_\alpha}} \quad (25)$$

At t=t_{reset}, the neuron voltage becomes equal to the threshold voltage:

$$v_C(t_{reset}) = V_{TH} = RI_S - RI_S e^{-t_{reset}^\alpha/\alpha RC_\alpha} \quad (26)$$

Therefore, the reset time (firing time) is found as:

$$V_{TH} - RI_S = -RI_S e^{-t_{reset}^\alpha/\alpha RC_\alpha} \quad (27)$$

$$(RI_S - V_{TH})/RI_S = e^{-t_{reset}^\alpha/\alpha RC_\alpha} \quad (28)$$

$$ln\left((RI_S - V_{TH})/RI_S\right) = ln\left(e^{-t_{reset}^\alpha/\alpha RC_\alpha}\right) \quad (29)$$

$$t_{reset}^\alpha = -\alpha RC_\alpha\, ln\left((RI_S - V_{TH})/RI_S\right) \quad (30)$$

$$t_{reset}^\alpha = \alpha RC_\alpha\, ln\left(RI_S/(RI_S - V_{TH})\right) \quad (31)$$

$$t_{reset} = \sqrt[\alpha]{\alpha RC_\alpha\, ln\left(RI_S/(RI_S - V_{TH})\right)} \quad (32)$$

If the refractoriness is also assumed, a dead time t_{ref} after a spike can be used, which would result an inter-spike interval as following:

$$T = t_{ref} + t_{reset} \quad (33)$$

$$T = t_{ref} + \sqrt[\alpha]{\alpha RC_\alpha\, ln\left(RI_S/(RI_S - V_{TH})\right)} \quad (34)$$

Then, the initial firing rate at the very beginning of current injection can be estimated as:

$$r = \frac{1}{T} = \frac{1}{t_{ref} + \sqrt[\alpha]{\alpha RC_\alpha\, ln\left(RI_S/(RI_S - V_{TH})\right)}} \quad (35)$$

Beginning from this rate, instantaneous firing rate would decrease along with a sustained current injection. The instantaneous firing rate is dependent on $t^{1-\alpha}$ and, theoretically, the firing rate never reaches to zero.

4.2. Simulation of the Model

In this study, we chose the membrane capacitance as 200 pF and the leakage resistance as 50 MΩ, which resulted a time constant of 10 ms [39]. The simulations were performed by solving following differential equation with Euler's method in python.

$$\frac{dv_C(t)}{dt} = \begin{cases} 0 & , \quad t \le t_{onset} \\ \frac{1}{RC_\alpha (t - t_{onset})^{1-\alpha}}\left(RI_S - v_C(t)\right), & t > t_{onset} \end{cases} \quad (36)$$

where t_{onset} is the onset time of the current stimulation.

Resting state membrane potential was assumed to be zero (V_R=0V), and threshold voltage (V_{TH}) to fire a spike was 10 mV. If the membrane potential (v_C) reached V_{TH} at time t, then $v_C(t+dt)$ is set to V_R. While solving for the membrane potential, we recorded its value in a separate variable. In order to emphasize spikes, we recorded the membrane potential at the time of spike as a peak spike voltage of 30 mV in the recording variable (Figure 3).

The Figure 3 shows the model response when stimulated with a current amplitude of 0.21 nA while the simulations are given for four different α values. The onset of the stimulus was 0.1 s, and its duration was 0.3 s. In order to understand the model's behavior, we ignored refractory period in these simulations (e.g., t_{ref}=0 s). If α is chosen 1, then the model equation turns into the basic LIF model, i.e., a model with exponential charging. It fires spikes at a constant rate during the stimulation period. As the α is decreased, the model starts to generate spikes with increasing interspike intervals as the time proceeds, which is considered as adaptation. Additionally, decreasing α increased the instantaneous firing rates at the onset of the stimulation period. However, the spike patterns (especially, at the very beginning of stimulation) generated with α values smaller than 0.5 are not plausible due to the refractoriness of the physiological neurons. Therefore, α should be chosen <0.5 and/or a non-zero t_{ref} should be used.

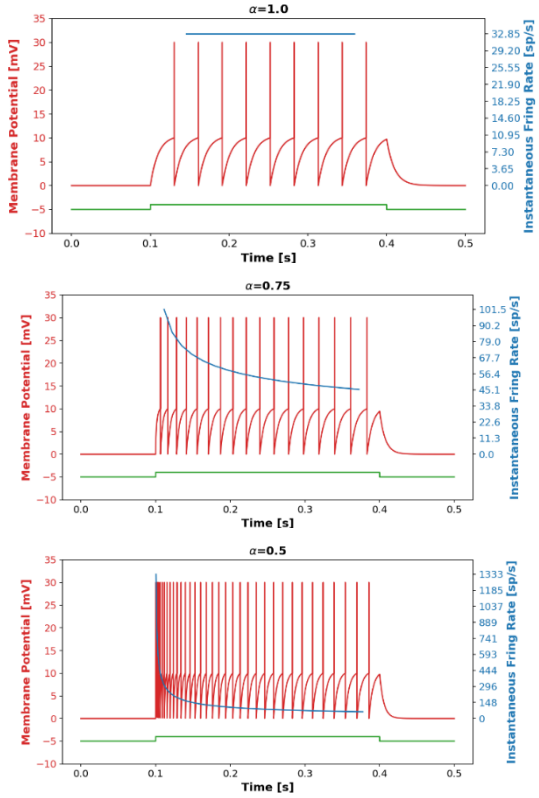

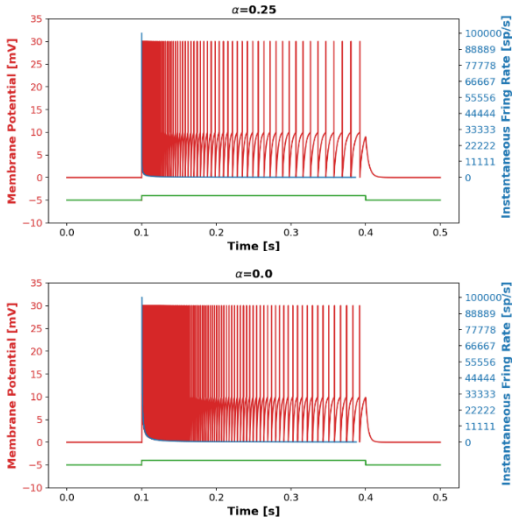

Figure 3 The CFD-based neuron model's membrane potential. Injected current was 0.21 nA, and α is varied between 0 and 1. Spikes are virtually demonstrated with a peak voltage of 30 mV. Stimulation period is shown with the green line

Although the adaptation rate seems to be increased with decreasing α, it actually didn't do so along the interval of α. Figure 4 shows the change of instantaneous firing rate normalized to its initial rate (i.e., r/r_{onset}). The adaptation rate increases with decreasing α until α=0.5, and then, it decreases with decreasing α. The same trend is observed with t_{ref} =0 ms and t_{ref} =5 ms. However, the adaptation rates were decreased for t_{ref} =5 ms.

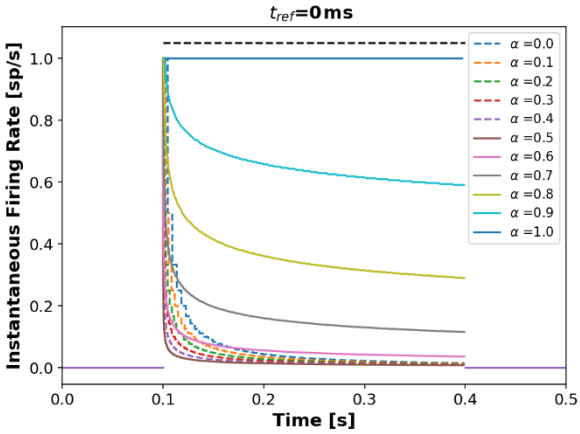

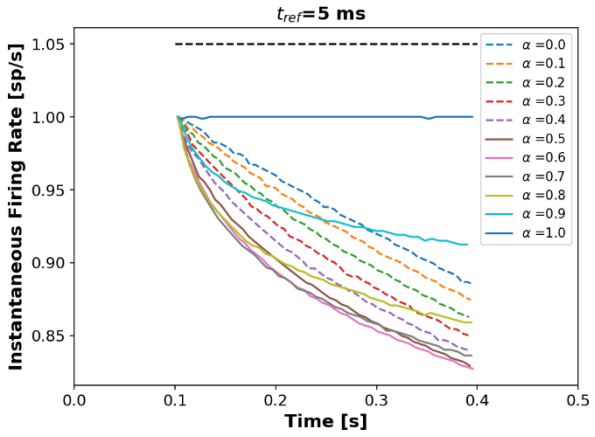

Figure 4 Adaptation profile of the model neuron. If refractoriness is ignored (upper panel; t_{ref}=0s), adaptation rate (rate of decrement of normalized instantaneous firing rat) increased with decreasing α until α=0.5, and then, it decreased as α was decreased further. Although a similar trend still exists with a refractory period of 5 ms (lower panel), the rate of adaptation significantly changed

In Figure 5, we inspected how the average firing rate of the model neuron changes with increasing stimulation current for different α values. As expected, the model doesn't fire until a certain threshold is reached (I_{TH}=0.2 nA with the chosen R and V_{TH}). Then, the firing rate increases with a decreasing rate. However, if the refractoriness is ignored, then the firing rate starts to exponentially increases after a certain input current. This is inconvenient with the behavior of the physiological neurons. On the other hand, if refractoriness is accounted for, then the firing rate plateaus at $1/t_{ref}$.

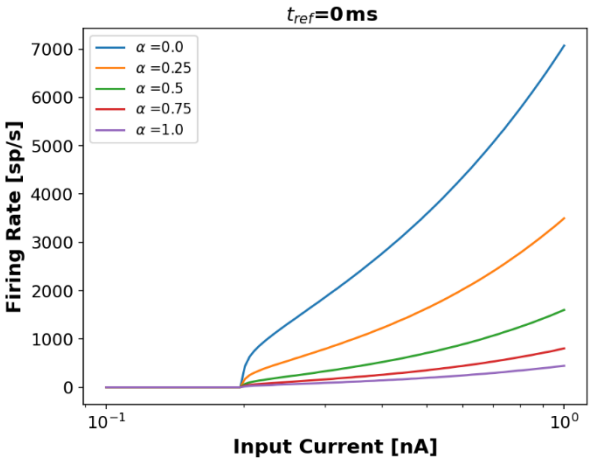

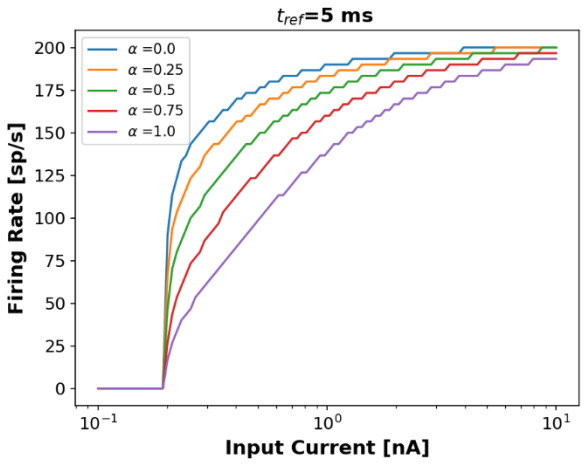

Figure 5 Change of average firing rate with increasing stimulation current. If the refractoriness is ignored (upper panel), then the firing rate doesn't reach a plateau but increases with increasing stimulation current. If a refractory period is chosen (lower panel; t_{ref}=5 ms), then the firing rate plateaus at $1/t_{ref}$

5. CONCLUSION

In this study, we demonstrated a conformal fractional derivative-based leaky integrate-and-fire neuron model. The model equations are easier and more efficient to implement compared to other fractional derivative-based models in literature. Additionally, it shows the adaptation behavior that is observed in physiological neurons and other fractional-order neuron models [35-37]. However, the model parameters, especially t_{ref} and α, should be chosen with care. For example, α values in the range of [0.5, 1.0] would probably result in more physiologically consistent spike patterns. Because the $t^{1-\alpha}$ term in the model equation radically increases the charge rate of the capacitor, if α<0.5. For example, if α is zero, then the initial rate of change in membrane potential would approximately be $I_S/(C_\alpha \Delta t^{1-\alpha})$ where Δt is the step size of the simulation. On the other hand, using a refractory period also limits the initial firing rate, therefore, resulting in a more physiologically consistent spiking pattern. Additionally, the difference in adaptation profile for α<0.5 and α>0.5 can be used in favor of modeling purposes (with a t_{ref}>0). For example, slowly adapting mechanoreceptive fibers innervating Merkel cells (SA-I) and Ruffuni endings (SA-II) in the skin shows adaptation

under sustained indentation of the skin [40,41]. However, the fibers innervating these two types of mechanoreceptors differ in means of the rate and pattern of adaptation; SA-II fibers adapt to the sustained stimulus at a constant rate, while SA-I fibers' adaptation consists of two phases (first a stepper decrement and then relatively slower decrement) [41]. Therefore, SA-I afferents can be modelled with α values greater than 0.5, and SA-II fiber can be modelled with α values smaller than 0.5. Finally, due to its mathematical simplicity, the proposed model can also be used in microcontroller- or microprocessor-based emulators to demonstrate spiking of a neuron silica conditions [42,43].

Acknowledgements

We thank to editors and reviewers for their time and effort to evaluate our manuscript and for their valuable feedbacks.

Funding

The author (s) has no received any financial support for the research, authorship or publication of this study

The Declaration of Conflict of Interest/ Common Interest

No conflict of interest or common interest has been declared by the authors.

Authors' Contribution

The authors contributed equally to the study.

The Declaration of Ethics Committee Approval

This study does not require ethics committee permission or any special permission.

The Declaration of Research and Publication Ethics

The authors of the paper declare that they comply with the scientific, ethical and quotation rules of SAUJS in all processes of the paper and that they do not make any falsification on the data collected. In addition, they declare that Sakarya University Journal of Science and its editorial board have no responsibility for any ethical violations that may be encountered, and that this study has not been evaluated in any academic publication environment other than Sakarya University Journal of Science.

REFERENCES

[1] L. Lapicque, "Recherches quantitatives sur l'excitation electrique des nerfs traitee comme une polarization," Journal de Physiologie et de Pathologie Generalej, vol. 9, pp. 620-635, 1907.

[2] N. Brunel and M.C. Van Rossum, "Lapicque's 1907 paper: from frogs to integrate-and-fire," Biological Cybernetics, vol. 97, no. 5-6, pp. 337-339, 2007.

[3] A. L. Hodgkin and A. F. Huxley, "A quantitative description of membrane current and its application to conduction and excitation in nerve," The Journal of Physiology, vol. 117, no. 4, pp. 500-544, 1952.

[4] R. FitzHugh, "Impulses and physiological states in theoretical models of nerve membrane," Biophysical Journal, vol. 1, no. 6, pp. 445-466, 1961.

[5] J. Nagumo, S. Arimoto and S. Yoshizawa, "An active pulse transmission line simulating nerve axon," Proceedings of the IRE, vol. 50, no. 10, pp. 2061-2070, 1962.

[6] R. FitzHugh, "Mathematical models of excitation and propagation in nerve," Biological Engineering, vol. 1, no. 9, pp. 1-85, 1969.

[7] E. M. Izhikevich, "Simple model of spiking neurons," IEEE Transactions on Neural Networks, vol. 14, no. 6, pp. 1569-1572, 2003.

[8] E. M. Izhikevich, "Which model to use for cortical spiking neurons?" IEEE

Transactions on Neural Networks, vol. 15, no. 5, pp. 1063-1070, 2004.

[9] E. M. Izhikevich and F. Hoppensteadt, "Classification of bursting mappings,". International Journal of Bifurcation and Chaos, vol. 14, no. 11, pp. 3847-3854, 2004.

[10] E. M. Izhikevich, J. A. Gally and G. M. Edelman, "Spike-timing dynamics of neuronal groups," Cerebral Cortex, vol. 14, no. 8, pp. 933-944, 2004.

[11] B. Ross, "The development of fractional calculus 1695–1900," Historia Mathematica, vol. 4, no. 1, pp. 75-89, 1977.

[12] I. Podlubny "Fractional differential equations: an introduction to fractional derivatives, fractional differential equations, to methods of their solution and some of their applications," Elsevier, 1998.

[13] A. A. Kilbas, H.M Srivastava and J.J. Trujillo, "Theory and applications of fractional differential equations," Elsevier, 2006.

[14] A. Babiarz, A. Czornik, J. Klamka and M. Niezabitowski, "Theory and applications of non-integer order systems," Lecture Notes Electrical Engineering, vol. 407, 2017

[15] X.J. Yang, "General fractional derivatives: theory, methods, and applications," Chapman and Hall/CRC, 2019.

[16] T.J. Freeborn, "A survey of fractional-order circuit models for biology and biomedicine," IEEE Journal on Emerging and Selected Topics in Circuits and Systems, vol. 3, no. 3, pp. 416-424, 2013.

[17] G.W. Leibnitz, "Leibnitzen's Mathematische Schriften," Hildesheim, vol.2, pp. 301-302, 1962.

[18] A. Karcı, "Fractional order derivative and relationship between derivative and complex functions," Mathematical Sciences and Applications E-Notes, vol. 2, no. 1, pp. 44-54, 2004.

[19] R. Khalil, M. al Horani, A. Yousef, M. Sababheh, "A new definition of fractional derivative," Journal of Computational and Applied Mathematics, vol. 264, pp. 65–70, 2014.

[20] T. Abdeljawad, "On conformable fractional calculus," Journal of Computational and Applied Mathematics, vol. 279, pp. 57-66, 2015.

[21] D. Zhao and M. Luo, "General conformable fractional derivative and its physical interpretation," Calcolo, vol. 54, no. 3, pp. 903-917, 2017.

[22] R. Sikora, "Fractional derivatives in electrical circuit theory–critical remarks," Archives of Electrical Engineering, vol. 66, no. 1, pp. 155-163, 2017.

[23] M. Lewandowski and M. Orzyłowski, "Fractional-order models: The case study of the supercapacitor capacitance measurement," Bulletin of the Polish Academy of Sciences Technical Sciences, vol. 65, no. 4, pp. 449-457, 2017.

[24] R. Kopka "Estimation of supercapacitor energy storage based on fractional differential equations," Nanoscale Research Letters, vol. 12, no. 1, pp. 636, 2017.

[25] T. J. Freeborn, A. S. Elwakil and A. Allagui, "Supercapacitor fractional-order model discharging from polynomial time-varying currents," in 2018 IEEE International Symposium on Circuits and Systems (ISCAS), pp. 1-5, 2018.

[26] T. J. Freeborn, B. Maundy and A.S. Elwakil, "Measurement of supercapacitor fractional-order model parameters from voltage-excited step response," IEEE Journal on Emerging and Selected Topics in Circuits and Systems, vol. 3, no. 3, pp. 367-376, 2013.

[27] A. Kartci, A. Agambayev, N. Herencsar and K. N. Salama, "Series-, parallel-, and inter-connection of solid-state arbitrary fractional-order capacitors: theoretical study and

experimental verification," IEEE Access, vol. 6, pp. 10933-10943, 2018.

[28] E. Piotrowska, "Analysis the conformable fractional derivative and Caputo definitions in the action of an electric circuit containing a supercapacitor," in "Photonics applications in astronomy, communications, industry, and high-energy physics experiments 2018" vol. 10808, pp. 108081T, International Society for Optics and Photonics, 2018.

[29] U. Palaz and R. Mutlu, "Analysis of a capacitor modelled with conformable fractional derivative under dc and sinusoidal signals," Celal Bayar University Journal of Science, vol. 17, no. 2, pp. 193-198, 2021.

[30] A. A. H. A. Mohammed, K. Kandemir and R. Mutlu, "Analysis of parallel resonance circuit consisting of a capacitor modelled using conformal fractional order derivative using Simulink," European Journal of Engineering and Applied Sciences, vol. 3, no. 1, pp.13-18, 2020.

[31] U. Palaz and R. Mutlu, "Two capacitor problem with a lti capacitor and a capacitor modelled using conformal fractional order derivative," European Journal of Engineering and Applied Sciences, vol. 4, no. 1, pp. 8-13, 2021.

[32] E. Piotrowska, "Analysis of fractional capacitor and coil by the use of the Conformable Fractional Derivative and Caputo definitions," In 2018 IEEE International Interdisciplinary PhD Workshop (IIPhDW) (pp. 103-107), 2018.

[33] E. Piotrowska, "Analysis of fractional electrical circuit with sinusoidal input signal using Caputo and conformable derivative definitions," Poznan University of Technology Academic Journals. Electrical Engineering, vol. 97, pp.155-167, 2019.

[34] E. Piotrowska and L. Sajewski, "Analysis of an electrical circuit using two-parameter conformable operator in the Caputo sense," Symmetry, vol. 13, no. 5, pp. 771, 2021.

[35] B. N. Lundstrom, M. H. Higgs, W. J. Spain and A. L. Fairhall, "Fractional differentiation by neocortical pyramidal neurons," Nature Neuroscience, vol. 11, no. 11, pp. 1335-1342, 2008.

[36] W. Teka, T.M. Marinov and F. Santamaria, "Neuronal spike timing adaptation described with a fractional leaky integrate-and-fire model," PLoS Computational Biology, vol. 10, no. 3, pp. e1003526, 2014.

[37] O. Taşbozan and A. Kurt, "New exact solutions of fractional Fitzhugh-Nagumo equation," Journal of the Institute of Science and Technology, vol. 9, no. 3, pp. 1633-1645, 2019.

[38] W. Gerstner, W. M. Kistler, R. Naud and L. Paninski, "Neuronal dynamics: From single neurons to networks and models of cognition," Cambridge University Press, 2014.

[39] F. Amzica and D. A. G. Neckelmann,"Membrane capacitance of cortical neurons and glia during sleep oscillations and spike-wave seizures," Journal of Neurophysiology, vol. 82, no. 5, pp. 2731-2746, 1999.

[40] İ. Devecioğlu and B. Güçlü, "Asymmetric response properties of rapidly adapting mechanoreceptive fibers in the rat glabrous skin," Somatosensory & Motor Research, vol. 30, no. 1, pp. 16-29, 2013.

[41] E. P. Gardner and K. O. Johnson, "Touch" in E. R. Kandel, J. H. Schwartz, T. M. Jessell, S. A. Siegelbaum, and A. J. Hudspeth (Eds.), "Principles of neural science", 5th ed., pp. 498-529. New York: McGraw-Hill, 2012.

[42] I. Devecioglu, S. C. Yener and R. Mutlu, "Demonstration of synaptic connections with unipolar junction transistor based neuron emulators," International Journal of Engineering Transactions B: Applications, vol. 33, no. 11, pp. 2195-2200, 2020.

[43] F. Tulumbaci, M. H. Eryildiz and R. Mutlu, "A simple lapicque neuron emulator," in 6th International Conference on Electrical Engineering and Electronics (EEE'20) (13.08.2020-15.08.2020).

SAKARYA ÜNİVERSİTESİ
FEN BİLİMLERİ ENSTİTÜSÜ DERGİSİ

Sakarya University Journal of Science
SAUJS

ISSN 1301-4048 e-ISSN 2147-835X Period Bimonthly Founded 1997 Publisher Sakarya University
http://www.saujs.sakarya.edu.tr/

Title: Artificial Intelligence Based Determination of Cracks in Eggshell Using Sound Signals

Authors: Zekeriya BALCI, İsmail YABANOVA

Recieved: 2021-12-28 00:00:00

Accepted: 2022-05-06 00:00:00

Article Type: Research Article

Volume: 26
Issue: 3
Month: June
Year: 2022
Pages: 579-589

How to cite
Zekeriya BALCI, İsmail YABANOVA; (2022), Artificial Intelligence Based Determination of Cracks in Eggshell Using Sound Signals. Sakarya University Journal of Science, 26(3), 579-589, DOI: 10.16984/saufenbilder.848213
Access link
http://www.saujs.sakarya.edu.tr/tr/pub/issue/70993/848213

Sakarya University Journal of Science 26(3), 579-589, 2022

Artificial Intelligence Based Determination of Cracks in Eggshell Using Sound Signals

Zekeriya BALCI[1], İsmail YABANOVA[*2]

Abstract

Although the egg is a cheap food source, it is one of the valuable nutritional sources for people because of its rich nutritional values. It is also among the most consumed foods in daily nutrition. With the increase in egg production, it is very difficult to collect them with the human power in the egg production farms, to classify them according to their weights and to separate the defective (dirty and broken) eggs. Therefore, the mechanization has become a necessity in large capacity production farms. Cracks and fractures may occur in the egg shell as a result of exposure to external factors such as the transportation of eggs. The cracks or fractures that are formed leave the egg vulnerable to disease-causing micro-organisms. Before the egg sorting and packing, the broken and cracked eggs must be separated. This process is commonly carried out with manpower by which it is very difficult to obtain the necessary efficiency. In this study, the egg crack detection was performed by using Support Vector Machines (SVM) and Artificial Neural Network (ANN). As a result of the application of studied methods, the accuracy values of crack detection process were 0.99 for ANN and 1 for SVM. In addition, a data acquisition and processing program was developed in LABVIEW environment to detect cracks in real time.

Keywords: Cracked egg detection, artificial neural networks, support vector machines, LABVIEW.

* Corresponding author: iyabanova@gmail.com
[1] Van Yüzüncü Yıl University/Çaldıran Vocational School/Electronics And Automation Department
E-mail: balcizekeriya29@gmail.com
https://orcid.org/0000-0002-1389-1784,
[2] Manisa Celal Bayar University/Hasan Ferdi Turgutlu Technology Faculty/Electrical Engineering Department
ORCID: https://orcid.org/0000-0001-8075-3579

1. INTRODUCTION

Eggs are one of the basic foods preferred by people for their daily nutrition because of their rich nutrient content and low cost for which egg consumption is increasing. With the increase in egg consumption, the capacity increase in egg production farms is unavoidable and many machines have been developed due to increase in high production capacity. These machines carry out processes such as the collection, transport, and classification of eggs according to their weights, sorting of dirt, blood, and condition i.e. broken and cracked, based on some parameters. Cracks and fractures may occur in the egg shell when exposed to physical effects during the harvesting processes such as collection, transportation and packaging. The cracks in the egg shell can make the egg vulnerable to harmful micro-organisms. An infected egg may threaten the health of human beings and eliminate the food safety. In order to eliminate or minimize these problems caused by cracked eggs, it is important to detect and separate the cracked eggs at the production stage [1-3].

Studies for the detection of egg cracks have been focused on acoustic signal processing and image processing methods [4]. Many studies have been carried out for crack detection using acoustic signals from the mechanical effect applied to the eggshell that will not harm the egg. The Pearson correlation coefficient method was used to detect egg crack detection with 90% accuracy [5]. Acoustic signals obtained from the egg shell by applying the Support Vector Data Definition method, the egg crack detection was possible with 90% accuracy [6]. Wavelet transform application to acoustic signals obtained from eggshell and trained SVM with these data was reported that a crack detection with 98.9% accuracy was achieved [7]. A similar studied with the same principle of wavelet transform application to acoustic signals obtained from the egg shell the crack detection was reported with 95% accuracy [8]. They also emphasized that there are significant differences between the energy values of the signals in solid and cracked eggs. The transformation of the acoustic signals obtained from the egg into a frequency domain helped determine the cracks in the egg shell with the accuracy of 96.1% using the calibration model method. In another study, [9] reported that they performed cracked egg detection with 90% accuracy by applying Halanobis distance method to acoustic signals that they obtained from egg shells. The feature extraction was applied to acoustic signals obtained from brown and white eggs and examined them in time and frequency space [4]. Using these signals, they have trained the artificial intelligence model.

Another method used in the detection of cracked eggs has been the image processing method. Fang and Youxian [10] stated that they carried out the crack detection process with an accuracy of 88% through the images they obtained from the egg. They reported that they tried to detect cracks by using many image processing methods and that the best method for their studies was the morphological (structural) image processing method. In order to determine micro-cracks a vacuum suction force was applied to the egg by li et al [1] and who stated that micro-cracks in eggshell was detected with 100% accuracy with image processing methods. They also reported that their systems were for a single egg, that the light source had a significant effect on the result, and that the system speed was not suitable for the industry. Omid et al [11] determined egg crack detection using egg images and fuzzy logic method with 94.5% accuracy. Öztürk and Gangal [12] identified the defective and clean eggs by using image processing methods for the detection of dirt and crack in the egg shell with 93% accuracy, 92% of dirty eggs and 88% of cracked eggs.

In this study, crack detection process was performed in real time by using SVM and ANN method by using acoustic signals formed by application of a mechanical impact to the egg shell which does not cause any damage in egg shell. For the training of SVM and ANN methods, 50 cracked and 50 intact eggs were used. The training of ANN and SVM models was realized with 99% and 100% accuracy, respectively. In addition, the trained ANN and SVM models were tested in real time with 40 cracked, 60 intact egg samples, except for eggs

used for training, using real-time crack detection program. At the end of the testing procedure, the eggs were classified with the accuracy of 100%. In the literature, it was observed that the signals obtained from the egg shell were transferred to the frequency domain and then the feature was extracted and then crack detection was employed. In this study, the acoustic signals obtained from the egg shell were used without any pre-processing procedure and the crack detection process was carried out successfully.

2. MATERIAL AND METHOD

2.1. Experimental Setup

The experimental setup developed consists of power supply, operational amplifier and control circuit, CompactRIO (cRIO), software for collecting, analyzing and visualizing the data. Figure 1 shows the system developed for application. The following sections describe the components in detail.

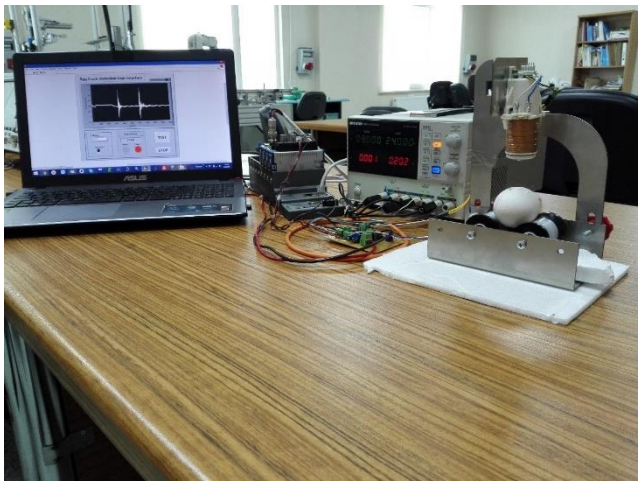

Figure 1 General view of system components

2.1.1. CompactRIO

The production of CompactRIO National Instruments (NI) is a configurable industrial controller for application with modular units [13],[14]. In this study, NI-9215 analog input module and NI-9375 digital input output module was used with cRIO 9074. cRIO technical specifications are given below.

• Operating voltage between + 19V DC and 30V DC.

• 400 MHz processor speed.

• 256 MB internal memory.

• Xilinx Spartan-3 2M FPGA.

• Ethernet and RS232 communication support.

• 8 modular units.

2.1.2. Egg Support Unit and Mechanical Impact Unit

The egg support unit and the mechanical impact unit where the egg is positioned are given in Figure 2. With this unit, a mechanical impact is applied to one egg placed on the rollers and the sound signals generated by this effect are collected with a microphone.

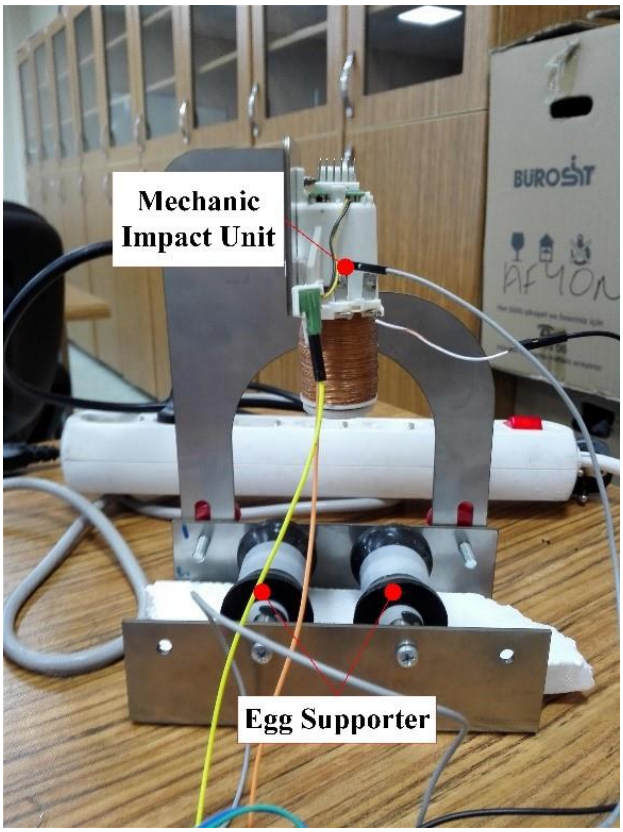

Figure 2 General view of egg support unit and mechanical impact unit

The mechanical impact or unit consists of a hollow tube on which a coil is wound and a

cylindrical hammer moves inside the tube. This moving part enables the formation of acoustic signals by a soft collision that will not damage the egg's shell, and this event is illustrated in Figure 3.

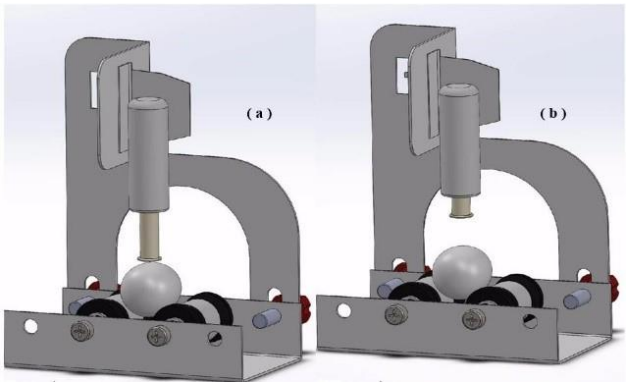

Figure 3 Impact position on egg (a), starting position (b)

2.1.3. Signal Amplifier and Control Circuit

In order to strengthen the acoustic signals obtained from the egg shell and to control the mechanical effect unit, an electronic card was designed using the L293D driver IC, the LN358N amplifier IC and the passive circuit elements required for the circuit is shown in Figure 4.

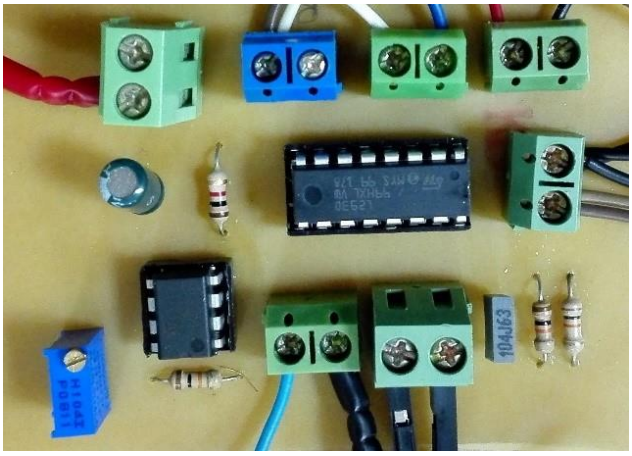

Figure 4 Signal amplifier and control circuit

2.2. Classification Method

2.2.1. Artificial Neural Networks

ANNs can be defined as structures created by human learning, the ability to hide the information learned, and the ability to mimic skills such as the ability to predict new data encountered by using learned knowledge [15-17].

ANN structures are systematic structures consisting of parallel processing capability and parallel connection process elements, connections belonging to the network and information stored. A simple ANN model is given in Figure 5. ANN entry and values of results are trained with the known training set. Following the training process, they are tested with the value of the output value they produce compared to the input value that they did not observe before and with the control of the error value according to the output value. ANNs have the advantages of being fault tolerant, learning by using examples, applicability to complex problems, compliance with real - time problem solutions [16-18].

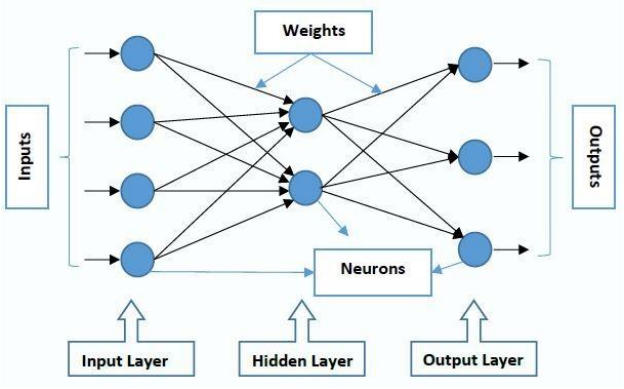

Figure 5 A simple artificial neural network sample diagram [15]

2.2.2. Support Vector Machines

The SVM aims to find the right to distinguish the problem samples into the classes they belong to, and based on statistical learning methods, which has been proposed by V. Vapnik as a theory in the 1960s [19]. Considering that each problem data is represented as a point in the data space, one can refer to the purpose of the SVM as to create a distinction plane that can distinguish the points of different classes [20, 21]. In Figure 6 (a), it can be seen that the two different classes can be drawn correctly. However, the SVM is to find the optimum (Fig. 6 (b)) separator plane that can distinguish the main objective problem data

at the maximum accuracy level [22]. SVM have been applied in many areas such as the classification of facial expressions, classification of types of deterioration in power quality, asynchronous motor broken rotor rod fault detection, face recognition, voice recognition [23-25].

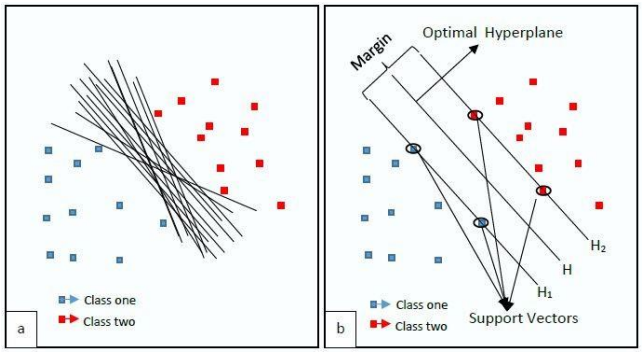

Figure 6 Lines that can separate samples (a) and optimal line (hyperplane) (b) for SVM [20], [27]

2.3. Developed Programs for Crack Detection

LABVIEW software, which is marketed as an object-oriented development environment by NI has been used for computerization of acoustic signals obtained from egg shell, visualization of triggering and manipulation of control signals [26]. For crack detection, a program has been developed primarily for data collection from the system. The data obtained from this program were developed in artificial intelligence training programs and training was provided for ANN and SVM. Then a program for real-time crack detection was developed. These programs are given under sub-headings.

2.3.1. Data Acquisition Program

The data acquisition program developed in the LABVIEW environment is given in Figure 7 to create the training data set which is necessary for the training of SVM and ANN structures created in this study. When the "Get Data" button is pressed, a mechanical impact is applied to the egg based on the sampling time specified and the resulting sound signal is received.

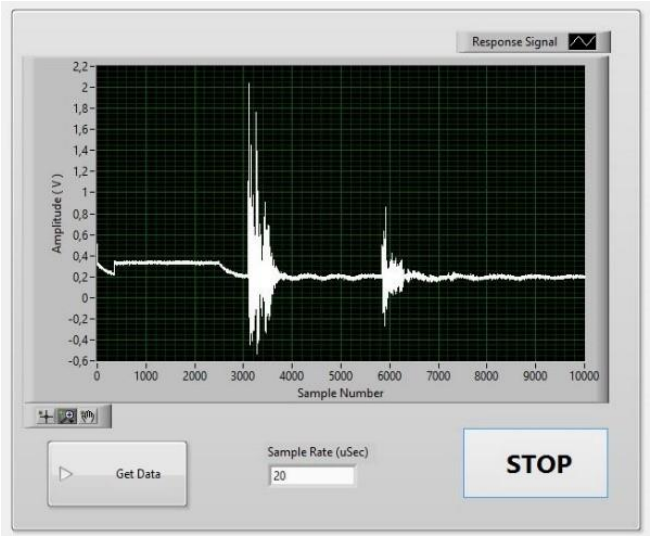

Figure 7 Data acquisition program developed in LABVIEW environment

2.3.2. AI Training Programs

For the training of ANN and SVM artificial intelligence models, LABVIEW program and AML (Analytics and Machine Learning Toolkit) tools developed by NI for LABVIEW software environment were used [27]. The programs prepared for the creation and training of ANN and SVM artificial intelligence models are shown in Figure 8 and Figure 9 respectively. By entering the desired parameters into these programs, the accuracy values generated by the training of the data set can be seen and ANN and SVM models can be saved.

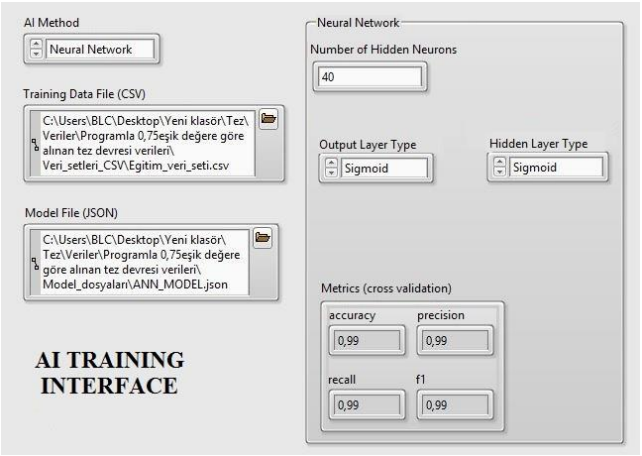

Figure 8 ANN training program

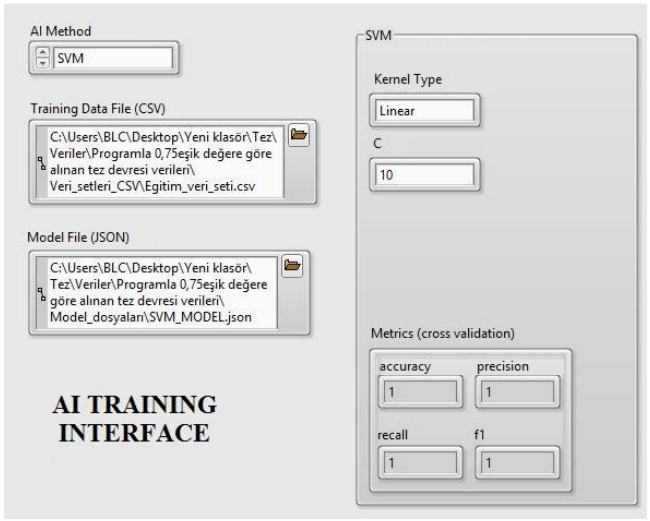

Figure 9 SVM training program

2.3.3. Real Time Crack Detection Program

The program developed in order to realize egg crack detection in real time using the trained SVM and ANN models is given in Figure 10. By pressing the "RUN" button, the card which controls the mechanical impact unit sends a signal for the mechanical effect to be performed. As a result of the mechanical impact, the acoustic signals from the egg are transferred to the computer via the experimental device. For cracked eggs, the mechanical impact was applied to cracked area or the vicinity of the cracked area. The response signal obtained during this process is shown in the "Response Signal" graph screen given in Figure 10. Then, the data belonging to the egg is obtained from the response signal according to the values entered in the threshold value and the number of data to be received in the program in Figure 10. Data is received according to threshold value, and then the egg response data is passed through the program to the selected classification method and, the classifier gives the class label for the egg and the process for an egg is completed.

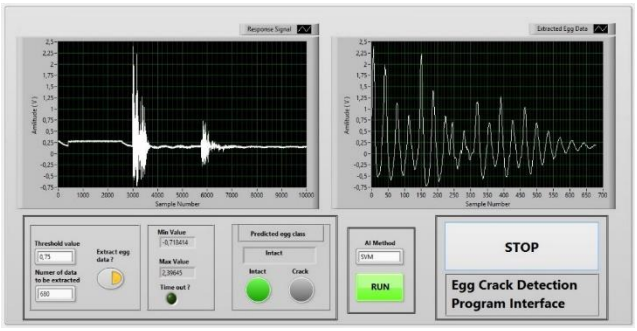

Figure 10 Real-time egg crack detection program

3. RESULTS AND DISCUSSIONS

In this study, the primary aim is to classify intact and cracked eggs correctly. For this purpose, a total of 200 eggs were purchased from the same supplier: M (53-63 g) quality class 90 cracked and 110 intact. A sample image of the purchased intact and cracked eggs is shown in Figure 11 and the response signal curves from the eggs are given in Figure 12.

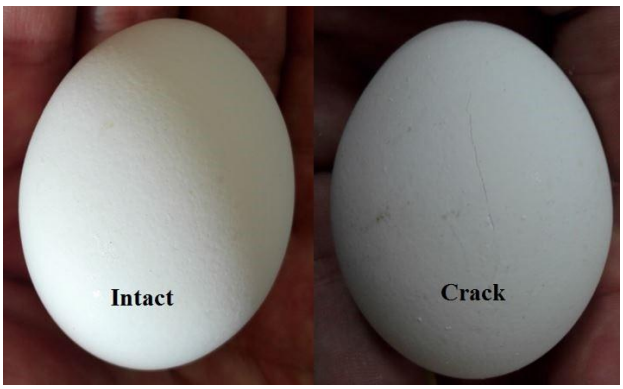

Figure 11 Sample egg images belonging to groups (intact and cracked)

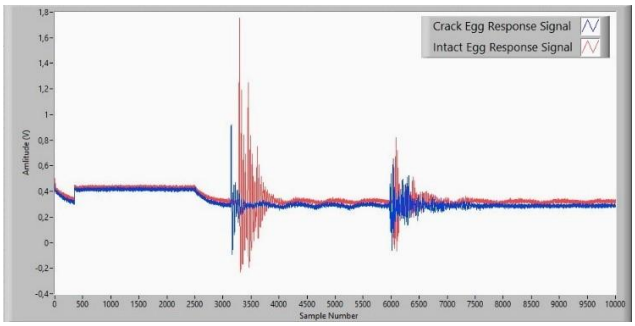

Figure 12 Response signal graphs of intact and cracked egg

Figure 11 shows the crack on the egg, however, some eggs may have micro cracks and these

cracks are not visible under normal conditions and atmospheric pressure. Figure 13 shows the image of an egg with a micro-crack in its circumference, marked by a yellow line.

Figure 13 Image of the egg under micro-cracking under normal pressure

As can be seen in Figure 13, there is no cracked area on the egg surface under atmospheric pressure prior to any external force or impact applied onto the egg. However, when a squeezing action of hand i.e. an external force is applied to the egg with a micro-crack, the cracked area becomes noticeable as shown in Figure 14. In addition, the fact that micro-cracks cannot be seen under normal pressure may be a problem in machine vision methods [1].

Figure 14 Image of micro-cracked egg under compression

For the training of SVM and ANN, 50 intact and 50 cracked eggs data were obtained with the program given in Figure 7. The data from the eggs were obtained as 10,000 sample points with a sampling frequency of 50 kHz. The response signal obtained from an intact egg is given in Figure 15.

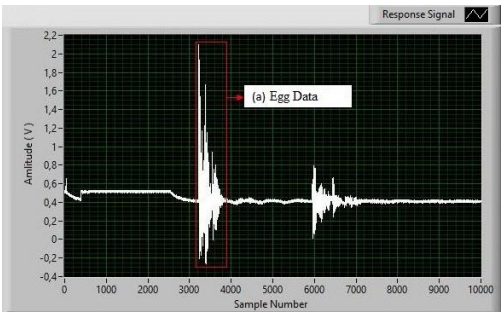

Figure 15 Intact egg response signal graph

In Figure 15, the data of the intact sample egg is indicated by (a). As can be seen in the figure, the response signal received from the egg contains noise signals along with the egg data, and signals from the testing environment. 680 data samples were selected starting from the first data point exceeding the 0.75V threshold value from the raw data. This way, the response signal at 10,000th sample point length is largely free of interference signals and 680 sample point length

egg data has been eventually obtained. In addition, the number of entries for the methods to be used for the classification by this process is also reduced. Figure 16 shows the response signal of the egg data cropped according to the threshold value.

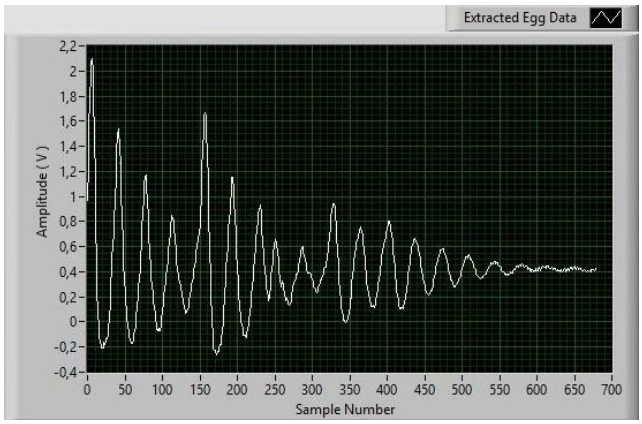

Figure 16 Egg signal obtained according to the threshold value

The data from cracked egg was obtained by applying a mechanical impact force perpendicular to the cracked area or its vicinity. However, sample data were collected away from the crack zone. In Figure 17, a cracked egg is marked with a cracked area and a point away from the cracked zone. Figure 18 is a graph of the signal (1) from the crack region and the signal (2) was obtained from the intact egg and signal (3) was obtained at the point away from the crack region given in Figure 17. On examining the signals from specimens given in Figure 18, the peak values in the response signal obtained from the point (3) away from the crack zone increased relative to the response signal (1) obtained from the crack zone and the duration of the signal is prolonged. In this context, the response signal graph obtained from the distal region was found to move away from the signal curve taken from the fracture zone and close to the intact egg response signal.

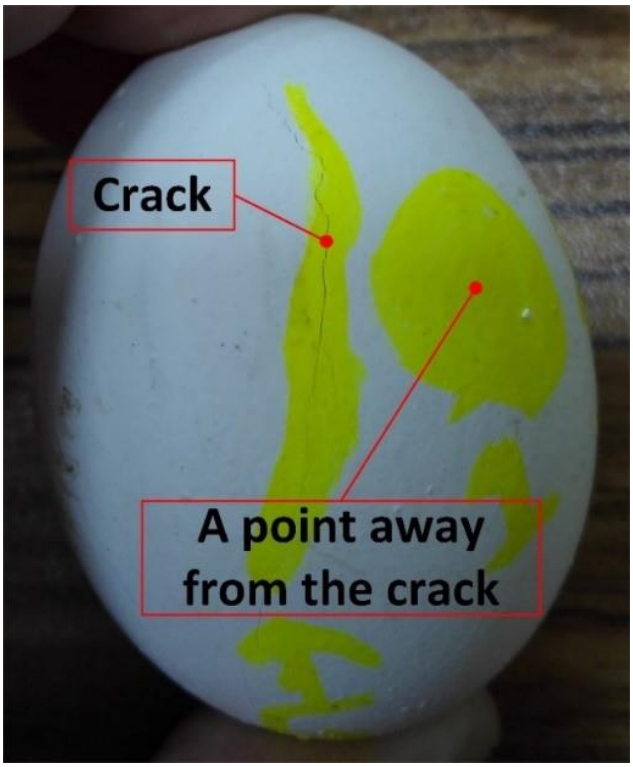

Figure 17 Image of a cracked region of a cracked egg and a point in the distance

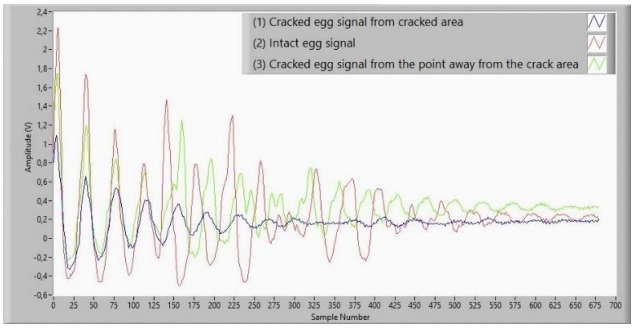

Figure 18 Intact egg and cracked signal from different points of the egg

In order to create the data sets for the training of SVM and ANN models, a total of 100 eggs data were collected, including 50 cracks and 50 intact eggs. The remaining 40 cracks and 60 intact egg samples were separated by the real-time egg crack detection program to further test the SVM and ANN structures. The data set consists of 680 sampling points collected at 20us sampling time. The program developed for the creation and training of ANN model is given in Figure 8. The implemented ANN model is feed-forward neural net that applies gradient descent algorithm which has one hidden layer. As can be seen from the figure 8, there are 40 neurons in the hidden layer

in the ANN model and sigmoid function was chosen as the activation function for the hidden and the output layer. The program algorithm divides the training data into three and allocates one-third of the remaining data for the test for training. The training process was carried out with a value of 0.99 as shown in the "Cross Verification Values" section of the given program. As can be seen in the figure 9, the linear function is selected as the kernel function for SVM structure and c, the value of the penalty parameter, is 10. The accuracy of the SVM model in the training process was 1.

For the real-time egg crack detection program in Figure 10, ANN and SVM models were tested in real time with 40 cracked, 60 intact egg samples. The test results showed that SVM and ANN models were found to correctly classify all 100 eggs into the classes they belong to and this process was realized in real time. While the estimation result for the ANN egg class was around 120 milliseconds, it was found that the SVM egg class estimation result produced around 20 milliseconds. It was stated that the training process had an accuracy of 1 for SVM and an accuracy of 0.99 for ANN. In this context, it can be claimed that in terms of training success and the duration of production of estimation result, SVM for this study gives better results than ANN.

4. CONCLUSIONS

Eggs are one of the main food sources. Eggs may contain cracks in their shells due to exposure to the processes such as harvesting, transporting and packaging in the egg production farms. The cracks can leave the egg vulnerable to bacteria and harmful microorganisms. In this study, it was aimed to determine the cracks of the eggs by using SVM and ANN artificial intelligence methods. During the formation of SVM and ANN models, 100 eggs were used, 50 of them were intact and 50 of them were cracked eggs. The training process of artificial intelligence methods was 0.99 for ANN and 1 for SVM. These accuracy values were found to be above the studies in the literature. In addition, a real time egg crack detection process in the LABVIEW environment has been developed. With the help of egg crack detection program, using 40 cracked and 60 intact eggs, which were not used in the training of ANN and SVM structures, were tested in real time. As a result of the test procedure, it was seen that eggs were classified correctly by both models. With the program developed within the scope of this study, it was possible to detect egg cracks in real time by the entering the egg data to SVM and ANN models without applying a pre-signal processing method. In addition, in terms of accuracy and the duration of production of the estimation result, it was observed that SVM model gave better results than the ANN model. It was concluded that both models would provide the desired high detection speed criterion easily in industrial applications.

Funding

The author has no received any financial support for the research, authorship or publication of this study.

The Declaration of Conflict of Interest/ Common Interest

No conflict of interest or common interest has been declared by the authors.

Authors' Contribution

The authors contributed equally to the study.

The Declaration of Ethics Committee Approval

This study does not require ethics committee permission or any special permission.

The Declaration of Research and Publication Ethics

The authors of the paper declare that they comply with the scientific, ethical and quotation rules of SAUJS in all processes of the paper and that they do not make any falsification on the data collected. In addition, they declare that Sakarya University Journal of Science and its

editorial board have no responsibility for any ethical violations that may be encountered, and that this study has not been evaluated in any academic publication environment other than Sakarya University Journal of Science.

REFERENCES

[1] Y. Li, S. Dhakal, Y. Peng, "A machine vision system for identification of micro-crack In eggshell", Journal of Food Engineering, vol. 109, pp. 127-134, 2012.

[2] J. Strnková, Š. Nedomová, "Eggshell crack detection using dynamic frequency analysis", MENDEL International Conference on Soft Computing, Brno, pp. 603-608, 2013.

[3] L. Sun, X.K. Bi, H. Lin, J.W. Zhao, J.R. Cai, "On-line detection of eggshell crack based on acoustic resonance analysis", Journal of Food Engineering, vol. 116, no. 1, pp. 240-245, 2013.

[4] H. Wang, J. Mao, J. Zhang, H. Jiang, J. Wang, "Acoustic feature extraction and optimization of crack detection for eggshell", Journal of Food Engineering, vol. 171, pp. 240-247, 2016.

[5] B. De Ketelaere, P. Coucke, J. De Baerdemaeker, "Eggshell crack detection based on acoustic resonance frequency analysis, Journal of Agricultural Engineering Research, vol. 76, no. 2, pp. 157-163, 2000.

[6] H. Lin, J.W. Zhao, Q.S. Chen, J.R. Cai, P. Zhou, "Eggshell crack detection based on acoustic response and support vector data description algorithm", European Food Research and Technology, vol. 230, no. 1, pp. 95-100, 2009.

[7] X. Deng, Q. Xiaoyan, H. Chen, H. Xie, "Eggshell crack detection using a wavelet-based support vector machine", Computers and Electronics in Agriculture, vol. 70, no. 1, pp. 135-143, 2010.

[8] P. Li, Q. Wang, Q. Zhang, S. Cao, Y. Liu, T. Zhu, "Non-destructive detection on the egg crack based on wavelet transform", International Conference on Future Computer Supported Education, Seoul, pp. 372-382, 2012.

[9] C. Jin, L. Xie, Y. Ying, "Eggshell crack detection based on the time-domain acoustic signal of rolling eggs on a step-plate", Journal of Food Engineering, vol. 153, pp. 53-62, 2015.

[10] W. Fang, W. Youxian, "Detecting preserved eggshell crack using machine vision", International Conference of Information Technology-Computer Engineering and Management Sciences, ICM, Nankin, pp. 62-65, 2011.

[11] M. Omid, M. Soltani, M. H. Dehrouyeh, S. S. Mohtasebi, H. Ahmadi, "An expert egg grading system based on machine vision and artificial intelligence techniques", Journal of Food Engineering, vol. 118, no. 1, pp. 70-77, 2013.

[12] N. Öztürk, A. Gangal, "Görüntü işleme teknikleri ile beyaz yumurtalar üzerindeki yumurta kabuğu kusurlarının algılanması", 22nd Signal Processing and Communications Applications Conference, Trabzon, pp. 810-813, 2014.

[13] Wikipedia, "CompactRIO", Available: https://en.wikipedia.org/wiki/CompactRIO, [Accessed: May 28, 2018].

[14] National Instruments, "CompactRIO", Available: http://www.ni.com/compactrio/, [Accessed: December 23, 2017].

[15] E. Öztemel, "Yapay Sinir Ağları", Papatya Yayınclık, Istanbul, Turkey, 2006.

[16] A. Yangın, "Yapay sinir ağı teknikleri kullanarak eğitim yayıncılığı sektöründe

veri madenciliği", M.S. thesis, Comp. Eng. Dept., Aydın Univ., İstanbul,Turkey, 2017.

[17] Ö. F. Sezer, "Sürekli tavlama hatlarında enerji giderinin kalite ve boyut değerlerine göre optimize edilmesi ve geçişlerde operatör davranışlarının modellenmesi", Ph.D. diss., Sakarya Univ., Sakarya, Turkey, 2017.

[18] A. Aksakal, "Türkiye'deki resmi dairelerde talep tarafı yönetimi ve yapay zeka uygulamaları", M.S. thesis, Kırıkkale Univ., Kırıkkale, Turkey, 2017.

[19] Ö. Karal, "Destek vektör regresyon ile EKG verilerinin sıkıştırılması", Journal of the Faculty of Engineering and Architecture of Gazi University, vol. 2, pp. 742-756, 2018.

[20] A. Yahyaoui, "Göğüs hastalıklarının teşhis edilmesinde makine öğrenmesi algoritmalarının kullanılması", Ph.D. diss., Sakarya Univ., Sakarya, Turkey, 2018.

[21] E. Tuncer, "Uyku evrelemesinde çeşitli dalgacık ve sınıflandırıcıların performans analizi", M.S. thesis, Kocaeli Univ., Kocaeli, Turkey, 2015.

[22] İ. Yabanova, M. Yumurtacı, "Destek vektör makineleri kullanarak dinamik yumurta ağırlıklarının sınıflandırılması", Journal of the Faculty of Engineering and Architecture of Gazi University, vol. 33, no. 2, pp. 393-402, 2018.

[23] T. Güneş, P. Ediz, "Yüz ifade analizinde öznitelik seçimi ve çoklu SVM sınıflandırıcılarına etkisi", Journal of the Faculty of Engineering and Architecture of Gazi University", vol. 24, no. 1, pp. 7-14, 2009.

[24] İ. Aydın, M. Karaköse, E. Akın, "Zaman serisi veri madenciliği ve destek vektör makinalar kullanan yeni bir akıllı arıza sınıflandırma yöntemi", Journal of the Faculty of Engineering and Architecture of Gazi University, vol. 23, no. 2, pp. 431-440, 2008.

[25] S. Ekici, S. Yildirim, M. Poyraz, "Energy and entropy-based feature extraction for locating fault on transmission lines by using neural network and wavelet packet decomposition", Expert Systems with Applications, vol. 34, no. 4, pp. 2937-2944, 2008.

[26] A. Kutlu, C. Turan, "Elektronik deney modüllerinin LabView ile kontrolü", Süleyman Demirel Üniversitesi Uluslararası Teknolojik Bilimler Dergisi, vol. 2, no. 3, pp. 1-8, 2010.

[27] National Instruments, "LabVIEW analytics and machine learning toolkit", Available: http://sine.ni.com/nips/cds/view/p/lang/en/nid/216169 /, [Accessed: March 14, 2018].

[28] N. Bagherzadi, "Post-operative prognostic prediction of esophageal cancer cases using bayesian networks and support vector machines" M.S. thesis, Middle East Tech. Univ., Ankara, Turkey, 2014.

SAKARYA ÜNİVERSİTESİ
FEN BİLİMLERİ ENSTİTÜSÜ DERGİSİ

Sakarya University Journal of Science
SAUJS

ISSN 1301-4048 e-ISSN 2147-835X Period Bimonthly Founded 1997 Publisher Sakarya University
http://www.saujs.sakarya.edu.tr/

Title: Thermal Effect Estimation of Smartphone Virtual Reality Headsets on Human Eye by Finite Element Method

Authors: Niyazi ULUAYDIN, Selim ŞEKER

Recieved: 2021-07-18 00:00:00

Accepted: 2022-05-06 00:00:00

Article Type: Research Article

Volume: 26
Issue: 3
Month: June
Year: 2022
Pages: 590-599

How to cite
Niyazi ULUAYDIN, Selim ŞEKER; (2022), Thermal Effect Estimation of Smartphone Virtual Reality Headsets on Human Eye by Finite Element Method. Sakarya University Journal of Science, 26(3), 590-599, DOI: 10.16984/saufenbilder.972989
Access link
http://www.saujs.sakarya.edu.tr/tr/pub/issue/70993/972989

Sakarya University Journal of Science 26(3), 590-599, 2022

Thermal Effect Estimation of Smartphone Virtual Reality Headsets on Human Eye by Finite Element Method

Niyazi ULUAYDIN*[1], Selim ŞEKER[2]

Abstract

Smartphones (SP) terminals are becoming the most popular media for virtual reality (VR) and augmented reality (AR) effects with their central processing unit (CPU) and video capabilities. Simple VR headsets with reasonable costs can host smartphones, and they can together be used for many different applications. But with the outbreak of Covid-19 pandemic, their usage has become essential for many people working from their homes. VR and AR capabilities provide a much richer experience for entertainment, gaming, and video conferencing. The increasing popularity of 3D virtual worlds add up to this usage. On the technology side, multi-radio connectivity is supported both on terminal and network side. A certain risk may arise when using SP VR headsets for such applications requiring a broadband Internet connectivity. SPs with multi-radio connectivity feature may elevate specific absorption rate (SAR) values in those cases. The smartphone used for VR and AR applications is positioned in front of the eyes; and there is very limited ventilation in VR/AR headsets. Authors' model aims simulate these exposure scenarios in 4G and 5G mobile telecommunication frequencies by finite element method (FEM); and, possible thermal and non-thermal risks of related electromagnetic (EM) radiation on human eye according to the outputs of the model are discussed.

Keywords: Electromagnetic radiation effects, SAR, smartphone, Virtual Reality headset, Thermal effects on human eye, 5G.

1. INTRODUCTION

The SP terminals and the mobile telecommunication technologies both have great developments in recent years. The number of mobile users has passed beyond 5 billion as of 2022 [1]. On the terminal side, SPs are now equipped with more powerful processors and with much higher resolution displays. Similarly, the new generation mobile telecommunication

* Corresponding author: korkut@uluaydin.com
[1] Boğaziçi University
ORCID: https://orcid.org/ 0000-0002-9512-0077
E-mail: selim.seker@uskudar.edu.tr
[2] Üsküdar University/Faculty of Engineering and Natural Sciences/Department of Electrical-Electronics Engineering
ORCID: https://orcid.org/ 0000-0002-0980-3219

technologies can now support broadband Internet connectivity with much lower latencies. In order to sustain the broadband access in dense urban area, the mobile telecommunication industry supports mobile broadband Internet connectivity by the fixed line broadband Internet access through a secondary wireless local area network (WLAN/Wi-Fi) technology. For this reason, almost all new SP terminals support two simultaneously working radio units.

The SP AR/VR headset users have dramatically increased during the corona virus disease 2019 (COVID-19) pandemic for social distancing reasons and is expected to pass beyond 1 billion users in 2022 [2,3]. In the case of ~~a~~ SP VR headset usage, the application would generally require broadband Internet access. In new classes of SP terminals, which are supporting two simultaneous radio accesses such as Wi-Fi and Long Term Evolution (LTE/4G or 5G or beyond) concurrently, high data throughputs can be achieved [. The SP VR headset hosts the SP terminal right before the eyes. The headsets are made of lightweight materials, and these materials have little or no electromagnetic (EM) shielding properties. Therefore, there will be EM radiation exposure from a very short distance at a right angle. Secondly, most of the SP VR headsets fully limit the natural air flow to block the ambient light from surroundings for a better visual experience. Since the subject human will supposedly have a visual experience on a SP VR headset for a certain period, the wireless connectivity will be on for the same period. This kind of usage can build up higher than normal thermal heating from EM radiation.

In this study, the authors are going to simulate these thermal effects on human eye by finite element method (FEM). This EM effect can be detrimental especially on eyes, since human eye cools itself by corneal evaporation and retinal blood perfusion [4,5]. Lacking any of those would increase the temperatures to levels that could pose immediate risks. One may presume retinal blood perfusion unchanged, whereas SP headset surely limits the natural cooling of the eyes with ambient air. Our literature survey has not come across with any studies on the subject.

The rest of the paper is organized as follows: Section 2 describes employed simulation model and methodology; Section 3 presents simulation results; Section 4 provides the brief discussion of the simulation results, and finally Section 5 discusses experimental findings and its possible thermal and non-thermal effects on human eye.

2. SIMULATION MODEL AND METHODOLOGY

2.1. Simulation Model

We have used the IEEE head phantom model for Specific Absorption Rate (SAR) calculation in the simulation software Comsol Multiphysics (MP) 4.3 (FNL License No: 17073372) [5]. Comsol MP is based on finite element method (FEM). FEM approach has a high computational complexity, but it defines objects with curvature better than the finite difference time domain method (FTDT) [5,7]. For the eye part, we have used the realistic three-dimensional (3D) eye model by Bobby Dyer from the web [8]. We have simplified this eye model as if eye tissue is either sclera or vitreous humour to decrease the immense computational load. And finally, this eye model is embedded as a separate domain into the IEEE head phantom model in our simulation software (Figure 1) [6-8].

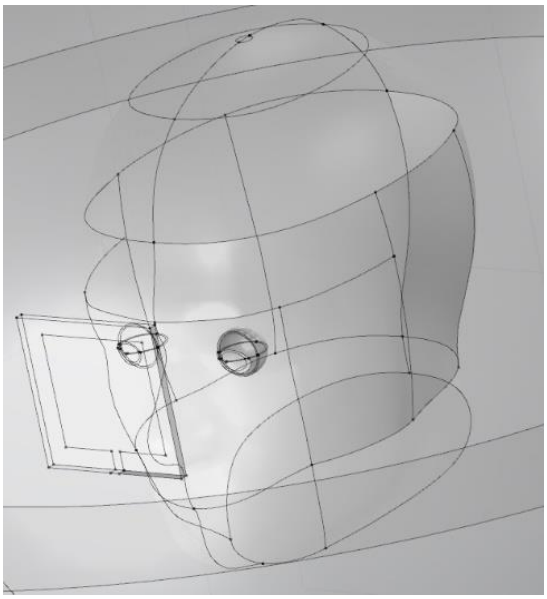

Figure 1 IEEE head phantom model with eyes.

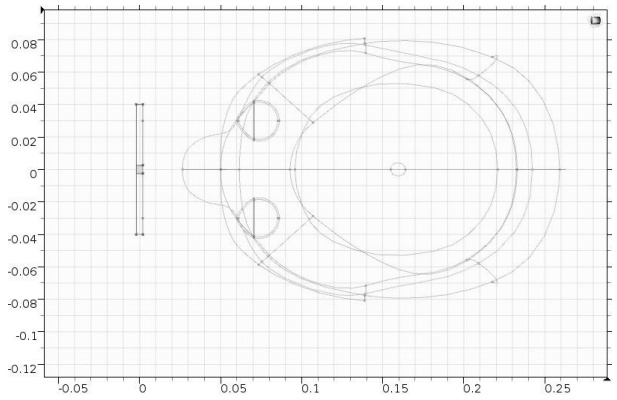

Figure 2 Top-down view of central antenna position at 5cm according to IEEE head phantom model with eyes (all values in meter).

Two uniform lump ports are used to resemble the SP EM sources with nominal output powers as in the original model SAR setting with equal powers of 1.6 W to match the smartphone SAR limit [9]. One of the EM sources is fixed at Wi-Fi frequency on 2.45 GHz, and the other EM source is parametric at mobile telecommunication frequency bands of 4G and 5G at 800, 900, 1800, 2100, 2300, and 2600 MHz. We have assumed both antennas to be in the same position in the central axis of eyes vertically and in central plane of eye, horizontally (Figure.2). On the side antenna scenario, both antennas are horizontally shifted 0.03 m from the central axis to align with one of the eyes. The distance from antenna to the phantom model is also parametric to investigate the effects of EM propagation and heating in the eye from different SP VR headsets.

The SAR model solves the vector Helmholtz equations in the head and eye domains for each of the frequencies and transfers the SAR solution onto the Pennes' bioheat equation to calculate the corresponding temperature rise in related domains [7].

2.2. Simulation Parameters and Settings

Our IEEE phantom model uses the 3D magnetic resonance imaging-based tissue separation [10] to use appropriate blood perfusion, conductivity, and permittivity properties for brain [11, 12]. We take the retinal blood perfusion rate to be the same with brain (Table.1).

Table 1 Human Head Tissue Blood Perfusion Rates.

Part	Perfusion Rate
Brain	2·10-3 (ml/s)/ml
Bone	3·10-4 (ml/s)/ml
Skin	3·10-4 (ml/s)/ml

Table 2 Tissue Conductivity Values [S/m].

Frequency (MHz)	Sclera	Vitreous Humour	Brain
800	1.130272	1.608266	0.730524
900	1.166726	1.636162	0.766504
1800	1.601727	2.032478	1.15308
2100	1.789117	2.221833	1.310172
2300	1.925249	2.363649	1.422798
2450	2.033048	2.478094	1.511336
2600	2.145607	2.599401	1.603296

Table 3 Tissue Relative Permittivity Values

Frequency (MHz)	Sclera	Vitreous Humour	Brain
800	55.561417	68.925781	46.251328
900	55.27013	68.90184	45.805496
1800	53.567787	68.573364	43.544899
2100	53.125057	68.417976	43.054611
2300	52.839252	68.301758	42.754364
2450	52.627628	68.208023	42.538925
2600	52.417377	68.108711	42.329929

We have modelled the eye as a single tissue. Thus, we have used two sets of conductivity (σ) and relative permittivity (ε_r) to understand the effects representing the eye as if it is sclera only (lower water content) or vitreous humour only (higher water content) (Table 2-3). In the simulations, all frequency dependent values are piecewise linearly interpolated between 800 and 2600 MHz values.

As mentioned before, the SP VR headsets limit the airflow inside. The SP also produces heat towards the face by its display. In our samplings, we have found out that the SP VR headset inner volume was equal or less than 0.0015 m^3. During its operation, the air inside the SP VR headset will have high vapor pressure in a short time with corneal and epidermal evaporation. Naturally, further evaporation from the cornea surface will be limited. For these reasons, we have taken the eye-air boundary as thermal insulation. Finally,

we have totally neglected eye movement in VR usage.

We set the simulation environment to be under standard pressure at 25°C, and the temperature scale is normalized to 0 to represent the fluctuation from the nominal biological base temperature of 37°C. The heat capacity of blood is taken as 3639 J/(kg·K) and the density of blood is taken as 1000 kg/m³.

There has been extensive academic research on human eye temperature distribution [4, 5, 13-15]. Infrared detection, which is the most recent and non-invasive empirical technique, has shown that the cornea surface temperature for human eye can be referred as 34.3°C [5]. Similarly, the retinal blood temperature can be referred as 37°C [5, 13]. We have set the initial conditions of the simulation respective to these figures, which have a great effect on the outcome for different domains.

The simulations used one frequency of the radio units fixed at 2450 MHz representing the wireless connection, whereas the other radio unit frequency spanned the frequencies of 800, 900, 1800, 2100, 2300, and 2600 MHz, representing the mobile network connection. Eye tissue has been simulated as either it is made of all sclera or vitreous humour. The distance is calculated by the gap between the antennas and the forehead in the model. There is an additional 1 cm depth difference between the forehead and the eye. Having sampled different SP VR headsets, we have decided to make different simulations at 4 different distance values as 2, 3, 5, and 7 cm, which were dominant in our VR gap sampling.

3. SIMULATION OUTCOMES AND THEIR DISCUSSIONS

3.1. Simulation Outcomes

We have made the simulation over 4 different distances running over a 60- minute exposure to detect distance effects and possible saturation times. The general saturation values were around 15th minute. For lower frequencies with higher tissue penetration the retinal part of the eye could build up more heat until the 20th minute. For higher frequencies, the saturation happened around the 12th minute mark. The highest rise in temperature was observed at 5 cm for central antenna position and at 3 cm for side antenna position. Finally, the tissue type also affects the temperature rise.

In figures 3, 4, and 5, one can observe the temperature increase from concurrent 2450 MHz and 2600 MHz EM sources. Figure 5 shows the whole model, whereas figures 3 and 4 show the eye domain isolated from the rest of the phantom to visualize the temperature distribution in detail.

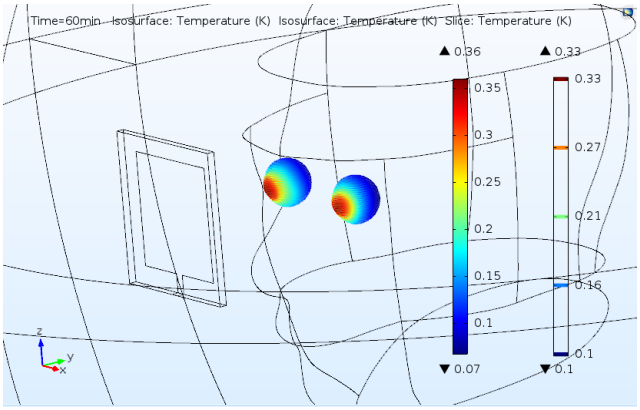

Figure 3 Isosurface temperature rise plot in human eye as vitreous humour tissue only exposed to 2450 MHz-2600 MHz with central antennas at 5 cm.

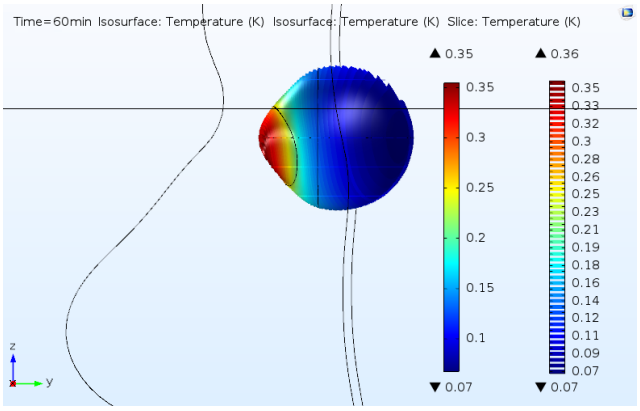

Figure 4 Side-view 25 slice isosurface temperature rise plot in human eye as vitreous humour tissue only exposed to 2450 MHz-2600 MHz with central antennas at 5 cm.

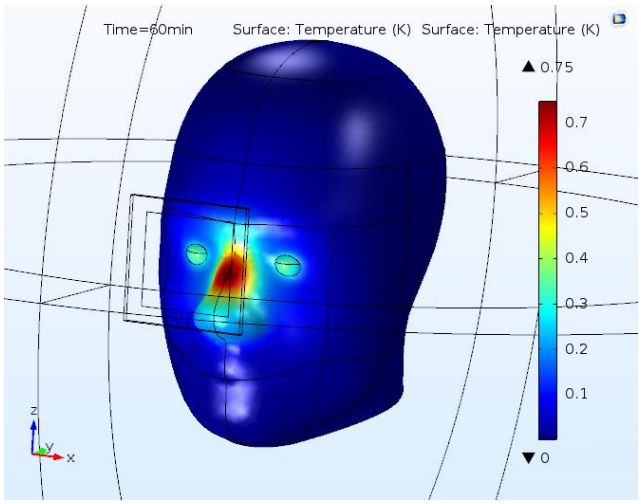

Figure 5 Surface temperature rise plot in human eye as vitreous humour tissue only exposed 2450 MHz-2600 MHz with central antennas at 5 cm.

In tables 4 and 5, one can observe the corneal and retinal temperature increase at 5 cm distance between the face and the SP terminal. The highest temperature increase happens at 5 cm with vitreous humour tissue only eye domain with 0.07 ^{o}C (Table 5).

Table 4 Simulation results at 5 cm with central antennas (eye tissue-sclera).

Frequency (MHz)	Corneal Temp.	Retinal Temp.
800-2450	0.12 ^{o}C	0.03 ^{o}C
900-2450	0.14 ^{o}C	0.03 ^{o}C
1800-2450	0.16 ^{o}C	0.03 ^{o}C
2100-2450	0.23 ^{o}C	0.05 ^{o}C
2300-2450	0.20 ^{o}C	0.05 ^{o}C
2450-2600	0.34 ^{o}C	0.06 ^{o}C

Table 5 Simulation results at 5 cm with central antennas (eye tissue-vitreous humour).

Frequency (MHz)	Corneal Temp.	Retinal Temp.
800-2450	0.14 ^{o}C	0.03 ^{o}C
900-2450	0.16 ^{o}C	0.03 ^{o}C
1800-2450	0.17 ^{o}C	0.03 ^{o}C
2100-2450	0.25 ^{o}C	0.05 ^{o}C
2300-2450	0.21 ^{o}C	0.05 ^{o}C
2450-2600	0.35 ^{o}C	0.07 ^{o}C

3.2. Simulation Outcomes' Discussions

The simulations have shown interesting results. The corneal temperature increase has reached 0.35^{o}C at a distance of 5 cm from face with 2450-2600 MHz pair in central antennas scenario (Figure 6). In the side antennas scenario, the corneal temperature increase has further reached 0.7^{o}C at a distance of 3 cm from face with 2450-2600 MHz pair (Figure 7). It is important remember that natural cornea temperature is 34.3^{o}C and the initial conditions are set accordingly as 2.7^{o}C below nominal body temperature of 37 ^{o}C. So, there is a total increase of 3.05^{o}C with central antennas and 3.41^{o}C with side antennas, respectively. To assess this risk, one should consider other factors as blinking rate and evaporation rate.

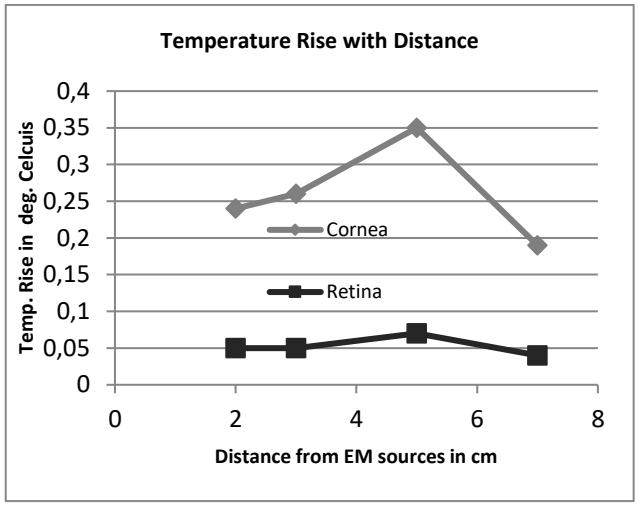

Figure 6 Temperature rise plot in human eye as vitreous humour tissue only exposed to 2450 MHz-2600 MHz central antennas at varying distances.

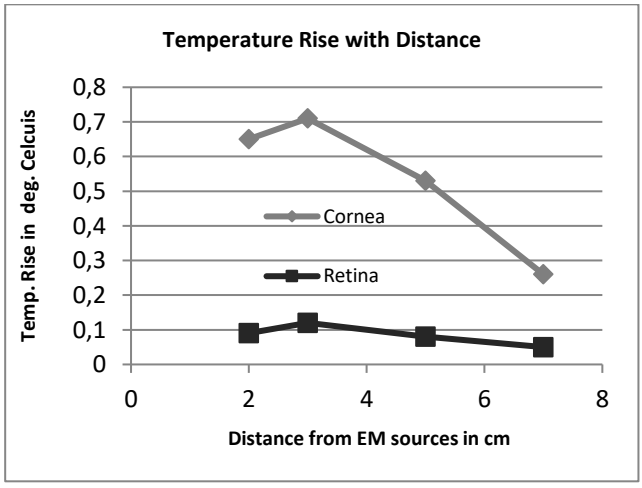

Figure 7 Temperature rise plot in human eye as vitreous humour tissue only exposed to 2450 MHz-2600 MHz side antennas at varying distances.

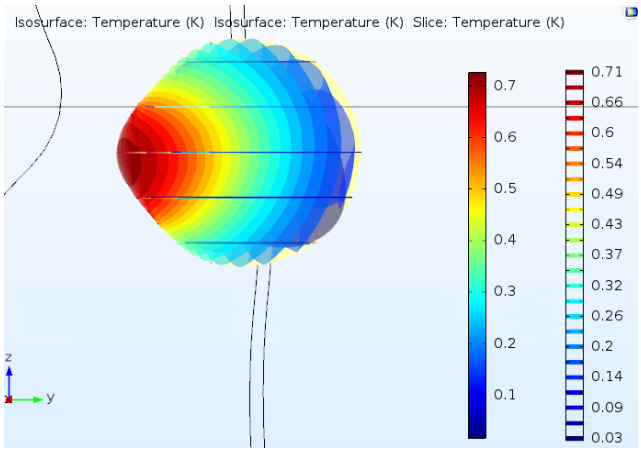

Figure 8 Side-view 25 slice isosurface temperature rise plot in human eye as vitreous humour tissue only exposed to 2450 MHz-2600 MHz with side antennas at 3 cm.

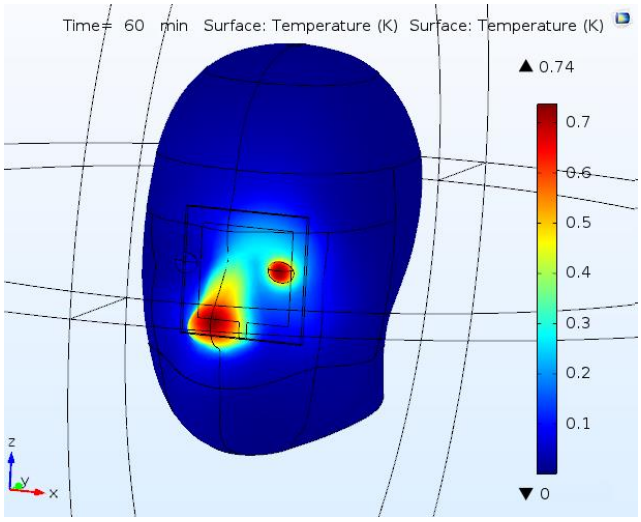

Figure 9 Surface temperature rise plot in human eye as vitreous humour only tissue exposed to 2450 MHz-2600 MHz with side antennas at 3 cm.

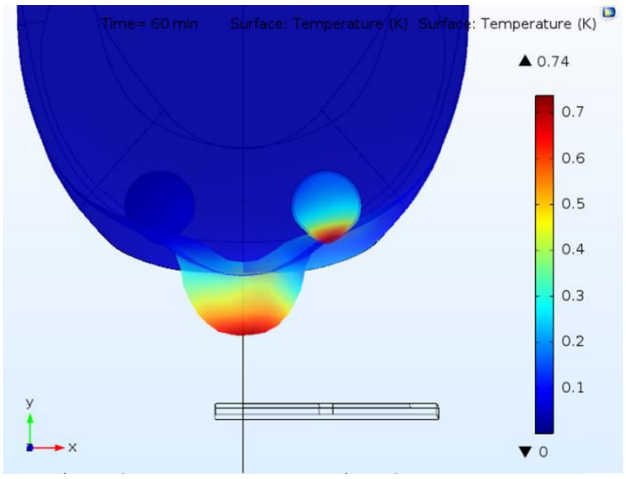

Figure 10 Transparent top-down view temperature rise plot in human eye as vitreous humour tissue only exposed to 2450 MHz-2600 MHz with side antennas at 3 cm.

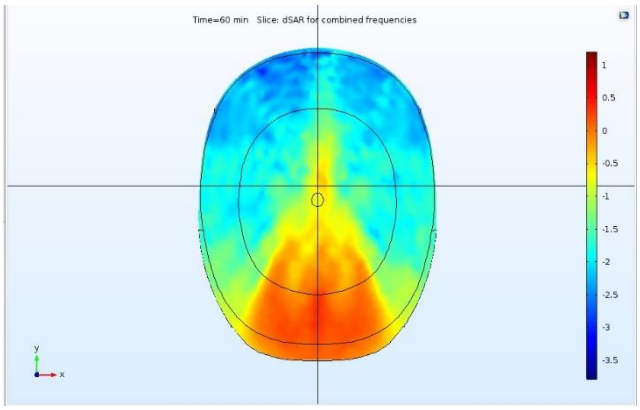

Figure 11 dSAR values on x-y plane with z=2.5 cm by 2450 MHz-2600 MHz with central antennas at 5 cm distance.

There is a verified relation between attention and blinking rate [16, 17]. During periods of increased cognitive load and focus on objects in the environment, the blinking rate decreases [16, 18]. Another study found decreased blinking rate during video terminal usage [19]. A VR environment not only increases the focus on objects, but also maximizes the cognitive load on the occipital and frontal lobes [20]. Nonetheless, if emotional stress is also involved, the blinking frequency has a strong correlation with the stress level [20]. Recalling our thermal isolation assumptions, the blinking would have marginal effects in a saturated vapor pressure environment. With the extra effects of decreasing blinking rates [16-20], it is quite a fair approximation, since the

vapor pressure saturation may be achieved earlier in real world conditions than in simulations.

On the retinal part, retinal temperature increase is safe at 0.25^{o}C at most by former retinal prosthesis research [21]. Certain retinal side effects such as retinal whitening, oedema, and fundus lesions can be observed with temperature rise over this value up to 2^{o}C. And 2^{o}C can be taken as a damage threshold level from cadaver and FEM studies [21]. In our first set of simulations, the highest corneal temperature increase was 0.35^{o}C at a distance of 5 cm from face with 2450-2600 MHz pair (Figure 6). The highest temperature increase was rather on the nose (Figure 5).

Side antenna thermal effects were much more subtle. This time, both figures were almost doubled at the distance of 3 cm from face with 2450-2600 MHz (Figure 7,8). The corneal temperature increase reaches a total of 3.41^{o}C, whereas retinal increase is at 0.12^{o}C. This could be more disturbing for a child since their eye size is bigger compared to his/her cranium [22]. Another interesting observation in the side antennas' scenario is that only one of the eyes has an observable effect (Figure 9,10). The highest accumulated heat effect always occurred with 2450-2600 MHz pair in both cases.

On the logarithmic SAR values, there is a certain penetration into the center of the head, where endocrine glands may be affected (Figure 11). Athermal EM effects are statistically observable in pituitary glands [23,24]. At this level, one can presume similar effects on hypothalamus-thalamus and pineal glands, since they have similar tissue properties [25,26]. These endocrine glands have a vital effect on the hypothalamic–pituitary–adrenal (HPA) axis response and the circadian cycle (CC) of the body, respectively.

4. CONCLUSIONS

Our simulation results do not impose any immediate thermal biological effects; nonetheless, it may be possible to observe disturbing effects like dry eye syndrome with utilization of applications triggering high attention and high stress on SP VR headset.

The utilization of SP VR headsets for children may also raise concerns. Children up to age of 7 have bigger eyes relative to their head size and they are more prone to the effect of EM radiation. Our model provides the SAR penetration for the adult human head from SP VR headsets (Figure 11). Thus, one can assume further SAR penetration for a child head. It is possible to oversize the eye domain in our model, and one can simulate SP VR headset usage of children to an extent, too.

On the athermal effects, we have readily observed the effects on hypothalamus, thalamus, and pineal glands (Figure 11). There are similar SAR penetration values for the pituitary and parotid glands, too. For the first case, the antennas are positioned in an alignment with these three glands, and the nasal cavity may form a waveguide for the waves. In the latter case, there is no alignment but this time the distance is shorter, and there is not much of tissue to absorb the waves because of orbital and oral cavity. The first three are still more important on the homeostasis of humans, and thermal and athermal effects would be much more important because of HPA and CC. Such effects were already reported, too.

Our primary aim was to investigate the possible biological effects of SP VR headset usage with two concurrently active radio units' exposure. We have included all LTE bands below 3GHz such as 2300 and 2600 MHz. Our model has a novel approach over the classical SAR head phantom model with a special focus on a specific organ. Our model can further be customized for any other head organ in a similar way. Observed results of athermal effects on a specific part of the head confirmed by a group of studies can this way be linked back to a thermal threshold for that specific organ, such as pituitary glands. This new approach can totally change the classical thermal effect-only SAR exposure public safety standards. All EM exposure studies with confirmed observable athermal effects will be able to propose a more secure exposure standard with our SAR phantom head model modification approach.

During the COVID-19 pandemic, VR/AR headset usage has further increased with distance working and home entertainment use. Therefore, we kindly recommend limiting the SP VR headset usage for children with the duration of 15 minutes at most based on our current saturation time measurements. It is equally important to provide air ventilation mechanism into the new SP VR headset designs.

Funding

The authors would like to thank Bogaziçi University for supporting this study as part of the scientific research project BAP-9860.

The Declaration of Conflict of Interest/ Common Interest

No conflict of interest or common interest has been declared by the authors.

Authors' Contribution

The first author contributed 70%, the second author 30%.

The Declaration of Research and Publication Ethics

The authors of the paper declare that they comply with the scientific, ethical and quotation rules of SAUJS in all processes of the paper and that they do not make any falsification on the data collected. In addition, they declare that Sakarya University Journal of Science and its editorial board have no responsibility for any ethical violations that may be encountered, and that this study has not been evaluated in any academic publication environment other than Sakarya University Journal of Science.

REFERENCES

[1] Groupe Speciale Mobile Association https://www.gsma.com/, fetched at Feb 28, 2022.

[2] Statistica - Number of mobile augmented reality (AR) active users worldwide https://www.statista.com/statistics/1098630/global-mobile-augmented-reality-ar-users/, fetched at Feb 28, 2022.

[3] Groupe Speciale Mobile Association - A whole new ball game: when your living room becomes the sports stadium https://data.gsmaintelligence.com/research/research/research-2020/a-whole-new-ball-game-when-your-living-room-becomes-the-sports-stadium, Aug, 2020.

[4] Y. Diao, S.-W. Leung, Y. He, et al., "Detailed modeling of palpebral fissure and its influence on SAR and temperature rise in human eye under GHZ exposure," Bioelectromagnetics, vol. 37, no. 4, pp. 256-263, 2016.

[5] Y. K. E. Ng and E. H. Ooi, "FEM simulation of the eye structure with bioheat analysis," Computer methods and programs in biomedicine, vol. 82, no. 3, pp. 268-276, 2006.

[6] Comsol Multiphysics, www.comsol.com , COMSOL 4.3/4.3a FNL License No: 17073372.

[7] Comsol Absorbed Radiation (SAR) in Human Brain Model, https://www.comsol.com/model/absorbed-radiation-sar-in-the-human-brain-2190, fetched at July 28, 2021.

[8] Human Eye Model by Bobby Dyer, https://grabcad.com/library/human-eye-model/files , 2012.

[9] FCC Specific Absorption Rate for Cellular Phones https://www.fcc.gov/general/specific-absorption-rate-sar-cellular-telephones, fetched at July 28, 2021.

[10] G. Schmid, G. Neubauer, and P. R. Mazal, "Dielectric properties of human brain tissue measured less than 10 h postmortem at frequencies from 800 to 2450 MHz,"

Bioelectromagnetics, vol. 24, no. 6, pp. 423-430, 2003.

[11] Levoy, M.: MRI data originally from Univ. of North Carolina (downloaded from the Stanford volume data archive at http://graphics.stanford.edu/data/voldata/ fetched at July 28, 2021).

[12] FCC Body Tissue Dielectric Properties https://www.fcc.gov/general/body-tissue-dielectric-parameters , fetched at July 28, 2021.

[13] E. H. Ooi, W.-T. Ang, and E. Y. K. Ng, "Bioheat transfer in the human eye: a boundary element approach," Engineering Analysis with Boundary Elements, vol. 31, no. 6, pp. 494-500, 2007.

[14] A. Karampatzakis and T. Samaras, "Numerical modeling of heat and mass transfer in the human eye under millimeter wave exposure," Bioelectromagnetics, vol. 34, no. 4, pp. 291-299, 2013.

[15] C. Li, Q. Chen, Y. Xie, and T. Wu, "Dosimetric study on eye's exposure to wide band radio frequency electromagnetic fields: Variability by the ocular axial length," Bioelectromagnetics, vol. 35, no. 5, pp. 324-336, 2014.

[16] T. Sakai, R. Yoshida, H. Tamaki, et al. "Electrodermal activity based study on the relationship between visual attention and eye blink," IEEE 9th International Conference In Sensing Technology (ICST), pp. 596-599, 2015.

[17] R. Yoshida, T. Sakai, Y. Ishi, et al. "Electrodermal activity-based feasibility study on the relationship between attention and blinking," International Journal on Smart Sensing & Intelligent Systems, vol. 9, no. 1, 2016.

[18] H. Ledger, "The effect cognitive load has on eye blinking," The Plymouth Student Scientist, vol. 6, no. 1, pp. 206-223, 2013.

[19] T. Schlote, G. Kadner, and N. Freudenthaler, "Marked reduction and distinct patterns of eye blinking in patients with moderately dry eyes during video display terminal use," Graefe's archive for clinical and experimental ophthalmology, vol. 242, no. 4, pp. 306-312, 2004.

[20] M. Haak, S. Bos, S.,Panic, and L. J. M. Rothkrantz, "Detecting stress using eye blinks and brain activity from EEG signals," Proceeding of the 1st driver car interaction and interface, pp. 35-60, 2009.

[21] N. L. Opie, A. N. Burkitt, H. Meffin, and D. B. Grayden, "Heating of the eye by a retinal prosthesis: modeling, cadaver and in vivo study," IEEE Transactions on Biomedical Engineering, vol. 59, no. 2, pp. 339-345, 2012.

[22] O. P. Gandhi, "Yes the children are more exposed to radiofrequency energy from mobile telephones than adults," IEEE Access, vol. 3, pp. 985-988, 2015.

[23] K. M. Abu Khadra, A. M. Khalil, M. Abu Samak, and A. Aljaberi, "Evaluation of selected biochemical parameters in the saliva of young males using mobile phones," Electromagnetic biology and medicine, vol. 34, no. 1, pp. 72-76, 2015.

[24] F. Söderqvist, M. Carlberg, and L. Hardell, "Biomarkers in volunteers exposed to mobile phone radiation," Toxicology letters, vol. 235, no. 2, pp. 140-146, 2015.

[25] S. A. Geronikolou A. Chamakou, A. Mantzou A., et al. "Frequent cellular phone use modifies hypothalamic–pituitary–adrenal axis response to a cellular phone call after mental stress in healthy children and adolescents: A pilot study," Science of the Total Environment, vol. 536, pp. 182-188, 2015.

[26] Z. Sienkiewicz, C. Calderón, K. A. Broom, D. Addison, et al. "Are Exposures to Multiple Frequencies the Key to Future

Radiofrequency Research?," Frontiers in public health, vol. 5, 2017.

SAKARYA ÜNİVERSİTESİ
FEN BİLİMLERİ ENSTİTÜSÜ DERGİSİ

Sakarya University Journal of Science
SAUJS

ISSN 1301-4048 e-ISSN 2147-835X Period Bimonthly Founded 1997 Publisher Sakarya University
http://www.saujs.sakarya.edu.tr/

Title: A New Novel Synchronization Index of Brain Networks in Hyperbolic EEG Dynamics

Authors: Rüştü Murat DEMİRER

Recieved: 2021-09-22 00:00:00

Accepted: 2022-05-06 00:00:00

Article Type: Research Article

Volume: 26
Issue: 3
Month: June
Year: 2022
Pages: 600-607

How to cite
Rüştü Murat DEMİRER; (2022), A New Novel Synchronization Index of Brain Networks in Hyperbolic EEG Dynamics. Sakarya University Journal of Science, 26(3), 600-607, DOI: 10.16984/saufenbilder.999015
Access link
http://www.saujs.sakarya.edu.tr/tr/pub/issue/70993/999015

Sakarya University Journal of Science 26(3), 600-607, 2022

A New Novel Synchronization Index of Brain Networks in Hyperbolic EEG Dynamics

Rüştü Murat DEMİRER*[1]

Abstract

The functional connectivity of brain connectivity changes its pattern over time i.e. dynamics, even in the resting state with an infinite number of degrees of freedom with local couplings. Recently, quantifying the level of synchrony has received considerable attention. We hypothesized that time-varying instantaneous phase synchronization over local couplings are defined in hyperbolic space and different brain regions can identify failures, flexibility, and stability in network dynamics. Our goal is to understand the phase synchronization changes of the beta-gamma band, and in addition, to investigate Shannon entropy based on phase synchronization stability. Whole EEG dynamics from local phase synchronizations was used to detect treatment resistance from both hemispheres in OCD patients. Temporal filtering and Hilbert transforms were performed to infer beta-gamma band phase difference activity from the EEG brain dynamics. Then, the response beta-gamma band phase stability was quantified using a new phase synchronization index (PSI). Results indicated significantly changed phase synchronization of the response and non-response to treatment, patients in OCD patients in F7 electrode. Greater phase fluctuations of beta-gamma synchronizations in treatment resistance OCD is claiming phase deficiencies within neural populations. This study first provides experimental and theoretical support for characterizing cycle structure depends on the non-Euclidian dynamics of neural phase synchrony caused by disturbances of underlying neurotransmitter systems, as reflected in different normal and disease states.

Keywords: Hilbert Transform Shannon Entropy, SVM algorithm, Tass Synchronization

1. INTRODUCTION

Structural and functional interactions do not only depend on the strength of the number of neuron activations but also depend on how often we pick the spikes but the precise timing of the spikes underlying neural assemblies is also essential to the brain dynamics with coherent and incoherent dynamics. The phase synchronizations may be a general neural pattern for representing sequential events for learning, plasticity, and memory [1].

* Corresponding author: murat.demirer@isikun.edu.tr
[1] Işik University, Faculty of Engineering and Natural Sciences, Department of Electrical-Electronic Engineering
ORCID: https://orcid.org/0000-0002-5508-741X

The idea of phase synchronization (PS) is to understand the precise timing among brain regions [1-5]. This claims that there would be a relation in the phase dynamics of the oscillations in the non-identical local neural populations. In previous studies, the synchronization degree was estimated with a method presented [2]. In this approach, the Tass synchronization index is described by the average dynamics of the phase difference among various spatial oscillators over a time window assuming this analytic dynamic is stationary over the given time interval. The Hilbert transform is used to obtain complex dynamics. The Hilbert transform is a fundamental mathematical operator in many different areas because there is a close relation to causality [6]. It states that the real- and imaginary parts of a causal signal are related by the Hilbert transform which constructs an analytic signal in complex space. Gabor has proposed the Hilbert transform who has proved that all information about the analytic signals compact in the amplitude of the signal [6]. Moreover, the phase of the signals can be calculated from the amplitude and its conjugation (imaginary part) from Hilbert Transform. This means that Hilbert Transform causes to two-dimensional embedding of the limit cycle which is called strange attractor. The analytic signal z_t can be represented in Equation (1):

$$z_t = v_t + iv_t{}' = A_t e^{j\phi(t)}$$
$$v_t{}' = \frac{1}{\pi} p.v. \int_{-\infty}^{\infty} \frac{z(\tau)}{t-\tau} d\tau \quad (1)$$

in one channel, j where $v(t)$ and $v'(t)$ are the real and imaginary parts of the analytic signal. $p.v$ denotes the Cauchy principal value of the singular integral. After Hilbert transform is applied to each channel separately, we obtain an analytic signal $z_j(t)$.Analytic amplitude,$A_j(t)$ was obtained by $A_j(t) = \sqrt{v_j^2(t) + v_j'(t)^2}$. The analytic phase of each channel, $\varphi_j(t)$ for the $j = 1 \ldots 18$ electrodes were given by the arctangent of the ratio of the imaginary part of the real part as shown in Equation (2). The analytic phase is discontinuous and jumps from $-\frac{\pi}{2}$ to $\frac{\pi}{2}$.

$$\varphi_j(t) = \tan^{-1} \frac{v_j'(t)}{v_j(t)} \quad (2)$$

The analytic amplitude for each channel $A_j(t)$ is the norm of each sampled point as shown in Equation (3).

$$z_j(t) = v_j(t) + iv_j'(t) \quad (3)$$

The degree of synchrony was based on Hilbert Transform proposed by a method. Tass applied the method to each channel independently [7]. Tass index is calculated which is based on distributions of Shannon entropy values of phase differences of a sliding window during the time interval assumed stationary for each electrode pair.

We obtained Tass Index by implementing $\Delta\varphi(t)_{i,j} = \left|\varphi_i(t) - \varphi_j(t)\right|$ spatial phase difference signals between i and j channels over predefined window length, $T\ (msec)$. The index was generalized to channel pairs by calculating the distribution (histogram) of complex differences $\Delta\varphi(t)$ after subtracting the means for each coupled electrode pair within sliding window length in T msec. The window length was estimated at two times the frequency at the peak of the Power Spectral Density-PSD_T of the spatial averaged EEG channels after band-pass FIR filter is applied. The window length was applied at the sampling period $f_s = 125\ Hz$ over total 350-sec recording time. In Tass synchronization index, Shannon entropy can be defined based on (normalized histograms) p_k of phase difference distributions, $\Delta\varphi(t)_{i,j}$ given in time window as shown in Equation (4).

$$e(t) = -\sum_{k=1}^{N} p_k \ln\ p_k \quad (4)$$

where $p_k(t)$ probability was the relative distribution of phase values $\Delta\varphi(t)_{i,j} mod\ 2\pi$ difference signals between i and j electrode within the k. th. bin. The number of bins is (i.e. $N = 100$). This synchronization index changes instantaneously. This index is normalized by $\hat{e}$ thus the index changes between zero and one as shown in Equation (5).

$$q(t) = (\hat{e} - e(t))/\hat{e} \quad (5)$$

where $\hat{e} = \ln N$ as constant and N is the number of bins (e.g. 100 bins of 0.06 radians of resolution between $-\pi$ and $+\pi$ radians). The $q\ (t)$ was zero

for a uniform distribution and one for a delta distribution of phase values [8].

2. GENERAL REQUIREMENTS

We define multichannel EEG signals over a predefined window length of d sampling steps, which lasts $T_w = d * (1/f_s)\ (msec)$. Then, we define $\mathbb{C}^d$ space which defines the sliding window of complex dimension n for each electrode. Throughout this paper, we slide the window over all samples, in $z \in \mathbb{C}^d$ as column vectors in $d \times 1$ matrix form $z = (z_{t-1}, \dots, z_{t-d})^T$, where the symbol T stands for the transpose of the vector. For $z \in \mathbb{C}^d$, the conjugate of z, denoted by $\bar{z}$, is defined by $\bar{z} = (\bar{z}_{t-1}, \dots, \bar{z}_{t-d})^T$. For $z \in \mathbb{C}^d$ and $w = (w_{t-1}, \dots, w_{t-d})^T \in \mathbb{C}^d$, we write the inner product $\langle z, w\rangle := \sum_{t=1}^{d} z_t \bar{w}_t$ and in other words $|z| := \langle z, z\rangle^{1/2} = (|z_{t-1}|^2 + \cdots + |z_{t-d}|^2)^{1/2}$ which is the sum of analytic amplitudes. In another word, $|z| :=< z, z >$ also denotes the dissipative power of the frame after de-meaning. The expectation value of each window at each electrode can then be explained within $a = (a_1, \dots, a_1)^T \in \mathbb{C}^d$, copies of a_1 complex values with $n-$ times. we set $\mathbb{B}^d(a, r) = \{z \in \mathbb{C}^d : |z - a| < r\}$. We transformed d-dimensional $\mathbb{B}^n$ the ball into the unit ball $\mathbb{B}^d(0,1)$ by dividing each de-meaned sample value with $|z|$ and letting $\mathbb{B}^d(0,1) = \{z \in \mathbb{C}^d : |z - a| < 1\}$ which explains normalized complex pseudo-variance.For $z, w \in \mathbb{D}$ acquired sliding vectors from an electrode pair, the pseudo-hyperbolic distance is defined [7] as shown in Equation (6).

$$\rho(z, w) = \left|\frac{z-w}{1-\bar{w}z}\right| \qquad (6)$$

representing simultaneous (or conjunctive) presence presynaptic firing of neural populations z and postsynaptic firing populations w at different regions.

We introduced a new Entropy Synchronization index improved from the Tass Synchronization Index. First, we define two pairs of channels (vectors) over window length for $z, w \in D$ within the unit disk (normalized). Let $z^i = (z_t, z_{t-1}, \dots z_{t*T-1})$ and $z^j = (w_t, w_{t-1}, \dots w_{t+T-1})$, $i \neq j$ complex vectors from i and j electrodes with T representing a sliding time window in msec. Complex spatial differences of each of two vectors (windows) over the scalp can represent synchronization better due to including both phase and amplitude coupling of spatial synchronization scheme simultaneously. The system architecture is shown in Figure 1.

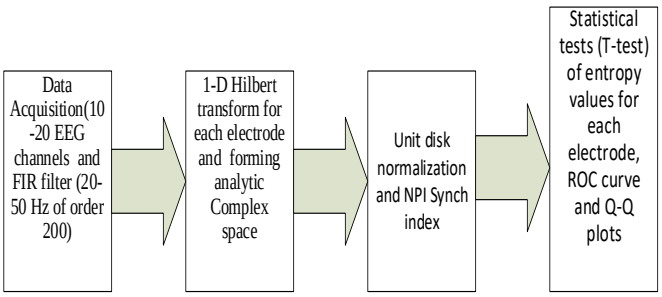

Figure 1 The architecture of the information pipeline

The pseudo-hyperbolic distance acquired from each paired vector represents L distribution from one source electrode, i, to other all possible representing spatial phase difference combinations over a time window. We implement a pseudo-hyperbolic distance function with its denominator is the inner multiplication of conjugate of $\bar{w}$ and z for each electrode pair, respectively. The distance represents both anti-correlation and the analytic difference between two electrodes paired as shown in Figure 2. This is an example of whether 6 electrodes are used. Properties of K_n topology with the $n = 10 - 20$ electrode configuration:

- Each vertex in K_n has degree $n - 1$.
- K_n has $n(n-1)$ directed non-commutative edges explaining both top-down and bottom-up directions on the same edge which is the first approach.
- K_n contains the all directed edges out of graphs on n vertices.

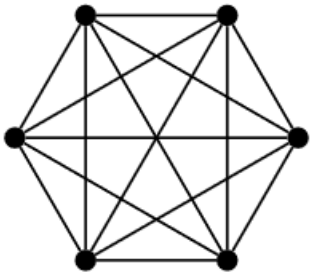

Figure 2 Complete topology of n =6 electrode K_6 connectivity. Each vertex represents an electrode from {Fp1, Fp2, ...} running through a time window of w^j, z^i vectors. Each index has a fan-out connection associated with pseudo-hyperbolic distances to other $L = (n-1)$ electrodes

The inner product of two complex vectors of all electrodes is the complex correlation distribution of whole EEG activity at each time window. Superscripts $\{i, j\}$ pair denotes electrode location numbers such as $\{Fp1, Fp2, \ldots\}$. From one channel indexed i to distances of all other channels excluding itself can give a fan-out degree of $L = (n-1)$ and $n = 18$ with the following equation (7) with an edge of K_{18} connectivity

$$\rho_i(z_t, w_t) = \sum_{k=1}^{L} \left| \frac{z_t^{\{i\}} - w_t^k}{1 - \bar{w}_t^k z_t^{\{i\}}} \right| \quad (7)$$

U denotes the total number of time windows, $t = 1, \ldots U$. Instantaneous pseudo-hyperbolic distance at a given t is normalized as $\overline{\rho^t} = \rho_i(z_t, w_t) / max\{\rho_i(z_t, w_t)\}$ from one channel distance divided by the maximum of all other L distances. In other words, the maximum operator is taken over all fan-out degrees of each electrode at a given time index, t. We finally obtain a distribution of normalized pseudo-hyperbolic distances as probability values over whole all-time windows either overlapped or non-overlapped. We then embedded pseudo-hyperbolic distance distributions into a Shannon entropy function representing probability distributions, $0 < \overline{\rho^t} < 1$ of one source to other all destinations derived from spatial phase distribution of histograms. Stochasticity is an inevitable characteristic of brain dynamics. We investigate the entropy of each electrode, i defined as ranging

$$e^{\{i\}}(t) = -\overline{\rho^t} \ln \overline{\rho^t} \quad (8)$$

through all U time windows as shown in Equation (8).

We then define the synchronization index which denotes the flexibility of pseudo-hyperbolic distance over all time windows for each electrode. NPI syn index for the i .th electrode can be defined in Equation (9) as

$$\overline{\Delta e_{Syn}^i} = \frac{\underbrace{max}_{U}(e^i) - \underbrace{min}_{U}(e^i)}{\underbrace{max}_{U}(e^i)} \quad (9)$$

The novel NPI syn index explains entropy change flexibility of fan-out degree in a given electrode.

3. THE RESEARCH FINDINGS AND DISCUSSION

In this study, 10-20 channel EEG data signals are filtered within a frequency band (20-50) Hz that includes beta-gamma frequency ranges. Using the phase and amplitude synchronization entropy paradigm, it was found that there was a significant difference between the resistive and non-resistive treatment groups in the beta-gamma band for the T3, T4, and Pz electrodes. Beta-gamma band represents cognitive deficits in OCD disorders [8].

This study showed that a decrease in beta-gamma power and phase synchrony with the relation of cognition in resistive patients with higher entropies. 14 patients with non-response to treatment and 20 patients with response to treatment in age from 20-55 years. They were recruited from Uskudar University NPI Hospital, Uskudar, Turkiye. The patients were diagnosed according to DSM-IV and World Health Organization ICD-10 for OCD. All patients were receiving medication at the time of recording and one group responded to treatment and the other group did not respond to medication.

For EEG paradigms, 10-20 electrode montage was recorded with removing eye-blinks artifacts through visual inspections. Moreover, EEG signals are analog filtered with an analog bandpass filter at 0.5-70 Hz with a 12-bit

resolution. A Notch filter is used for rejecting 50 Hz power line frequency. The sampling frequency $f_s$is set to 125 Hz. The sampling frequency is at least twice as high as the signal highest frequency ($f_s \approx 50$) which complies with the Nyquist theorem. Each subject was acquired for a 350 second (43750 data points) trial period corresponding to eyes-closed conditions. 19-channel EEG signals are demeaned to remove channel bias. A temporal band-pass FIR filter with an order of 200 was applied to get beta-gamma activity (20-50 Hz). After digital filtering, 10-20 channel EEG data for each subject are normalized to unit standard deviation(SD).

We found a significant condition effect for Fp2 ($p < 0.001$). The confidence level is 0.001. T3 and T5 are the electrodes that show the most significant differences for Δe_{NPI} over 12-50 Hz range.

We applied two different types of classification approaches for comparison. Logistic Regression and Support Vector Machine (SVM) as shown in figure 3 and figure 4 respectively. The estimated coefficients perfectly separate failures from successes for the selected channels with ($p<0.001$) as shown in Table 1.

Table 1 The p-values of two groups, response to treatment and non response to treatment groups

Fp1	0.013826
Fp2	5.101e-05
F3	0.10296
F4	3.139e-05
C3	3.661-e08
C4	3.893e-08
P3	0.0010078
P4	0.11867
01	1.72e-09
02	8.46e-10
F7	2.35e-08
F8	0.0030742
T3	4.91e-09
T4	1.18e-07
T5	8.91e-09
T6	1.092e-05
Fz	0.03221
Cz	2.9179e-08
Pz	1.3301e-08

For the fitted linear combination XB (entropic rate threshold) of the predictors, the sample proportions P of Y=36 from two groups in the data satisfy: XB <-0.253052: P=0 (OCD Response to treatment), XB>-0.253052: P=1 (OCD Nonresponse to treatment).

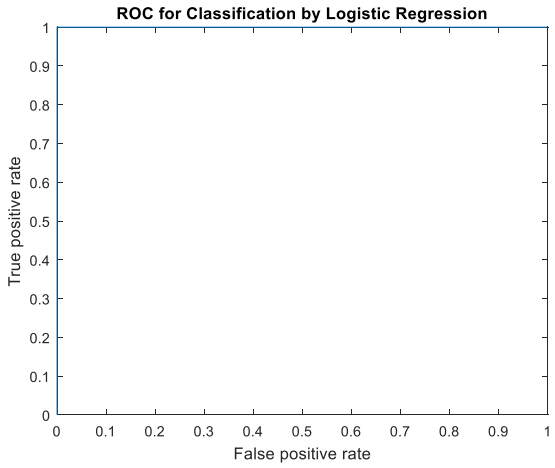

Figure 3 ROC Curve of Logistic Regression Classification for two groups (treatment response v.s. non-treatment response) using NPI Synch Index

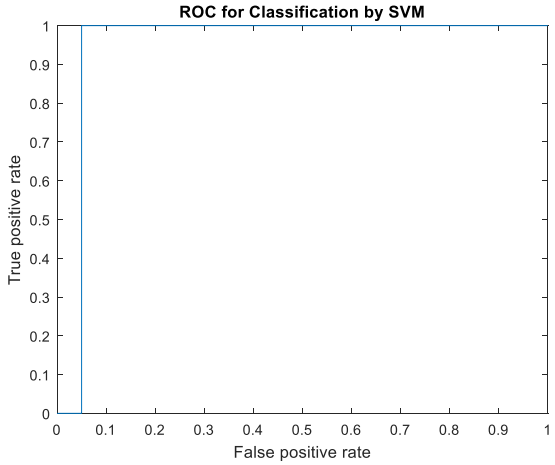

Figure 4 Support Vector Machine Classification for two groups (treatment response v.s. non-treatment response) using NPI Synch Index

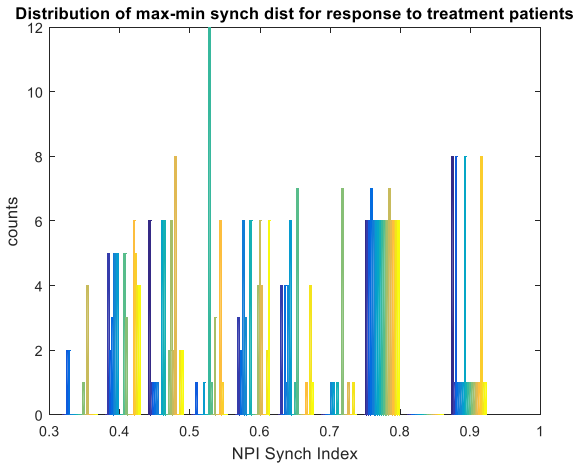

Figure 5 NPI Synchronization Index values distribution of beta-gamma band of EEG signals for a treatment response OCD patient at the full number of time windows. The vertical axis denotes the number of time windows

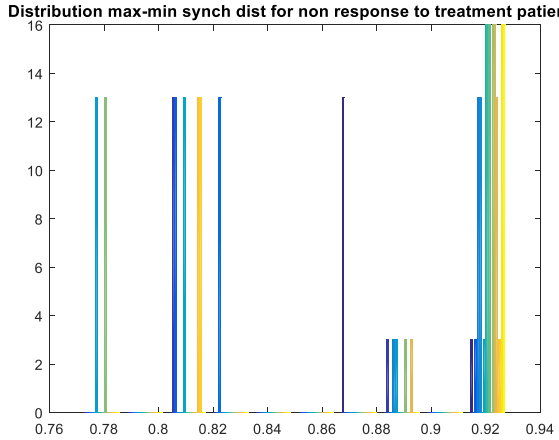

Figure 6 NPI Synchronization Index values distribution of beta-gamma band of EEG signals for a non-response to treatment resistance OCD patient at a full number of time windows. The vertical axis denotes the number of time windows

We concluded that NPI Synch Index distribution is a range of wide interval for response to treatment patients $(0.32 \leq NPI \leq 0.9)$ as shown in Figure 5 whereas this distribution changes over the very small interval $(0.78 \leq NPI \leq 0.93)$ for non-response to treatment patients as shown in Figure 6 during beta-gamma phase transitions. Q-Q statistical analysis of results demonstrated significance level between two groups (very significant deviation from linearized as one

group). Results display quantile-quantile plots of the one channel sample data for all cases versus the quantiles of the sample data of another channel over whole cases. If the samples come from the same distribution, then the plot appears linear. Q-Q plots as shown in Figure 7 and Figure 8 reveal that non-response to treatment patients do not change the standard normal quantiles over quantile of synchronization values, respectively. The patients' values are distinct depending on the patient clinical evaluations.

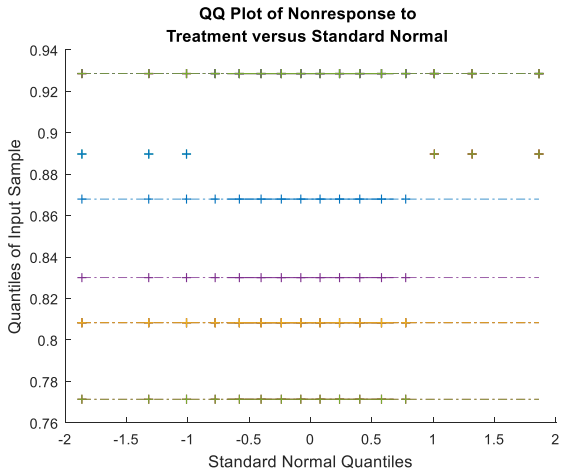

Figure 7 QQ Plots of treatment-resistant group

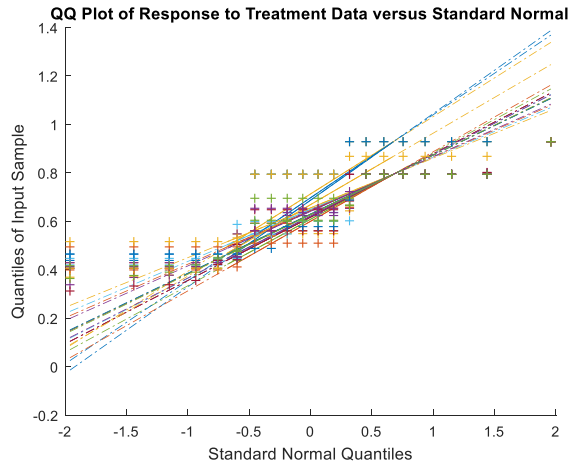

Figure 8 QQ Plots of response to treatment group

Acknowledgments

We would like to thank Prof. Dr. Nevzat Tarhan, for comments on manuscript. This work is supported by Üsküdar University NPI hospital under the Neuroimaging Research Group. That's why the developed biomarker was called the NPI Syn index.

Funding

The author (s) has no received any financial support for the research, authorship or publication of this study.

The Declaration of Conflict of Interest/ Common Interest

No conflict of interest or common interest has been declared by the authors.

Authors' Contribution

The author contributed 100 % to the study.

The Declaration of Ethics Committee Approval

This study does not require ethics committee permission or any special permission.

The Declaration of Research and Publication Ethics

The authors of the paper declare that they comply with the scientific, ethical and quotation rules of SAUJS in all processes of the paper and that they do not make any falsification on the data collected. In addition, they declare that Sakarya University Journal of Science and its editorial board have no responsibility for any ethical violations that may be encountered, and that this study has not been evaluated in any academic publication environment other than Sakarya University Journal of Science.

REFERENCES

[1] Freeman, Walter J.. "Origin, structure, and role of background EEG activity. Part 1. Analytic amplitude," Clinical Neurophysiology 115 (2004): 2077-2088.

[2] L Tass, P., Rosenblum, M. G., Weule, J., Kurths, J., Pikovsky, A., Volkmann, J., …

Freund, H.-J. (1998). "Detection of n:m Phase Locking from Noisy Data: Application to Magnetoencephalography," Physical Review Letters, 81(15), 3291–3294.

[3] Freeman, W. J., & Rogers, L. J. (2002). "Fine temporal resolution of the analytic phase reveals episodic synchronization by state transitions in gamma EEGs. Journal of Neurophysiology," 87(2).

[4] Kamaradova, D., Hajda, M., Prasko, J., Taborsky, J., Grambal, A., Latalova, K., Hlustik, P. (2016). "Cognitive deficits in patients with obsessive-compulsive disorder -electroencephalography correlates. Neuropsychiatric Disease and Treatment," 12,1119–25.

[5] Chen, Shaolin and David Kalaj. "Lipschitz continuity of holomorphic mappings with respect to Bergman metric," arXiv: Complex Variables (2017): n. pag.

[6] Koppleman W and Pincus JD, (1959) "Spectral representations for finite Hilbert transform," Math Z. vol. 71, pp. 399-407.

[7] Tass P, Kurths J, Rosenblum M, Weule J, Pikovsky A, Volkmann J, Schnitzler H, Freund H. In: Uhl C, editor. (1999), "Complex phase synchronization in neurophysiological data. Analysis of neurophysiological brain functioning," Berlin: Springer. p. 252–73.

[8] Freeman, Walter J.. "A pseudo-equilibrium thermodynamic model of information processing in nonlinear brain Dynamics," Neural networks : the official journal of the International Neural Network Society 21 2-3 (2008): 257-65.

SAKARYA ÜNİVERSİTESİ
FEN BİLİMLERİ ENSTİTÜSÜ DERGİSİ

Sakarya University Journal of Science
SAUJS

ISSN 1301-4048 e-ISSN 2147-835X Period Bimonthly Founded 1997 Publisher Sakarya University
http://www.saujs.sakarya.edu.tr/

Title: Important Factors Affecting the Quality of Indoor Air and a Bibliometric Analysis

Authors: Bahar TÜRK

Recieved: 2021-09-16 00:00:00

Accepted: 2022-05-11 00:00:00

Article Type: Research Article

Volume: 26
Issue: 3
Month: June
Year: 2022
Pages: 608-619

How to cite
Bahar TÜRK; (2022), Important Factors Affecting the Quality of Indoor Air and a Bibliometric Analysis. Sakarya University Journal of Science, 26(3), 608-619,
DOI: 10.16984/saufenbilder.996443
Access link
http://www.saujs.sakarya.edu.tr/tr/pub/issue/70993/996443

Sakarya University Journal of Science 26(3), 608-619, 2022

Important Factors Affecting the Quality of Indoor Air and a Bibliometric Analysis

Bahar TÜRK*[1]

Abstract

Indoor air quality is critical for human health, and as such, it must be continuously improved. As a result, it is critical to identify the factors influencing indoor air quality. In this context, the purpose of this study is to investigate the factors influencing indoor air quality and to conduct a bibliometric analysis of the studies on the subject. The method of bibliometric analysis was used to examine academic publications on indoor air quality published between 1975 and 2020. A total of 2398 academic studies from the Web of Science database were examined. According to the findings of the analyses, academic research has primarily been conducted in the fields of construction technology and environmental sciences, public environmental occupational health, and environmental engineering. Since 2010, there has been a significant increase in the number of publications. The year with the most publications was 2017, and especially after 2010, publications have been cited more and more. One-fourth of the publications were produced solely in the United States. Hong Kong Polytechnic University and Denmark Technical University had the most publications. It has been determined that ventilation and air flow rate are the most heavily researched factors affecting indoor air quality. On the other hand, a substantial amount of research has been conducted to investigate the effects of pollutants. Furthermore, publications on temperature, humidity, bacteria, and thermal comfort were discovered. There have been studies on indoor air quality in residential buildings, houses, schools, and hospitals.

Keywords: Air pollution, human health, bibliometric analysis, indoors environments, toxicity.

1. INTRODUCTION

Air quality is critical for human health, and the quality of indoor air is becoming increasingly important as people spend longer periods of time in enclosed areas [1, 2]. In the midst of today's pandemic (COVID-19), people

staying indoors for a long time and spreading the disease through the air emphasize the importance of indoor air quality once again. The factors

* Corresponding author: bahareturk@gmail.com
[1] Istanbul Technical University
ORCİD: https://orcid.org/0000-0002-1185-9174

affecting indoor air quality are discussed in this article. The factors that are effective in indoor environments and their effects will be revealed through an examination of the published studies. Between 1975 and 2020, academic publications on indoor air quality were analyzed using the bibliometric method. We analyzed 2398 academic studies that were registered in the Web of Science database [3].

1.1. Definition of IAQ

Due to the fact that individuals spend the majority of their time inside, exposure to indoor air pollution has a substantial influence on both human health and workplace performance. Both scientists and the general public have recently focused on the concerns associated with poor indoor air quality (IAQ), since research has demonstrated that indoor air is more polluted than outside air [4]. Indoor air quality, which cannot be fully defined due to the interaction of a variety of factors with varying and constantly changing levels, is generally defined as air that contains certain mixtures under normal conditions and is free of harmful substances to human health. The ASHRAE 62-1989 and 2001 standards define "satisfactory indoor air quality" as air in which 80% or more of those present do not express dissatisfaction with the quality of the air [5]. According to a similar definition, the US Environmental Protection The Environmental Protection Agency (EPA) defines healthy quality of indoor air as air that is free of known pollutants in harmful concentrations and approximately 80% of those who have been exposed to this air are satisfied with its quality [6].

The term "optimum quality of indoor air" refers to the air quality that is free of discomfort, disturbance, or health problems. The World Health Organization (WHO) defines better and healthier indoor air quality as not only the absence of disease, but also the sense of complete comfort experienced by individuals. On this basis, better and healthier indoor air can be air that is free of pathogens and comfortable for all occupants [7]. Indoor air pollution was identified by the World Bank as one of the most significant environmental aspects in developed countries in 1992 [8]. Indoor air pollution can be caused by two distinct sources. There are two types of pollution in the indoor environment: pollution caused by substances and activities within the space and pollution caused by the effect of pollutants entering the space from the outside.

1.2. Importance Of IAQ and Effects on Human Health

Approximately 90% of people end up spending a lot of their time indoors. Increasing the quantity of contaminants in indoor air might result in major health consequences. According to the World Health Organization, 4.3 million people die each year as a result of exposure to home air pollution [6]. Internal and external pollutants can contaminate the air in these enclosures. Numerous studies have been done to determine the causes of contaminants' physiological and psychological effects on humans when pollutants reach a predetermined level [9]. Many countries, boh high- and low-income, have identified indoor air quality issues as significant health risks. Air quality in the home affects particularly vulnerable population groups in residential, day-care, nursing homes, and other private settings as a result of indoor air pollution, poor health, or advanced age. In suitable humid conditions, microbial contamination is a significant factor in indoor air quality, causing the proliferation of hundreds of bacteria and fungi species [10]. Numerous organs in the human body are harmed by these pollutants, including the brain, lungs, skin, blood, kidneys, peripheral nervous system, and liver. Additionally, these pollutants attempt to enter our bodies through our breathing, making our bodies vulnerable to them [11-13].

1.3. Factors Effecting IAQ

Due to the fact that inadequate ventilation, a lack of air conditioning systems, human activities and a variety of materials, chemicals and gases primarily contribute to indoor pollution, various organizations such as United States Environmental Protection Agency (US EPA) and the World Health Organization (WHO) have recognized IAQ as a multidisciplinary

phenomenon and classified pollutants into several categories [14].

1.3.1. Temprature

In order to achieve thermal equilibrium, heat is exchanged in the human body through heat conduction. The body temperature is maintained between 36 and 37 degrees Celsius so that the organs do not get damaged and can work efficiently [15]. As a result, it is clear that the temperature of the environment in which humans live is also critical for maintaining a constant temperature. Therefore, indoor temperature is critical for indoor air quality. Due to the fact that extremely hot environments create more difficult working conditions, it is evident that a variety of health problems arise [16,17,18].

1.3.2. Thermal comfort

To continue living a comfortable life, an equilibrium of heat between a person and his or her environment must be achieved. It's all about the senses and feelings when it comes to thermal comfort. As a result, the principles of heat balance and comfort conditions are distinct. This is described by ASHRAE as a mental state expressing those who are content with their surroundings. Thermal comfort is aided by thermal stability, but it is not needed. Thermal equilibrium is not possible for someone in the thermal comfort zone. Thermal comfort can vary depending on individual preferences [19].

The characteristics of humans, their ages, sexes, dietary habits, body types, fat levels, heights, and weights, as well as their actions, clothing, and differences all affect thermal comfort, and there are no unbreakable rules [20, 21]. Thermal comfort parameters are classified into two types: individual and environment. Environmental factors include temperature, humidity, air flow, and average radiant temperature, while personal factors include metabolic activity level and clothing [22].

1.3.3. Relative Humidity

In terms of human health and quality, an environment's humidity should be between 40 and 60%. In humans, low humidity causes dryness of the respiratory airway, skin, eyes, and hair. Low humidity allows toxic compounds to penetrate the body more quickly and reduces the amount of water vapor in the air. Static electricity problems are often caused by low humidity levels in an area. High humidity levels impair people's ability to maintain thermal equilibrium and allow moisture to accumulate on the body's surface. Microorganisms grow more rapidly in high humidity. Humidity, in particular, can allow influenza virus to survive and spread [13].

Simultaneously, studies indicate that the COVID-19 virus's survival time increases as the humidity level in the environment increases [23, 24]. As a result, relative humidity is critical in determining the quality of indoor air.

1.3.4. Air Flow Rate

One of the environmental factors that influences quality of indoor air is the amount of airflow in a room. The airflow rate is the value of airflow in a given direction measured in units of time. In contrast, the airflow rate in the medium is the average of several samples taken from the medium and is measured in millimeters per second (m/s) [25].

The location and size of the intake air, the type and intensity of indoor activity, the ventilation system's location, the angle and power, the amount of air supplied, the relative humidity and the temperature of the environment influence the indoor airflow while low airspeeds are considered to be airless, high airspeeds are considered to be windy and unpleasant for occupants. The airflow limit values required to maintain a comfortable environment are determined by standards. According to ASHRAE, a comfortable environment should have an air flow rate of 0.15 m/s. This is different during the summer and winter seasons. Although human sensing of 0.1 m/s air is not possible, air of 0.2 m/s is usually considered comfortable. An airflow of 0.35 – 0.50 m/s on the other hand causes people to get agitated [26].

Standards are established for an ambient airflow rate of no more than 0.8 m / s. Airflows greater

than 1.5 m / s cause significant discomfort. The air velocity affects the thermal comfort of the user. The air speed is increasing and the water on the surface of the body evaporates faster and the person starts cooling down. The cooling increases as the increased air speed disappears and the available air mass decreases in humans. Air should be provided uniformly and at low speeds for comfort of the user during the design process or during use [27, 28].

1.3.5. Biological and Chemical Pollutants

When selecting building materials, it is critical to take biological considerations into account. According to [29], 30-40% organic material (ie wood, straw, reed) and 60-70% inorganic material (ie bricks, tiles, natural stone, lime) are used in buildings, except for materials that differ according to climatic conditions. Nowadays, between 90% and 100% of materials in modern buildings are synthetic, not related to nature, life and human metabolism, particularly in major cities. The structure, use, use and life expectancy of building materials are a result of indoor air pollution. Therefore, they should be classified as positive and negative when selecting building materials along with all associated characteristics so that those who are selected can minimize environmental damage over the material's life.

Indoor air quality is greatly influenced by the building materials. Krusche et al. [30] conducted research on ecological structures in 1982 for the purpose of classifying building materials. Krusche et al. [30] specified the following materials to be used:

- Pressed bricks and wood for the façade,
- Wood, brick, and mudbrick for the wall construction,
- Wallpaper, natural and man-made wood panels, bodywork, and fabric-covered surfaces
- Fluorine-coated stone, wood, and linoleum
- Carpets made of wool and linen
- As an insulating material, wood wool and straw are use d.
- Natural pigments, such as oil paints with a water base.

Krusche et al. [30] stated building materials that should not to be used in construction buildings as follows:

1. Tuile,
2. Mineral-based materials such as aluminum, zinc, lead, sheet metal, cement, asbestos boards,
3. Synthetic carpets,
4. Fiberglass, spread of perlite, moulds of polystyrene, plastic foam,
5. Paints with a synthetic resin base.

One of the most important biological and chemical pollutants in the indoor environment is volatile organic compounds. Volatile organic compounds (VOCs), sometimes called solvents, are organic molecules that readily evaporate at ambient temperature. The major contaminants in indoor air are volatile organic compounds (VOCs), which have a considerable influence on indoor air quality and hence on human health. Many VOCs are known to be toxic and considered to be carcinogenic, mutagenic, or teratogenic [31]. The degree of exposure to VOCs in an indoor setting is also highly dependent on the sources and rates of emission. The sources of VOCs in indoor air are numerous. Volatile organic compound emissions from building materials have been identified as the primary source of indoor air pollution.

Table 1 contains a list of VOCs and their sources that are often detected in indoor air.

As seen in the table, organic compounds are mostly prevalent in established buildings, wood-based paneling and furniture, and paints.In office environments, printers and copiers are significant source of volatile organic compounds (VOCs) in the air [32].

Table 1
Indoor air VOC classifications and emission sources [32,33]

VOC categories	Environment and sources
Aliphatic hydrocarbons	Established buildings, new and renovated buildings, carpets, floor coverings, paints, unflued gas heaters and electric ovens
Aromatic hydrocarbons	Established buildings, floor coverings, floor coverings, paints, unflued gas heaters and electric ovens
Alcohols	Established buildings, paints, unflued gas heaters and electric ovens
Ketones	Established buildings, floor coverings,
Aldehydes	Established buildings,
Esters	Established buildings, new and renovated buildings, floor coverings, paints
Siloxanes	unflued gas heaters and electric ovens
Organic acids	Established buildings, new and renovated buildings, carpets, floor coverings, paints
Other VOCs	Established buildings, new and renovated buildings, floor coverings, paints, unflued gas heaters and electric ovens

2. METHOD

In this study, academic studies published on indoor air quality between 1975 and 2020 were presented with the method of bibliometric analysis. Pritchard [34] pioneered the use of bibliometric analysis in the literature. According to Pritchard [34], the term "bibliometric" involves the use of statistical and mathematical tool that can be applied to various communication media such as books or other written material. Bibliometry originated in library studies and encompasses the study of books, articles,

publications, and citations in any discipline [35] In this context, 2398 academic studies published between the specified dates and registered in the Web of Science database were analyzed. The distribution of these studies were examined on the basis years, in which areas they were published, the number of citations they received, and the number of citations, countries where they were published. In addition and the most importantly, the number of publications carried out about the factors affecting indoor air quality is also revealed and the importance of these factors has been tried to be revealed. Finally, the distribution of the studies conducted for the type of indoor spaces where indoor air quality is examined has been revealed. Figure 2 shows the distribution of publications published on indoor air quality depending on the years. In this context, it has been determined that there has been a significant increase in the number of publications since 2010. The year with the highest number of publications was 2017, when 170 studies were conducted. On the other hand, 169 academic studies were presented in 2019.

3. FINDINGS

In the analyzes carried out, it was first investigated in which areas the indoor air quality was mostly examined. In this context, it has been determined that academic research has been mostly conducted in the fields of construction technology and environmental sciences, public environmental occupational health and environmental engineering. On the other hand, it has been observed that studies have been carried out in the fields of civil engineering, thermodynamics, energy fuels, mechanical engineering, meteorology and atmospheric sciences, electrical and electronic engineering (Figure 1). All of these areas stand out as areas where studies are carried out on improving indoor air quality. On the other hand, it is noteworthy that there is no medicine among these fields. However, it has been understood as a result of the literature survey that indoor air quality and human health are closely related.

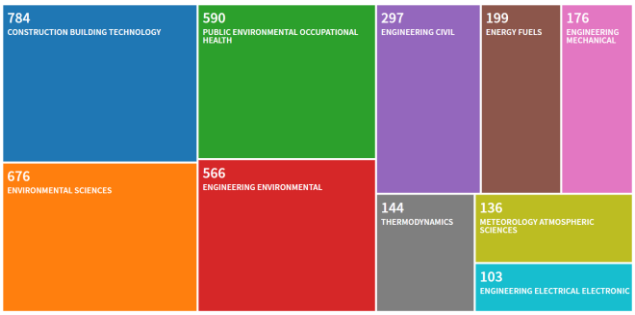

Figure 1 Treemap of areas publications on “Indoor air quality” [3]

Figure 2 shows the distribution of publications published on indoor air quality depending on the years. In this context, it has been determined that there has been a significant increase in the number of publications since 2010. The year with the highest number of publications was 2017, when 170 studies were conducted. On the other hand, 169 academic studies were presented in 2019.

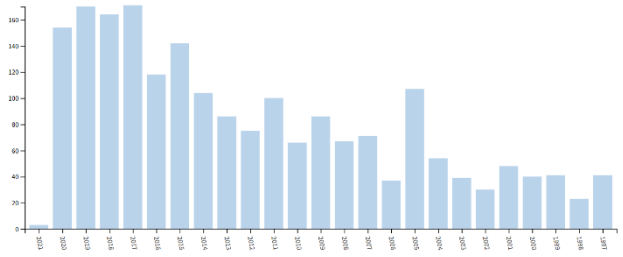

Figure 2 Distribution of publications by years [3]

The distribution of the publications carried out according to their types is shown in Figure 3. It was observed that the most common type of publication on indoor air quality was the articles published in journals. It was observed that 1414 articles on indoor air quality were published between 1975 and 2020 in academic journals. On the other hand, it has been determined that a significant amount of conference/symposium publications has been carried out on indoor air quality.

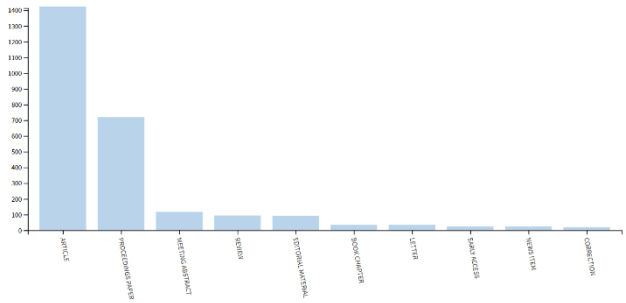

Figure 3 Distribution of publications by type [3]

The number of citations these studies received depending on the years is shown in Figure 3. In this context, it has been determined that especially the publications have been cited more and more after 2010. It was observed that 2398 publications received 29.298 citations in total. The first three study that received the most citations, respectively are related to "indoor air quality and health [10]", "indoor air quality and health symptoms in schools [35]" and "the effect of temperature, venlation and humidity on indoor air quality [16]".Due to the increase in the number of publications in 2010, it is seen that the number of citations has increased significantly since the same year.

Figure 4 Citation numbers of publications [3]

The distribution of the publications by country was examined and it was determined that the publications were made in 65 different countries in total. However, it was determined that one fourth of the publications were made in the USA alone. On the other hand, 67% of the studies were published in 10 countries where the most publications were made. These countries are shown in the table 2. In this context, it has been observed that the countries where the most publications are made are developed and developing countries.

Table 2
Countries with the highest number of publications [3]

Field: Countries/Regions	Record Count	% of 2,398	Bar Chart
USA	559	23.311 %	
Peoples R. China	330	13.761 %	
South Korea	125	5.213 %	
Canada	102	4.254 %	
England	100	4.170 %	
France	91	3.795 %	
Italy	91	3.795 %	
Portugal	87	3.628 %	
Germany	68	2.836 %	
India	63	2.627 %	

It was observed that the institutions with the highest number of publications were Hong Kong Polytechnic University and Denmark Technical University. In addition to the aforementioned educational institutions, it was determined that 26 publications were made by the US EPA.

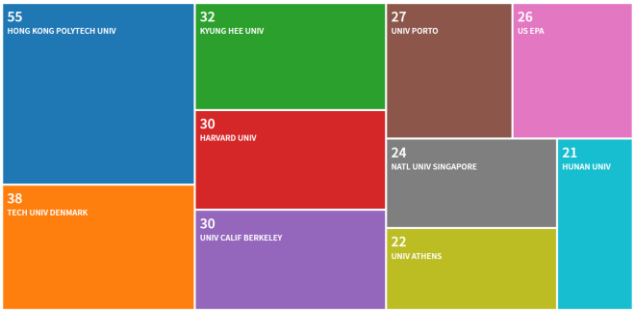

Figure 5 Institutions with the highest number of publications [3]

Since the main purpose of the study was to examine the factors affecting indoor air quality, the distribution of the publications dealing with the factors affecting indoor air quality was also

examined. In this context, it has been determined that among the factors affecting indoor air quality, ventilation and air flow rate are mostly examined. On the other hand, a significant amount of work has been carried out examining the effects of pollutants. In addition, it was observed that publications on temperature, humidity, bacteria and thermal comfort were also revealed.

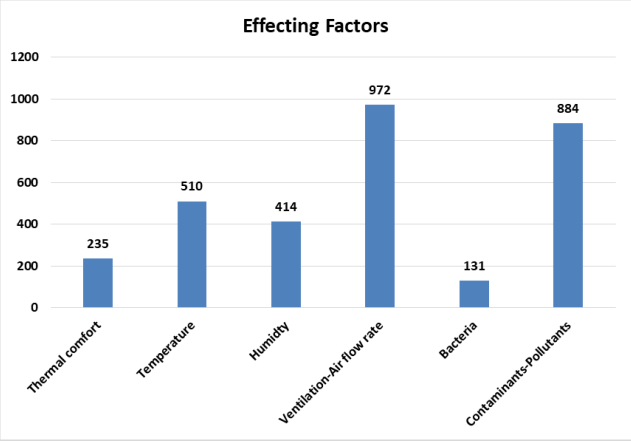

Figure 6 Distribution of publications examining factors affecting indoor air quality [3]

Considering the places where indoor air quality was examined, it was found that the workplacaes, offices and working environments were mostly examined. On the other hand, it has been observed that there are studies on indoor air quality in residential buildings, houses, schools and hospitals.

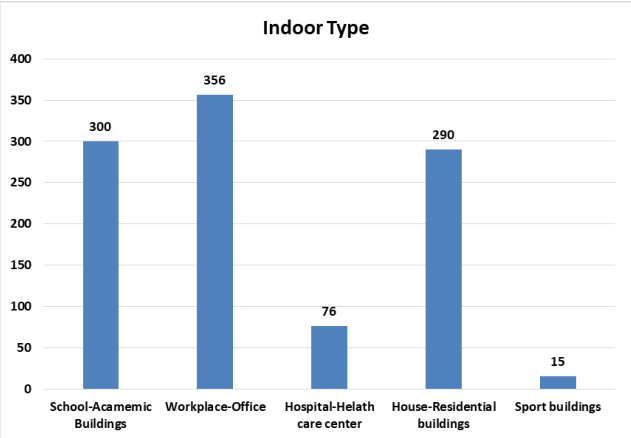

Figure 7 Distribution of publications examining specific indoor types [3]

4. CONCLUSION

As a result of the bibliometric analysis conducted in this study in which the factors affecting indoor air quality were examined, it was seen that the studies examining indoor air quality mostly worked on ventilation, air flow rate, indoor pollutants, volatile organic compounds, temperature and humidity. This shows that these factors affect indoor air quality. In addition to the analysis, in the literature review, it was also observed that humidity, temperature, air flow and pollutants are the most effective factors on indoor air quality.

Publications analyzed, generally conduct research on closed areas where people live collectively. In this context, it has been observed that studies have been carried out especially on indoor air quality in workplaces, schools and homes.

Considering the distribution of the publications, it was determined that there has been a significant increase in the number of publications, especially since 2010. It has also been found to be the most popular today. It has been observed that the number of citations received by the publications has increased especially with the increase in publications. It was note worthy that one fourth of the publications were made in the USA alone.

It is considered that the in-depth examination of only one factor that has an effect on indoor air quality in future studies will make a significant contribution to the literature.

Funding

The author has no received any financial support for the research, authorship or publication of this study." statement should be written.

The Declaration of Conflict of Interest/ Common Interest

No conflict of interest or common interest has been declared by the authors.

Authors' Contribution

The first author contributed 100%,

The Declaration of Ethics Committee Approval

This study does not require ethics committee permission or any special permission.

The Declaration of Research and Publication Ethics

The author of the paper declare that I comply with the scientific, ethical and quotation rules of SAUJS in all processes of the paper and that I do not make any falsification on the data collected. In addition, I declare that Sakarya University Journal of Science and its editorial board have no responsibility for any ethical violations that may be encountered, and that this study has not been evaluated in any academic publication environment other than Sakarya University Journal of Science."

REFERENCES

[1] H. Chao, D.K. Milton, J. Schwartz, H.A. Burge, "Dustborne fungi in large office buildings" Mycopathologia, vol. 154, no. 2, pp. 93-106, 2002.

[2] L. Molhave, "Sick building syndrome" Encyclopedia of Environmental Health, vol. 3, pp. 61-67, 2011.

[3] Web of Science, www.webofscience.com (Access Date: 16.04.2021)

[4] EPA "Indoor Air Pollution and Health." Report Series No. 104. 2013. Available online: https://www.epa.ie/pubs/reports/research/health/IndoorAirPollutionan, 2020.

[5] ASHRAE "ASHRAE Handbook, 2001 Fundamentals, Chapter 8: Thermal Comfort, The American Society of Heating, Refrigerating and Air-Conditioning" Atlanta, USA, 2003.

[6] EPA, "An Office Building Occupants Guide to Indoor Air Quality, UnitedStatesEnvironmentalProtectionn Agency" Indoor Environments Division, Washington, DC, 1997.

[7] WHO, "The right to healthy indoor air, Report on WHO Meeting Bilthoven, Netherlands" 15-17 May 2000, WHO Regional Office for Europe, 2000.

[8] E. A. Unobe, "Political Instability and the Possibility for a Sustainable Democratic Rule in Nigeria" Nigeria Journal of Political Science, vol. 9, no. 1, 2003.

[9] R. Kosonena, F. Tan, "Assessment of productivity loss in air-conditioned buildings using PMV index" Energy and Buildings, vol. 36, pp. 987-993, 2004.

[10] W.C. Sing, "A new engineering approach for indoor air quality management in building" Ph.D. Dissertation, The Hong Kong Polytechnic University, Hong Kong, 2007.

[11] A.P. Jones, "Indoor air quality and health. Atmospheric environment" vol. 33, no. 28, pp. 4535-4564, 1999.

[12] J. Sundell, "On the history of indoor air quality and health" Indoor air, vol. 14, pp. 51-58, 2004.

[13] P. Wolkoff, "Indoor air humidity, air quality, and health–An overview" International journal of hygiene and environmental health, vol. 221, no. 3, pp. 376-390, 2018.

[14] WHO, "Indoor Air Pollution: National Burden of Disease Estimates" WHO: Geneva, Switzerland, 2007. (accessed on 5 June 2019).

[15] I. I. Geneva, B. Cuzzo, T. Fazili, W. Javaid, "Normal body temperature: a systematic review" In Open Forum Infectious Diseases (Vol. 6, No. 4, p. ofz032). US: Oxford University Press, 2019.

[16] L. Fang, G. Clausen, P.O. Fanger, "Impact of temperature and humidity on the perception of indoor air quality" Indoor air, vol. 8, no. 2, pp. 80-90, 1998.

[17] L.Fang, D. F. Wyon, G, Clausen, P.O. Fanger, "Impact of indoor air temperature and humidity in an office on perceived air quality, SBS symptoms and performance" Indoor air, vol. 14, pp. 74-81, 2004.

[18] D. A. Krawczyk, B. Wadolowska, "Analysis of indoor air parameters in an education building" Energy Procedia, vol. 147, pp. 96-103, 2018.

[19] S. Schiavon, T. Hoyt, A. Piccioli, "Web application for thermal comfort visualization and calculation according to Standard 55" In Building Simulation, vol. 7, no. 4, pp. 321-334, 2014.

[20] F. Bauman, T. Webster, "Outlook for underfloor air distribution*"* UC Berkeley: Center for the Built Environment. Retrieved from https://escholarship.org/uc/item/5v60x5 7q, 2001.

[21] A.H. Sekhar, A.L. Devi, "Voltage profile improvement and power system losses reduction with multi TCSC placement in transmission system by using firing angle control model withheuristic algorithms" In 2016 International Conference on Signal Processing, Communication, Power and Embedded System, Paralakhemundi, Odisha, India, 2016, pp. 295-301.

[22] M. Kavgic, D. Mumovic, Z. Stevanovic, A. Young, "Analysis of thermal comfort and indoor air quality in amechanically ventilated theatre" Energy and Buildings, vol. 40, no. 7, pp. 1334-1343, 2008.

[23] Y. Ma, Y. Zhao, J. Liu, X. He, B. Wang, S. Fu, B. Luo, "Effects of temperature variation and humidity on the death of COVID-19 in Wuhan, China" Science of The Total Environment, vol. 724, p. 138226, 2020.

[24] B. Oliveiros, L. Caramelo, N. C. Ferreira, F. Caramelo, "Role of temperature and humidity in the modulation of the doubling time of COVID-19 cases" medRxiv. https://doi.org/10.1101/2020.03.05.2003 1872, 2020.

[25] J.D. Spengler, J. F. McCarthy, J. M. Samet, "Indoor air quality handbook" New York, United States, 2001.

[26] M. H. Sherman, "Efficacy of intermittent ventilation for providing acceptable indoor air quality (No. LBNL-56292)" Lawrence Berkeley National Lab.(LBNL), Berkeley, CA (United States), 2004.

[27] P. Wargocki, J. Sundell, W. Bischof, G. Brundrett, P. O. Fanger, F. Gyntelberg, P. Wouters,- " Ventilation and health in non industrial indoor environments: report from a European Multidisciplinary Scientific Consensus Meeting (EUROVEN)" Indoor air, vol. 12, no. 2, pp. 113-128, 2002.

[28] G. C. Da Graça, Q. Chen, L. R. Glicksman, L. K. Norford, "Simulation of wind-driven ventilative cooling systems for an apartment building in Beijing and Shanghai" Energy and buildings, vol. 34, no. 1, p.1, 2002.

[29] A. Akman, "İnsan sağlığı, Sağlıklı Yapı ve Yapı Biyolojisi" Yapı Dergisi, vol. 279, pp. 80-89, 2005.

[30] P. Krusche, M. Krusche, D. Althaus, I. Gabriel, “Okologisches Bauen Herausgegeben vo Umweltbundesamt” Wiesbaden und Berlin: Bauverlag, 1982.

[31] M. Rosana. Alberici, F. Wilson Jardim, "Photocatalytic destruction of VOCs in the gas-phase using titanium dioxide" Applied Catalysis B: Environmental vol. 14, pp.1-2, 1997.

[32] C.W. Lee, Y.T. Dai, C.H. Chıen, D.J. Hsu, “Characteristics and health impacts of volatile organic compounds in photocopy centers” Environmental Research, vol. 100, pp. 139-149, 2006.

[33] P.H. Fıscher, G. Hoek, H.V. Reeuwıjk, D.J. Brıggs, E. Lebert, J.V. Wıjnen, S. Kıngham, P.E. Ellıott, “Traffic related differences in outdoor and indoor concentrations of particles and volatile organic compunds in Amsterdam” Atmospheric Environment, vol. 34, pp. 3713-3722, 2000.

[34] A. Pritchard, “Statistical bibliography or bibliometrics” Journalof documentation, vol. 25, no. 4, pp. 348-349, 1969.

[35] N. De Bellis, “Bibliometrics and citation analysis: from the science citation index to cybermetrics” scarecrow press, 2009.

[36] J. M. Daisey, W. J. Angell, M.G. Apte, “Indoor air quality, ventilation and health symptoms in schools: an analysis of existing information” Indoor air, 13(LBNL-48287), 2003.

SAKARYA ÜNİVERSİTESİ
FEN BİLİMLERİ ENSTİTÜSÜ DERGİSİ

Sakarya University Journal of Science
SAUJS

ISSN 1301-4048 e-ISSN 2147-835X Period Bimonthly Founded 1997 Publisher Sakarya University
http://www.saujs.sakarya.edu.tr/

Title: Life Cycle Assessment of Microbial Electrolysis Cells for Hydrogen Generation Using TRACI Methodology

Authors: Seçil TUTAR ÖKSÜZ

Recieved: 2021-10-05 00:00:00

Accepted: 2022-05-12 00:00:00

Article Type: Research Article

Volume: 26
Issue: 3
Month: June
Year: 2022
Pages: 620-632

How to cite
Seçil TUTAR ÖKSÜZ; (2022), Life Cycle Assessment of Microbial Electrolysis Cells for Hydrogen Generation Using TRACI Methodology. Sakarya University Journal of Science, 26(3), 620-632, DOI: 10.16984/saufenbilder.1005044
Access link
http://www.saujs.sakarya.edu.tr/tr/pub/issue/70993/1005044

Sakarya University Journal of Science 26(3), 620-632, 2022

Life Cycle Assessment of Microbial Electrolysis Cells for Hydrogen Generation Using TRACI Methodology

Seçil TUTAR ÖKSÜZ*[1]

Abstract

Bioelectrochemical systems (BESs) use electrochemically active microorganisms to convert the chemical energy of organic matter into electrical energy, hydrogen, or other useful products through redox reactions. Microbial electrolysis cell (MEC) is one of the most common BESs which are able to convert organic substrate into energy (such as hydrogen and methane) through the catalytic action of electrochemically active bacteria in the presence of electric current and absence of oxygen. In the past decades, BESs have gained growing attention because of their potential, but there is still a limited amount of research is done for the environmental effects of BESs. This study initially provides an update review for MECs including general historical advancement, design properties, and operation mechanisms. Later, a life cycle assessment (LCA) study was conducted using a midpoint approach, which is TRACI methodology with EIO-LCA model to identify the potential impacts to the environment whether adverse or beneficial using the MECs to produce hydrogen with domestic wastewater as a substrate. The results show that the cumulative negative impacts were substantially larger than the positive impacts by contrast with the expectations, and the cumulative output data show that human health non-cancer impact provides the highest environmental effects than others mainly because of the inorganic chemicals, pumping and wastewater recycling equipment step. In addition, global warming potential and smog creation potential are also elevated mainly due to electricity usage, inorganic chemical and glassware reactor production. Later we are externally normalized each impact category to compare the results at the normalization level, and we again found that human health (cancer or non-cancer) potential provides the most negative impact on the environment in the MEC system originates on human health indicators.

Keywords: Microbial electrolysis cells, Life cycle assessment, Hydrogen generation, Wastewater treatment, TRACI

1. INTRODUCTION

The world population has continued to grow at a significant rate and is anticipated to exceed 9.7 billion by 2050 and nearly 11 billion in 2100 [1-3]. Related to urban development and population growth, there has been a significant increase in energy consumption [4]. According to the 2019 Annual Energy Outlook, crude oil reserves will run out by 2052, natural gas will run out by 2060,

* Corresponding author: stutar@ktun.edu.tr
[1] Konya Technical University/Faculty of Engineering and Natural Sciences/Environmental Engineering Department
ORCID: https://orcid.org/0000-0002-2713-7379

and coal will run out by 2090 if the fossil fuels's consumptions continue at the present rate [5]. Another challenge related to extensive consumption of fossil energy resources has been associated with a significant increase in the mass of greenhouse gases (GHG) (carbon dioxide, ozone, nitrous oxide, methane, water vapor, etc.), which are known to inhibit long-wavelength radiation from escaping into space, into the atmosphere. The effects of global warming has been already observed as higher sea levels, more severe storms, dirtier air, higher wildlife extinction rate, higher death rates, and so on [6]. Consequently, alternative sustainable energy resources are becoming more important because of declining fossil energy sources, global warming threats, environmental pollution, and reliance on fossil fuels exporting countries. On the other hand, related to urban development and population growth, especially in developed countries such as the US, wastewater generation has been significantly increased [7]. According to Connor, R. et al. (2017), around 20 percent of the world's wastewater is discharged into water bodies with applying treatment every day [8]. Discharging of untreated wastewater can cause waterborne illnesses such as diarrhea, hepatitis, cholera, meningitis, to name a few. It can also cause environmental risks, mainly because of eutrophication. In addition, GHG emissions, especially in the form of nitrous oxide and methane, can form decomposition of these waste streams [2, 9, 10]. According to the studies, untreated wastewater generates a GHG footprint roughly 3 times higher when the same wastewater is properly treated in a wastewater treatment plant. Even though the conventional wastewater treatment processes have advantages, such as low installation cost, fast start-up, flexible operation, and high wastewater treatment efficiency, they also have some drawbacks such as high energy requirements for their installation, maintenance, and operation [11]. Conventional aerobic treatment processes also produce large amounts of sludge, which is also costly to dispose of or treat, and may account for 35-60% of the total operating cost [12, 13]. According to the Environmental Protection Agency (EPA), about $25 billion is used to treat domestic wastewater and another $300 billion is spent to improve publicly owned treatment works every year in the United States [14]. Hence, current approaches to wastewater treatment account for 3-4% of the total energy consumption in the US with public water treatment services; other developed countries have similar statistics [15, 16]. For this purpose, improving current wastewater treatment systems with new sustainable technologies is an essential need to improve sustainability in wastewater besides eliminates adverse effects of global warming. At this point, producing hydrogen from wastewater is becoming very important since it is a clean and efficient fuel, especially if it is produced from sustainable energy sources.

Bioelectrochemical systems (BESs) have recently gained great attention as a promising technology that generates electricity, hydrogen, or other useful chemicals by oxidizing biodegradable organic matters using electrochemically active bacteria [10, 17]. Although many other applications of BESs have been studied, including harvesting value-added products (e.g., H2 and CH4); removing specific contaminants in wastewater such as heavy metals; and niche applications (i.e. biosensors), BESs have mainly been studied in terms of two applications, which are wastewater treatment and electricity generation during the last years. The main advantages of BESs are that they can be operated at room temperature, have high fuel conversion efficiency, and simultaneously wastewater treatment. Among BESs, microbial electrolysis cells (MECs) is a novel technology, which are able to convert organic substrate into energy (such as hydrogen) using electrochemically active bacteria by consuming electrical energy in the absence of oxygen [18]. Literature shows that hydrogen productions rates in MECs are between 80 to 100% if compared to other processes such as fermentation and water electrolysis [19, 20]. Also, effective applications of MECs can provide economic and environmental benefits. In this context, this study aims to analyze the environmental effects of microbial electrolysis cells for hydrogen production. In this study, we summarize the historical development of the MECs, operational principles, general design properties, application areas, advantages, and

challenges. Further, different MECs studies were reviewed to compile data, which aim to help us to evaluate, compare and validate the feasibility of this emerging technology. Therefore, we obtained data from previous studies which aim to generate hydrogen while treating wastewater and conduct a life cycle assessment of available MECs.

2. MICROBIAL ELECTROLYSIS CELLS

Event hough the idea of using microorganisms to produce electricity was first proposed in the early twentieth century by Potter, but first Cohen and later Davis and Yarborough constructed the first real MFC in 1962 [21, 22]. Although the interest in these systems slowed down until the 1990s, BESs have received more attention because of potential applications. BESs have been studied for a variety of applications, and they share the same principles, which is an oxidation half-reaction at the anode in which electrons are lost and a reduction half-reaction at the cathode in which electrons are gained [23]. MEC is one of the main type of BESs. In the anodic compartment, electrochemically active bacteria oxidize organic matter to generate electrons and protons. The generated electrons are transferred to the electrodes by three possible electron transfer processes including direct electron transfer via membrane redox proteins [24-26], mediated electron transfer via indigenous or exogenous redox molecules [27, 28], and conductive pili or nanowires that is formed on the bacteria cell surface connected to anode surface. In the meantime, the protons diffuse from the anode to the cathode through a separator. At the cathode, protons are reduced with a supply of additional voltage to produce hydrogen gas (Figure 1) [29]. For example, if glucose (C6H12O6) is used as an electron donor (298 oK, 1 bar, pH=7), the reactions occurring in each electrode can be expressed as in Eqs. (3) - (4) below:

Oxidation reaction at anode:
$C6H12O6 + 6H2O \rightarrow 6CO2 + 24H+ + 24e-$
$Eo = -95\ mVAg/AgCl5$ (1)

Reduction reaction at cathode:
$24H+ + 24e- \rightarrow 12H2$
$Eo = -613\ mVAg/AgCl$ (2)

Since the theoretical total cell potential (Eocell =Eocat-Eoan) is negative when glucose is used as a model electron donor under standard conditions, the reaction is not spontaneous. However, when a voltage is added (> 518 mV vs. Ag/AgCl), the reaction can be completed to form hydrogen gas.

As discussed in the previous section, BESs can effectively remove organic matter from wastewater within a reasonable amount of time. Even though MECs still not fully functioned in technology yet, MECs have great potential to become alternative traditional wastewater treatments methods.

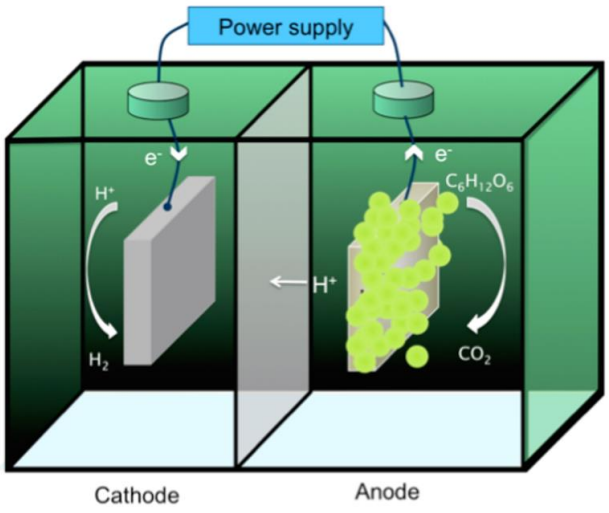

Figure 1 Schematic representation of a microbial electrolysis cell

Meanwhile, the hydrogen production rate was reported as 15 L/L/d with 100% of purity in a very first pilot-scale MEC study to treat domestic wastewater [30]. Another study showed that MECs can accomplish above 75% COD removal with real domestic wastewater applications with also an associated energy consumption which is reported below conventional wastewater technologies [19]. However, hydrogen recovery is not sufficiently high for practical applications of MECs with real wastewater. Also, when industrial wastewaters are used as substrate, MECs recover higher hydrogen due to the high concentration of organic matter in industrial wastewater, but these systems require some kind of amendment before being fed to the MECs. Besides wastewater, using different types of püre substrates results in generating other chemical

products such as methane (CH4), ethanol (EtOH), and hydrogen peroxide (H2O2) besides hydrogen. Table 1 shows selected MECs studies that used different types of wastewater, COD reduction and hydrogen generation rates. On the other hand, pure substrates, such as acetate, tend to provide the highest hydrogen production rates comparing wastewater. However, the primary concern generally is producing hydrogen when treating wastewater using this technology.

Table 1
Selected MECs performance parameters

Substrate Type	COD reduction (%)	H_2 gen. rate ($m^3/m^3/d$)	Ref.
Domestic wastewater	58±3	0.28±0.04	[31]
Domestic wastewater	25.4	0.041	[32]
Potato wastewater	79	0.74	[33]
Swine wastewater	75	0.9-1	[34]
Sludge wastewater	44.92	0.038	[35]
Dairy wastewater	92	0.2	[36]
Acetate	-	3.12	[37]
Acetate	-	50	[38]

Especially, during the last few decades, numerous studies have been carried out in the field of MECs, increasing its performance. MECs have advantages over other technologies because they have diverse applications including harvesting value-added products (e.g., H2); removing specific contaminants in wastewater such as heavy metals. However, as mentioned previously there are also limitations including low wastewater treatment efficiency in some of MECs, high energy loss, low coulombic efficiency and scale-up problems and cost of electrodes, etc. [39]. Even though these limitations, prospects of MEC technology are promising since several pilot-scale reactors have been developed, and research on MECs is continued [20]. Nevertheless, there have been many studies about MECs especially during the last decade, there are no many studies focused on the environmental benefits of MECs for hydrogen production using domestic wastewater.

This study initially aims to provide an update review for MECs including general historical advancement, design properties, and operation mechanisms. Then, a life cycle assessment (LCA) study was conducted using The Tool for the Reduction and Assessment of Chemical and Other Environmental Impacts (TRACI) characterization factors with EIO-LCA (The Economic Input-Output Life Cycle Assessment) model to identify the potential impacts to the environment whether adverse or beneficial using the MECs to produce hydrogen with domestic wastewater as a substrate.

3. METHODOLOGY

A life cycle assessment (LCA) is a methodology that investigates the environmental impacts of a product or process instead of the other technologies. LCA is also called cradle-to-grave analysis since it considers the product's or process's all the stages during the entire lifetime including manufacturing, construction, operation, repair, and dissemination. According to the International Organisation for Standardisation (ISO) in ISO 14040, LCA has four different basic stages including (1) goal and scope definition; (2) inventory analysis; (3) impact assessment; and (4) interpretation. However, we rearranged the algorithm by including reviewing and collecting technical data as a very first step and normalization of the data as another step, which is necessary for the selected midpoint approach in this study (Figure 2).

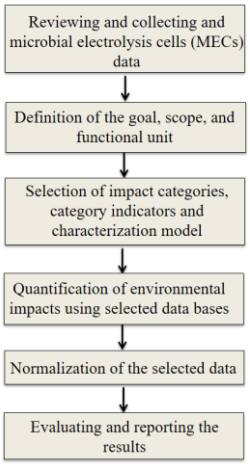

Figure 2 Methodology of life cycle assessment

The first part of a LCA study generally starts with defining the goal of the study, its scope and functional unit [40]. The ISO 14040 standard expresses that the goal of the study definition may include telling the intended use of the study, the reason for carrying the study, and to whom the results are aimed to be communicated and used as a comparative analysis [41]. According to the definition of the goal explained above, the goal of this current study is to identify that it is beneficial from an environmental point of view to converting wastewater to hydrogen using MECs. This study aims to provide sufficiently broad information related to environmental consequences. The primary aim of the study is to evaluate and validate the feasibility of this emerging technology. Therefore, the intended audience of the study will be the researchers and technical experts in the area of BESs technology [42]. In addition, the scope step should define a statement of the reason of the study, with detail and depth and show that applications of the results. When explaining the scope of the study, the functions of the product system; the functional unit; system boundary; life cycle impact assessment methodology; inventory data; data quality requirements; critical review considerations and comparison between systems should be considered and described [43].

Once the goal and the scope of the study are chosen, the next step is to set the functional unit, which should be chosen based on the goal of the study. The functional unit should provide a reference unit of comparison that the system (or product) can be compared to provide an equivalence [44]. Therefore, the primary aim of this study is to achieve higher pure hydrogen generation, so our function is hydrogen production, and the functional unit is pure hydrogen generation rate (m3-H2 /m3-reactor per day). However, if the projected aim is only wastewater treatment, then the functional unit will also change accordingly. In this case, the functional unit will be organic compound removal rate (mg-COD/m3 - reactor per day). According to ISO 14040, system boundary is specified to determine which unit processes that is included in the product system.

The initial boundaries of the system will be determined by the goal and the scope of the study. An overall scheme of MEC process and its possible system boundary for LCA is shown in Figure 3.

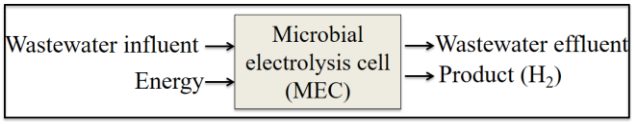

Figure 3 System boundary of a microbial electrolysis cell

After defining the goal, scope, and functional unit, the second step of LCA is life cycle inventory (LCI) step, which involves the data collection and calculation input and output flows to complete the inventory. This data collecion is actually the first step for a complete characterisation of the different streams to obtain a detailed inventory of all the inputs, outputs, emissions and other environmental impacts [45]. LCA studies sometimes can have data availability and/or quality problems within this phase. In our study, the preliminary inventory data is collected from previous MECs studies in the literature, laboratory experiments, and/or LCA databases. In addition, background information (e.g. chemicals production processes) is normally provided by free LCI databases such as Agribalyse, USDA, NEEDS, ELCD, bioenergiedat, USLCI.

The inventory of the MEC system has a long list, so we divided the process into three stages construction stage, operation stage, and electricity. While the construction stage includes pump, pumping equipment, plastic pipe, pipe fitting equipment, plastic, rubber products, electrode materials (carbon and graphite products), membrane, wiring, glass container, the operation stage includes wastewater and chemical requirements. The current study also assumes that construction and operation parameters such as temperature, retention times, pH, reactor configuration, etc. are in static conditions. Also, sludge and nutrient removal (nitrogen and phosphorus) were allocated in this study.

In an LCA, an important aspect to be considered is the selection of the appropriate impact categories, which is in life cycle impact

assessment (LCIA) stage. Two LCIA methods are used in the LCA as midpoint and endpoint approach. Endpoint approach (i.e. EPS, Ecoindicator 99). The primary aim of the endpoint approach is to be understood as issues of environmental concern, such as ecosystem, resource availability, human health, climate change, and etc. while categorizing them in damage level. On the other hand, midpoint approach (i.e. CML 2002, EDIP 2003, TRACI) consider the environmental impact at a level in cause-effect chain, which is also called problem level [46]. The main difference between midpoint and endpoint methods is that the way how category indicators show the impact categories [47].

TRACI is one of the midpoint approaches was developed by United States Environmental Protection Agency (US EPA), which draws simple cause and effect chains to demonstrate the point at which each impact category is characterized, and is one of the most used midpoint approaches in the US. Basically, TRACI method is used for general uses like environmentally sustainability or environmental pollution control. Different impact categories considered in this methodology include Global Warming Potential (GWP), Acidification Potential (AP), Human Health Criteria Air Potential (HHCAP), Eutrophication Potential (EP), Ozone Depletion Potential (ODP), Smog Creation Potential (SCP), Ecotoxicity Potential (ETP), Human Health Cancer Potential (HHCP), Human Health Non-Cancer Potential (HHCP), and Non-Renewable Energy (NRE) [48]. Among these common impact categories GWP, AP, HHCAP, ODP, and SCP are air-related categories, but EP, ETP, and HHCP are air, water, soil-related categories. After the impact categories are selected, the inventory data are classified to the selected categories, which is essential to define characterization factors. These characterization factors should reflect the relative contribution of an LCI result to the impact category indicator result into common units (such as kg SO_2 equivalent for acidification potential) [49]. In this study, we will identify significant impact categories by comparing them using normalization step to present suggestions to reduce the environmental impact can be made in the interpretation part. Detailed information about TRACI method can be found in the literature.

In our study, we also used The Economic Input-Output Life Cycle Assessment (EIO-LCA) model, was developed by Carnegie Mellon University, which estimates the materials and energy resources required for, and the environmental emissions resulting from, activities in the economy [50]. EIO-LCA provides us several outputs data based on raw materials that are used in the construction, operation, and electricity stages of MEC. We also have to indicate that electricity data includes electricity usage during operation. However, even though EIO-LCA does not provide us with the exact value of electricity usage during the production period of the construction stage, we know that a significant amount goes directly to electricity usage during construction [51].

Table 2
Selected MECs performance parameters

Impact category	Construction	Operation	Electricity
GWP (CO_2 eq.)	438,58	376,01	294,50
AP (SO_2 eq.)	4,62	1,66	1,69
HHCAP (PM10 eq.)	2,47	0,462	0,335
EP_{air} (N eq.)	0,144	0,019	0,025
EP_{water} (N eq.)	4E-04	8,25E-04	4,5E-06
ODP (CFC-11 eq.)	2,1E-03	7,55E-04	0
SCP_{air} (O_3 eq.)	93,10	7,55E-04	13,60
ETP_{low} (2,4-D eq.)	1,05	4,80E-04	3,41E-03
ETP_{high} (2,4-D eq.)	0,102	0,005	0,003
$HHCP_{low}$ (Benzene eq.)	0,101	0,049	0,05
$HHCP_{high}$ (Benzene eq.)	1,33	1,19	0,015
$HHNCP_{low}$ (Tolune eq.)	237,3	12,95	0
$HHNCP_{high}$ (Tolune eq.)	347,2	740,50	0
NRE (J)	0,016	0,005	0,025

3. RESULTS AND DISCUSSION

After all inputs and outputs data (construction, operation, and electricity based data of a MEC system) were obtained mainly from EIO-LCA software (Table 2), the results were scaled as needed and summed up all outputs. In this study, midpoint categories were GWP (CO2 eq.), AP (SO2 eq.), HHCAP (PM10 eq.), EP (N eq.), ODP (CFC 11 eq.), SCP (O3 eq.), ETP (2,4D eq.), HHCP (benzene eq.), HHNCP (toluene eq.), and NRE (MJ). Figure 4 shows the results from EIO-LCA output in dimessionless units, as summed total score. The impact results indicate wide dispersion of the effects between selected midpoints depending on material input, electricity usage, and emissions produced that occurred for each process. The last part of the current study aims to understand the implications of the selected method and draw conclusions.

GWP, SCP, and HHNCP are the most contributed overall impact categories in the current study (Figure 4). Results from the LCA of MEC study demonstrated that the most significant impact category of the inventory in terms of contribution to GWP, which compares emissions of greenhouse gasses using CO2 equivalents. The sources of GWP can be antropogenic and/or naturogenic as the other impact categories. The predominant contributors of GWP are inorganic chemicals (376,01 kg CO2 eq.), electricity consumption (294,50 kg CO2 eq.), and glassware reactor (316 kg CO2 eq.) The second significant impact category is HHNCP, which expressed the possible increase of toxicological health risks by releases of the substances except for cancer. For HHNCPhigh, the production of inorganic chemicals is the highest contributor to impacts (740,5 kg toluene eq.), while the second-highest contributors are pumping and wastewater recycling equipment (325,5 kg toluene eq.). On the other hand, the dominant contributors of HHNCPlow are pumping and wastewater recycling equipment (159,5 kg toluene eq.) and wires (57,5 kg toluene eq.), which use in the preparation of the electrodes. In the EIO-LCA model, the outputs are expressed as low and high estimates for some impact categories including ETP, HHCP, and HHNCP in TRACI methodology. For the HHNCP, EIO-LCA outputs for toluene equivalent emissions low and high are estimated. In the current study, we use the average of low and high results while representing it in Figure 4. And also another high significant impact category is SCP (also known as photochemical oxidation), which can define as the additional formation of ground-level ozone by releasing nitrogen oxides (NOx) and particulates. Even though the electricity (13,6 kg O3 eq.), pump equipment (10,06 kg O3 eq.), and inorganic chemicals (8,4 kg O3 eq.) create considerable impacts, the highest contributor is glassware equipments (61,50 kg O3 eq.), which are used as MEC reactors. Atmospheric emissions from melting activities, which are directly related, is the major source of envionmental impact during the glass production.

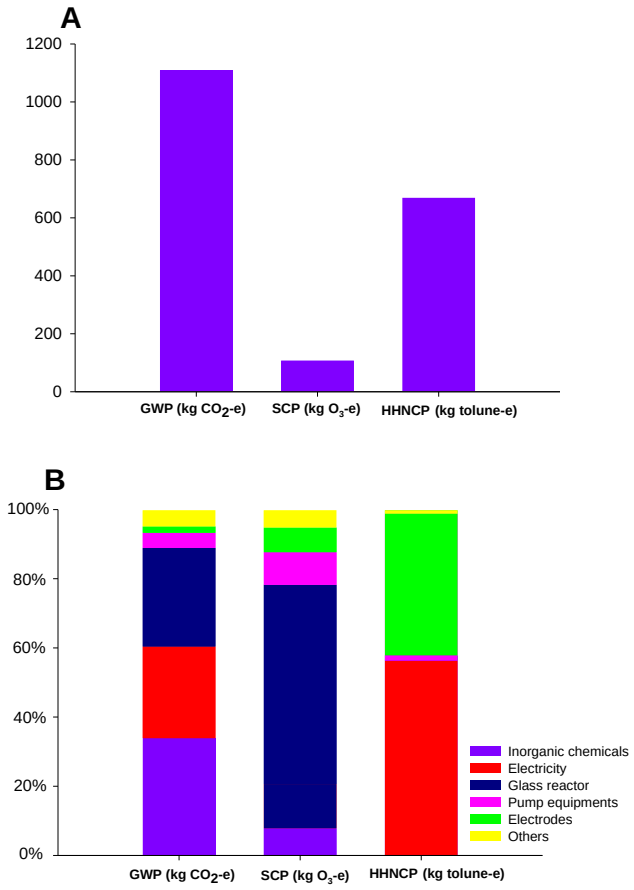

Figure 4 (A) The cumulative results from EIO-LCA output. (B) Percentage of the impact categories based on different materials and electricity

Figure 4A only demonstrates the selected impacts categories based on the EIO-LCA output. However, the other impact categories are shown

in Table 2 because these impact categories have low impacts, so it was difficult to plot in the same graph. It is also important to add that ODP does not include nitrous oxide emissions in TRACI methodology, so the environmental impact related to ODP was not high as expected [52].

Even though the selection of impact categories, category indicators, characterization models, classification of the results, and characterization are mandatory elements, normalization, grouping, weighting, and data quality analysis are optional elements in LCA. When we interpret the impact scores normalization process may help us for an additional step. We know that normalization factors are important for relating results to a common reference, so the midpoint and endpoint results are compared at the normalization level. Therefore, reporting the results with a better base is possible. In this study, we used the normalization factors, which were obtained from a study Ryberg, M. et al. (2014) conducted in [47]. They reported updated normalization factors for the TRACI method of US EPA using both US 2008 and US 2008-Canada 2005 based on US and Canadian emission and resource data-based inventory. Therefore, TRACI contains normalization data for the following reference systems: US 2008 and US 2008-Canada 2005, and we normalized the relative to the US 2008 annual per capita by dividing the indicator results by the selected reference values (Table 3) [48] .

Table 3
Selected MECs performance parameters

Impact category	Unit	Normalized Value
GWP	kg CO_2 eq.	7,4E12
AP	kg SO_2 eq.	2,8E10
EP	kg N eq.	6,6E9
ODP	kg CFC-11 eq.	4,9E7
SCP	kg O_3 eq.	4,2E11
ETP	kg 2,4-D eq.	2,3E10
HHCP	kg benzene eq.	1,7E3
HHNCP	kg tolune eq.	1,1E4

Figure 5 shows the externally normalized values of selected midpoints. We found that the highest impact category relative to US 2008 normalization values is HHNCP, which is found 6,5x10-2. As mentioned above, EIO-LCA outputs for toluene equivalent emissions for HHNCP are estimated as low and high. Therefore, we use the average of low and high results while representing the normalized data. Similarly, HHCP provides us with the second-highest normalized impact data with 7,9x10-4. For the current study, the highest normalized midpoint score was human health (cancer or non-cancer) potential, which indicates that the most negative impact on the environment in the MEC system originates on human health indicators.

Figure 5 shows that the other total normalized impact scores of GWP, AP, EP, ODP, SP, and ETP have higher environmental effects than other potentials (HHCAP and NRE). According to Fig. 5, it is assumed to be chemical and other construction materials production and usage is a predominant source of especially GWP and AP while especially glassware production elevated SCP. Among these impact categories, AP is mainly formed by the SOx and NOx from the combustion of the fossil fuels. The normalized results also show that EP and ETP indexes show a tendency to increase.

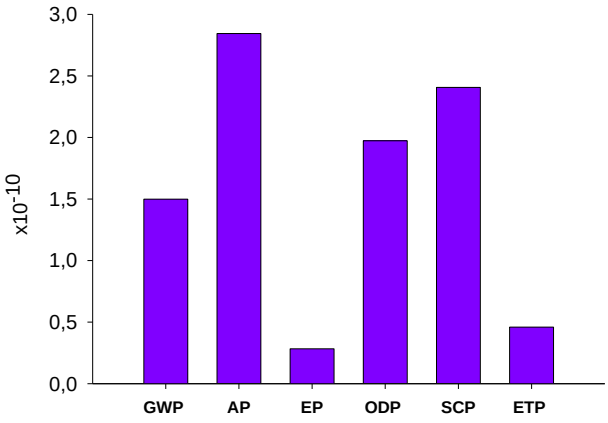

Figure 5 Externally normalized values of selected midpoints

As mentioned in the previous sections, the most important futures of MECs are hydrogen generation during wastewater treatment and also vastly reduce the amount of sludge produced. However, the current study only focused on hydrogen production when treating wastewater, and that's why we obtained higher negative environmental impacts, in which hydrogen production rate is not high enough to obtain more

positive environmental impacts. If the system boundary of this study expanded with including sludge removal, the results can move forward in the positive direction.

4. CONCLUSIONS

To summarize MECs have the potential for hydrogen generation while treating wastewater simultaneously. However, limited amounts of research are done on the environmental effects of MECs. This study provides an understanding of the environmental effects of MECs systems at the midpoint level as well as providing an update review for MECs including general historical advancement, design properties, and operation mechanisms. In this context, TRACI methodology was performed to identify the potential impacts of MEC on the environment at the midpoint level, which is the best available method for LCA. For internal optimization of the system, each impact category is externally normalized by using US normalization factors since it is very useful to examine which impact category has less or more significance in the overall system. The results provide that the positive environmental impacts were not larger as expected, which was mainly becuse of the construction stage. Even though MEC technology focuses on increasing hydrogen generation rate when treating wastewater, there should be other aspects that should be considered such as improving the operational parameters, innovating materials and, reducing the operational costs. Therefore, the emissions can be significantly reduced.

Acknowledgements

No acknowledgements has been declared by the author.

Funding

The authors received no financial support for the research, authorship or publication of this work.

The Declaration of Conflict of Interest/ Common Interest

No potential conflict of interest was reported by the authors.

The Declaration of Ethics Committee Approval

Ethics Committee Approval is not required.

The Declaration of Research and Publicatıon Ethics

In the writing process of this study, international scientific, ethical and citation rules have been followed.

Authors' Contribution

The authors contributed equally to the study.

The Declaration of Research and Publication Ethics

The authors of the paper declare that they comply with the scientific, ethical and quotation rules of SAUJS in all processes of the paper and that they do not make any falsification on the data collected. In addition, they declare that Sakarya University Journal of Science and its editorial board have no responsibility for any ethical violations that may be encountered, and that this study has not been evaluated in any academic publication environment other than Sakarya University Journal of Science.

REFERENCES

[1] J. Bongaarts, "Population policy options in the developing world," Science, vol. 263, no. 5148, pp. 771-776, 1994.

[2] E. Corcoran, Sick water?: the central role of wastewater management in sustainable development: a rapid response assessment. UNEP/Earthprint, 2010.

[3] M. M. Kent and C. Haub, "BULLETINDecember 2005," 2005.

[4] R. Avtar, S. Tripathi, A. K. Aggarwal, and P. Kumar, "Population–urbanization–energy

nexus: a review," Resources, vol. 8, no. 3, p. 136, 2019.

[5] I. E. Agency, World energy outlook 2020. OECD Publishing, 2020.

[6] S. F. Singer, Unstoppable global warming: Every 1,500 years. Rowman & Littlefield, 2006.

[7] D. J. V. Rooijen, "Implications of Urban development for water demand, wastewater generation and reuse in water-stressed cities: case studies from South Asia and sub-Saharan Africa," Loughborough University, 2011.

[8] R. Connor et al., "The united nations world water development report 2017. wastewater: the untapped resource," The United Nations World Water Development Report, 2017.

[9] U. WWAP, "United Nations world water assessment programme. The world water development report 1: Water for people, water for life," ed: UNESCO: Paris, France, 2003.

[10] S. T. Oksuz and H. Beyenal, "Enhanced bioelectrochemical nitrogen removal in flow through electrodes," Sustainable Energy Technologies and Assessments, vol. 47, p. 101507, 2021.

[11] M. Von Sperling, V. Freire, and C. de Lemos Chernicharo, "Performance evaluation of a UASB-activated sludge system treating municipal wastewater," Water Science and Technology, vol. 43, no. 11, pp. 323-328, 2001.

[12] L. Appels, J. Baeyens, J. Degrève, and R. Dewil, "Principles and potential of the anaerobic digestion of waste-activated sludge," Progress in energy and combustion science, vol. 34, no. 6, pp. 755-781, 2008.

[13] G. Zhen, X. Lu, H. Kato, Y. Zhao, and Y.-Y. Li, "Overview of pretreatment strategies for enhancing sewage sludge disintegration and subsequent anaerobic digestion: Current advances, full-scale application and future perspectives," Renewable and Sustainable Energy Reviews, vol. 69, pp. 559-577, 2017.

[14] K. Miller, K. Costa, and D. Cooper, "How to upgrade and maintain our nation's wastewater and drinking-water infrastructure," Washington, DC: Center for American Progress, 2012.

[15] P. L. McCarty, J. Bae, and J. Kim, "Domestic wastewater treatment as a net energy producer–can this be achieved?," ed: ACS Publications, 2011.

[16] B. E. Logan and K. Rabaey, "Conversion of wastes into bioelectricity and chemicals by using microbial electrochemical technologies," Science, vol. 337, no. 6095, pp. 686-690, 2012.

[17] D. Pant et al., "Bioelectrochemical systems (BES) for sustainable energy production and product recovery from organic wastes and industrial wastewaters," Rsc Advances, vol. 2, no. 4, pp. 1248-1263, 2012.

[18] D. Call and B. E. Logan, "Hydrogen production in a single chamber microbial electrolysis cell lacking a membrane," Environmental science & technology, vol. 42, no. 9, pp. 3401-3406, 2008.

[19] A. Escapa, M. San-Martín, R. Mateos, and A. Morán, "Scaling-up of membraneless microbial electrolysis cells (MECs) for domestic wastewater treatment: Bottlenecks and limitations," Bioresource technology, vol. 180, pp. 72-78, 2015.

[20] A. Escapa, R. Mateos, E. Martínez, and J. Blanes, "Microbial electrolysis cells: An emerging technology for wastewater treatment and energy recovery. From laboratory to pilot plant and beyond," Renewable and Sustainable Energy Reviews, vol. 55, pp. 942-956, 2016.

[21] M. R. Cohen, "Reason and nature," 1931.

[22] J. B. Davis and H. F. Yarbrough, "Preliminary experiments on a microbial fuel cell," Science, vol. 137, no. 3530, pp. 615-616, 1962.

[23] B. E. Logan, Microbial fuel cells. John Wiley & Sons, 2008.

[24] L. A. Meitl, C. M. Eggleston, P. J. Colberg, N. Khare, C. L. Reardon, and L. Shi, "Electrochemical interaction of Shewanella oneidensis MR-1 and its outer membrane cytochromes OmcA and MtrC with hematite electrodes," Geochimica et Cosmochimica Acta, vol. 73, no. 18, pp. 5292-5307, 2009.

[25] M. M. Pereira, J. N. Carita, and M. Teixeira, "Membrane-bound electron transfer chain of the thermohalophilic bacterium Rhodothermus marinus: a novel multihemic cytochrome bc, a new complex III," Biochemistry, vol. 38, no. 4, pp. 1268-1275, 1999.

[26] K. B. Koller, M. H. Fred, G. Fauque, and J. LeGall, "Direct electron transfer reactions of cytochrome c553 from Desulfovibriovulgaris Hildenborough at indium oxide electrodes," Biochemical and biophysical research communications, vol. 145, no. 1, pp. 619-624, 1987.

[27] S. R. Crittenden, C. J. Sund, and J. J. Sumner, "Mediating electron transfer from bacteria to a gold electrode via a self-assembled monolayer," Langmuir, vol. 22, no. 23, pp. 9473-9476, 2006.

[28] E. Marsili, D. B. Baron, I. D. Shikhare, D. Coursolle, J. A. Gralnick, and D. R. Bond, "Shewanella secretes flavins that mediate extracellular electron transfer," Proceedings of the National Academy of Sciences, vol. 105, no. 10, pp. 3968-3973, 2008.

[29] H. Liu, H. Hu, J. Chignell, and Y. Fan, "Microbial electrolysis: novel technology for hydrogen production from biomass," Biofuels, vol. 1, no. 1, pp. 129-142, 2010.

[30] E. Heidrich, J. Dolfing, K. Scott, S. Edwards, C. Jones, and T. Curtis, "Production of hydrogen from domestic wastewater in a pilot-scale microbial electrolysis cell," Applied microbiology and biotechnology, vol. 97, no. 15, pp. 6979-6989, 2013.

[31] R. D. Cusick, P. D. Kiely, and B. E. Logan, "A monetary comparison of energy recovered from microbial fuel cells and microbial electrolysis cells fed winery or domestic wastewaters," International Journal of hydrogen energy, vol. 35, no. 17, pp. 8855-8861, 2010.

[32] J. Chen et al., "System development and environmental performance analysis of a pilot scale microbial electrolysis cell for hydrogen production using urban wastewater," Energy Conversion and Management, vol. 193, pp. 52-63, 2019.

[33] P. D. Kiely, R. Cusick, D. F. Call, P. A. Selembo, J. M. Regan, and B. E. Logan, "Anode microbial communities produced by changing from microbial fuel cell to microbial electrolysis cell operation using two different wastewaters," Bioresource technology, vol. 102, no. 1, pp. 388-394, 2011.

[34] R. C. Wagner, J. M. Regan, S.-E. Oh, Y. Zuo, and B. E. Logan, "Hydrogen and methane production from swine wastewater using microbial electrolysis cells," water research, vol. 43, no. 5, pp. 1480-1488, 2009.

[35] K. Hu, L. Xu, W. Chen, S.-q. Jia, W. Wang, and F. Han, "Degradation of organics extracted from dewatered sludge by alkaline pretreatment in microbial electrolysis cell," Environmental Science and Pollution Research, vol. 25, no. 9, pp. 8715-8724, 2018.

[36] M. Hasany, S. Yaghmaei, M. M. Mardanpour, and Z. G. Naraghi, "Simultaneously energy production and dairy wastewater treatment using

bioelectrochemical cells: In different environmental and hydrodynamic modes," Chinese journal of chemical engineering, vol. 25, no. 12, pp. 1847-1855, 2017.

[37] B. Tartakovsky, M.-F. Manuel, H. Wang, and S. Guiot, "High rate membrane-less microbial electrolysis cell for continuous hydrogen production," International Journal of Hydrogen Energy, vol. 34, no. 2, pp. 672-677, 2009.

[38] A. W. Jeremiasse, H. V. Hamelers, and C. J. Buisman, "Microbial electrolysis cell with a microbial biocathode," Bioelectrochemistry, vol. 78, no. 1, pp. 39-43, 2010.

[39] B. Kumar, K. Agrawal, and P. Verma, "Microbial electrochemical system: A sustainable approach for mitigation of toxic dyes and heavy metals from wastewater," Journal of Hazardous, Toxic, and Radioactive Waste, vol. 25, no. 2, p. 04020082, 2021.

[40] G. Rebitzer et al., "Life cycle assessment: Part 1: Framework, goal and scope definition, inventory analysis, and applications," Environment international, vol. 30, no. 5, pp. 701-720, 2004.

[41] H. Baumann, "Environmental assessment of organising: towards a framework for the study of organisational influence on environmental performance," Progress in Industrial Ecology, an International Journal, vol. 1, no. 1-3, pp. 292-306, 2004.

[42] N. Vlasopoulos, F. Memon, D. Butler, and R. Murphy, "Life cycle assessment of wastewater treatment technologies treating petroleum process waters," Science of the Total Environment, vol. 367, no. 1, pp. 58-70, 2006.

[43] A.-C. P. a. E. Riise, "Defining the goal and scope of the LCA study," 2011.

[44] S. A. I. Corporation and M. A. Curran, "Life-cycle assessment: principles and practice," ed: National Risk Management Research Laboratory, Office of Research and …, 2006.

[45] A. Hospido, M. T. Moreira, M. Fernández-Couto, and G. Feijoo, "Environmental performance of a municipal wastewater treatment plant," The International Journal of Life Cycle Assessment, vol. 9, no. 4, pp. 261-271, 2004.

[46] H. A. U. de Haes, O. Jolliet, G. Finnveden, M. Hauschild, W. Krewitt, and R. Müller-Wenk, "Best available practice regarding impact categories and category indicators in life cycle impact assessment," The International Journal of Life Cycle Assessment, vol. 4, no. 2, pp. 66-74, 1999.

[47] A. H. Sharaai, N. Z. Mahmood, and A. H. Sulaiman, "Life cycle impact assessment (LCIA) using TRACI methodology: An analysis of potential impact on potable water production," Australian Journal of Basic and Applied Sciences, vol. 4, no. 9, pp. 4313-4322, 2010.

[48] M. Hauschild et al., "Recommendations for Life Cycle Impact Assessment in the European context-based on existing environmental impact assessment models and factors (International Reference Life Cycle Data System-ILCD handbook)," Institute for Environment and Sustainability (IES), retrieved from: http://lct. jrc. ec. europa. eu/assessment/projects, 2011.

[49] Y. Dong, M. Hossain, H. Li, and P. Liu, "Developing Conversion Factors of LCIA Methods for Comparison of LCA Results in the Construction Sector," Sustainability, vol. 13, no. 16, p. 9016, 2021.

[50] A. Shah, N. Baral, and A. Manandhar, "Technoeconomic analysis and life cycle assessment of bioenergy systems," in Advances in Bioenergy, vol. 1: Elsevier, 2016, pp. 189-247.

[51] A. I. Racoviceanu, B. W. Karney, C. A. Kennedy, and A. F. Colombo, "Life-cycle energy use and greenhouse gas emissions inventory for water treatment systems," Journal of Infrastructure Systems, vol. 13, no. 4, pp. 261-270, 2007.

[52] J. Lane and P. Lant, "Including N2O in ozone depletion models for LCA," The International Journal of Life Cycle Assessment, vol. 17, no. 2, pp. 252-257, 2012.

SAKARYA ÜNİVERSİTESİ
FEN BİLİMLERİ ENSTİTÜSÜ DERGİSİ

Sakarya University Journal of Science
SAUJS

ISSN 1301-4048 e-ISSN 2147-835X Period Bimonthly Founded 1997 Publisher Sakarya University
http://www.saujs.sakarya.edu.tr/

Title: Economic and Technical Performance Assessment of a Thermal Energy Storage System for Ancillary Services

Authors: Emin Selahattin UMDU, Levent BİLİR

Recieved: 2021-03-09 00:00:00

Accepted: 2022-05-16 00:00:00

Article Type: Research Article

Volume: 26
Issue: 3
Month: June
Year: 2022
Pages: 633-642

How to cite
Emin Selahattin UMDU, Levent BİLİR; (2022), Economic and Technical Performance Assessment of a Thermal Energy Storage System for Ancillary Services. Sakarya University Journal of Science, 26(3), 633-642, DOI: 10.16984/saufenbilder.1085215
Access link
http://www.saujs.sakarya.edu.tr/tr/pub/issue/70993/1085215

Sakarya University Journal of Science 26(3), 633-642, 2022

Economic And Technical Performance Assessment of a Thermal Energy Storage System for Ancillary Services

Emin Selahattin UMDU[1], Levent BİLİR*[1]

Abstract

Increasing renewables in energy mix results in lower emissions but also increased fluctuations in the electricity grid. Current thermal energy conversion-based systems will stay as main electricity generation in the grid, and they will support base loads of the system. Whether these systems are fossil or geothermal sourced they need adaptive technologies to harmonize with the changing network. This study aims to investigate feasibility and performance to satisfy response demands for a proposed thermal energy storage system connected to feed stream of thermal power generation to support ancillary services in a case study in Turkey. Tin is selected as the phase change material for its good inductive properties. It is demonstrated numerically that the evaluated heat storage tank, filled with tin, provides adequate time for thermal discharging within time limits to benefit from hourly ancillary power market. Using hourly pricing data for entire 2020, it is found that proposed system shows better economic performance than investment requirement of ROI over 11% as stated in various literature for renewable energy systems. Analysis of system economic performance shows a ROI of 16% and NPV is 17.8% higher than required investment.

Keywords: Thermal energy storage, ancillary services, NPV, economic analysis, ansys-fluent

1. INTRODUCTION

European Union's (EU) ambitious target of achieving at least an 80% reduction in greenhouse gas (GHG) emissions below 1990 levels by 2050, while maintaining or improving today's levels of electricity supply reliability, energy security, economic growth, and prosperity [1]; requires overcoming a series of technical obstacles. The resolution of the European Parliament stresses the important role of energy storage in addressing the flexibility needs of the energy system to reach our climate neutrality target. Further its vital role in security of electricity supply is highlighted.

Ancillary services refer to functions that help grid operators maintain a reliable electricity system. These services maintain the proper flow and direction of electricity, address imbalances

* Corresponding author: levent.bilir@yasar.edu.tr
[1] Yaşar University
E-mail: selahattinumdu@gmail.com
ORCID: https://orcid.org/ 0000-0002-8227-6267, https://orcid.org/0000-0003-3950-5367

between supply and demand, and help the system recover after a power system event. In systems with significant variable renewable energy (RE) penetration, additional ancillary services may be required to manage increased variability and uncertainty. Ancillary services can be renovated to use renewable energy sources. For this purpose, renewable energy cannot be injected into the electricity grid due to lack of demand can be stored and deliver it to the grid in peak times. These applications vary in size starting from 100 (kW) to 2 (MW) with a target discharge range of 20 (mins) to 1.5 (hrs). It helps electricity system for supply and demand balancing and reduce emissions by helping to displace fossil fuels with renewable energy. In this respect (1) European Council, EC economic recovery plan 'Next Generation EU' includes storage as one of the investment priorities to boost economic growth and resilience in the EU, (2) support the uptake of energy storage to achieve the EU decarbonization objectives, (3) will support investments in the next financing period [2].

The power generation capacity in power plants cannot be utilized to the grid in periods where demand is reduced, and this results in economic losses and increased environmental impact. For example, energy demand decreases significantly during night-time. Because of the tariff schemes and variable pricing, geothermal and other thermal power plants become uneconomical for up to six hours during low grid demand. In addition, due to the decrease in heat supplying fluid temperatures coming from either furnaces or geothermal wells in all operating periods of power generation, nominal power generation decreases, and efficiency losses are observed.

Similarly, in power plants that use any other energy sources such as wind, solar, fossil fuel, nuclear etc., there is a decrease in capacity utilization and thus efficiency losses in periods of low demand. In this case, the power generation can be kept at a nominal value and when the demand is low and generated power can be stored as sensible or latent heat, which can be used later directly or indirectly for power generation to supply peak loads on the grid. Thus, providing both economic, operational, and environmental benefits.

There are three types of methods in thermal energy storage where their advantages and disadvantages are summarized in Table 1. These methods are sensible thermal energy storage (STES), latent thermal energy storage (LTES) and thermo-chemical energy storage (TCES) [3].

Table 1
Overview of heat storage applications for power generation type

	Advantages	**Disadvantages**
STES	the simplest and the most technologically advanced	Low thermal energy storage density is achieved
LTES	Moderate energy intensity among the three methods Energy storage and reuse process takes place at constant temperature	There is low thermal conduction for the materials used In long-term use, material structure deterioration may occur There is a loss of heat
TCES	Long-term storage is possible The volume required for storage is comparatively small There is no heat loss	The system is complex Requires high initial investment

In the present study, a thermal energy storage tank, filled with tin as the storage medium, is also taken into consideration and its behaviour during discharge is investigated. Time dependent numerical simulations are performed using Ansys-Fluent software for different thermal oil flow rate values. The use of metals and alloys or molten salts provides a high phase change temperature, which in turn enables a high sensible heat storage capacity along with a high latent heat storage opportunity. The high temperature values obtained in power plants require such storage media. For instance, Vigneshwaran et. al [4], performed an experimental and numerical investigation on a heat storage system which uses cast iron as the storing medium. They tested the system's thermal behaviour for different temperature ranges. Bashir and Giovannelli [5] evaluated Mg_2Si, MgSi and AlSb, which have very high melting temperature values, as thermal energy storage mediums integrated with a solar

receiver. They reported the optimum design point of the receiver. Zeneli et. al [6] evaluated silicon based latent heat energy storage system to achieve storage at very high temperatures. Different vessel designs and their effect on silicon melting rate were considered. Royo et al. [7] evaluated an energy storage tank for an industrial furnace and analysed the melting and solidification of the molten salt used as the phase change material.

This study aims to investigate performance of thermal energy storage system connected to feed stream of a power plant other standalone systems to support ancillary services for a case study in Turkey. System aims to balance grid by integrating into daily ancillary power market for load flow. Emphasis is put on the capability of responding economic benefits of the thermal energy storage system for grid operations.

2. SYSTEM DESCRIPTION AND SELECTION OF HEAT STORAGE MEDIA

A thermal power plant is selected as a case since it already has thermal energy to electricity conversion capacity, and proposed system can be applied with a minimum capital investment for current infrastructure. The layout of the proposed system is given in Figure 1. The system store heat in times of grid needs load management of demand side and increases the temperature of the fluid fed to turbines when demand increases, and grid need reserve power. In case there is no demand for load from the system, energy is stored from grid tariff which is lower than reserve prices. Induction is used to store thermal energy and system discharge is through a network of heat exchangers.

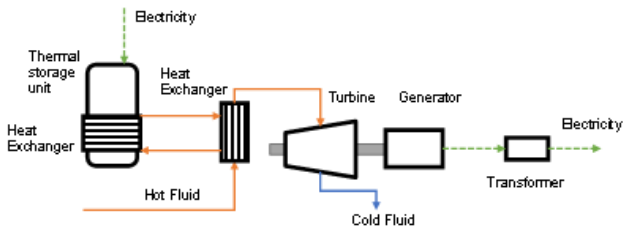

Figure 1 Proposed system layout

Firstly, different metals are inspected for their capacity to satisfy requirements for curtailment applications of heat storage by proposed system. Curtailment minimization services use energy storage to absorb that cannot be injected into the electricity grid due to lack of demand, either delivering it to the electricity grid when needed or converting it into another energy vector to be delivered to the relevant grid. These services are utilized a few times a day and typically they have an energy storage range of size range of 1 kW to 1 GW, discharge duration range of 20 minutes to 1.5 h. In the proposed system, turbines are already operational and increased steam input can be reflected to nominal values in less than 30 seconds [8].

Induction heating (IH) is preferred since it offers contactless, fast, and efficient heating of conductive materials with delivered power efficiency of 90% [9]. Because of its contactless nature and fast response times, it is selected for thermal energy loading for the system. Thus, fast load use and charge of the system can be applied within grid management criteria for load management systems. There is a wide range of parameters for selection of thermal storage material which can be charged by induction heating yet density, latent and sensible heat, and penetration dept of the material during induction are considered in selection.

The depth of this current flow is influenced by different material properties. This depth is called penetration depth and is given by Eq. 1;

$$\delta = \sqrt{\frac{\rho}{\pi f \mu}} \tag{1}$$

where, ρ is specific electrical resistance, μ is permeability and f is frequency. This effect causes approximately 86% of the power will be concentrated in the current penetration depth [10]. Thus, to achieve a fast and uniform heating through induction of the heat storage material zinc, aluminum, copper, mild carbon steel, nickel and tin are considered as candidates and penetration depths are calculated and compared.

Penetration depts calculations of candidate metals that were used select heat storage materials are given in Figure 2. Mild carbon steel and tin has the highest and very similar penetration depths.

Tin is selected over iron since tin melts at 232 °C and its phase change in target heat storage range gives an opportunity to use latent heat together with sensible heat unlike mild carbon steel which melts at between 1350 to 1530 °C based on its carbon concentration.

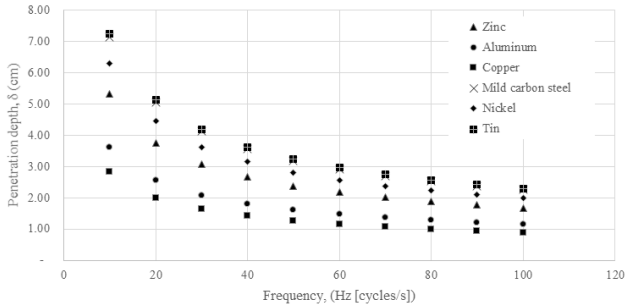

Figure 2 Calculated penetration depth of the storage material candidates.

3. CONSIDERED THERMAL ENERGY STORAGE TANK

3.1. Dimensions of the Thermal Energy Storage Tank

The schematic view of the considered thermal energy storage tank is presented in Figure 3. It is consisted of a cylindrical tank with a 0.5 (m) diameter and 0.5 (m) height. The total volume of the tank is approximately 0.1 (m^3). There are 41 vertical cylindrical pipes made of aluminum with an inside and outside diameter of 26.9 (mm) and 33.7 (mm), respectively.

Table 2
Thermophysical Properties of Tin and Therminol XP Heat Transfer Fluid

	Tin [11]	**Therminol XP [12]**
Density (kg/m^3)	6990	761
Specific heat solid (J/kg.K)	209.34	2600
Thermal conductivity (W/m.K)	28.28	0.0933
Viscosity (kg/m.s)	1.2×10^{-3}	8.41×10^{-4}
Latent heat of fusion (J/kg)	59,000	-
Melting point (°C - K)	232 (505)	-

The inside of the tank is filled with tin metal with the thermophysical properties given in Table 2. The energy extraction is modelled and solved in the current study, so therminol XP heat transfer fluid is sent to the tank through the the cylindrical pipes with different velocities in order to observe what will be the extraction of the storage thermal energy inside the tank. The thermophysical properties of the therminol XP heat transfer fluid is also summarized in Table 2.

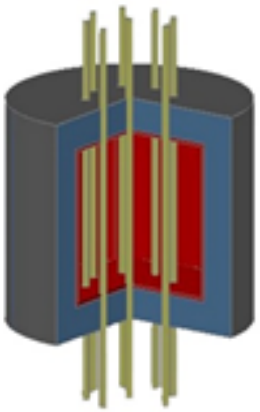

Figure 3 Schematic view of the considered thermal energy storage tank.

3.2. Numerical Modelling of the Thermal Energy Storage Tank

As the tank and the pipes passing through the tank constitute a symmetrical geometry, only ¼ of the whole tank is modelled with Space Claim software and then meshed using Ansys-Fluent R19 software as illustrated in Figure 3 and Figure 4. As it can be seen from Figure 4, the inside part of the pipes, through which therminol XP heat transfer oil flows, is meshed finer with a fine boundary layer in order to solve the flow field.

Side view of the generated meshes can be seen in Figure 4. After many trials, it is decided to use 500 elements along the height of the storage tank model in order to get stable and physically realistic results. The total control volume number for the entire storage tank model is 10,773,600. As, the storage tank is symmetrical, the side surfaces except the curved one which is the wall of the storage tank, are defined as symmetry. All the other surfaces are defined as wall, and it is assumed that the entire storage tank is perfectly isolated. The inside of the storage tank is defined as tin material, while the pipes are defined as aluminum and the inside volumes of the pipes are

defined as therminol XP heat transfer fluid. The upper sides of the pipes are defined as velocity inlet surfaces, where the velocity of therminol XP is defined as 0.01, 0.05 and 0.1 (m/s) for different cases and the inlet temperature is defined as 102 °C (375 K), which is a typical value of the return geothermal fluid for a geothermal plant, for all cases. The exit surfaces of the pipes are defined as outflow. The initial temperature is taken as 250 °C (523 K) for the thermally full charged storage tank. Finally, the time step is taken as 5 (s) and iterations are continued until the convergence criteria of 10^{-3} for continuity, 10^{-6} for momentum and 10^{-8} for energy equations are achieved.

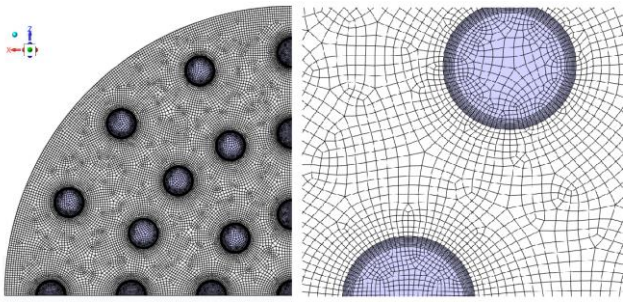

(a) (b)

Figure 4 a) Upside view of the meshes for the evaluated ¼ segment of the thermal energy storage tank, b) Closer view of the meshes

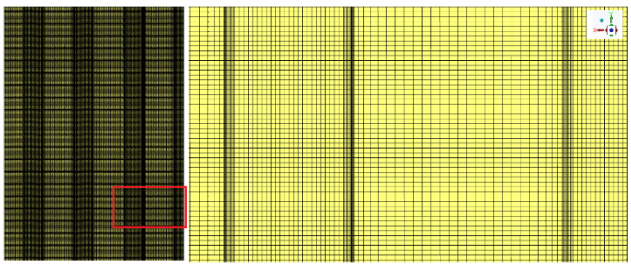

(a) (b)

Figure 5 a) Side view of the meshes for the evaluated ¼ segment of the thermal energy storage tank b) Closer view of the meshes

3.3. Numerical Results

As a result of simulations with therminol inlet velocities of 0.01 (case 1), 0.05 (case 2) and 0.1 (case 3) (m/s), it is found that the discharge period is the longest for case 1 as expected, followed by case 2 and the shortest discharge period is for case 3. It is also concluded that the discharge time can be kept between 15 minutes and 1 hour with the evaluated configuration, which falls inside the recommended discharge time of 20 (mins) to 1.5 (hrs). In Figures 6, 7 and 8, the temperature distribution and the liquid fraction of tin material are illustrated. It can be seen from Figure 6 that for the case 1, with a 0.01 (m/s) therminol XP inlet velocity, there is still some small portion of unsolidified tin even at the end of one hour, and the temperature of the tin starts to decrease from the solidifying temperature of 505 (K). When the therminol velocity increases to 0.05 (m/s) (case 2), a similar case is encountered at the end of 30 minutes. However, for the case 3, where the inlet velocity of therminol XP is 0.1 (m/s), the solidifying process is significantly faster and at the of 15 minutes, nearly all tin material solidifies. The reason of this fast solidifying process for the case 3 is that the therminol flow becomes turbulent when its velocity is 0.1 (m/s), while the flow is laminar for the velocity values of 0.01 (m/s) and 0.05 (m/s). As a final outcome, the heat discharge rate and the complete solidifying process time can be controlled by adjusting the therminol inlet velocity and the desired discharge time can be reached in the therminol XP inlet velocity range.

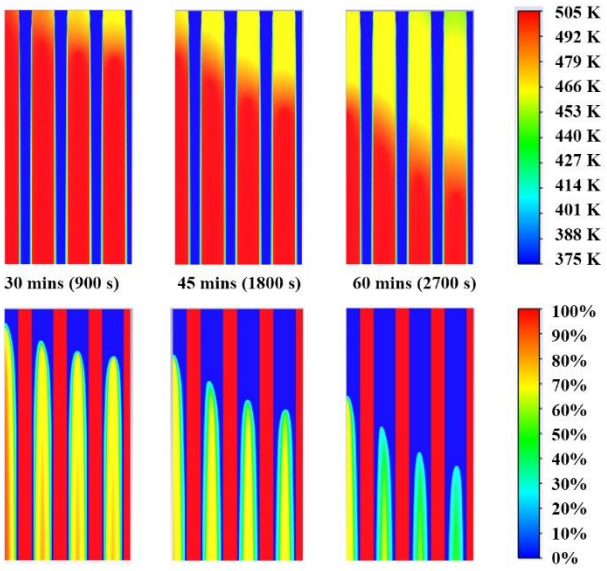

Figure 6 The temperature distribution (upper figures) and the liquid fraction (lower figures) of tin material for case 1

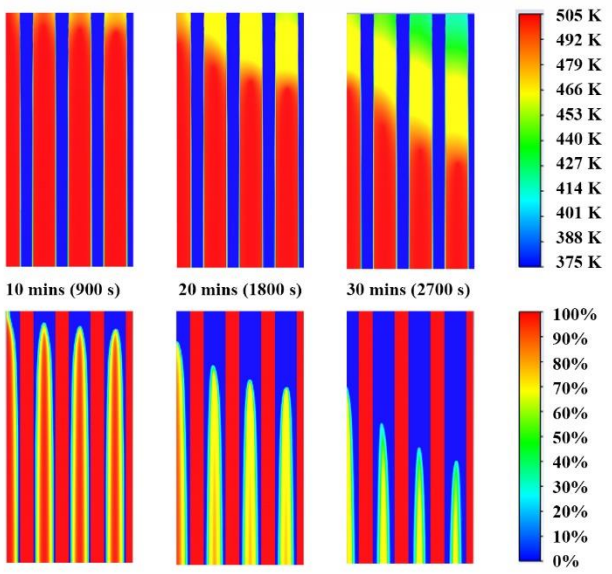

Figure 7 The temperature distribution (left figures) and the liquid fraction (right figures) of tin material for case 2.

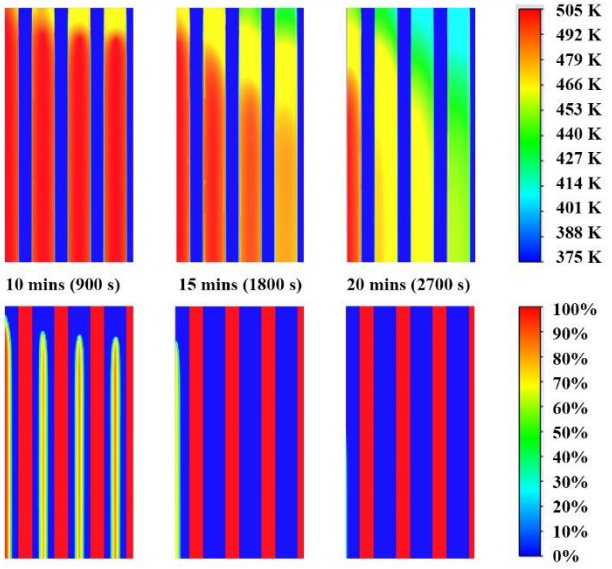

Figure 8 The temperature distribution (left figures) and the liquid fraction (right figures) of tin material for case 3.

4. ECONOMIC ANALYSIS

Study on the entire 2020-year hourly grid data supplied from Turkish Electricity Transmission Corporation energy market management system transparency tool [13] shows that 6,268 hours system support need for a total of 5,332 GWh energy, and demand site management requires 5,776 hours of operation with 3,203 GWh energy to be used to balance the system. Hourly demands for both operations are studied to find possible points for storage and discharge cycles for the described system. The hourly grid support and load management data are given Figures 9 and 10.

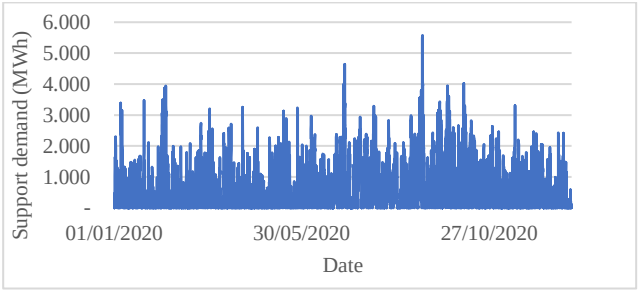

Figure 9 Turkey electric grid ancillary systems hourly support demand data.

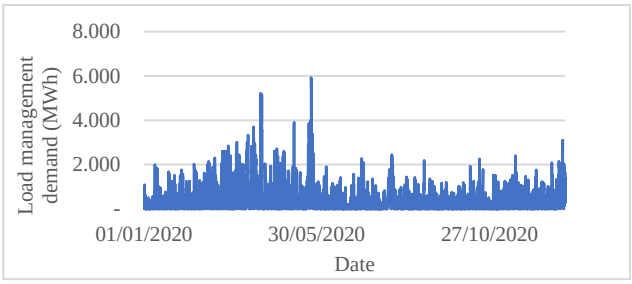

Figure 10 Turkey electric grid ancillary systems hourly load management data.

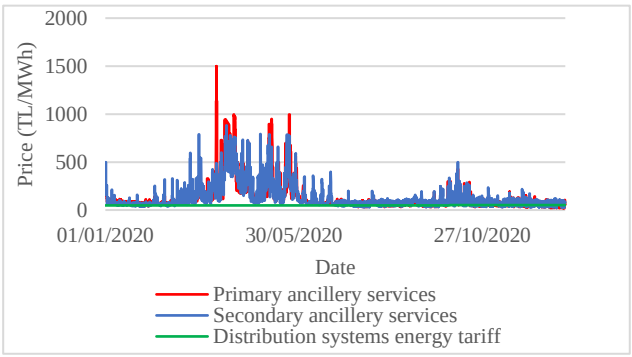

Figure 11 Hourly dynamic rates for ancillary services for both services and grid system tariffs throughout 2020

Modelling studies show that the system can satisfy response time needs stated for ancillary services, and different operational temperature capacities are compared for 1 unit with 1 m^3 of heat storage material tin and shown in Figure 11. The stored thermal energy at maximum temperature is calculated by the relationship given below;

$$Q = m_{sto}C_{p,solid}(T_{melt} - T_{min}) + m_{sto}L_{sto} + m_{sto}C_{p,liquid}(T_{max} - T_{melt}) \quad (2)$$

where, m_{sto} = mass of thermal storage material

$C_{p,solid}$ = specific sensible heat of thermal storage material in solid phase

$C_{p,liquid}$ = specific sensible heat of thermal storage material in liquid phase

L_{sto} = latent heat of fusion of thermal storage material

T_{melt} = melting temperature of the of thermal storage material

T_{min} = Minimum practical operational temperature of the unit

T_{max} = Maximum thermal storage temperature of the unit

As expected, heat storage capacities are increasing as the maximum heat storage temperature increases as shown in Figure 12. Yet maximum temperature that can be applied when conventional materials used in the feasibility study is limited to approximately 1,000 °C. Thus, this temperature is chosen as the maximum operating temperature for economic analysis. Designed storage unit contains 1m^3 of tin for heat storage. Details of each storage unit is given in Table 3 where 2 units working together were considered for economic analysis.

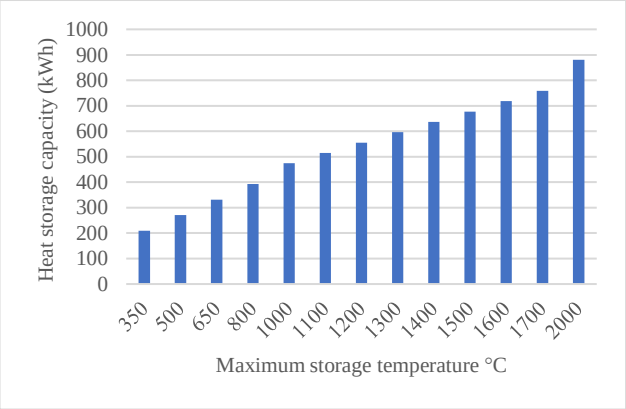

Figure 12 Calculated heat storage capacities of units with 1 m^3 of heat storage material.

Table 3
Details on heat storage unit

Heat storage medium	Tin
Density of heat storage medium (g/cm^3)	6.99
Mass of heat storage medium (kg)	6,990
Volume of heat storage medium (m^3)	1
Module geometry	cylinder
Specific Heat Capacity Solid (j/g°C)	0.2177
Specific Heat Capacity liquid (j/g°C)	0.2093
Latent Heat of Fusion (j/g)	59
Melting Point (°C)	232
Boiling Point (°C)	2,602
Lowest operational Temperature (°C)	120
Highest operational Temperature (°C)	1,000
Heat storage capacity (j)	1,706,657,732
Heat storage capacity (Kcal)	40,7901.4
Heat storage capacity (kWh)	474.1

The revenue streams are calculated by hourly pricing scheme described in detail by Electricity Market Ancillary Services Regulation [14]. Energy supplied to the grid is calculated with storage and conversion efficiencies of 98% and 60% respectively. Following discharge operation system is charged with the benefit of load management services to gain extra revenue, else grid system services tariff is used for charging of the system where induction heating efficiency of 90% was used. 2020 daily market data shows that a total of 6312 cycles can be completed with a 0.95 MW thermal energy stored and 0.50 MW delivered to the system. Hourly prices vary between 18 to 1499 TL/MWh with an average of 135.2 TL for primary and 25 to 844 TL/MWh with an average of 139.1 TL for secondary markets. Hourly data are directly used in calculations rather than averages, which yields to 133.68 TL/cycle average revenue. And yearly cumulative total revenue for 2020 case is calculated as 843,811.72 TL for 2-unit system.

Net present value (NPV) and return of investment (ROI) methods are used to evaluate the performance of the system. The NPV value of required investment by the discounted sum of all cash flows received is shown below.

$$NPV = \sum_1^n \frac{R_t}{(1+i)^n} \quad (3)$$

where,

R_t = Net cash flow at time t

i = interest rate

t = time of the cash flows

Average yearly interest rate, 12.43%, where operational lifetime of the system is taken as 20 years. ROI is calculated by;

$$ROI = \frac{Net\ return\ of\ investment}{cost\ of\ investment} \times 100\% \qquad (4)$$

The results for the calculations of economic analysis are given in Table 4, where ROI is 16% and NPV is 6,136,685.64 TL, which is 17.8% higher than current investment required. Based on study of Zhou et. al., investors typically require making returns of at least 10 – 11% since renewable or green energy markets are considered as stable [15], thus the proposed system is found above investor requirements.

Table 4
Results of economic analysis.

Number of units	2
Unit system cost (TL)	2,027,057.50
Unit Storage material cost (TL/kg)	165.50
Unit Total Storage material cost (TL)	578,422.50
Total system Cost (TL)	5,210,960.00
Interest	12.43%
Investment lifetime	20
NPV (TL)	6,136,685.64
ROI	16%

5. CONCLUSIONS

This study investigates the performance and economic benefits of the thermal energy storage system for Turkey as a case for ancillary services. The following conclusions are gained:

- The evaluated heat storage tank, filled with tin, provides adequate time for discharging the stored energy.
- Current regulations of daily energy market make it possible to use the proposed system with a 0.95 MW thermal energy stored and 0.50 MW delivered to the system for 6,312 cycles. Larger systems can also benefit similarly yet there is a trade-off for slightly lower market opportunities.
- Proposed system shows better economic performance than investment requirements where system ROI is 16% and NPV is 6,136,685.64 TL, which is 17.8% higher than investment required.
- The real obstacle for reaching higher economic and practical gain is materials and equipment that can withstand higher temperatures above 1,000 °C. Also, higher temperature heat transfer fluids are required.

Acknowledgments

The authors gratefully acknowledge the support from Yaşar University.

Funding

This study is supported by Yaşar University under the grant; Yaşar Üniversitesi – Scientific Research - No: BAP-080.

The Declaration of Conflict of Interest/ Common Interest

No conflict of interest or common interest has been declared by the authors.

Authors' Contribution

The authors contributed equally to the study.

The Declaration of Ethics Committee Approval

This study does not require ethics committee permission, or any special permission" should be included under this heading.

The Declaration of Research and Publication Ethics

The authors of the paper declare that they comply with the scientific, ethical and quotation rules of SAUJS in all processes of the paper and that they do not make any falsification on the data

collected. In addition, they declare that Sakarya University Journal of Science and its editorial board have no responsibility for any ethical violations that may be encountered, and that this study has not been evaluated in any academic publication environment other than Sakarya University Journal of Science

List of symbols

T_{melt}	Melting Temperature of the of Thermal Storage Material
T_{min}	Minimum Practical Operational Temperature of the Unit
T_{max}	Maximum Thermal Storage Temperature of The Unit
m_{sto}	Mass of Thermal Storage Material
$C_{p,solid}$	Specific Sensible Heat of Thermal Storage Material in Solid Phase
$C_{p,liquid}$	Specific Sensible Heat Of Thermal Storage Material in Liquid Phase
L_{sto}	Latent Heat of Fusion of Thermal Storage Material
R_t	Net Cash Flow at Time t
I	Interest Rate
t	Time of The Cash Flows
ρ	Specific Electrical Resistance
μ	Permeability
f	Frequency
δ	Penetration Depth

List of Abbreviations

EU	European Union's
GHG	Greenhouse Gas
RE	Renewable Energy
EC	European Council
IH	Induction heating
NPV	Net present value
ROI	Return of Investment
STES	Sensible Thermal Energy Storage
LTES	Latent Thermal Energy Storage
TCES	Thermo-Chemical Energy Storage

REFERENCES

[1] Roadmap 2050, A Practical Guide to A Prosperous, Low-Carbon Europe Technical Analysis, https://www.roadmap2050.eu/attachments/files/Volume1_fullreport_PressPack.pdf, (Accessed: 08.03.2021).

[2] ITRE (Committee on Industry, Research and Energy), "Follow up to the European Parliament non-legislative resolution on a comprehensive European approach to energy storage", P9_TA-PROV (2020) 0198, 10 July 2020.

[3] B. Cárdenas, L. Noel, "High temperature latent heat thermal energy storage: Phase change materials, design considerations and performance enhancement techniques" Renewable and Sustainable Energy Reviews, vol.27, pp.724-737, 2013.

[4] K. Vigneshwaran, G.S. Sodhi, P. Muthukumara, A. Guhac, S. Senthilmurugana, "Experimental and numerical investigations on high temperature cast steel based sensible heat storage system" Energy, vol. 251, 113322., 2019.

[5] M.A. Bashir, A. Giovannelli, "Design optimization of the phase change material integrated solar receiver: A numerical parametric study". Applied Thermal Engineering, vol. 160, 114008., 2019.

[6] M. Zeneli, I. Malgarinos, A. Nikolopoulos, N. Nikolopoulos, P. Grammelis, S. Karellas, E. Kakaras, "Numerical simulation of a silicon-based latent heat thermal energy storage system operating at ultra-high temperatures" Applied Energy, vol. 242, pp. 837-853, 2019.

[7] P. Royo, L. Acevedo, V.J. Ferreira, T. García-Armingol, A.M. Lopez-Sabiron, G. Ferreira, "High-temperature PCM-based thermal energy storage for industrial furnaces installed in energy-intensive industries". Energy, vol. 173, pp. 1030-1040, 2019.

[8] M. Dulau, B. Dorin, "Mathematical modelling and simulation of the behaviour of the steam turbine" Procedia Technology vol.12, pp. 723-729, 2014.

[9] O. Lucía, P. Maussion, E. J. Dede, J. M. Burdío, "Induction heating technology and its applications: past developments, current technology, and future challenges" IEEE Transactions on industrial electronics, vol. 61, no. 5, pp. 2509-2520, 2013.

[10] V. Rudnev, D. Loveless, R.L. Cook, "Handbook of induction heating" CRC press, 2017.

[11] Wikipedia, Tin Physical Properties, https://en.wikipedia.org/wiki/Tin, accessed: 03.05.2021

[12] Therminol, Therminol XP Physical Properties, https://www.therminol.com/sites/therminol/files/documents/TF-8694_Therminol_XP_Technical_Bulletin.pdfi, accessed: 03.05.2021

[13] Turkish Electricity Transmission Corporation energy market management system transparency tool, https://tpys.teias.gov.tr/, accessed April 2022

[14] TEİAŞ, Turkish Electricity Transmission Corporation, "Electricity Market Ancillary Services Regulation", Elektrik Piyasasi Yan Hizmetler Yönetmeliği, 26.20.2018, Official Gazette (in Turkish)

[15] X. Zhou, W. Christian, C. Ben, "The energy transition and changing financing costs", Oxford Sustainable Finance Programme, Smith School of Enterprise and The Environment, University of Oxford, April 2021.